SEQUENTIAL AND INCOMPLETE FUSION BREAK-UP REACTIONS WITH 70 MeV ^{7}Li

Thesis

Submitted by

THOMAS DAVINSON, B.Sc.

for the degree of

DOCTOR OF PHILOSOPHY

Department of Physics,

University of Edinburgh,

SEPTEMBER, 1986.

'The British postgraduate student
is a lonely, forlorn soul, uncertain
of what he is doing or whom he is
trying to please ....'

David Lodge,
"Changing Places".

ABSTRACT

The mechanisms involved in the production of fast particles in ^{7}Li induced reactions on ^{12}C, ^{60}Ni, ^{96}Zr, ^{120}Sn and ^{208}Pb at a bombarding energy of 70 MeV have been investigated.

The total break-up yield has been estimated by inclusive measurements of $Z = 1$ and $Z = 2$ charged particles. Large yields of d,t and α-particles were observed. The total break-up yield represents a substantial fraction of the reaction cross section.

To determine the reaction mechanisms involved and their quantitative contribution to the total break-up yield, exclusive experiments have been performed.

Kinematically complete particle-particle coincidence measurements unambiguously identified the sequential break-up reactions $(^{7}Li, {}^{7}Li^{*}_{4.63} \rightarrow \alpha + t)$, $(^{7}Li, {}^{6}Li^{*}_{2.18} \rightarrow \alpha + d)$, $(^{7}Li, {}^{8}Be_{gs} \rightarrow \alpha + \alpha)$ and $(^{7}Li, {}^{8}Be^{*}_{2.94} \rightarrow \alpha + \alpha)$. The reaction mechanism involved is production of a particle unstable ejectile (by inelastic excitation and/or particle transfer) in a peripheral collision with the target. In addition, a non-sequential (or 'direct') reaction mechanism has been identified for α-t coincidences from ^{96}Zr, ^{120}Sn and ^{208}Pb. Absolute cross-sections are presented.

Particle γ-ray coincidence measurements for the reactions $^{7}Li + {}^{120}Sn$ and $^{7}Li + {}^{208}Pb$ determined the absolute yields for the incomplete fusion reaction channels. The dominant reaction channels were $(^{7}Li, \alpha x n \gamma)$ and $(^{7}Li, t x n \gamma)$.

DECLARATION

Except where indicated, the data presented in this thesis was obtained by myself and other members of the Edinburgh Nuclear Physics Group. The data analysis and interpretation is entirely my own work. This thesis has been composed by myself.

ACKNOWLEDGEMENTS

I would like to thank:

My supervisors, Dr. Alan Shotter and Dr. Derek Branford for their enthusiasm, support, encouragement and patience.

Dr. Neil Sanderson for advice, abuse and for teaching me much of how experiments should be done.

Dr. Volker Rapp and his amazing fingers.

Dave Brightly, Peter Noake and Vic Pucknell for their help and great patience on software matters both trivial and non-trivial.

Rob Berry, Joe Salvini and Ken Wray for their help with the data collection hardware.

Janet Groves who prepared the silicon surface barrier detectors used in this work.

The N.S.F. crews who provided the beams.

Dr. Peter Twin, Director of the N.S.F., for affording me the use of the facilities there.

Dr. Alan Flowers for his help in the hardware 'wars' of 1982.

Ian Yorkston for his help on some of the data collection runs.

Gordon Turnbull, the Edinburgh Nuclear Physics Group technician, who made detector mounts and other essential experimental components.

Professors Cowley and Wallace, the Heads of the Edinburgh University Physics Department, for the use of facilities there.

The S.E.R.C. for providing a research studentship.

Mrs. Chester for her skill and hard work in producing a typescript to her usual high standards.

Denise, for perspective, nagging, support and a decent cup of coffee.

My parents, who continue to wonder when I will get a 'real' job, but who loved and encouraged me anyway.

CONTENTS

C O N T E N T S (Contd.)

CHAPTER 1

INTRODUCTION

> 'For most readers this will be warning enough.
> ... The book [sic], is not, and was not intended
> to be, either synoptic or encyclopaedic. It is
> not a vade mecum, but a cursus infamam'
>
> James Blish, 'Faust Aleph-Null'

1.1 Preamble

A large amount of data exists on light ($A \lesssim 4$) and heavy-ion induced reactions. Different reaction modes are identifiable (Figure 1.1). The continuum region represents a significant fraction of the total reaction cross section and is generally interpreted as break-up of the projectile in a peripheral collision with the target. Of current interest, are the break-up reaction mechanisms which contribute to this continuum region.

Deuteron break-up was the first and most generally studied break-up process. Oppenheimer and Phillips (Op 35a, Op 35b) proposed a model where the interaction of the deuteron in a Coulomb field causes break-up. The experiments of Helmholz et al. (He 47) studied deuteron break-up at high incident energies where the nuclear field became the main cause of break-up. Helmholz observed a narrow beam of neutrons from 190 MeV deuterons on a variety of targets. The average energy of the neutrons was found to be close to that of the beam velocity. These results prompted Serber (Se 47) to develop a simple geometric model which still forms a basis for understanding this type of reaction.

Light-ion induced reactions have been extensively analysed

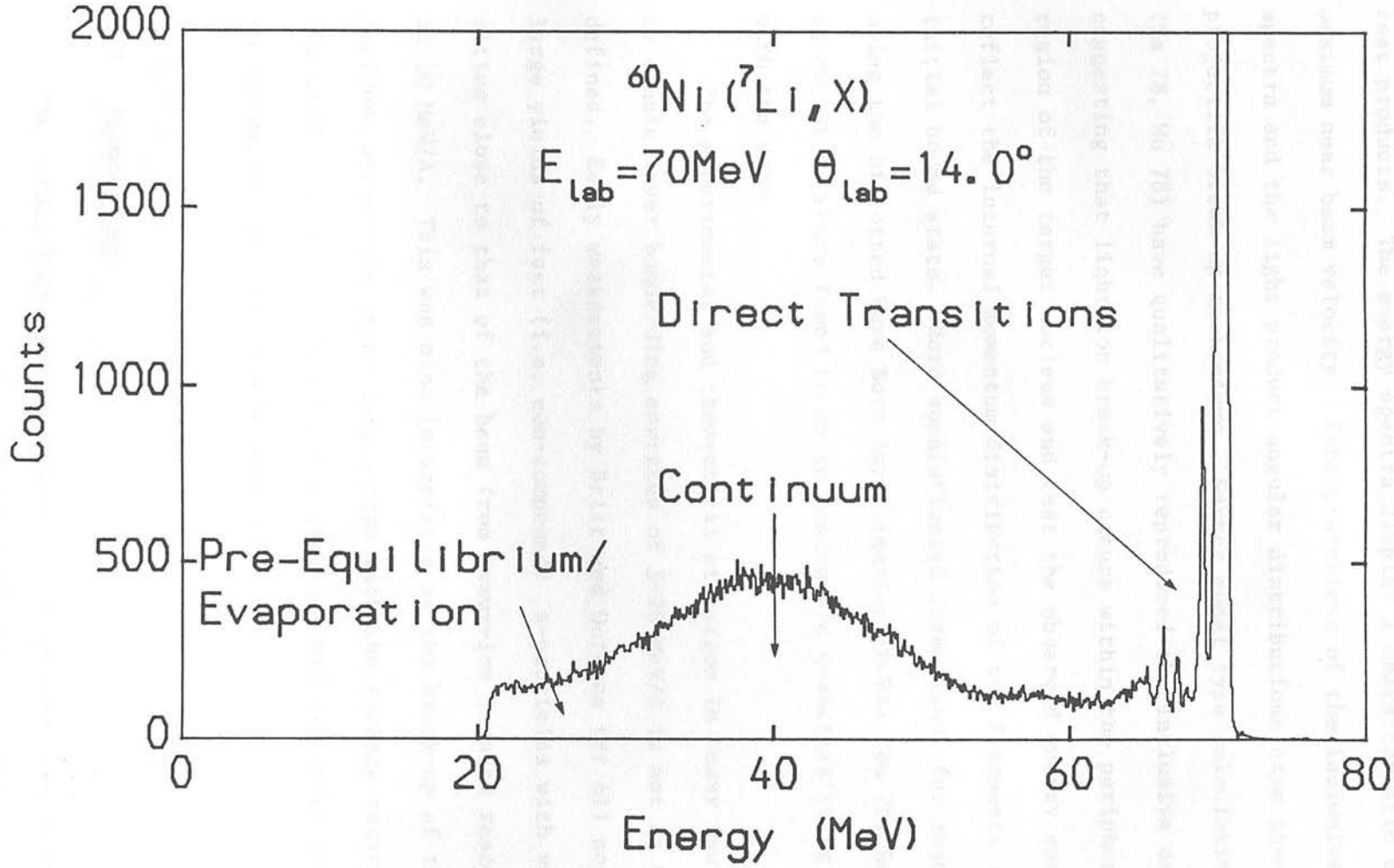

Figure 1.1: Energy spectrum showing features typical of light ion and heavy-ion induced reactions in the energy range 5 - 20 MeV/A.

(Se 47, Ma 78, Wu 78, Bu 78). It is observed that a large fraction of the total reaction cross section goes into the production of lighter, fast products. The energy spectra display a characteristic broad maximum near beam velocity. Interpretations of the inclusive energy spectra and the light product angular distributions have involved projectile break-up mechanisms. Serber model type calculations (Ma 78, Wu 78) have qualitatively reproduced the inclusive data suggesting that light-ion break-up occurs within the peripheral region of the target nucleus and that the observed energy spectra reflect the internal momentum distribution of the fragments in their initial bound state. More sophisticated formalisms, for example using the Distorted Wave Born Approximation (DWBA) (Bu 78, Ba 80b, Sh 80, Sh 84b) are found to be in reasonable quantitative agreement with the data.

The experimental and theoretical situation in heavy ion break-up studies over bombarding energies of 5-20 MeV/A is not as well defined. Early measurements by Britt and Quinton (Br 61) noted large yields of fast (i.e. non-compound) α-particles with velocities close to that of the beam from heavy-ion induced reactions at 10 MeV/A. This was also interpreted as the break-up of the incident projectile in an interaction with the surface region of the target nucleus. However, only recently has attention focussed on the mechanisms involved in such reactions.

1.2 Terminology

The terminology used by workers studying light and heavy-ion break-up reactions is both confused and confusing. Set out below

are some key words and their definitions within the context of this thesis. Preferred terminology is signified by an asterisk. Some definitions are illustrated schematically in Figure 1.2.

Break-up*; fragmentation*

These terms have the same meaning. A reaction (irrespective of mechanism) with three or more particles in the final state.

Elastic break-up*

A break-up reaction with the target remaining in the ground state.

Inelastic break-up*; non-elastic break-up; spectator break-up

Break-up reaction (e.g. $a+A \rightarrow b+x+A \rightarrow b+B$) in which fragment b is emitted. A+x interact strongly but the reaction mechanism (inelastic, transfer, compound, etc.) is not specified.

Sequential break-up*; resonance break-up

A break-up reaction in which the interaction of the projectile (or projectile-like fragment) in the nuclear and/or Coulomb field of the target produces an ejectile in a definite state above particle threshold and subsequently decays into the particle channel. Note that some authors also use the term non-sequential break-up* (or direct break-up or fragmentation) to distinguish reaction modes which are not associated with an excited state of the projectile (or PLF).

Incomplete fusion*; massive transfer, break-up fusion

These terms have the same meaning. Break-up reaction in which fragment b is emitted. The subsystem A+x fuses and generally de-excites by emission of protons, neutrons, γ-rays and/or by fission.

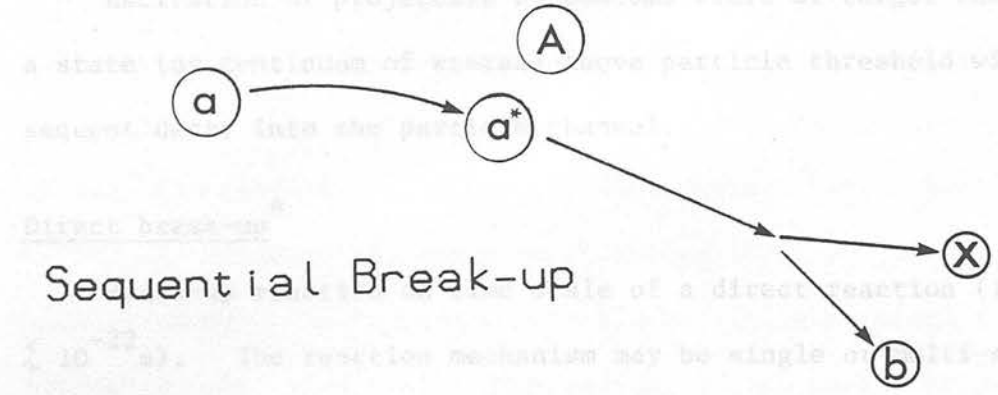

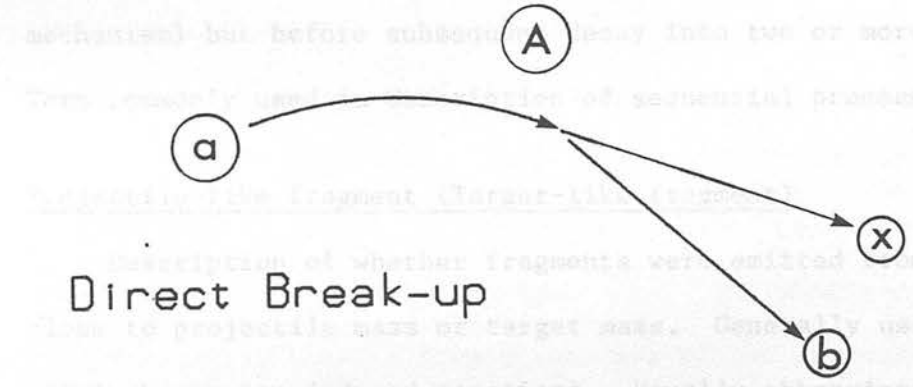

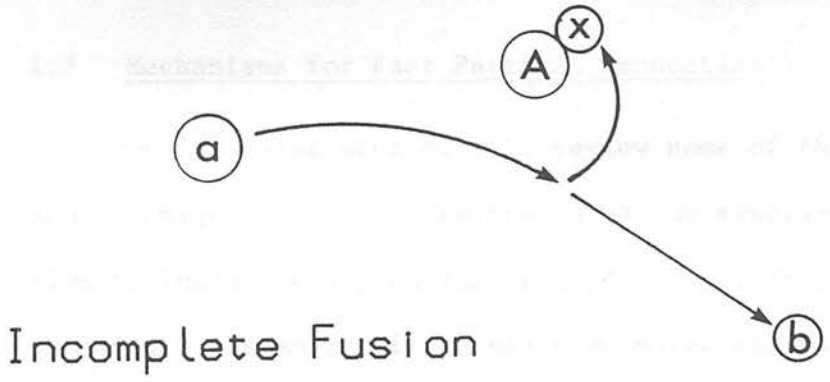

FIGURE 1.2: Pictorial illustration of some of the reaction mechanisms defined in Section 1.2.

Coulomb break-up*

Excitation of projectile by Coulomb field of target nucleus to a state (or continuum of states) above particle threshold with subsequent decay into the particle channel.

Direct break-up*

Break-up reaction on time scale of a direct reaction (i.e. $\lesssim 10^{-22}$ s). The reaction mechanism may be single or multi-step.

Ejectile*

Projectile after interaction with target (irrespective of mechanism) but before subsequent decay into two or more fragments. Term commonly used in description of sequential processes.

Projectile-like fragment (Target-like fragment)

Description of whether fragments were emitted from ejectile close to projectile mass or target mass. Generally used in asymmetric heavy-ion induced reactions. Usually abbreviated to PLF (or TLF).

1.3 Mechanisms for Fast Particle Production

The following section will review some of the theoretical models and techniques used to interpret break-up reactions. Their application to inclusive and exclusive experimental measurements will be examined. A summary of exclusive measurements of heavy-ion induced break-up reactions and their interpretation will be presented.

(a) Spectator-participant model

A simple heuristic model for the basic mechanism of the break-up

process is the spectator participant model. The projectile is considered to be a bound cluster pair (say, b+x). In a peripheral collision with a heavy target, one of the clusters, say x, may interact with the target (the participant) and the other, b, which is observed (the spectator) may be left undisturbed. This is equivalent to the geometric approach of Serber (Se 47). This model usually assumes the target to be a black (i.e. absorbing) sphere of radius R. If a projectile with radius r has an impact parameter $r_{int} < (R - r)$ it will be absorbed (no break-up). If the impact parameter $r_{int} > (r + R)$ (i.e. large), there is no break-up (ignoring Coulomb effects). In peripheral collisions, $(R+r) > r_{int} > (R-r)$ there is a probability that part of the projectile will interact (the exact nature of the interaction is unimportant at this stage) with the target while the other continues undisturbed with its original velocity. The observed fragment energy spectrum results from a coupling of the internal momentum distribution of the constituents of the projectile to the projectile velocity in the laboratory frame of reference. This is then multiplied by a phase space factor. If the probability that a given fragment has momentum $\underline{p}$ in the projectile is

$$P(\underline{p}) = |\psi(\underline{p})|^2 \tag{1.1}$$

where

$$\psi(\underline{p}) = \frac{1}{\hbar^{3/2}} \int \psi(r)\exp[-(i/\hbar)\underline{p}\cdot r]d^3r \ . \tag{1.2}$$

and $|\psi(r)|^2 d^3r$ is the probability of a spectator-participant separation r in volume element d^3r. The differential cross section may be written as

$$\frac{d^2\sigma}{d\Omega_b dE_b} \propto |\psi(\underline{p})|^2 \, m_b \, (2m_b E_b)^{\frac{1}{2}} \qquad (1.3)$$

where $\underline{p} = \underline{p}_b - \underline{p}_{beam}$ and fragment x is absorbed by the target nucleus. This model was applied successfully to the data of Helmholz et al. (He 47) who studied the bombardment of Be, Cu and U targets by 190 MeV deuterons. Angular distributions, peak energies and peak positions were satisfactorily reproduced, although a Coulomb correction was introduced to account for a systematic variation of the angular distributions with target Z. This model has also been applied to break-up reactions with ^{3}He and ^{4}He projectiles. Matsuoka et al. (Ma 78) studied 70 MeV ^{3}He + ^{90}Zr using a Yukawa type wave function for the internal motion of the constituents of the projectile. Wu et al. (Wu 78) examined 140 MeV ^{4}He + ^{209}Bi using an Eckart type wave function for the internal motion. Qualitatively, general trends of the peak energies, widths and angular distributions were reproduced. However substantial renormalisation of the angular distribution was required to obtain a fit to the data. Tabor et al. (Ta 81a) have analysed the shapes of inclusive energy spectra of outgoing fragments from ^{16}O and ^{18}O induced reactions at 72 and 141 MeV. A slightly modified version of the Serber model which assumed a two-body final state was found to be in better agreement with the data than a model involving a multibody final state.

Similar models have been developed for relativistic collisions ($\sim$ GeV/A). In the abrasion-ablation model the momentum distribution of the observed fragments is parameterised by a Gaussian distribution (Fe 73, Go 74).

$$\frac{d^3\sigma}{dp^3} \propto e^{-p^2/2\sigma^2} \qquad (1.4)$$

where

$$\sigma^2 = \sigma_o^2 \left[\frac{m_b (m_{proj} - m_b)}{m_{proj} - 1} \right] \quad (1.5)$$

and

$$\sigma_o^2 = \frac{p_F^2}{5} \quad (1.6)$$

where p_F is the Fermi momentum. Equation (1.4) may be transformed into the laboratory frame to obtain

$$\frac{d^2\sigma}{d\Omega_b dE_b} \propto m_b (2m_b E_{proj})^{\frac{1}{2}} \exp - \left[\frac{E_{proj} - 2(E_b E_{proj})^{\frac{1}{2}} \cos\theta + E_b}{\sigma^2} \right] \quad (1.7)$$

and it is possible to predict inclusive energy spectra and angular distributions. It should be noted that equation (1.4) may be deduced by assuming that fragmentation is based upon the equilibrium statistical decay of the projectile subsequent to its excitation to an effective temperature T giving (Go 74)

$$\sigma_b \propto \sum_i e^{-Q_i/T} \quad (1.8)$$

where Q_i is the threshold for the production of fragment b in a particular channel i, and

$$T = \frac{p_F^2}{5m} \quad . \quad (1.9)$$

Viyogi et al. (Vi 78) have reported 213 MeV/A ^{40}Ar induced reactions. The abrasion-ablation model satisfactorily reproduced the systematics of the normalised isotopic production cross sections. The projectile excitation model was found to be inadequate in this

respect. The value of p_F extracted from $\langle\sigma_o\rangle$ was found to be in disagreement with the value of p_F deduced from electron scattering experiments.

Buenard et al. (Bu 76) have examined the absolute and relative isotope production cross sections for $^{16}O + ^{208}Pb$ peripheral reactions at 20 MeV/A and 2.1 GeV/A. Two striking observations are made: the absolute inclusive isotope production cross sections are very similar for both energies and the relative element yields are the same for both energies. Hüfner et al. (Hu 77) noted that, whilst the cross-sections might be similar at 20 MeV/A and 2.1 GeV/A, the physics involved was different. The similarity was attributed to the peripheral nature of the collision in that only a few nucleons participated in the peripheral reaction and that the excitation cross section was limited by geometry. Within the context of a projectile excitation model this similarity may reflect that there is a limiting temperature to which fragments may be excited and still survive to be observed. If so, this saturation is effective at relatively low projectile energies, say $\sim$ 10 MeV/A.

(b) PWBA formalism

In the plane wave Born approximation (PWBA) it is assumed that the distortions of the scattering wave function by the nuclear and Coulomb fields are small. The scattering wave functions in the entrance and exit channels are therefore approximated by plane waves. In the spectator-participant approach (sometimes termed PWSM - plane

wave spectator model) the projectile a is considered to be a binary system (b+x) where b is the spectator and x the participant. The T-matrix element in the prior-form for the reaction a+A → b+x+A is given by

$$T_{if}^{prior} = \langle \chi_f^{(-)} | W_i | \chi_i^{(+)} \rangle \tag{1.10}$$

where

$$W_i = V_{xA}(\underline{r}_{xA}) \tag{1.11}$$

and

$$|\chi_i^{(+)}\rangle = e^{i\underline{q}_a \cdot \underline{R}_a} \phi_{bx}(\underline{r}_{bx})\phi_b(\xi_b)\phi_x(\xi_x)\phi_A(\xi_A) \tag{1.12}$$

$$\langle \chi_f^{(-)}| = e^{-i\underline{q}_b \cdot \underline{R}_b - i\underline{q}_x \cdot \underline{R}_x} \phi_b(\xi_b)\phi_x(\xi_x)\phi_A(\xi_A) \tag{1.13}$$

where ϕ represents the intrinsic wave functions of a, A, b and x and ξ their internal coordinates. Substituting (1.13) and (1.12) into (1.10) and integrating over the internal coordinates, the matrix element separates into

$$T_{if}^{prior} \propto \int V_{xA}(\underline{r}_{xA}) e^{-i(\underline{q}_a - \underline{q}_b - \underline{q}_x)\cdot \underline{r}_{xA}} d\underline{r}_{xA} \times \int \phi_{bx}(\underline{r}_{bx}) e^{-i\underline{q}\cdot \underline{r}_{bx}} d\underline{r}_{bx} \; . \tag{1.14}$$

The cross section is then proportional to the product of the square of equation (1.14) and a phase space factor. In accord with Serber's model the cross section is determined by the internal momentum space wave function of the projectile. However, in contrast with the Serber model, there is now a participant-target interaction expressed in terms of a T-matrix. Shyam et al. (Sh79b) demonstrated that (in

comparison with the Serber model) PWBA reduces the predicted width of the inclusive energy spectrum to approximately the values observed for the reactions ^{209}Bi (α, ^{3}He) at 140 MeV (Wu 78) and ^{62}Ni (α, ^{3}He) at 172.5 MeV (Bu 78). Values of the cross section obtained in this model grossly overestimated the experimental data. This is due to the break-up T-matrices being too large and is a consequence of the simplistic one-step approach employed. More realistic approaches would require the inclusion of more complex processes and absorption effects. Shyam et al. further concluded that the direct extraction of the momentum space wave function was not possible.

McVoy and Nemes (Mc 80) using a 'local momentum' PWBA concluded the ^{16}O + ^{208}Pb and ^{16}O + Au data of Gelbke et al. (Ge 77a, Ge78a) Bi 80b) at bombarding energies of 140-314 MeV result from direct fragmentation or transfer reactions into the continuum. The internal motion within the projectile is responsible for most of the width of the inclusive energy spectrum. The modified PWBA employing local (Coulomb corrected) rather than asymptotic momenta, handles both transfer and projectile break-up and distinguishes between final state wave functions for binary reactions only. However, the predicted widths for the two reactions differ by only 50%. It is concluded that this is insufficient to reliably distinguish the two reaction mechanisms. Further, the absolute magnitudes of the cross sections predicted by PWBA are totally unreliable. Again, this is a consequence of a naive participant–target interaction and the exclusion of more complex reaction processes.

(c) DWBA formalisms

The post-form DWBA T-matrix is defined as

$$T_{fi}^{post} = \langle \chi_f^{(-)} | W_f | \chi_i^{(+)} \rangle$$

where $\chi_f^{(-)}$ and $\chi_i^{(+)}$ are the distorted waves of the outgoing and incoming reaction channels. For the elastic break-up reaction $a+A \rightarrow b+x+A$ (where a is considered to be a bound cluster pair b+x) $|\chi_i^{(+)}\rangle$ and $\langle \chi_f^{(-)}|$ may be written as

$$|\chi_i^{(+)}\rangle = |\chi_a^{(+)} \phi_a \phi_b\rangle$$

$$\langle \chi_f^{(-)}| = \langle \chi_b^{(-)} \chi_x^{(-)} \phi_b \phi_x \phi_A|$$

and $$W_f = V_{bx}(\underline{r}_{bx})$$

where ϕ represents the intrinsic wave functions of a, A, b and x, ξ their internal coordinates and $\chi_a^{(+)}$, $\chi_b^{(-)}$ and $\chi_x^{(-)}$ represent the optical model scattering wave functions generated by the appropriate optical potentials. In the formalism of Baur et al. (Ba 76, Ba 84) the post-form T-matrix element may be written as

$$T_{\underline{q}_a \rightarrow \underline{q}_b \underline{q}_x} = \iint d^3r_{bx} d^3R_{A-bx} \chi_b^{(-)}(\underline{R}_{b-Ax})^* \chi_x^{(-)}(\underline{r}_{xA})^* \times V_{bx}(\underline{r}_{bx}) \phi_{bx}(\underline{r}_{bx}) \chi_a^{(+)}(\underline{R}_A - b_x) \qquad (1.15)$$

where q_i denotes the momenta of a, b and x in the initial and final states. The coordinate system is illustrated in Figure 1.3. To

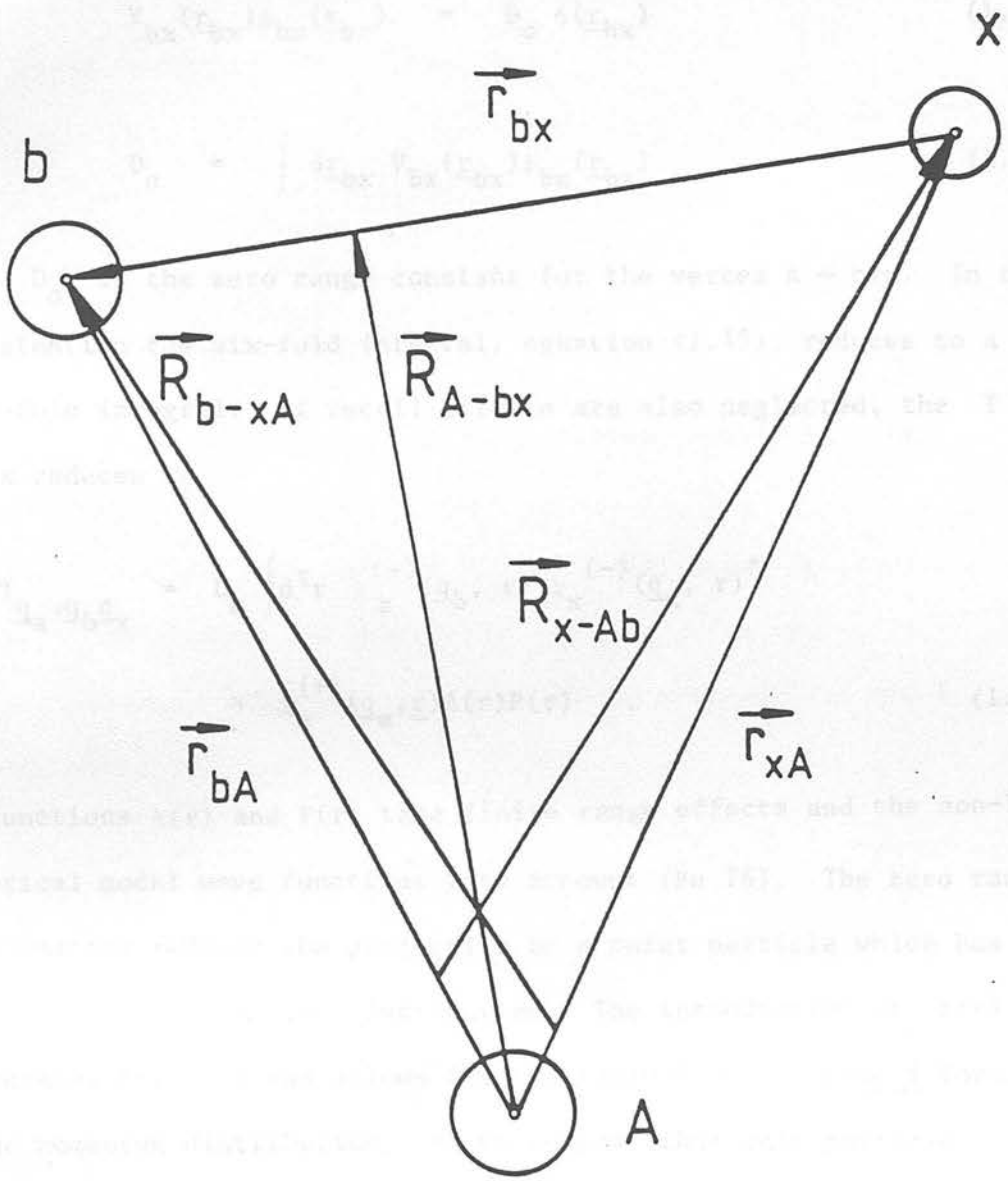

FIGURE 1.3: Coordinate system for DWBA calculations.

express the final state as a product wave function it is assumed that A is much heavier than a. The interaction of b and x is denoted by $V_{bx}(\underline{r}_{bx})$ and ϕ_{bx} is the internal wave function of a. For light-ion reactions, equation (1.15) is evaluated by introducing the zero-range approximation

$$V_{bx}(\underline{r}_{bx})\phi_{bx}(\underline{r}_{bx}) = D_o\,\delta(\underline{r}_{bx}) \tag{1.16}$$

where

$$D_o = \int d\underline{r}_{bx}\; V_{bx}(\underline{r}_{bx})\phi_{bx}(\underline{r}_{bx}) \tag{1.17}$$

where D_o is the zero range constant for the vertex a → b+x. In this approximation the six-fold integral, equation (1.15), reduces to a three-fold integral. If recoil effects are also neglected, the T matrix reduces to

$$T_{\underline{q}_a \to \underline{q}_b \underline{q}_x} = D_o \int d^3r\; \chi_b^{(-)}(\underline{q}_b,\, r)^* \chi_x^{(-)}(\underline{q}_x,\, r)^* \times \chi_a^{(+)}(\underline{q}_a, \underline{r})\Lambda(r)P(r) \quad . \tag{1.18}$$

The functions $\Lambda(r)$ and $P(r)$ take finite range effects and the non-locality of optical model wave functions into account (Ba 76). The zero range approximation reduces the projectile to a point particle which has an infinitely broad momentum distribution. The introduction of $\Lambda(r)$ compensates for this and allows for the inclusion of *a priori* forms of the momentum distribution. If we suppose that only particle b is detected, the contribution of the elastic break-up to the inclusive cross section can be obtained by integrating over the angle of emission of the unobserved particle x. This is achieved by a

partial wave expansion of the matrix element (1.15). The double differential cross section is then written as

$$\left.\frac{d\sigma}{d\Omega_b dE_x}\right|_{\text{elastic}} = \frac{m_a m_b m_x}{(2\pi)^5 \hbar^6} \frac{q_b q_x}{q_a} \sum_{\ell_x m_x} |T_{\ell_x m_x}|^2. \qquad (1.19)$$

$T_{\ell_x m_x}$ is a reduced T-matrix which is analogous to the T-matrix for bound state stripping and is given by

$$T_{\ell_x m_x} = D_o \int d^3r \, \chi_b^{(-)}(\underline{q}_b, \underline{r})^* \, \chi_{\ell_x}(\underline{q}_x, \underline{r}) Y_{\ell_x m_x}(\hat{\underline{r}})^*$$

$$\times \chi_a^{(+)}(\underline{q}_a, \underline{r}) \Lambda(r) P(r) \qquad (1.20)$$

where $Y_{\ell_x m_x}(\hat{\underline{r}})$ denotes the spherical harmonic describing the angular dependence of the wave function $\chi_{\ell_x}(\underline{q}_x, \underline{r})$.

The inclusive cross section for inelastic break-up reactions may be extracted from the transition amplitudes for the elastic break-up process, using the unitarity of the S-matrix for the break-up reaction

$$a + A \rightarrow b + \{A + x\}_c \qquad (1.21)$$

where c is a definite two-body final state of the system $B = A + x$.

The T-matrix is now evaluated by substituting $\chi^c_{\ell_x}$ for χ_{ℓ_x} in equation (1.20). $\chi^c_{\ell_x}$ is termed the wavefunction of the transferred particle and its radial component is regarded as the radial form factor for the subsystem $\{x + A\}_c$ resulting in given channel c. $\chi^c_{\ell_x}$ is evaluated by introducing the surface approximation which assumes that the main contribution to the transition amplitude comes from the peripheral

region of the nucleus (i.e. for $r > R_o$, where R_o represents the range of the nuclear interaction). $\chi^c_{\ell_x}$ may now be expressed in terms of the radial wave functions χ_{ℓ_x} for elastic scattering and the scattering matrix elements $S_{\ell_x c}$ which connect the elastic channel ℓ_x to the inelastic channel c.

$$\chi^c_{\ell_x}(\underline{r}) = \left(\frac{m_x q_x}{m_c q_c}\right)^{\frac{1}{2}} \frac{S_{\ell_x c}}{S_{\ell_x \ell_x} - 1} \{\chi_{\ell_x}(\underline{q}_x, \underline{r}) - j_{\ell_x}(\underline{q}_x, \underline{r})\} \quad (1.22)$$

where j_ℓ is the Bessel function and m_c and q_c the mass and momentum of the subsystem $\{x + A\}_c$ in channel c. As before integration over the angles of $\underline{q}_c$ will produce a reduced T-matrix element for the inelastic component of the inclusive break up cross section

$$T^c_{\ell_x m_x} = \left(\frac{m_x q_x}{m_c q_c}\right)^{\frac{1}{2}} \frac{S_{\ell_x c}}{S_{\ell_x \ell_x} - 1} D_o \int d^3r \, \chi^{(-)*}_{qb}(\underline{q}_b, \underline{r})$$

$$\times [\chi_{\ell_x}(\underline{q}_x, \underline{r}) - j_{\ell_x}(\underline{q}_x, \underline{r})] \quad (1.23)$$

$$\times Y_{\ell_x m_x}(\hat{\underline{r}})^* \chi^{(+)}_a(\underline{q}_a, \underline{r}) \Lambda(r) P(r)$$

with zero range approximation, finite range and non-locality corrections. Channel c dependence is now expressed in the term

$$\left(\frac{m_x q_x}{m_c q_c}\right)^{\frac{1}{2}} S_{\ell_x c}$$

of equation (1.23). The contribution of the inelastic processes to the inclusive cross section is obtained by summing over all inelastic channels

$$\left.\frac{d^2\sigma}{d\Omega_b dE_b}\right|_{\text{inelastic}} = \frac{m_a m_b m_x}{(2\pi)^5 \hbar^6} \frac{q_b q_x}{q_a} \sum_{\ell_x m_x} \sum_{\ell_x \neq c} \frac{|S_{\ell_x c}|^2}{|S_{\ell_x x} - 1|^2} D_o$$

$$\times \left| \int d^3r \, \chi_b^{(-)*}(\underline{q}_b, \underline{r}) [\chi_{\ell_x}(\underline{q}_x, \underline{r}) - j_{\ell_x}(\underline{c}_x, \underline{r})] \right.$$

$$\left. \times \, Y_{\ell_x m_x}(\hat{\underline{r}})^* \, \chi_a^{(+)}(\underline{q}_a, \underline{r}) \Lambda(r) P(r) \right|^2 . \qquad (1.24)$$

The unitarity of the S-matrix (Ja 70) leads to

$$\sum_{\ell_x \neq c} |S_{\ell_x c}|^2 = |1 - S_{\ell_x \ell_x}|^2 . \qquad (1.25)$$

Further, the definitions of the elastic and total reaction cross sections are (Ja 70)

$$\sigma_{\ell_x}^{\text{elastic}} = \frac{\pi}{q_x^2} (2\ell + 1) |1 - S_{\ell_x \ell_x}|^2 \qquad (1.26)$$

and

$$\sigma_{\ell_x}^{\text{reaction}} = \frac{\pi}{q_x^2} (2\ell + 1)(1 - |S_{\ell_x \ell_x}|^2) \qquad (1.27)$$

hence

$$\left.\frac{d^2\sigma}{d\Omega_b dE_b}\right|_{\text{inelastic}} = \frac{m_a m_b m_x}{(2\pi)\hbar} \frac{q_b q_x}{q_a} \sum_{\ell_x m_x} \frac{\sigma_{\ell_x}^{\text{reaction}}}{\sigma_{\ell_x}^{\text{elastic}}} \left[T_{\ell_x m_x} - T_{\ell_x}^{(0)} \right]^2 \qquad (1.28)$$

where

$$T_{\ell_x m_x}^{(0)} = D_o \int d^3r \, \chi_b^{(-)*}(\underline{q}_b, \underline{r}) j_{\ell_x}(\underline{q}_x, \underline{r}) Y_{\ell_x m_x}(\hat{\underline{r}})^*$$

$$\times \, \chi_a^{(+)}(\underline{q}_a, \underline{r}) \Lambda(r) P(r) . \qquad (1.29)$$

For the total inclusive double differential cross section (i.e. A(a,b)) expressions (1.19) and (1.28) are summed. Thus Baur et al. produce a theoretical calculation of the total inclusive yield by consideration of the imaginary part of the forward elastic scattering amplitude within the context of the optical theorem rather than by consideration of individual exclusive processes.

DWBA models have been used to analyse a variety of inclusive and exclusive measurements. DWBA formalisms have been applied to the break-up of deuterons (Kl 81, Pa 78, Ma 82). Kleinfeller et al. (Kl 81) studied the reactions $^{27}A\ell$, ^{62}Ni, ^{93}Nb, ^{119}Sn, ^{181}Ta, ^{232}Th (d,pX) at 15 MeV and 25 MeV. A mass dependence of the total break-up yield of $A^{1/3}$ and $A^{2/3}$ was observed. Elastic and inelastic break-up modes were identified. DWBA calculations predicted elastic break-up peaked at forward angles with inelastic break-up contributing strongly, especially at backward angles (as expected on classical grounds). Although the DWBA calculations were in reasonable quantitative agreement with the data, systematic trends were not so well reproduced, especially for large A, low E_p where discrepancies in excess of an order of magnitude were observed. Kleinfeller et al. invoked a separate Coulomb break-up mechanism to account for this, which qualitatively produced the desired correction. Pampus et al. (Pa 78) examined the reactions $^{27}A\ell$, ^{62}Ni, ^{93}Nb, ^{119}Sn, ^{181}Ta (d, pX) at 25.5 MeV. Qualitative fits to the inclusive proton spectra were obtained, but quantitatively the theoretical predictions were poor, especially at low A and for backward angles. Matsuoka et al. (Ma 82) investigated the reactions ^{12}C, ^{51}V, ^{118}Sn(d,pn) at 56 MeV. Measuring the p-n angular correlation

they demonstrated that elastic break-up of the deuteron accounted for ∿ 40% of the total break-up yield at forward angles. Analysis was performed with prior-form DWBA. This analysis included Coulomb break-up in the same framework as nuclear break-up since the transition amplitude was expressed in terms of n-N and p-n interactions. Qualitatively the predictions of this model were in agreement with the data. However p-n correlations on the same side of the beam were up to an order of magnitude out for all targets. A subsequent analysis of the data by Baur et al. (Ba 84), using post-form DWBA produced much improved quantitative fits to the data, prompting the conclusion that the post-form DWBA was the more realistic physically.

Matsuoka et al. have studied both inclusive and exclusive reactions for ^{12}C, ^{51}V, $^{90}Zr(^{3}He,d)$ and ^{12}C, ^{51}V, $^{90}Zr(^{3}He,pd)$ at 90 MeV (Ma 78, Ma 80). The p-d correlation data revealed a prominent elastic break-up mode. This data was subsequently analysed by Shyam et al. (Sh 80) within the post-form DWBA using standard values for the optical model parameters and D_o. Fits to data were quantitatively satisfactory. However, the limited data available for proton–deuteron correlations on the same side of the beam indicated that the fits are poorer in this region and represent little improvement over the PWBA analysis presented by Matsuoka originally (Ma 80).

Recently, Aarts et al. (Aa 85) have compared data (Aa 82) for the reactions ^{28}Si, $^{58}Ni(^{3}He,pd)$ at 52 MeV with the post-form DWBA. Fits to the inclusive deuteron angular distribution and the p-d angular correlations are in good quantitative and qualitative

agreement with the data. Shyam et al. (Sh 84b) have tested the post form DWBA with exclusive measurements of the inelastic breakup reaction ^{165}Ho(^{3}He,d) at 100 MeV (Mo 84). They obtain good agreement between the absolute values of the integrated elastic and inelastic break-up cross section and DWBA predictions at forward and backward angles. The ratio between elastic and inelastic break-up is also satisfactorily reproduced. Budzanowski et al. studied Ni(α,^{3}He) at 172.5 MeV (Bu 78) and Ni(α,t) and Ni(α,tp) reactions at 172.5 MeV. The limited amount of data was found to be in good agreement with post-form DWBA predictions. Shyam et al. (Sh 83) have reported on systematic trends in the inclusive reactions ^{58}Ni, ^{90}Zr, ^{120}Sn, ^{209}Bi(α,^{3}He), (α,t) at 172.5 MeV and in particular the yield ratios of (α,^{3}He):(α,t). It is concluded that systematic variations in this ratio are due to difference in the Coulomb interactions of ^{3}He-target and t-target interactions which are implicitly considered in the DWBA description but lacking in simpler models.

To date, little heavy-ion induced reaction data has been examined using DWBA and no clear picture has emerged of the viability of DWBA in application to these reactions. In work on ^{6}Li break-up at 156 MeV, Neumann et al. (Ne 80, Ne 82) attempted an analysis within a standard post-form DWBA calculation. This was only partially successful. Some gross features of the inclusive spectra and the angular distributions were not reproduced. This was interpreted as a signal of the failure of the zero-range approximation (together with an unrealistic Lorentzian-type finite range correction factor). The requirement for finite range calculations to interpret heavy-ion induced break-up reactions was further emphasised by Baur et al. (Ba 79) in an analysis of the ^{197}Au(^{9}Be,^{8}Be)

break-up reaction bombarding energies of between 18 and 26 MeV (i.e. below the Coulomb barrier). Semiclassical methods were applied to calculation of the T-matrix for a post-form DWBA calculation. Satisfactory fits to the data were only obtained by modifying the T-matrix with appropriate formulations of finite-range effects. The necessity for a formal full recoil calculation with an evaluation of the six-dimensional DWBA matrix element was avoided.

(d) Incomplete fusion

One of the earliest observations of incomplete fusion was that of Sikkeland et al. (Si 62), who determined the momentum transfer (and hence the mass transfer) to the residual nucleus in reactions between 'light' heavy-ions ($6 \leq A \leq 20$) and heavy fissionable targets. In addition to compound nucleus formation (complete momentum transfer) they observed partial, or incomplete, momentum transfer. This was interpreted as capture by the target of a fragment rather than of the projectile. Similar measurements by Back et al. (Ba 80a) on the systems $^{16}O+ ^{238}U$ and $^{16}O+ ^{239}Pu$ at 315 MeV found evidence for α and ^{8}Be transfer followed by neutron evaporation. Inamura et al. (In 77) introduced the technique of particle-γ correlation measurements to explore the reaction $^{14}N+ ^{159}Tb$ at 95 MeV. Coincidences between 'fast' α-particles and γ-rays were studied, the latter being used to identify the residual nucleus. Inamura et al. concluded that the partial cross sections for the reaction $^{159}Tb(^{14}N, \alpha x n \gamma)^{169-x}Yb$ were centred in the vicinity of the critical angular momentum for fusion. The observation of fast outgoing fragments

indicated processes other than compound nucleus formation. Similar studies by Castenada et al. (Ca 78, Ca 80), Utsonomiya et al. (Ut 83, Ut 84), Zolnowski et al. (Zo 78), Yamada et al. (Ya 79), Siwek-Wilczyńska (Wi 79a, Wi 79b) and Wilczyński (Wi 80) have established the incomplete fusion mechanism for reactions with ^{6}Li to ^{20}Ne projectiles at bombarding energies of $\sim$ 7-20 MeV/A on heavy targets.

Parker et al. (Pa 84a, Pa 84b) have measured the excitation functions and differential recoil range distributions of target residues from $^{12}C+^{51}V$ complete fusion and incomplete fusion reactions in the energy range 3-8 MeV/A. For incomplete fusion processes the recoil velocity of the target residue is dependent on the momentum (and hence the mass) transferred in the reaction. By examining the range distribution of recoil radioisotopes stopped in a multi-element foil stack they were able to infer the individual contributions of competing reaction mechanisms.

Recently Wilschut et al. (Wi 83) have reported the measurements of particle-x-ray correlations to identify the residual nucleus in complete fusion and incomplete fusion reactions of $^{14}N+^{159}Tb$ and $^{14}N+^{197}Au$ at 140 MeV. In comparison with particle-γ correlation studies (particularly those at high incident projectile energies) they note that the X-ray spectra are less complex. In consequence the identification of Z for the residual nuclei is made easier and it is possible to identify yields for a large number of exit channels in a straightforward way. One disadvantage of this technique is the requirement for X-ray multiplicities for every reaction channel studied in order to determine the absolute cross sections.

A simple model of incomplete fusion reactions has been introduced

by Siwek-Wilczyńska (Wi 79a) to account for the threshold behaviour of the reactions $^{160}Gd(^{12}C, \alpha x n \gamma)^{168-x}Er$ and $^{160}Gd(^{12}C, 2\alpha x n \gamma)^{164-x}Dy$. They proposed a bin model making use of a generalised concept of entrance channel critical angular momenta. Entrance channel critical angular momenta were calculated with liquid drop contact forces (Wi 73) as

$$(\ell_{crit} + \tfrac{1}{2})^2 = \frac{\mu(C_1+C_2)^3}{\hbar^2}\left[4\pi\gamma\frac{C_1C_2}{C_1+C_2} - \frac{Z_1Z_2e^2}{(C_1+C_2)^2}\right] \qquad (1.30)$$

where γ is the surface tension coefficient, μ the reduced mass, C_1 and C_2 are the half-density radii. At low energies, complete fusion dominates until, with increasing energy, the critical angular momentum for complete fusion, $\ell_{crit}(^{12}C + ^{160}Gd)$, is exceeded. Thereafter ^{8}Be-capture commences. Beyond the critical angular momentum for ^{8}Be-capture, $\frac{3}{2}\,\ell_{crit}(^{8}Be + ^{160}Gd)$, α-capture commences. With increasing energy the α-capture critical angular momentum, $3\ell_{crit}(\alpha + ^{160}Gd)$, is exceeded and multibody fragmentation (i.e. $^{12}C \rightarrow 3\alpha$) becomes dominant. At higher energies the cross section for multibody fragmentation is limited by the hard grazing angular momentum ℓ_{hg}. At this point the balance of nuclear, Coulomb and centrifugal forces are insufficient for capture. The reaction cross section is given by,

$$\sigma_R = \frac{2\pi\mu E_{cm}}{\hbar^2}\sum_{\ell=0}^{\ell_{hg}}(2\ell+1) \quad . \qquad (1.31)$$

This model is illustrated schematically in Figure 1.4. It is assumed that: i) the orbital angular momentum of the projectile and its energy are shared amongst the fragments according to their mass (i.e. $\ell_{crit}(i + target) = \frac{m_i}{m_{proj}}\ell_i$) and (ii) that if two reaction

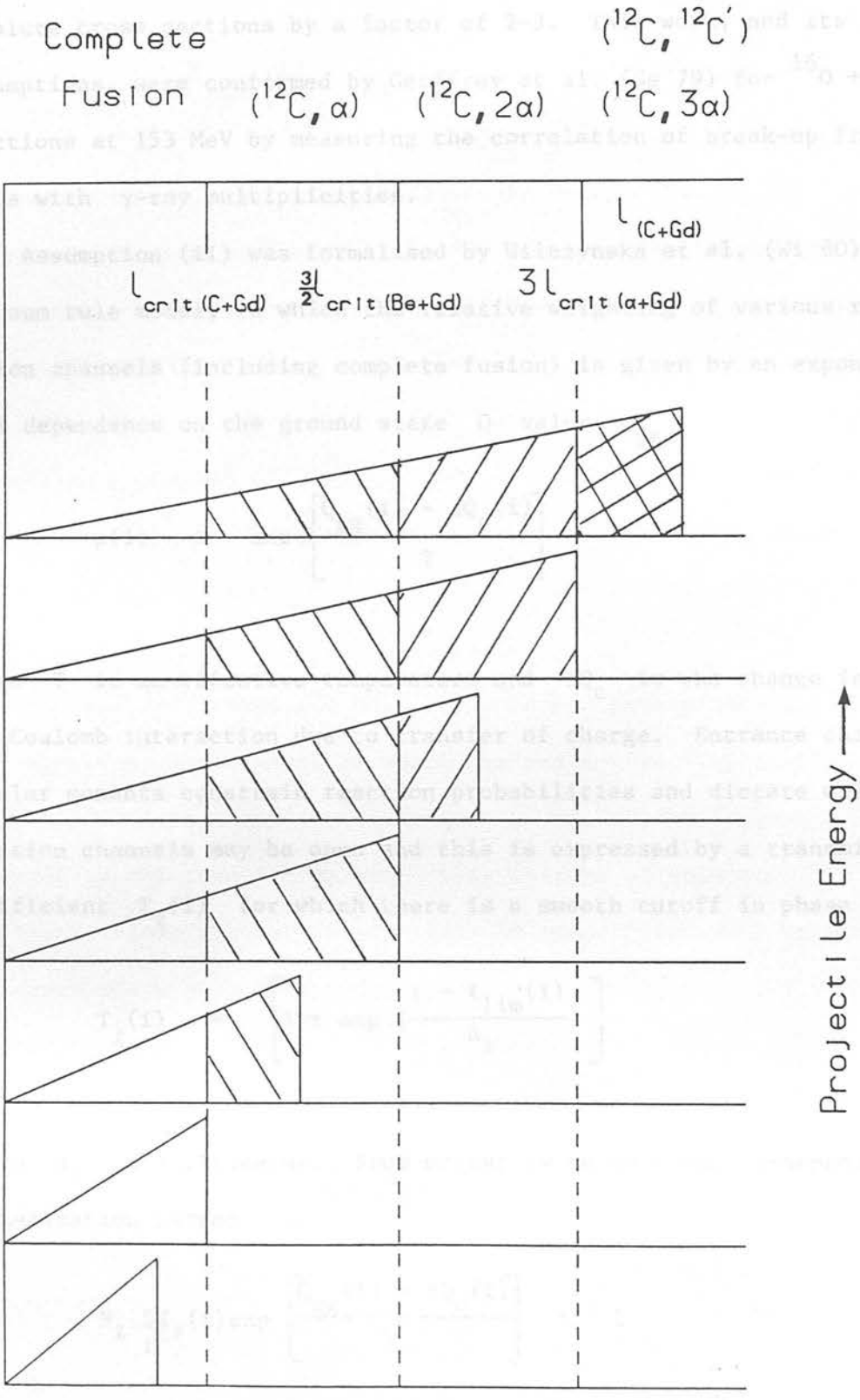

FIGURE 1.4: Schematic illustration of the 'bin model'.

channels are open the heavier fragment is preferentially captured. Qualitatively this model reproduces the data but overpredicts the absolute cross sections by a factor of 2-3. This work, and its assumptions, were confirmed by Geoffrey et al. (Ge 79) for $^{16}O + ^{154}Sm$ reactions at 153 MeV by measuring the correlation of break-up fragments with γ-ray multiplicities.

Assumption (ii) was formalised by Wilczynska et al. (Wi 80) in the sum rule model, in which the relative weighting of various reaction channels (including complete fusion) is given by an exponential dependence on the ground state Q value Q_{gg}

$$p(i) \sim \exp\left[\frac{Q_{gg}(i) - \Delta Q_c(i)}{T}\right] \tag{1.32}$$

where T is an effective temperature and ΔQ_c is the change in the Coulomb interaction due to transfer of charge. Entrance channel angular momenta constrain reaction probabilities and dictate which reaction channels may be open and this is expressed by a transmission coefficient $T_\ell(i)$ for which there is a smooth cutoff in phase space

$$T_\ell(i) = \left[1 + \exp\left(\frac{\ell - \ell_{lim}(i)}{\Delta_\ell}\right)\right] \tag{1.33}$$

where Δ_ℓ is a parameter. From unitarity we have the ℓ-dependent normalization factor

$$N_\ell \sum_i T_\ell(i) \exp\left[\frac{Q_{gg}(i) - \Delta Q_c(i)}{T}\right] = 1 \tag{1.34}$$

given that all reaction channels are included. The reaction cross section for a particular reaction channel is then

$$\sigma_i = \pi\lambda\!\!\!^{-2} \sum_{\ell=0}^{max} (2\ell+1)T_\ell(i)p(i)/(\sum_j T_\ell(j)p(j)). \qquad (1.35)$$

The sum rule model is a critical distance model, that is, for collisions within the hard grazing radius complete fusion and incomplete fusion are the only processes that will occur. The sum rule model has satisfactorily accounted for the binary reaction cross sections from incomplete fusion reactions of $^{14}N + ^{159}Tb$ at 140 MeV and the excitation functions of $(^{12}C,\alpha)$ and $(^{12}C,2\alpha)$ on ^{160}Gd over bombarding energies of 90-200 MeV (Wi 79a, Wi 79b, Wi 79c). However these data demonstrate that incomplete fusion processes account for only 30% of the inclusive break-up yield.

Udagawa and Tamura (Ud 80, Ud 81, Ta 81b) have proposed a two step break-up fusion model in which the projectile elastically breaks up on impact and then subsequently one of the fragments is captured by the target. An attractive feature of this model is that it treats incomplete fusion processes in competition with break-up processes where both fragments escape. A one-step DWBA calculation is used to obtain the probability of break-up and the imaginary part of the heavy-ion optical potential is used to obtain the fusion probability. They obtain the following expression for the break-up fusion cross section

$$\frac{d^2\sigma}{d\Omega_b dE_b} = \frac{m_b m_x}{(2\pi\hbar^2)} \frac{k_b}{k_x} \sum_i \frac{P_i}{|S_i|^2} \Sigma|\beta_{\ell m}(k_b)|^2 \qquad (1.36)$$

$\beta_{\ell m}(k_b)$ is the amplitude of the break-up process in which b is

emitted with momentum k_b and x with an angular momentum (ℓ, m) relative to the target A. P_{ℓ_x} denotes the penetrability between x and A and hence describes the absorption of x by A. $|S_{\ell_x}|$ is the elastic scattering reflection coefficient and because it is small for small ℓ_x, $^1/|S_{\ell_x}|^2$ is large and hence low ℓ partial waves contribute significantly to the break-up fusion process. For the reaction $^{14}N + ^{159}Tb$ at 115 MeV good agreement was obtained with the relative yields of energy binned α-particle angular correlations and the α-energy spectra at different angles.

e) Particle-particle correlations

We have seen in the previous section that incomplete fusion processes account for only a fraction of the total break-up cross section. For $^{14}N + ^{159}Tb$ at 140 MeV van Driel (Dr 81) has reported that only ∿ 30% of the measured heavy-ion inclusive cross section at $\theta_{HI} = 20°$ is due to incomplete fusion processes. Intuitively one might look for the missing strength in final states involving three or more particles and, more specifically, in particle-particle correlations.

Extensive α-HI correlation data are available for ^{14}N induced reactions on ^{12}C(Bh 81), ^{27}Al (Bh 81, Bi 79, Ko 82), ^{58}Ni (Bh 79, Bh 81, Go 84), ^{93}Nb (Ko 82, Fu 83) and ^{159}Tb (Bh 82, Dr 81, Dr 80) for incident energies of 5-15 MeV/A. Bhowmik et al. (Bh 78) studied the in-plane correlations between α-particles and heavy ions for $^{11}B + ^{12}C$ and $^{11}B + ^{58}Ni$ at 116 MeV. They concluded that α-emission proceeded on a time-scale comparable with the projectile/target

collision time. This experimental study was extended to (^{14}N,X) reactions (X = ^{6,7,8}Li, ^{7,9,10}Be, ^{10,11,12}B, ^{11,12,13}C) on ^{12}C, ^{27}Aℓ, and ^{58}Ni at 148 MeV (Bh 79, Bh 81). It was demonstrated that the differential cross sections for the α-HI correlations could be factorised as

$$\frac{d^4\sigma(\theta_{HI},\theta_\alpha)}{d\Omega_{HI}d\Omega_\alpha dE_\alpha dE_{HI}} = C\,\frac{d^2\sigma(\theta_{HI})}{d\Omega_{HI}dE_{HI}}\,\frac{d^2\sigma(\theta_\alpha)}{d\Omega_\alpha\,dE_\alpha} \qquad (1.37)$$

where $d^2\sigma/d\Omega_{HI}dE_{HI}$ and $d^2\sigma/d\Omega_\alpha dE_\alpha$ are the inclusive heavy-ion and α double differential cross sections and C is a constant for a fixed HI detection angle, absolute cross sections for α-HI correlations could be reasonably reproduced with $C = 0.5b^{-1}$. The success of this parameterization implies that the emission of the fragments is spatially uncorrelated. Bhowmik et al. concluded that the process was time-ordered, with the α-particle being emitted at an early stage of the reaction prior to the formation of deep-inelastic fragments. van Driel (Dr 80) has indicated that such a time ordering may be unnecessary provided that the process is fast and the α-particle is emitted while the projectile and target strongly interact. van Driel et al. (Dr 80, Dr 81, Bh 82) studied α-HI correlations from ^{14}N + ^{159}Tb reactions at 112, 140 and 168 MeV. This study represented an improvement on previous work in that the α and HI detectors were separately moved to provide correlations for fixed α and fixed HI detection angles. Further, position sensitive detectors were used which provided improved resolution in the determination of the opening angles between outgoing fragments from break-up reactions.

Insufficient statistics were obtained to confirm equation (1.37).

However the factorisation of the energy integrated double differential cross section was confirmed, i.e.

$$\frac{d^2\sigma(\theta_{HI},\theta_\alpha)}{d\Omega_{HI}\, d\Omega_\alpha} = C \frac{d\sigma(\theta_{HI})}{d\Omega_{HI}} \frac{d\sigma(\theta_\alpha)}{d\Omega_\alpha} \quad . \tag{1.38}$$

Fits to the data (for Li, Be and B fragments in coincidence with α-particles) at 112, 140 and 168 MeV yielded values of C not significantly different from the $0.5b^{-1}$ obtained by Bhowmik et al., despite the large difference in target mass. Interestingly, the values of C obtained showed no systematic variation with projectile energy and described correlation data for fixed α and HI detection angles equally well. For angles where the detectors were close to each other a strong enhancement of yield was obtained over the predictions of factorisation. This was demonstrated to be due to the sequential break-up of projectile-like fragments. For B + α and Be + α correlations, events were concentrated around the Q_3(gs) values, indicating that the residual nucleus was left in its ground state or at low excitation. Li + α correlations were scattered over a range of Q_3 values, indicating a greater degree of inelasticity in the reaction mechanism.

Recently Goldhoorn et al. (Go 84) has repeated the work of Bhowmik et al. (Bh 81) for the reaction $^{14}N + ^{58}Ni$ at 148 MeV. With improved resolution in the determination of the opening angles between the outgoing fragments they observed a significant sequential break-up yield in contrast to the previous work of Bhowmik et al. More recently Fukuda et al. (Fu 83) has reached similar conclusions in a study of $^{14}N + ^{93}Nb$ at 208 MeV. van Driel (Dr 80) concludes

that at 140 MeV the combination of sequential break-up, fragmentation (i.e. non-sequential break-up) and incomplete fusion account for 83%, 70% and 41% of the inclusive differential Be, B and C cross sections respectively. This is consistent with the heavy-ion inclusive cross section being explained by these three processes alone.

Similarly, much data is available for α-HI correlations with ^{16}O induced reactions on ^{12}C (Ra 81), ^{27}Al (Ha 77, Sa 83b, ^{58}Ni (Ho 77), ^{69}Ni (Lü 85), Ti (Ho 80), ^{93}Nb (Yo 80), ^{197}Au, ^{208}Pb (Ge 77a, Bi 80b) in the incident energy range 4-20 MeV/A. The data also display two components - sequential and non-sequential. However the interpretation of such data is more varied. Gelbke et al. (Ge 77a, Bini et al. (Bi 80b) Harris et al. (Ha 77), Sasagase et al. (Sa 83), Rae et al. (Ra 80) and Lücking (Lü 85) have all indicated the observation of sequential break-up of projectile-like fragments. Conversely Ho et al. (Ho 77) interpreted their data in terms of a sequential break-up of target-like fragments excited by deep-inelastic collisions followed by the emission of an α-particle. They proposed pre-equilibrium emission from a locally heated zone (or 'hot spot') in the TLF. In comparison Young et al. (Yo 80) in a study of $^{16}O + ^{93}Nb$ at 204 MeV concluded that the α-HI correlations were explicable in terms of sequential break-up via highly excited states of TLF and PLF components. However, this conclusion would seem to be suspect. Bhowmik et al. (Bh 82) have noted that the $^{14}N + ^{159}Tb$ α-HI correlation data cannot, because of the kinematics, be ascribed to break-up of TLF. Further they note that the break-up of TLF would result in the symmetry angle of the non-sequential break-up component depending upon the HI detection angle, contrary to observation. Rae et al.

(Ra 80, Ra 81) have studied the break-up of 140 MeV ^{16}O into the $^{12}C + \alpha$ channel on ^{12}C, ^{13}C and ^{28}Si. Experimentally x-y position sensitive telescopes were used to obtain a large solid angle without loss of resolution in the opening angle between the ^{12}C and α. The α telescope was located at $\theta_\alpha = 13°$, the HI telescope at $\theta_{HI} = -10°$ - an appropriate geometry to enhance the yield of sequential break-up events. Notably the $9.88(2^+)$, $10.36(4^+)$ and $11.06(4^+)$ excited states of ^{16}O were, in contrast to other states, populated uniformly for a wide range of Q_3 values. Rae et al. speculated that these states were populated by a 'quasi-free' scattering process which produced both 'resonant' (i.e. sequential and 'non-resonant' (i.e. non-sequential or direct) break-up components.

Bice et al. (Bi 82) have studied the reaction mechanisms in ^{12}C induced reactions on ^{208}Pb in the incident energy range 11-19 MeV/A. Absolute cross sections for the reactions $^{208}Pb(^{12}C, ^{12}C^* \rightarrow \alpha + ^{8}Be)$, $^{208}Pb\ (^{12}C, ^{8}Be_{gs})$ and $^{208}Pb\ (^{12}C, ^{8}Be_{2.94})$ were determined by α-α, α - ^{8}Be and α-α-α correlations. Because of the low relative energies in the centre of mass frame between fragments, the detection system consisted of three particle telescopes in close vertical geometry. These measurements, together with the ^{12}C induced incomplete fusion reaction data of Siwek-Wilczynska et al. (Wi 79a, Wi 79b) account for $\sim$ 80% of the observed inclusive α yield from ^{12}C induced reactions at 15 MeV/A. At higher bombarding energies multibody fragmentation processes (i.e. $^{12}C \rightarrow 3\alpha$) became prominent. Wilczynska et al. (Wi 79c) estimated the magnitude of the multibody process for $^{12}C + ^{160}Gd$ at 10 and 17 MeV/A by measuring the average α-multiplicity from in-plane α-α angular

correlations. They observed a rapid increase in yield for the $^{12}C \rightarrow 3\alpha$ channel with increasing bombarding energy.

The reaction mechanisms involved in the break-up of lighter projectiles have also been studied. The sequential break-up of α-particles (via the 20.1 MeV state) has been observed (Ja 76, Ka 79). The unambiguous identification of the sequential break-up of ^{6}Li (via the 2.18 MeV (3^+) state) has been reported at low energies by Scholz et al. (Sc 77) and at higher energies by Castenada et al. (Ca 80) and Katori et al. (Ka 84). Some authors (Ge 78b, Ge 80), Ca 80) have identified a non-sequential component in the break-up of ^{6}Li. However Rapp (Ra 85b) has demonstrated that these events can arise from sequential break-up via more highly excited α-decaying states of ^{6}Li which possess large widths. Whilst this does not suggest that there is no non-sequential (or 'direct') component to ^{6}Li break-up, the strength of the direct break-up yield at the bombarding energies so far studied must be regarded as only a small fraction of the non-sequential events observed and certainly small in comparison to the sequential channel. Shotter et al. (Sh 81) have reported the identification of the sequential break-up of ^{7}Li (via the 4.63 ($\frac{7}{2}^-$) state). Further, for ^{7}Li + ^{208}Pb at forward angles they observe a non-sequential (or 'direct') break-up process. In comparison to ^{6}Li break-up studies, this identification is unambiguous. There is a large separation between the $\frac{7}{2}^-$ state and the α+t threshold (2.16 MeV as compared to 0.711 MeV for ^{6}Li), the $\frac{7}{2}^-$ state has a narrow width (Γ = 93 keV) and the states above the $\frac{7}{2}^-$ state have relatively narrow widths.

Applications of particle-particle correlations to α-transfer reactions and spectroscopic studies have been attempted. Rae et al.

(Ra 84a, Ra 85a) have described the study of the sequential break-up reaction $^{12}C(^{18}O, ^{18}O^* \rightarrow ^{14}C+\alpha)$ at 82 MeV with α-HI correlations to examine the α-decaying states of $^{18}O^*$. By measuring the correlations as a function of the reaction angle θ^* of $^{18}O^*$ in the centre of mass frame it is noted that the angular correlations shift with θ^* at a rate proportional to the spin of the state of the excited ejectile. Further much information is revealed about the reaction mechanisms involved.

Stahel (St 79) and van Driel (Dr 80) have reported spectroscopic studies of neutron rich nuclei by the $(\alpha, ^2He \rightarrow p+p)$ reaction. These reactions were described by zero-range and finite range DWBA and provided useful spectroscopic information about high spin states. However, the clearest results were obtained for targets with a small number of available sub-shells and small Q_3 values. For other targets the number of high-spin states observed made interpretation difficult.

The application of break-up studies to transfer reaction studies involving an unbound product was further explored by Bice et al. (Bi 81). They studied the α-transfer reaction $^{12}C(^{10}B, ^6Li^*_{2.18} \rightarrow \alpha+d)\,^{16}O$ at 68 MeV and observed transitions to the $K^\pi = 0^+$ rotational band of ^{16}O. This type of experiment is a potentially useful tool to study the clustering structure of nuclei.

(f) The Adiabatic Model

Double-folding models based upon the M3Y effective nucleon-nucleon interaction (where the real part of the potential is generated

by folding the ground state densities of the colliding nuclei with an effective nucleon-nucleon interaction) have been successful in explaining the optical potentials for nucleons and a wide variety of heavy-ions. However, serious problems exist for ^{6}Li, ^{7}Li and ^{9}Be projectiles and analyses of elastic scattering data indicate that the real part of the potential requires renormalisation by a factor of $\sim$ 0.6, otherwise the diffractive structure of the observed angular distributions are not reproduced despite wide variations in the normalisation of the imaginary part of the potential. This effect is commonly understood to arise from the fact that these systems are all weakly bound and therefore that the coupling of the break-up channels to the elastic channel is expected to be strong.

Some investigations to understand the coupling of break-up effects to the elastic channel have involved the adiabatic approximation. The adiabatic approximation represents one limiting case of the superposition of nuclei during scattering and is the assumption that the total volume is conserved and no compression occurs. Explicitly this requires that any excitation of the system is small in comparison to the energy of the projectile. This assumption works best for low excitations in high energy collisions.

This approach was first applied to the elastic scattering of deuterons by Johnson and Soper (Jo 70) and Amakawa et al. (Am 79a, Am 79b, Am 81, Am 82). The excitation energy of the p-n relative motion in a three-body model of the system is neglected. The p-n relative coordinate becomes a fixed parameter and the Schrödinger equation for the three body system is reduced to a differential equation dependent on the centre of mass position vector of the neutron-proton relative to the target. Amakawa and Austern (Am 83)

calculated the p-n correlations for 56 MeV deuterons on ^{12}C and ^{51}V for comparison with the data of Matsuoka et al. (Ma 82). Using global optical model parameters for the proton-target, neutron-target local interactions at half the incident deuteron energy, they achieved satisfactory fits to the data. In comparison to the prior-form DWBA calculations of Matsuoka et al. (Ma 82) the adiabatic calculation gave substantially improved fits for proton–neutron correlations on the same side of the beam. Amakawa and Austern also noted that the failure of the prior-form DWBA for small q was because the prior-form DWBA s-wave break-up cross section significantly exceeded the predictions of a full coupled channels calculation for small q but was in agreement for large q.

Thompson and Nagarajan (Th 81) have studied the effects of break-up on the elastic scattering of 156 MeV ^{6}Li on ^{12}C, ^{40}Ca and ^{208}Pb. The three-body wave function of the projectile and target $\psi(\underline{R},\underline{r})$ is given by

$$(T_R + H_{\alpha d}(r) + V(\underline{R},r) - E)\psi(\underline{R},\underline{r}) = 0 \qquad (1.39)$$

where E is the energy of the system, $\underline{r}$ the separation of the centre of masses of the α and d, $\underline{R}$ the separation of the ^{6}Li centre of mass and the target, $H_{\alpha d}(r)$ the intrinsic Hamiltonian of ^{6}Li. T_R is the kinetic energy operator for the relative motion of the ^{6}Li and target and $V(\underline{R},\underline{r})$ the sum of the optical potentials for α-target, d-target at $^{2}/3$ and $^{1}/3$ of the projectile energy respectively. With the adiabatic approximation $H_{\alpha d} \equiv \varepsilon_o$ (the binding energy of ^{6}Li) we have

$$(T_R + V(\underline{R}.\underline{r}) + \varepsilon_o - E)\psi(\underline{R},\underline{r}) = 0 \ . \qquad (1.40)$$

As for the deuteron case, equation (1.40) reduces to a set of coupled equations dependent on $\underline{r}$. Inclusion of the break-up channels in these calculations produced substantially improved fits to the data in comparison to calculations considering only the elastic channel.

A similar formalism was used by Nagarajan et al. (Na 82) to fit the elastic scattering data of 89 MeV ^{7}Li on ^{40}Ca and ^{48}Ca. Inclusion of strong coupling between the ground state and the 0.48 MeV ($\frac{1}{2}^{-}$) states of ^{7}Li failed to account for the data. It was demonstrated that the inclusion of coupling to 4.63 MeV ($\frac{7}{2}^{-}$) state and the direct break-up channels, was required to obtain fits to the data.

From the work on ^{6}Li and ^{7}Li it was concluded that there was a strong coupling between the break-up channels and the elastic channel. Although no direct comparison between the adiabatic model and the results of calculations using doubly folded potentials can be made, it was further suggested that the required normalisation of double folding potentials was related to the break-up effects.

Thompson and Nagarajan (Th 83) have further studied the non-sequential (or 'direct') break-up data of ^{7}Li + ^{208}Pb at 70 MeV (Sh 81). They adopted the adiabatic approximation as a realistic three-body model of the reaction. Agreement with the data was obtained by considering the nuclear component of the break-up only. Inclusion of a Coulomb component overpredicted the data by a factor of about 3. This indicates, as expected, that the treatment of the (long-range) Coulomb force and its polarising effect on the ^{7}Li projectile is inadequate.

(g) Coupled Discretised Continuum Channels (CDCC)

Yahiro et al. (Ya 82, Ya 84) and Sakuragi et al. (Sa 83) have studied the elastic, inelastic and break-up reactions (here break-up is considered to be an elastic sequential process to the continuum) of projectiles by application of microscopic cluster-model wave functions to describe the bound and unbound states of projectiles. These states of the projectile are explicitly considered by performing coupled channel (CC) calculations in which all the CC form factors are derived by doubly folding the M3Y nucleon-nucleon interaction into the diagonal and transition clusters of the projectile and target ground state.

The total wave function of the projectile-target system is

$$\psi = \sum_{ij} \phi_i(\xi_a)\phi_j(\xi_A)\chi_{ij}(r_{aA}) \qquad (1.41)$$

where $\phi_{i(j)}$ represents state i(j) of the projectile(target) and χ_{ij} the relative motion between the projectile in state i and the target in state j. These states refer to the ground and the continuum break-up states of the projectile. The continuum is truncated by restricting the relative angular and linear momenta ℓ and q, of the clusters within the projectile. The q-continuum is then discretised for each ℓ. The exact relative wave function is averaged over q within bins of width Δq. This averaged wave function is then assumed to be the wave function of the discretised projectile break-up state corresponding to Δq. The set of discretised relative wave functions is included in $\phi_i(\chi_a)$. The set of CC equations for χ is then

$$- [\frac{h^2}{2m} \nabla^2 + V_{ijij}(\underline{r}_{aA}) - E - \varepsilon_{ij})]\chi_{ij}(\underline{r}_{aA})$$

$$= \sum_{i'j'} V_{iji'j'}(\underline{r}_{aA})\chi_{i'j'}(\underline{r}_{aA}) \qquad (1.42)$$

where the factor $V_{iji'j'}$ is given by

$$V_{iji'j'}(\underline{r}_{aA}) = \int \phi_i(\xi_a)\phi_j(\xi_A)|V_{M3Y}|\phi_{i'}(\xi_a)\phi_{j'}(\xi_A)d\xi_a d\xi_A \quad .(1.43)$$

Solution of the simultaneous CC equations obtains the S-matrix elements for elastic scattering and excitation of the discretised break-up states. Continuous S-matrix elements for the break-up into the continuum states may be given, as a function of q, by interpolation of the discrete S-matrix elements with respect to q. The break-up cross section is now

$$\sigma_{bu} = \frac{(2j+1)}{q_a^2} \sum_{(J-\ell|\leq\ell\leq|J+\ell|} \int_0^{q_{max}} |S_\ell^J(q)|^2 dq \qquad (1.44)$$

where J is the total angular momentum and q_a the incident momentum of the projectile.

This approach has been applied (Ya 82, Ya 84) to the deuteron elastic break-up data of Matsuoka et al. (Ma 82) and (Ka 85) to the ^{3}He elastic break-up data of Aarts et al. (Aa 82). Quantitatively good fits to the data were obtained and were of comparable quality with post-form DWBA calculations of Baur et al. (Ba 83) and Aarts et al. (Aa 85) which have been discussed previously. CDCC calculations indicate that the break-up cross section is strongly influenced by multi-step processes among the break-up channels and by the choice of distorting potentials. For low q these effects

are coherent but for high q they nearly cancel (Cf. failure of prior-frame DWBA for low q (Ma 82, Am 83)).

Sakuragi et al. (Sa 83) have applied CDCC methods to ^{6}Li elastic scattering and break-up. The introduction of continuum break-up channels produced excellent fits to the elastic scattering data of ^{6}Li + ^{28}Si at 99 MeV and ^{6}Li + ^{40}Ca at 156 MeV. Katori et al. (Ka 84) has reported on the sequential break-up of ^{6}Li (via the 2.18 MeV (3^{+}) state) on ^{12}C at 178 MeV. Comparison (Ka 85) with CDCC calculations for $^{12}C(^{6}Li, ^{6}Li^{*}_{3+})$ at 169 MeV shows satisfactory agreement. Further, Sakuragi et al. (Sa 83) extract a dynamic polarisation potential due to ^{6}Li break-up and demonstrate that in the surface region, the real part is strongly repulsive with a small imaginary part and conclude that this accounts for the normalisation factor $N_R \sim 0.6$ required for double folding single channel calculations. Interestingly, Sakuragi et al. (Sa 83) comment that elastic break-up of ^{6}Li by ^{28}Si at 99 MeV occurs in the peripheral region, much beyond the grazing distance. For smaller impact parameters elastic break-up is inhibited, conclusions which are qualitatively confirmed by Neumann et al. (Ne 80) in their study of the inclusive break-up reactions of ^{6}Li on ^{90}Zr and ^{208}Pb at 156 MeV.

h) Summary

The experimental data reviewed falls into two categories - inclusive and exclusive measurements. All inclusive measurements exhibit the following features:

(i) peripheral reactions,

(ii) large yields of fast (i.e. non-compound) particles

(iii) energy spectra exhibiting broad 'bell' shaped maxima centred near beam velocity,

(iv) yields strongly forward peaked.

The fact that various models are successful in describing these qualitative features of the data indicates that the data is relatively insensitive to the modelling techniques available. Exclusive experiments identify outgoing reaction channels and hence restrict the number of contributing reaction mechanisms. In this sense, they should represent sensitive tests of theoretical models because the restrictions imposed on the exit channels define, to some degree, the parameters of the collision and the possible interactions of the projectile (and its constituents) with the target.

Light-ion break-up reactions have been qualitatively and quantitatively described by DWBA and CDCC formalisms. Sequential break-up processes have been identified for light-ions. However, it is more usual to make the distinction between elastic and inelastic break-up processes. Particle-particle correlations from heavy-ion induced reactions have identified sequential and non-sequential break-up mechanisms for projectile-like fragments. The incomplete fusion reaction mechanism for asymmetric heavy-ion reactions has been firmly established by particle-γ correlations. The combination of reaction mechanisms identified by particle-particle and particle-γ correlations are able to account satisfactorily for the inclusive break-up yield. As for light-ions, many models predict the qualitative features of the experimental data but few quantitative analyses have been performed to date. There is some evidence that

zero-range DWBA methods are inadequate and that a formulation including finite range effects for heavy-ion induced reactions will be required. CDCC methods have begun to be applied to heavy-ion particle-particle correlations. Heavy-ion induced incomplete fusion reactions have been successfully described by the sum rule model. Microscopic calculations have been made (various formulations of break-up fusion exist) but require normalisation. Reliable, absolute DWBA calculations are required for detailed microscopic understanding of these reaction mechanisms.

The combination of inclusive and exclusive measurements of light and heavy-ion induced break-up reactions represents a powerful tool in understanding the structure and systematics of the total reaction cross section and the evolution of reaction mechanisms with energy. Projectile break-up studies offer the opportunity to obtain projectile and target spectroscopic data and to study the clustering structure of 'light' heavy-ions.

1.4 Three-body Kinematics

A three-body reaction with two particles in the final state may be written as

$$a + A \rightarrow b_1 + b_2 + A + Q_3 \qquad (1.45)$$

and is conventionally described by three-body kinematics. If the energies and emission angles of b and x are measured in coincidence, as in the experiments described in this thesis, then there is sufficient information to define all kinematic variables. Such experiments are termed kinematically complete. More specifically

let us consider a three-body final state proceeding via sequential decay. This may happen in the following ways:

$$a + A \rightarrow (b_1+b_2)^* + A \rightarrow b_1 + b_2 + A \tag{1.46}$$

$$a + A \rightarrow b_1 + (b_2+A)^* \rightarrow b_1 + b_2 + A \tag{1.47}$$

$$a + A \rightarrow b_2 + (b_1+A)^* \rightarrow b_1 + b_2 + A \tag{1.48}$$

where the asterisk denotes that the reaction proceeds through an intermediate unbound state which subsequently decays into two particles. All these mechanisms must be considered. However, it is possible in a kinematically complete experiment to select a region of phase space where one of the above dominates. The experiments discussed here were designed to detect the mechanism described by equation (1.46). All other reaction paths have been neglected.

The definition of an appropriate centre of mass (CM) frame of reference enables comparison between laboratory frame measurements with CM calculations. For the mechanism of interest here, equation (1.46), the most suitable CM system is the sequential decay relative to coordinate system C'(i) where i is the first emitted particle. C'(3) is the system used here.

From energy and momentum conservation we have the following equation relating the laboratory frame energies E_1 and E_2 (see Figure 1.5).

$$\varepsilon = \frac{1}{m_1+m_2} \{m_1E_1 + m_2E_2 - 2(m_1m_2E_1E_2)^{\frac{1}{2}} \cos\theta_{12}\} \tag{1.49}$$

and

$$E_{CM} = E_1 + E_2 - \varepsilon \tag{1.50}$$

where ε is the relative energy between b_1 and b_2 in the CM and

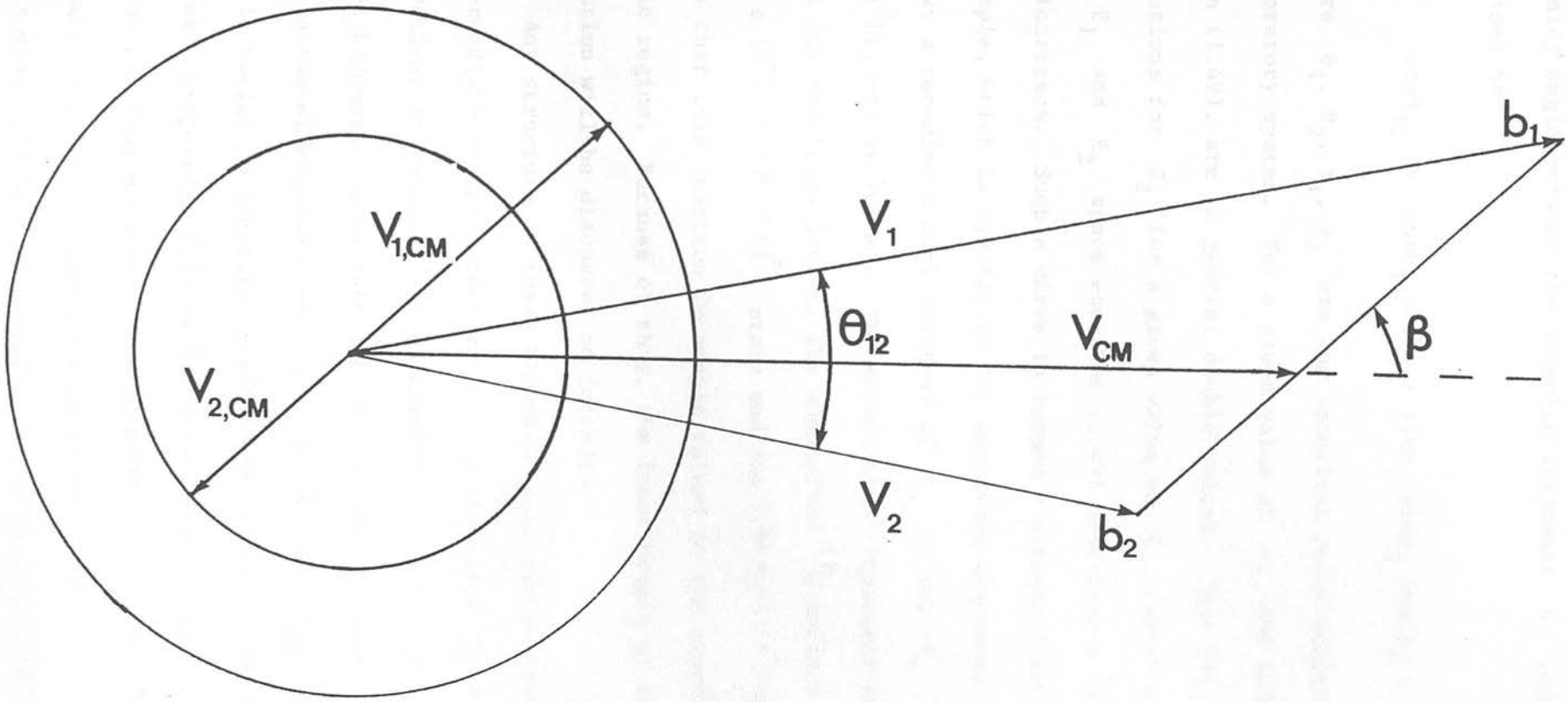

FIGURE 1.5: Velocity vector diagram for the reaction a + A → (b+x) + A → b + x + A.

E_{CM} is the CM energy of the composite $(b_1+b_2)^*$ system. θ_{12} is the opening angle between the outgoing fragments b_1 and b_2 and is defined by

$$\cos\theta_{12} = \cos\theta_1 \cos\theta_2 + \sin\theta_1 \sin\theta_2 \cos(\phi_1 - \phi_2) \qquad (1.51)$$

where θ_1, θ_2, ϕ_1, ϕ_2 are the spherical polar angles defined in the laboratory system. For a given value of ε, the solutions of equation (1.49), are in general double valued. That is, there exist two solutions for E_2 for a given value of E_1 (upper and lower branch) In E_1 and E_2 space equation (1.49) describes a closed curve as ε increases. Such a curve is termed a kinematic locus. As an example, which is typical of the reactions discussed here, Figure 1.6 shows a two-dimensional spectrum of E_α versus E_t for the reaction $^{12}C(^7Li,\alpha+t)$ at 70 MeV. The solid curves represent the kinematic loci for reactions leaving the unobserved ^{12}C nucleus in the ground state (0^+), 4.4 MeV (2^+) state and the 9.64 MeV (3^-) state. It can be seen that this reaction is single valued in the experimentally observable region. Because of this, the lower branch of the kinematical solution will be discussed no further.

Any structure on these kinematic loci can be associated with intermediate states formed during the reaction. In analysis it is convenient to generate one-dimensional spectra by projecting (i) a given kinematic locus onto the E_1 and/or E_2 axis, and (ii) the entire two-dimensional spectrum onto the line ε_{min}. Projection (i) is useful to identify intermediate states of the $(b_1+b_2)^*$ system. Projection (ii) is useful in identifying states populated in the residual nucleus. From equation (1.49), it can be seen that a small value of ε implies a small value for θ_{12}. Since the experiments discussed here investigate reactions that form intermediate

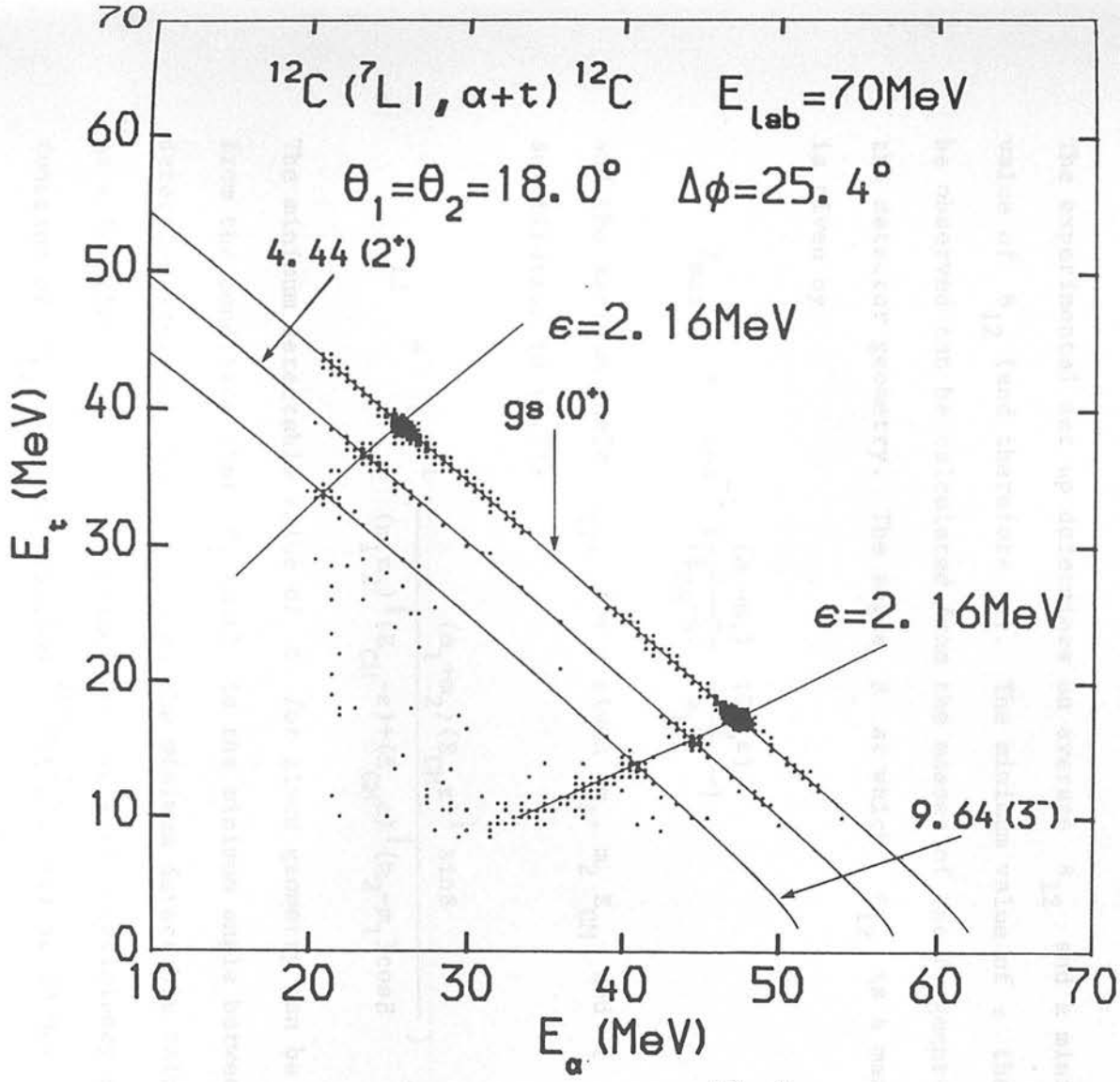

Figure 1.6: Two-dimensional correlation spectrum for the reaction $^{12}C(^{7}Li, \alpha+t)$. Kinematic locii corresponding to the ground state (0^+), 4.44 MeV(2^+), 9.64 MeV(3^-) states of ^{12}C are shown. Locii corresponding to ε = 2.16 MeV are also shown.

systems $(b_1+b_2)^*$ near threshold, we require the detection of b_1 and b_2 with small relative energies in the CM. θ_{12} is therefore chosen to be small. From the velocity diagram in Figure 1.5, we have

$$\beta = \cos^{-1}\left\{\frac{-(m_1+m_2)E_2 + m_1\varepsilon + m_2E_{CM}}{2(m_1m_2E_{CM}\varepsilon)^{\frac{1}{2}}}\right\} . \qquad (1.52)$$

The experimental set up determines an average θ_{12} and a minimum value of θ_{12} (and therefore ε). The minimum value of ε that may be observed can be calculated from the masses of the fragments and the detector geometry. The angle β at which θ_{12} is a maximum is given by

$$\beta_{max} = \cos^{-1}\left\{\frac{(m_2-m_1)}{(E_{CM}-\varepsilon)}\ \frac{(E_{CM}\varepsilon)}{m_1m_2}\right\} \qquad (1.53)$$

and the maximum angle θ_{12}, for a given m_1, m_2 E_{CM} and ε is by substitution in (1.53)

$$\theta_{12} = \tan^{-1}\left\{\frac{(m_1+m_2)(E_{CM}\varepsilon)^{\frac{1}{2}}\sin\beta}{(m_1m_2)^{\frac{1}{2}}(E_{CM}-\varepsilon)+(E_{CM}\varepsilon)^{\frac{1}{2}}(m_2-m_1)\cos\beta}\right\} . \qquad (1.54)$$

The minimum detectable value of ε for given geometry can be calculated from the condition that $\theta_{12}(max)$ is the minimum angle between the two detection systens. Figure 1.7 shows the minimum detectable value of ε as a function θ_{12} and the coincidence detection efficiency as a function of θ_{12} for the reaction $^{208}Pb(^7Li, \alpha+t)$ at 70 MeV. It can be seen that the efficiency peaks when the two detectors are close to each other. A near exponential decrease is seen as the counter separation increases. As the angular separation increases the coincidences observed are weighted toward larger values of ε.

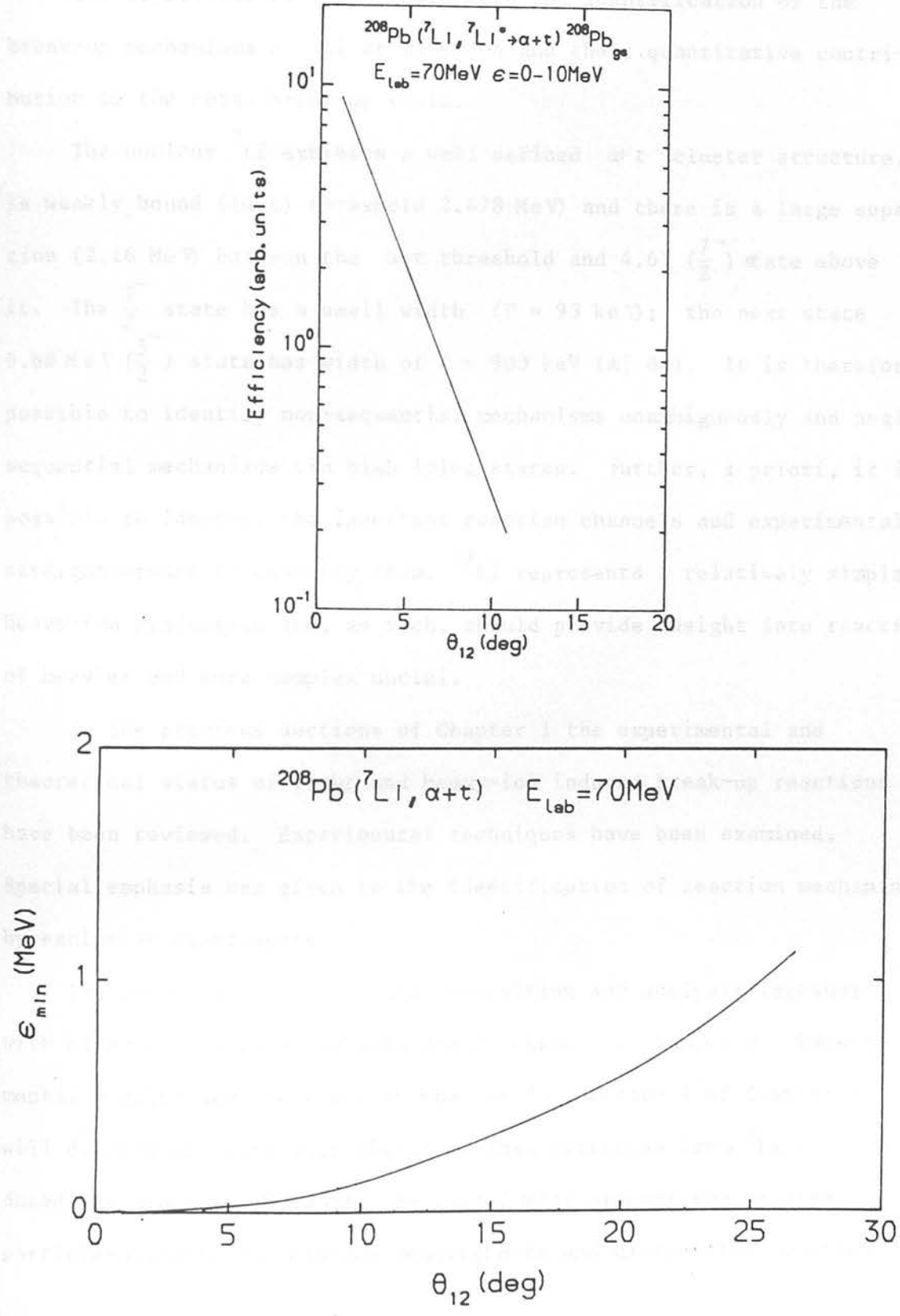

FIGURE 1.7: Illustration of variation of coincidence detection efficiency for a sequential break-up reaction as a function of θ_{12}.

1.5 Objectives and Structure of Thesis

The objectives of this thesis were the identification of the break-up mechanisms of ^{7}Li at 10 MeV/A and their quantitative contribution to the total break-up yield.

The nucleus ^{7}Li exhibits a well defined α+t cluster structure, is weakly bound ((α-t) threshold 2.478 MeV) and there is a large separation (2.16 MeV) between the α+t threshold and 4.63 ($\frac{7}{2}^{-}$) state above it. The $\frac{7}{2}^{-}$ state has a small width (Γ = 93 keV); the next state 6.68 MeV ($\frac{5}{2}^{-}$) state has width of Γ = 900 keV (Aj 84). It is therefore possible to identify non-sequential mechanisms unambiguously and neglect sequential mechanisms via high lying states. Further, a priori, it is possible to identify the important reaction channels and experimentally straightforward to quantify them. ^{7}Li represents a relatively simple heavy-ion projectile and, as such, should provide insight into reactions of heavier and more complex nuclei.

In the previous sections of Chapter 1 the experimental and theoretical status of light and heavy-ion induced break-up reactions have been reviewed. Experimental techniques have been examined. Special emphasis was given to the identification of reaction mechanisms by exclusive experiments.

The detection systems, data acquisition and analysis together with other experimental details are discussed in Chapter 2. Experimental results are presented in Chapter 3. Section 1 of Chapter 3 will discuss the inclusive yields of fast particles from ^{7}Li induced reactions at 10 MeV/A. Section 2 will present the results of particle-particle correlation measurements and discuss the reaction

mechanisms involved. Section 3 describes the results of particle-γ correlation studies. Finally, Section 4 will discuss the contribution of exclusive measurements to the total break-up yield. A summary of the data presented will be given in Chapter 4 and conclusions will be drawn. Future experimental and theoretical work will be identified.

CHAPTER 2

EXPERIMENTAL METHOD

'Excellent! If the adjustment spoils the beam, we will try the opposite change and it will improve it.'

Remark attributed to E.O. Lawrence

2.1 Accelerator, Beamlines and Scattering Chambers

All the experimental results presented here were obtained using the SERC 20MV Tandem Van-de -Graaf accelerator at the Nuclear Structure Facility (NSF), Daresbury. Figures 2.1 and 2.2 respectively depict the NSF and the general layout of the experimental areas. For this work, $^{7}Li^{-}$ ions were extracted from a Middleton source and accelerated to an energy E_o ($\lesssim$ 500 keV). The low-energy negative ion beam was then analysed by a 90° inflection magnet with a mass resolution of 0.4% prior to injection into the accelerator. The beam was accelerated towards the centre terminal which was held, accurately, at a potential +V (during these experiments V was about 17.4 MV). The $^{7}Li^{-}$ ions were stripped by transmission through a thin carbon foil and the final charge state, q, selected via an offset quadrupole charge state separator. A $^{7}Li^{3+}$ beam was then accelerated away from the positive centre terminal and analysed by a 90° analysing magnet with an energy resolution of 0.01% prior to injection into the beamline of the experimental area at an energy, $E = E_o + (1 + q)V$. Beam extracted from the accelerator by the analysing magnet was initially defined by a set of image slits set at ± 1 mm, giving a beam spot size of 2×2 mm^2. Energy resolution defined by the image slits, the stability of the analysing magnet and accelerating potential was $\sim$ 0.01%.

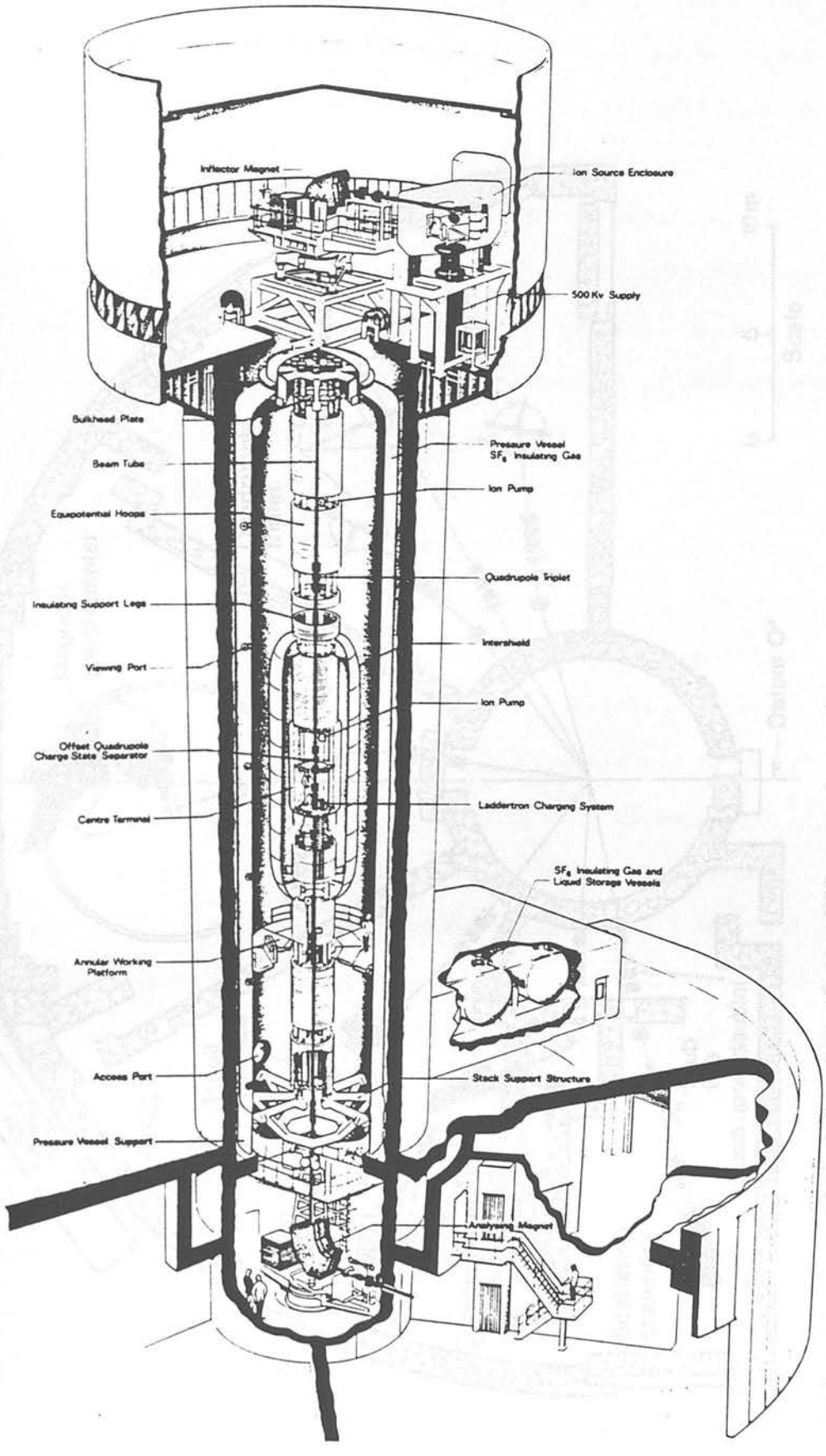

FIGURE 2.1: Cutaway diagram of the 20 MV Tandem Van-de - Graaf of the NSF, Daresbury.

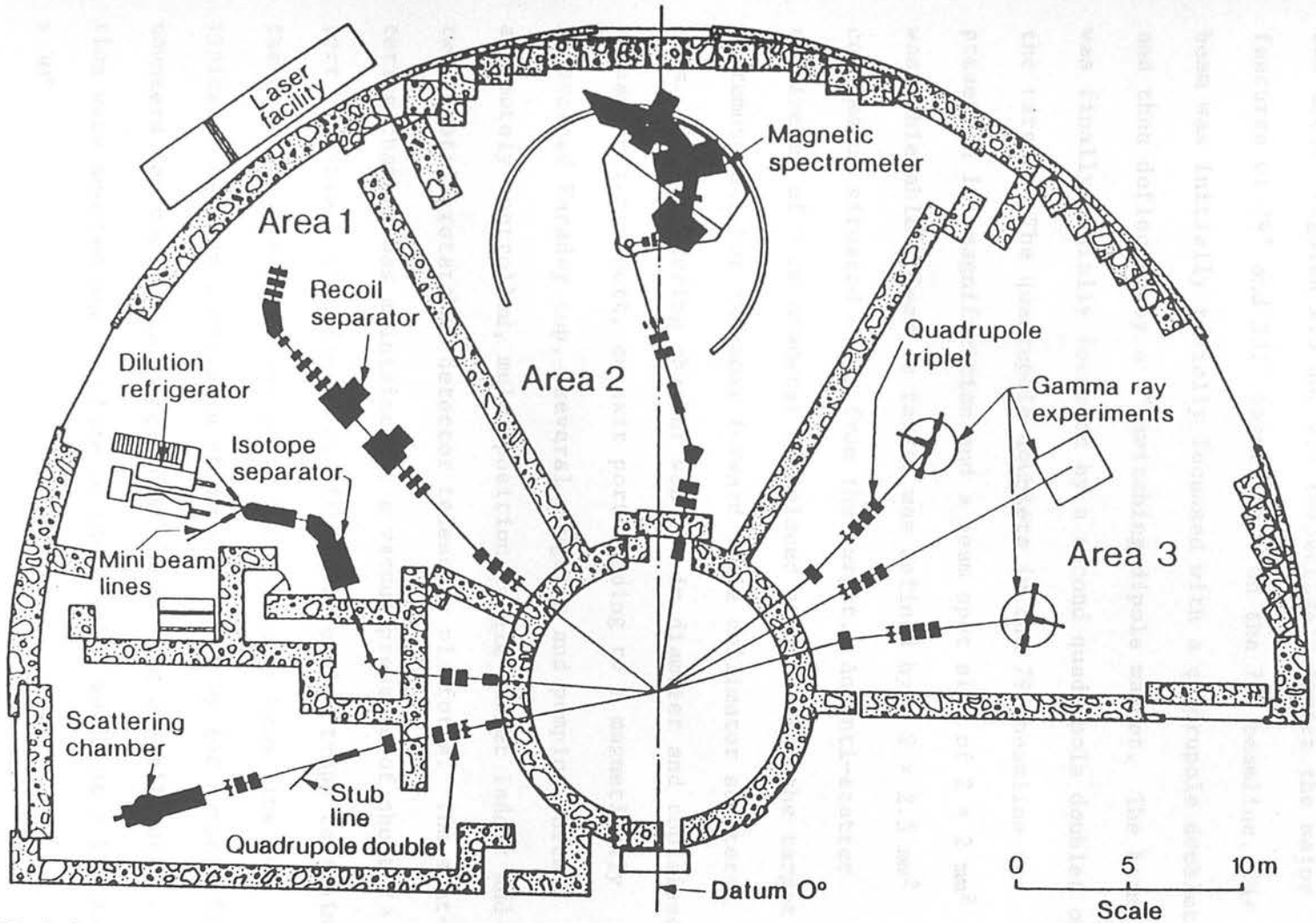

FIGURE 2.2: Schematic diagram of the NSF experimental areas.

In the work presented here, two beamlines were used. For particle-particle coincidence measurements the 79° beamline was used. For particle-γ coincidence measurements the 232° beamline was used. Figures 2.3 and 2.4 respectively depict the major features of 79° and 232° beamlines. On the 79° beamline, the beam was initially radially focussed with a quadrupole doublet and then deflected by a 5° switching dipole magnet. The beam was finally radially focussed by a second quadrupole doublet onto the target. The quadrupole doublets in the 79° beamline represent a 1:1 magnification and a beam spot size of 2×2 mm^2 was achievable. Beam on target was defined by a 2×2.5 mm^2 collimator situated 0.75m from the target. An anti-scatter collimeter of 4 mm diameter was placed at 0.2m from the target to remove all but the most forward angle collimator scattered beam. The scattering chamber was 1 m in diameter and contained a beam entrance port, an exit port leading to a magnetically suppressed Faraday cup, several roughing and pumping ports. a remotely controlled, multi-position / angle target ladder and two remotely rotatable detector telescope platforms. The scattering chamber was maintained at a vacuum pressure of about 2×10^{-5} torr by three diffusion pumps with water-cooled traps to minimise the back streaming of pump oil. The adjoining beam line was typically kept at a pressure of 5×10^{-6} torr by ion pumps. Single counters for monitoring target degradation and overall normalisation were mounted out of plane on the chamber walls at $\pm$ 15° and $\pm$ 30°.

On the 232° beamline, the beam was initially deflected by a

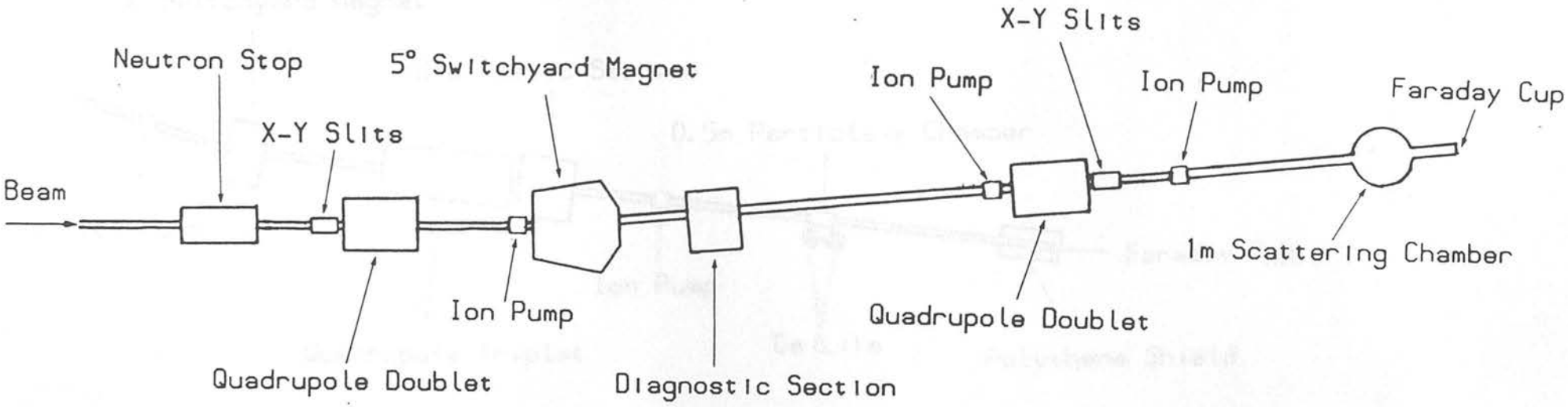

NOT TO SCALE

FIGURE 2.3: Plan diagram of 79° beamline.

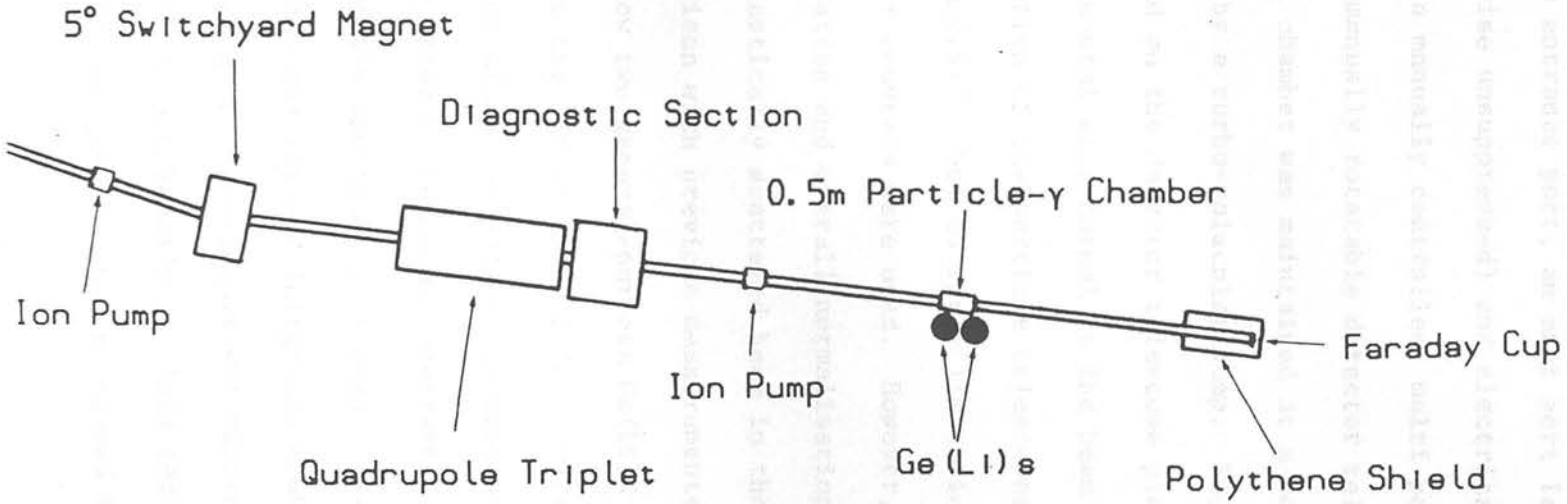

NOT TO SCALE

FIGURE 2.4: Plan diagram of 232° beamline.

5° switching dipole magnet. It was then radially focussed onto the target by a quadrupole triplet. Beam on target was defined by a 4mm diameter collimator situated 0.2m from the target. An anti-scatter collimator of 6mm diameter was placed at 0.1m from the target. The particle-γ chamber was 0.5m in diameter and contained a beam entrance port, an exit port leading to a distanced (but otherwise unsuppressed) and electrically isolated Tantalum beam-stop, a manually controlled, multi position/angle target ladder and a manually rotatable detector telescope platform. The scattering chamber was maintained at a vacuum pressure of about 5×10^{-5} torr by a turbo-molecular pump. Two particle telescopes were mounted on the detector telescope platform which rotated about a horizontal axis normal to the beam direction. The angular separation of the particle telescopes was fixed at a value of $(20.0 \pm 0.1)°$. Due to space limitations within the chamber, no monitor counters were used. However, the monitoring of target degradation and overall normalisation was achieved by observing the elastically scattered beam in the particle telescopes and comparison with previous measurements. The chamber was designed to allow two general-purpose Ge(Li)s to be placed in close proximity to the target. The Ge(Li)s were located in and out of the reaction plane defined by the beam axis and the plane of rotation of the detector telescope platform. The chamber walls between the Ge(Li)s and the target were of steel and 2mm thick.

Beam quality and integrity, when it was first focussed and during the experiments was monitored by a diagnostic section in each beamline. This section contained a quartz scintillator (which could be viewed by a TV camera), an

x-y beam profile monitor, a Faraday cup and a centrally aligned aperture, all of which could be remotely inserted into the beam-line. Electrometer readouts were available on all collimators and were used to ensure that all beams were properly aligned and focussed during an experiment.

Strong permanent magnets were placed around the collimators of all detector telescopes to deflect electrons that were ejected from the target by the beam.

2.2 Targets

Only solid targets were used in the work presented here. All targets consisted of a thin, self-supporting sheet of the enriched target material. Typical target thicknesses were 400-4000 $\mu g/cm^2$ with an area of about 1 cm^2. All targets were mounted on aluminium target holders, of which up to five could be stacked on the target ladder. Primary determination of the target thicknesses was made after each experiment by measuring the energy loss of 5.48 MeV α-particles (from a ^{241}Am source) during transmission through the target. Secondary determination came from the elastic scattering of the beam into the particle telescopes and the monitor counters. Target thicknesses determined in this way are estimated to be accurate to within ± 10%. For targets with a low melting point, such as ^{208}Pb, it was necessary to continually monitor the integrity of the target during its bombardment with beam. This was accomplished by measuring, at a fixed laboratory angle, the amount of elastically scattered beam per unit charge of beam current incident upon the

target. Further, beam currents used in these experiments were low, typically < 50 enA in particle-particle coincidence measurements and < 2 enA in particle-γ coincidence measurements. However, this is more directly related to the requirement to achieve acceptable counting rates in the detectors used.

Blank target frames were mounted on all target ladders to monitor supurious scattering and background from the beam. Particle-particle and particle-γ coincidence rates were negligible under these conditions.

An upper limit on the amount of light contaminants on the ^{60}Ni, ^{96}Zr, ^{120}Sn and ^{208}Pb targets was established to be 25 $\mu g/cm^2$. In comparison to the typical thickness of these targets (1000-4000 $\mu g/cm^2$) light contaminants contributed a negligible amount of events to cross section estimates.

2.3 Detection Systems

The design of the geometry of a detection system for a kinematically complete measurement of two break-up products from the decay of an unbound ejectile is determined by four main factors:

(i) The range of relative energies ε to be detected,

(ii) energy resolution,

(iii) true coincidence rate,

(iv) an acceptable ratio for true to random coincidences.

The minimum relative energy, ε_{min}, observable depends upon θ_{12}, the angular separation between the two counters. The detection efficiency of break-up products is enhanced when the angular separation between

the two telescopes is similar to the maximum opening angle of the decay fragments (in the laboratory frame). Factors (ii) to (iv) cannot be independently optimised. Energy resolution requirements mandate small solid angles. However, large solid angles are required to produce a satisfactory true coincidence rate and achieve a large value for the ratio of the true to random coincidences. A reasonable compromise between these conflicting requirements is depicted schematically in Figure 2.5. The detection system consists of two identical $\Delta E - E$ particle telescopes arranged symmetrically above and below the reaction plane. Not shown are the reject counters, placed behind each E detector, which vetoed any high energy events in which the particle completely traversed the $\Delta E - E$ system. Table 2.1 summarises the dimensions of the detection geometries used in this experiment. Geometry A possesses the largest solid angle and hence a large true coincidence efficiency. The horizontal acceptance angle is 4.2° which gives rise to the kinematic broadening of the peaks observed in the energy spectra, and represents the most significant contribution to the energy resolution. Typical energy resolution was about 500-800 keV (FWHM), depending upon the reaction observed. Geometry B has a smaller solid angle and hence a reduced true coincidence efficiency. However, it possesses a smaller and better defined value of θ_{12}, which implies a smaller minimum value of ε may be observed. For three-body kinematics calculations, an average value for θ_{12} was taken because of the large size of the collimators. Similarly values for θ_1, θ_2, ϕ_1, ϕ_2 were defined as the angles associated with the centre of each collimator.

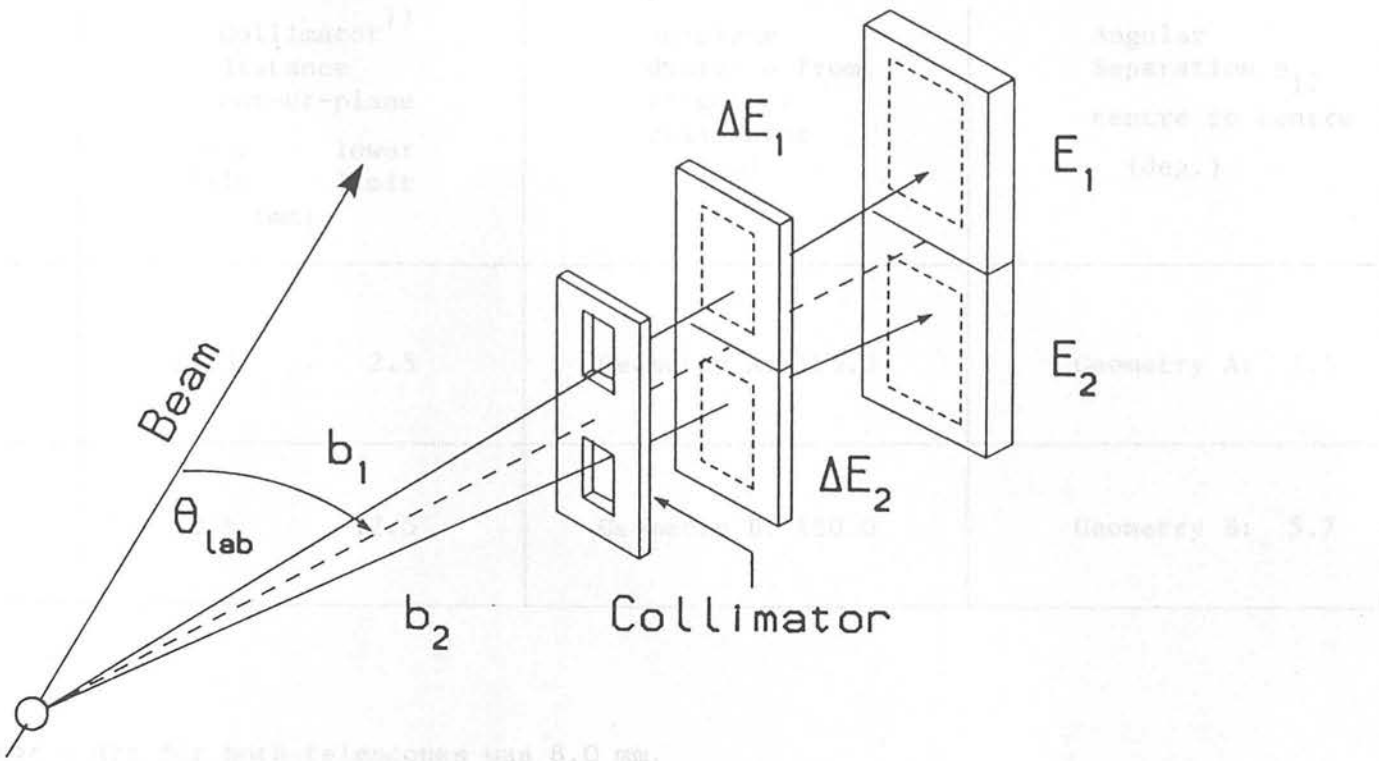

FIGURE 2.5: Schematic diagram of particle-particle coincidence detection system.

TABLE 2.1: Particle-Particle Correlation Detection System Geometry

Telescope	Collimator[1] distance out-of-plane upper limit (mm)	lower limit (mm)	In-plane distance from target to collimator (mm)	Angular Separation θ_{12} centre to centre (deg.)
1	12.5	2.5	Geometry A: 115.0	Geometry A: 7.5
2	-2.5	-12.5	Geometry B: 150.0	Geometry B: 5.7

1) Collimator width for both telescopes was 8.0 mm.

The detection system for particle-γ coincidence measurements was required to produce a satisfactory true coincidence rate and a large value for the ratio of the true to random coincidences. The geometry adopted is shown schematically in Figure 2.6. It can be seen that two Ge(Li)s were brought into close proximity with the target. Ge(Li)A was located in the reaction plane at $\theta_\gamma = 135°$. Ge(Li)B was located out of the reaction plane at $\theta_\gamma = 90°$. Target to detector centre was approximately 0.1m in each case. Two identical $\Delta E_1 - \Delta E_2 - E$ particle telescopes with large solid angles were mounted on the detector telescope platform to maximise the true coincidence rate and the available beam time. Table 2.2 summarises the detection geometry used.

2.4 Detectors

For particle-particle coincidence measurements the ΔE counters used were 200 mm^2 silicon surface barrier detectors with thicknesses of about 200 μm. The E counters were 10×15 mm^2 lithium drifted silicon (Si(Li)) detectors with thicknesses of about 4500 μm. The E_{rej} counters were 10×15 mm^2 silicon surface barrier detectors with thickness of about 500 μm. Low activity, annular α-particle sources (^{241}Am) were positioned between the detectors of the particle telescopes and were employed for testing and calibration purposes. With the $\Delta E - E$ detector telescopes described it was possible to detect tritons of energies between 8 and 45 MeV and alpha particles of energies between 19 and 112 MeV.

For particle-γ coincidence measurements the ΔE_1 counters used

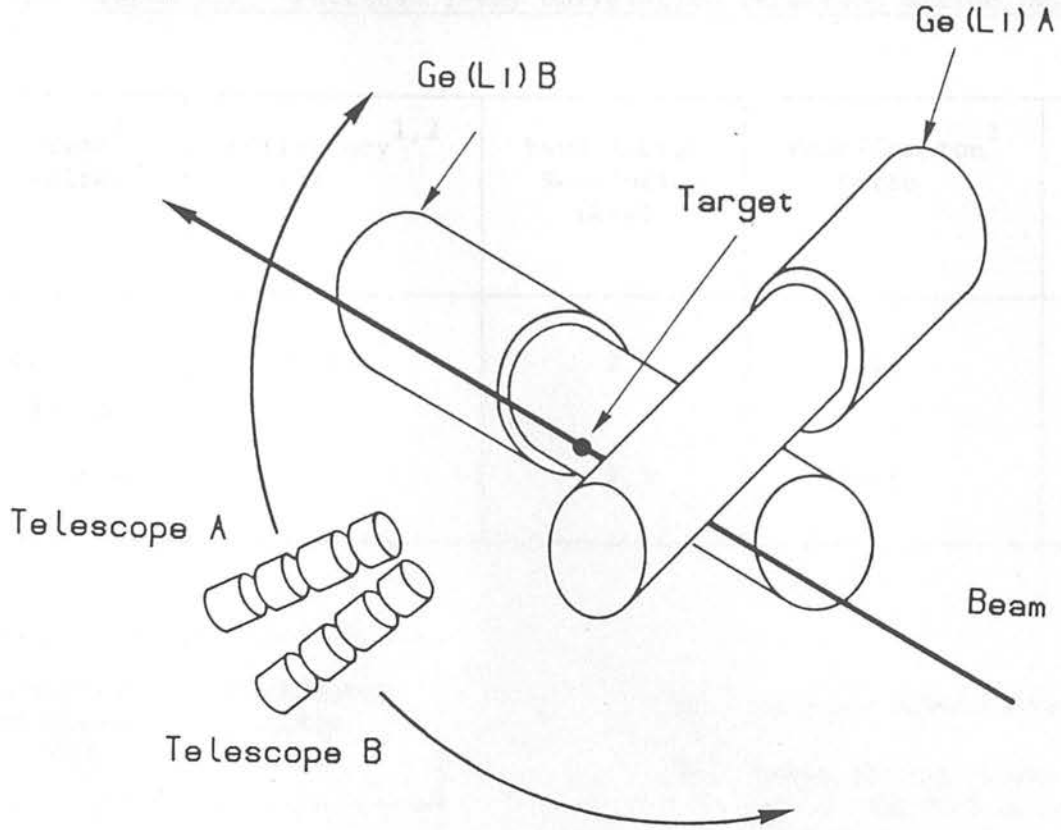

Figure 2.6: Schematic diagrem of particle γ-ray coincidence detection system.

TABLE 2.2 Particle γ-ray Correlation Detection System Details

Detector	Type[1] (size)	Efficiency[1,2] (%)	FWHM Energy Resolution (keV)	Peak/Compton[1] Ratio	Absolute Photo-peak Detection Efficiency[3] (%)	Distance from Target to Detector Centre (cm)
Ge(Li)A	Co-axial ($135cm^3$)	24.4	2.1	51:1	0.043 ± 0.003	10.1 ± 0.2
Ge(Li)B	Co-axial ($157cm^3$)	27.2	2.3	46:1	0.043 ± 0.003	10.1 ± 0.2

Telescope	Target to Collimator (cm)	Collimator Size (cm)
A[4]	9.6 ± 0.1	1.00 ± 0.05(ϕ)
B	8.8 ± 0.1	1.00 ± 0.05(ϕ)

1) Source: EG&G ORTEC specification.

2) Ratio of area under photopeak to that of a 3" × 3" NaI(Tℓ) detector, measured at 1333 keV with source-detector distance of 0.25m.

3) Measured with a calibrated ^{152}Eu source at the target position at a γ-ray energy of 1408 keV.

4) Most forward detector telescope.

were 200 mm^2 silicon surface barrier detectors of about 150 μm thickness. The ΔE_2 counters were 200 mm^2 silicon surface barrier detectors with thicknesses of about 700 μm. The E counters were 200 mm^2 lithium drifted silicon (Si(Li)) detectors with thicknesses of about 3000 μm. E_{rej} counters of the ΔE_2 type were employed. The $\Delta E_1 - \Delta E_2 - E$ detector telescopes described were able to detect tritons of energies between 6 and 40 MeV and α-particles of energies between 15 and 100 MeV.

Two general purpose co-axial Ge(Li) detectors were used. Energy and absolute photopeak efficiency calibrations were obtained by using calibrated γ-ray sources placed at the target position. Details are given in Table 2.2.

2.5 Data Acquisition

Figure 2.7 shows a simplified block diagram of the electronics used in acquiring all particle-particle coincidence data. The ΔE counters were connected to voltage-sensitive preamplifiers which provided a fast pickoff signal for coincidence timing and a buffered output for input into a charge-sensitive preamplifier. The fast ΔE preamplifier output signal was further amplified in the experimental area by a fast, fixed gain, 100 MHz d.c. amplifier. All fast signals were transmitted by low capacitance 50Ω cables to minimise degradation of the signal rise time. The E, E_{rej} and monitor counters were all directly connected to charge-sensitive preamplifiers. All detectors were biased through the charge-sensitive preamplifiers. The slow,

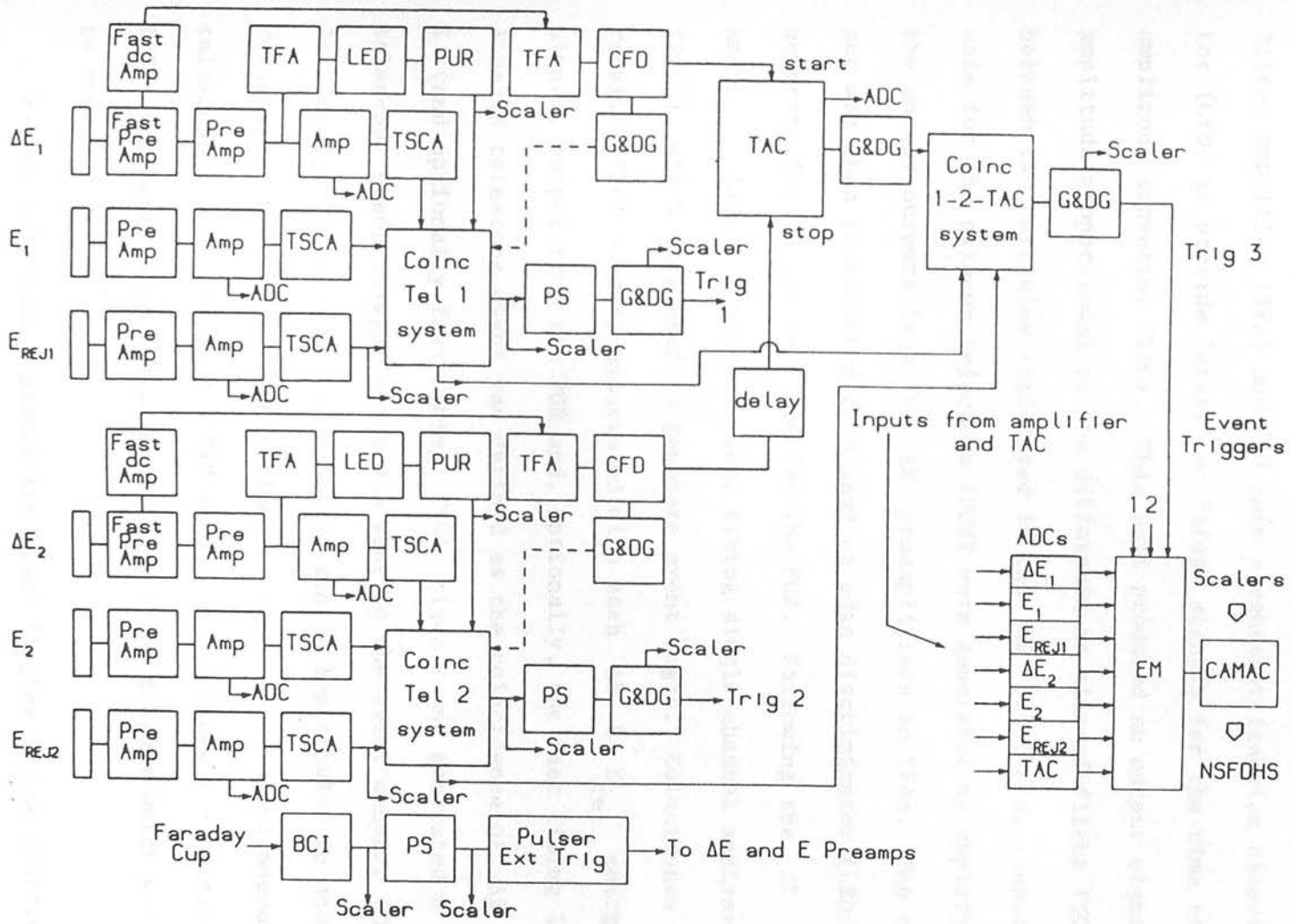

FIGURE 2.7: Block diagram of electronics used for particle-particle coincidence data acquisition.

analogue energy outputs, from the charge-sensitive preamplifiers were transmitted by 50Ω cables. The length of cable runs from the experimental area to the control room was approximately 80m. In the control room, the fast signals were amplified by a timing filter amplifier (TFA) and fed into a constant fraction discriminator (CFD) to provide 'start' or 'stop' signals for the time to amplitude convertor (TAC). This unit produced an output signal with amplitude proportional to the difference in time-of-flight (TOF) between two particles registered in the ΔE detectors. Input signals for the pile-up rejectors (PUR) were generated by amplifying the energy outputs from the ΔE preamplifiers in TFAs. The output was then transmitted to a leading edge discriminator (LED) to generate fast negative logic for the PUR. Following the ΔE, E and E_{rej} linear amplifiers were timing single channel analysers (TSCA) which were used to generate event logic. Coincidence units received TSCA outputs associated with each ΔE, E, E_{rej} energy signal, output from the PUR and, optionally, the fast timing logic. A valid telescope event was defined as the coincidence of ΔE and E (and optionally fast timing) TSCA signals and generated a telescope event trigger which was sent to the event manager (EM). In addition, a valid telescope event sent a logic pulse to another coincidence module which determined if there was a simultaneous telescope 1 - telescope 2 - TAC event. A telescope 1 - telescope 2 - TAC coincidence produced a coincidence event trigger which was sent to the EM.

Figure 2.8 shows a simplified block diagram of the electronics used in acquiring all particle-γ coincidence data. The methodology

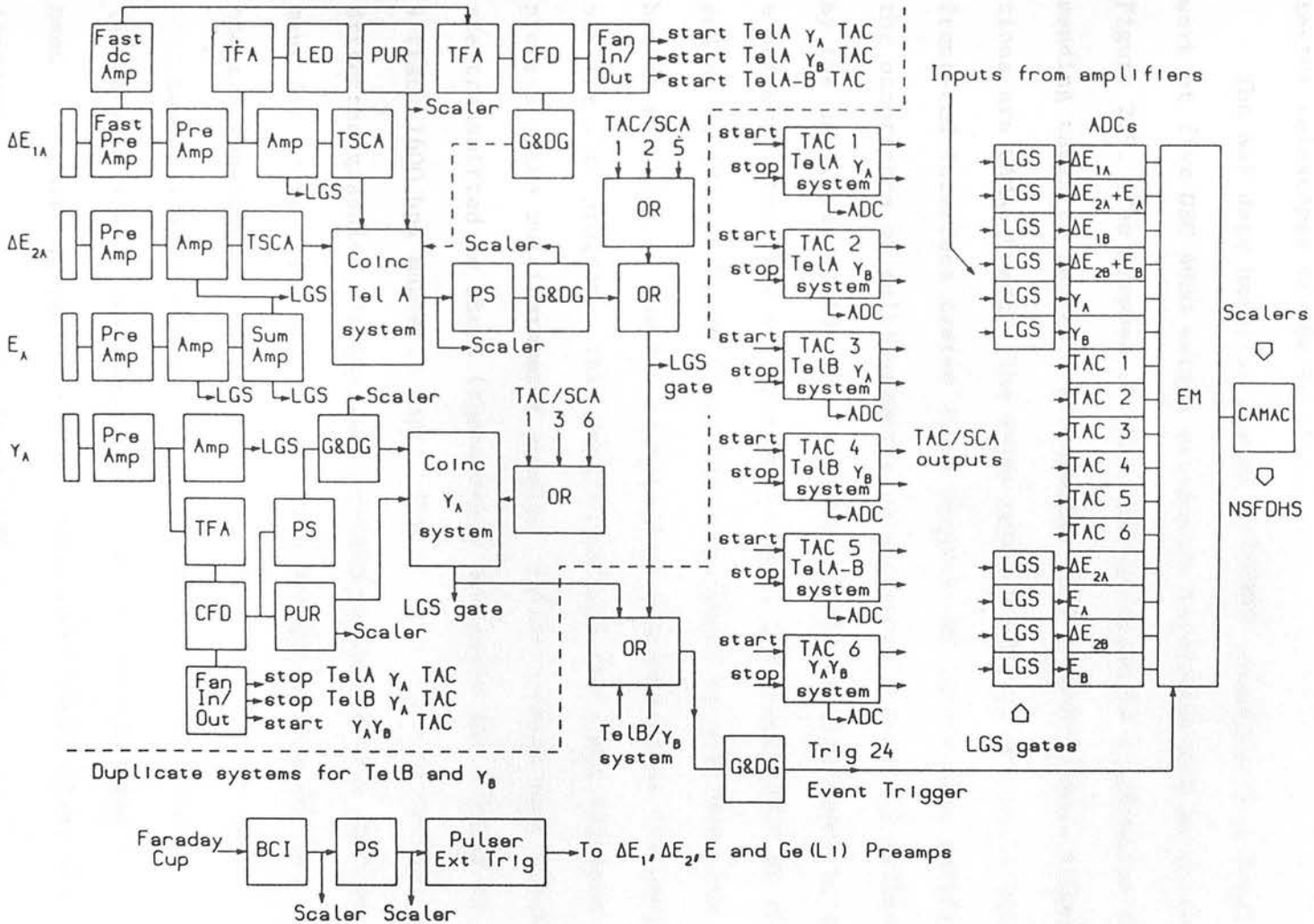

FIGURE 2.8: Block diagram of electronics used for particle γ-ray coincidence data acquisition.

is similar to the particle-particle coincidence system. The logic was structured to provide an event trigger for the EM from any combination of two (or more) valid events from either of the detector telescopes or the Ge(Li)s.

The NSF data handling system (NSFDHS) consists of a local network of five GEC 4000 series processors interconnected as shown in Figure 2.9. The purpose of this configuration is to disperse demanding tasks to separate processors. All interprocessor communications are CAMAC based. The event manager (EM) is an intelligent front-end interface system which accepts ADC interrupts, verifies the occurrence of multiparameter coincidences previously defined by the user, passes ADC data to either CAMAC singles store or to a buffered store for multiparameter data, and clears ADCs at the end of an event. The EM flags the A-processor to read down its buffer when full. The A (accumulation)-processor runs the user's on-line sort program. This program defines the event triggers and processes the multiparameter events. Multiprocessor data blocks are transmitted to the R (resources)- processor for writing to 9-track 1600 bpi magnetic tape. The C (control) - processor drivesthe graphics displays and provides an interactive environment for controlling data acquisition and displaying on-line spectra generated by the user's program in the A-processor.

Logic signals sent to the EM are termed event triggers. In the experiments described, two types of event trigger were used. In particle-particle coincidence experiments three direct triggers were used. They are defined by the user's on-line sort program which sets up an internal register of the EM. When presented with a direct trigger, the EM examines the register and

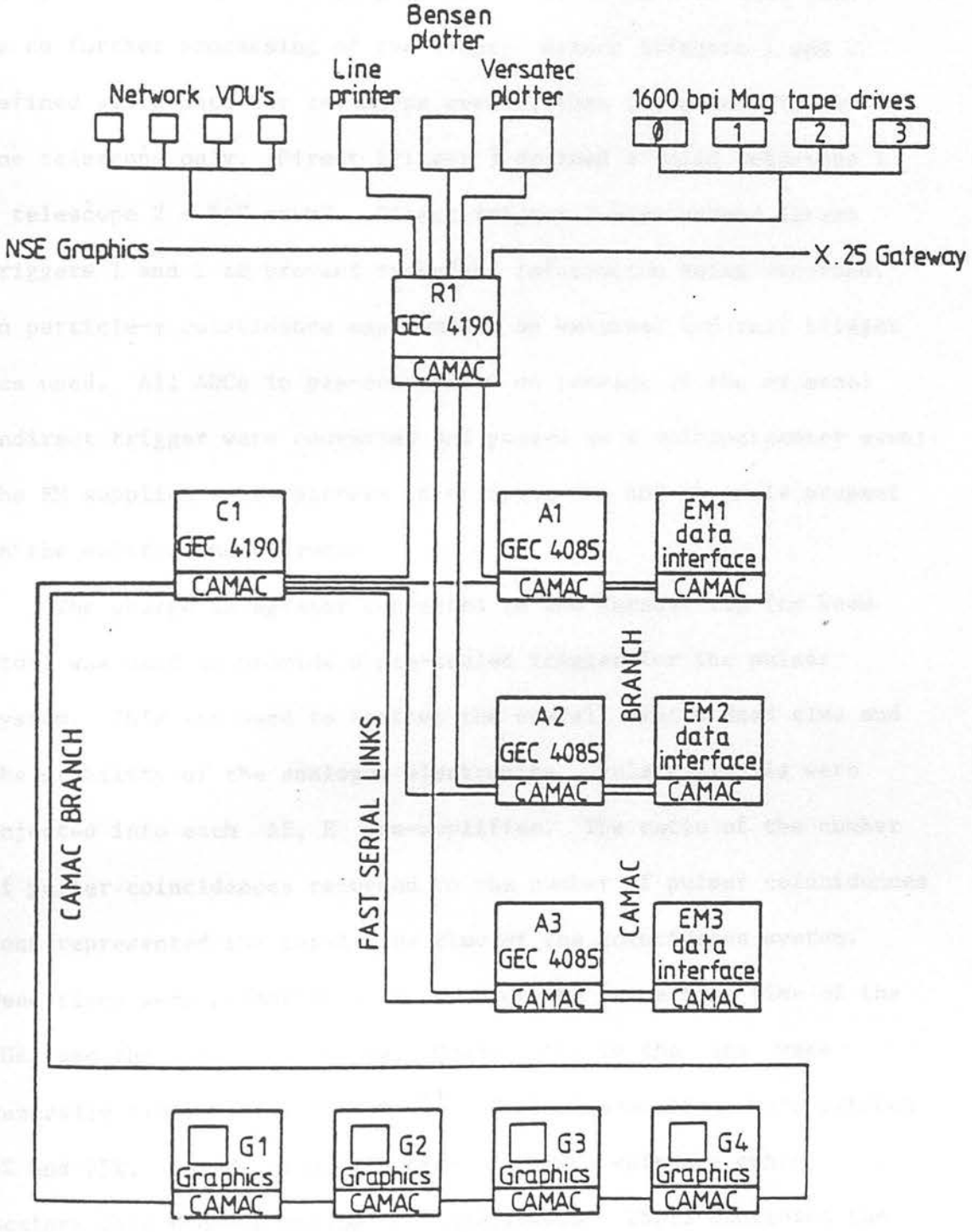

FIGURE 2.9: Block diagram showing configuration of the NSF. Data Handling System.

verifies that all required ADCs are in pre-conversion. If this is so, coincidence gates are supplied to the ADCs and at the end of the pre-conversion cycle they go into conversion. If not, there is no further processing of the event. Direct triggers 1 and 2 defined valid detector telescope events, that is, events involving one telescope only. Direct trigger 3 defined a valid telescope 1 - telescope 2 - TAC event. Direct trigger 3 also vetoed direct triggers 1 and 2 to prevent redundant information being recorded. In particle-γ coincidence experiments an external indirect trigger was used. All ADCs in pre-conversion on receipt of the external indirect trigger were converted and passed as a multiparameter event. The EM supplied a bit pattern identifying the ADC channels present in the multiparameter event.

The charge integrator connected to the Faraday cup (or beam stop) was used to provide a pre-scaled trigger for the pulser system. This was used to monitor the overall system dead time and the stability of the analogue electronics. Pulser signals were injected into each ΔE, E pre-amplifier. The ratio of the number of pulser coincidences recorded to the number of pulser coincidences sent represented the total live time of the coincidence system. Dead times were primarily a function of the inspection time of the PURs and the ΔE count rates. Count rates in the ΔEs were generally limited to $\leq 20{,}000\ s^{-1}$. Typical dead times were between 1% and 25%. In addition, a number of CAMAC, software controlled, scalers were updated during the experiments. These monitored the number of telescope events, TAC events, coincidence events, event triggers, pulser events, pile-up events and the pre-scaling of event and pulser triggers.

2.6 Data Analysis

Event-by-event multiparameter data were analysed off-line by sorting the stored binary data on the Edinburgh/DL GEC 4160 work station. All event sorting was performed with the program CHAOS (Da 83b). Data display and analysis was handled by the DL interactive graphics system.

Particle identification was performed, both on and off-line, by generating in software, the standard light-ion identification algorithm (Go 64)

$$PI \propto TZ^2M^{n-1} \propto (\Delta E + E)^n - E^n \quad . \qquad (2.1)$$

The exponent n assumed values $1.69 \lesssim n \lesssim 1.76$ and was optimised by viewing a two-dimensional PI versus $(\Delta E + E)$ plot. Figure 2.10 shows a typical particle identification spectrum. Figures 2.11 and 2.12 show typical TAC spectra. Note that the spectra are for any particle-particle or particle-γ coincidence respectively. During sorting, software gates were established in the particle identification, TAC and energy spectra. In the analysis of particle coincidence data total energy and projected energy spectra were created for each coincidence channel under investigation. In addition, total energy and projected energy spectra were created by gating on regions of the TAC spectra outside the real + random coincidence peak. This provided an estimate of the random coincidences occurring. In practice random events represented $\lesssim$ 1% of the coincidences in the channels investigated and were neglected. Energy calibrations were determined by ^{241}Am α-energy spectra and fitting

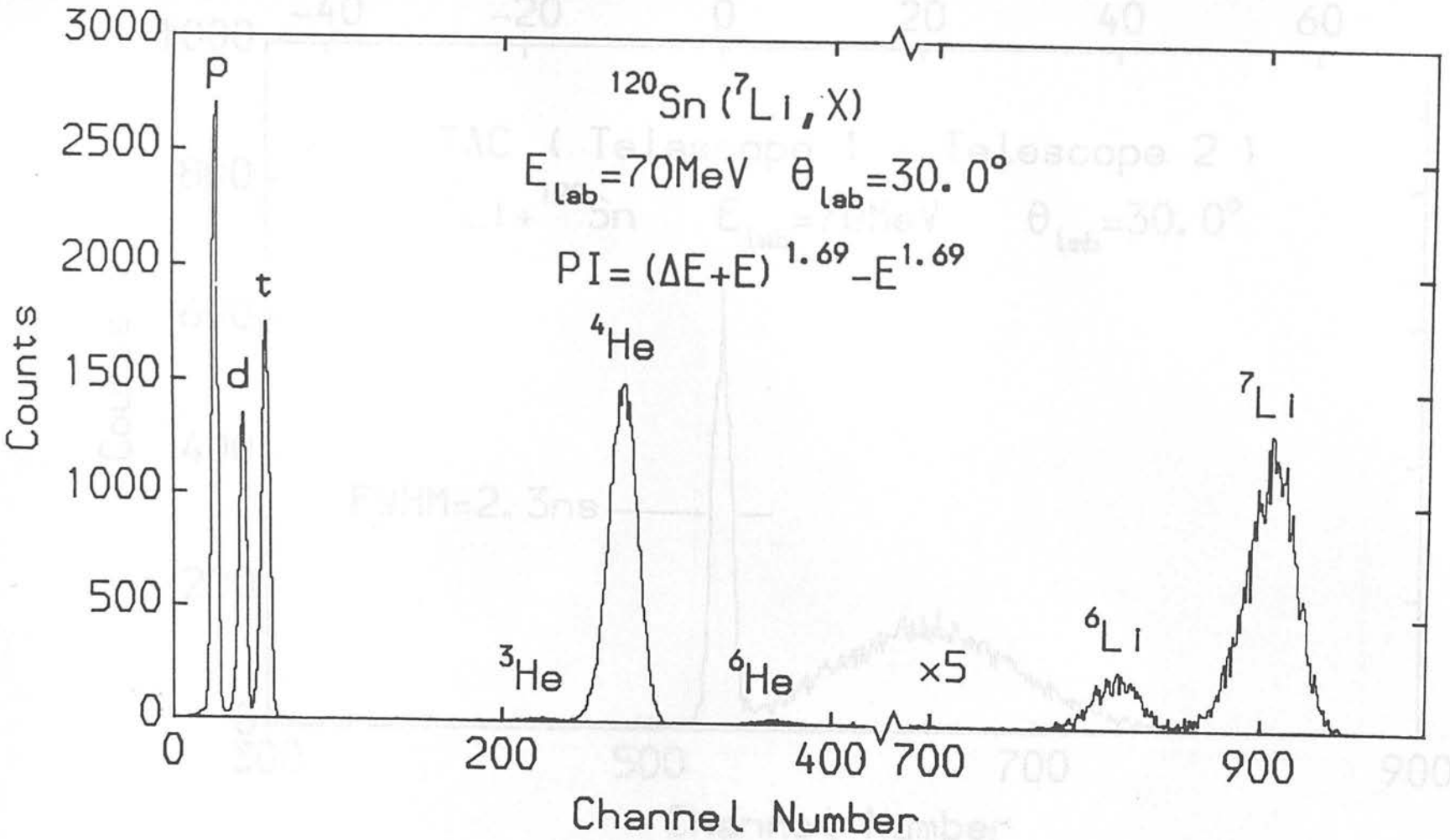

FIGURE 2.10: Typical particle identification spectrum.

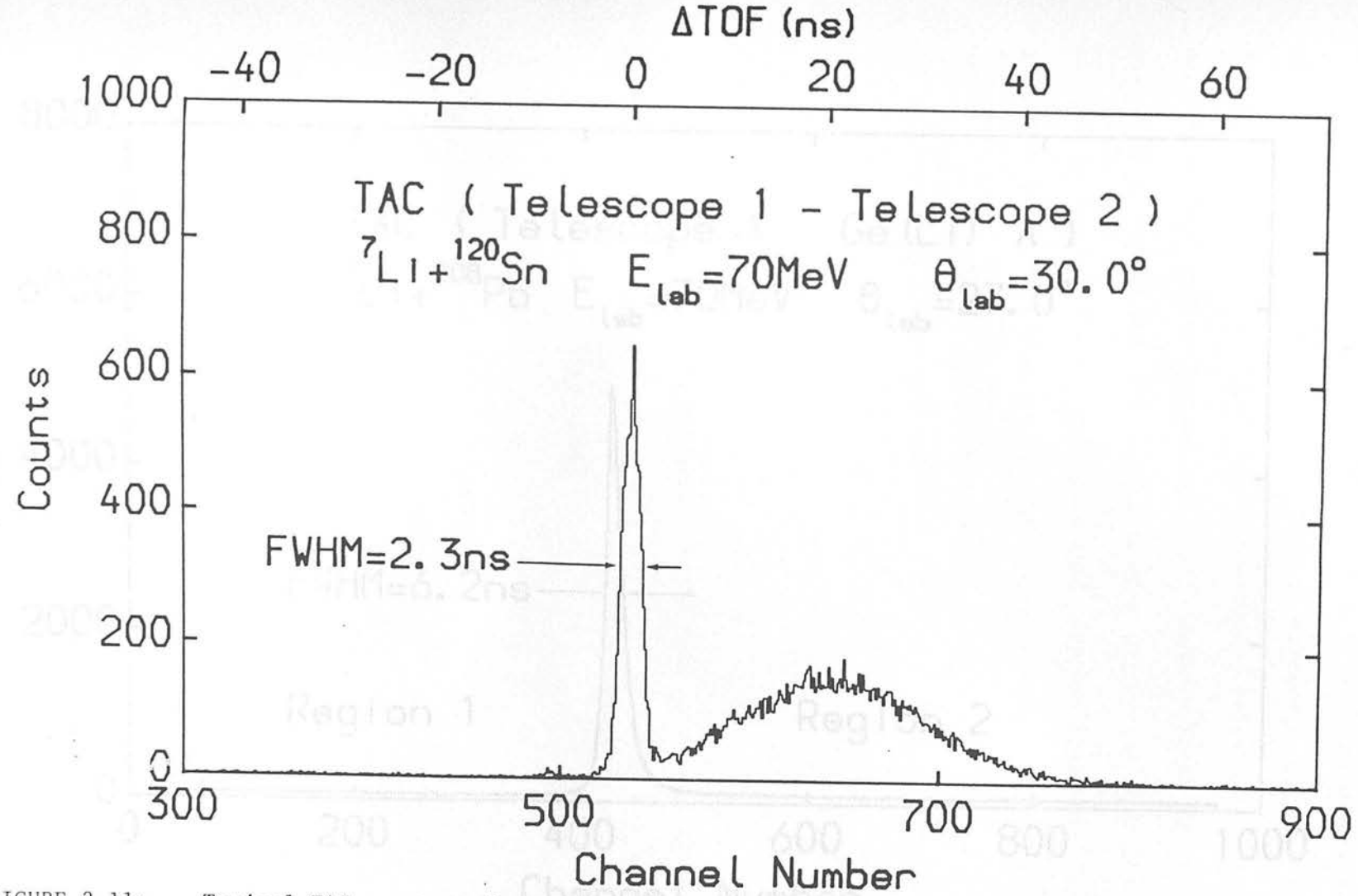

FIGURE 2.11: Typical TAC spectrum for any particle-particle coincidence. Broad peak to the right of the real + random peak is from pulser-pulser coincidences.

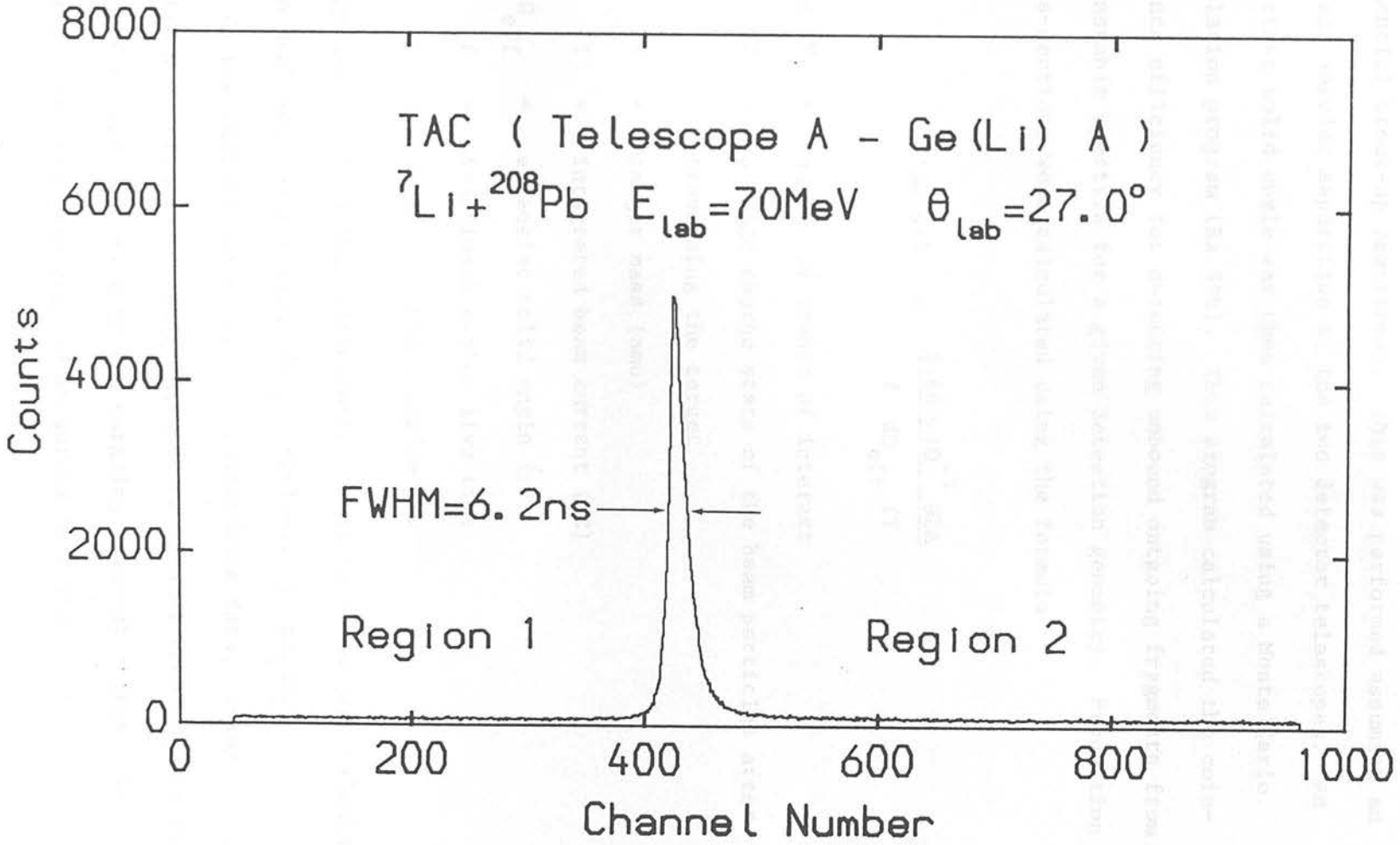

FIGURE 2.12: Typical TAC spectrum for any particle γ-ray coincidence.

to known transitions in the detector telescope singles data. Projected energy spectra were analysed with three-body kinematics by converting the observed particle energy to a relative energy (for sequential break-up reactions). This was performed assuming an average angular separation of the two detector telescopes. An effective solid angle was then calculated using a Monte Carlo simulation program (Ra 84b). This program calculated the coincidence efficiency for detecting unbound outgoing fragments from an unstable ejectile for a given detection geometry. Production cross-sections were calculated using the formula

$$\frac{d\sigma}{d\Omega}(\text{mb/sr}) = \frac{2.66 \times 10^{-7}\ NZA}{I\ d\Omega_{eff}\ fT} \qquad (2.2)$$

where N = number of counts of interest

Z = average charge state of the beam particles after traversing the target

A = target mass (amu)

I = integrated beam current (μC)

$d\Omega_{eff}$ = effective solid angle (sr)

f = fractional system live time

T = target thickness (mg/cm^2) .

Energy integrated double differential cross sections were calculated in an analogous manner with $d\Omega_{eff}$ replaced by $d\Omega_1 d\Omega_2$.

In the analysis of particle-γ coincidence data, γ-ray energy spectra were created for each coincidence channel under investigation and binned according to the outgoing fragment energy. In addition, spectra were created by gating on region 1 of the particle-γ

TAC spectrum to provide an estimate of the random coincidences occurring. In general, random events represented < 3% of the coincidences in the channels investigated and were neglected. Spectra were also generated by gating on region 2 of the particle-γ TAC spectrum to obtain particle-γ coincidences from events involving states of the residual nucleus where $0 < \tau_{\frac{1}{2}} < 250$ns. Production cross sections were calculated using the formula

$$\frac{d\sigma}{d\Omega}\ (\text{mb/sr}) = \frac{2.66 \times 10^{-7}\ NZA}{I\ d\Omega_{eff}\ fT\ I_{\gamma}} \qquad (2.3)$$

where N is the number of counts of interest in the photopeak associated with the residual nucleus of the reaction channel, I_{γ} is the fractional intensity of the photopeak of interest, and $d\Omega_{eff}$ is $d\Omega$ (detector telescope solid angle) × the absolute photopeak efficiency at energy E_{γ}.

CHAPTER 3

EXPERIMENTAL RESULTS AND DISCUSSION

'You see what you want to see'

L. Wittgenstein

3.1 Inclusive ^{7}Li Induced Reactions at 10 MeV/A

In this section, the inclusive yields of outgoing charged particles (p, d, t, ^{3}He and ^{4}He) from ^{7}Li induced reactions at 10 MeV/A on ^{12}C, ^{60}Ni, ^{96}Zr, ^{120}Sn and ^{208}Pb are presented. Inclusive measurements were performed simultaneously with particle-particle and particle γ-ray correlation measurements by pre-scaling singles detector telescope events. Figures 3.1 to 3.5 display typical inclusive energy spectra of charged particles at forward angles. Figures 3.6 to 3.10 display typical inclusive energy spectra of charged particles at backward angles. The threshold at the low energy end of the spectra is due to the thickness of the ΔE detector and the lower level threshold of the E detector TSCA (see Section 2.5). With the exception of the inclusive proton energy spectra, all spectra exhibit broad structureless peaks with maxima at energies close to

$$E_{fragment} = (m_{fragment}/m_{projectile})E_{projectile} + Q_3(gs)$$

(i.e. about beam velocity). This is characteristic of projectile break-up. The inclusive ^{4}He energy spectra exhibit a low energy evaporative component at forward and backward angles. The inclusive d, t and ^{3}He energy spectra also exhibit an evaporative component, particularly at backward angles on the lighter targets. The inclusive proton energy spectra show no broad structureless peaks and

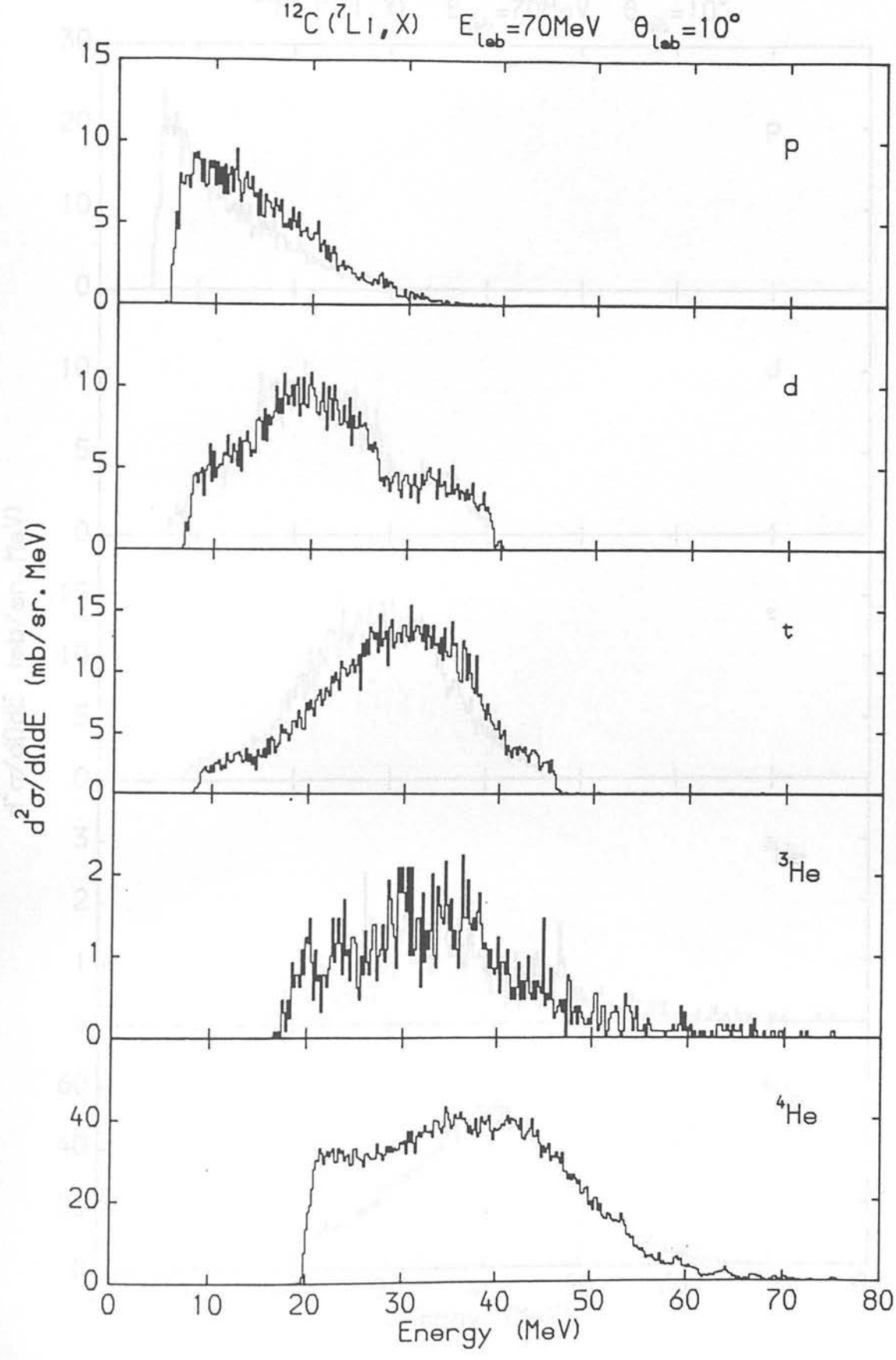

FIGURE 3.1: Inclusive energy spectra of outgoing charged particles from the reaction 70 MeV ^{7}Li + ^{12}C at forward angles.

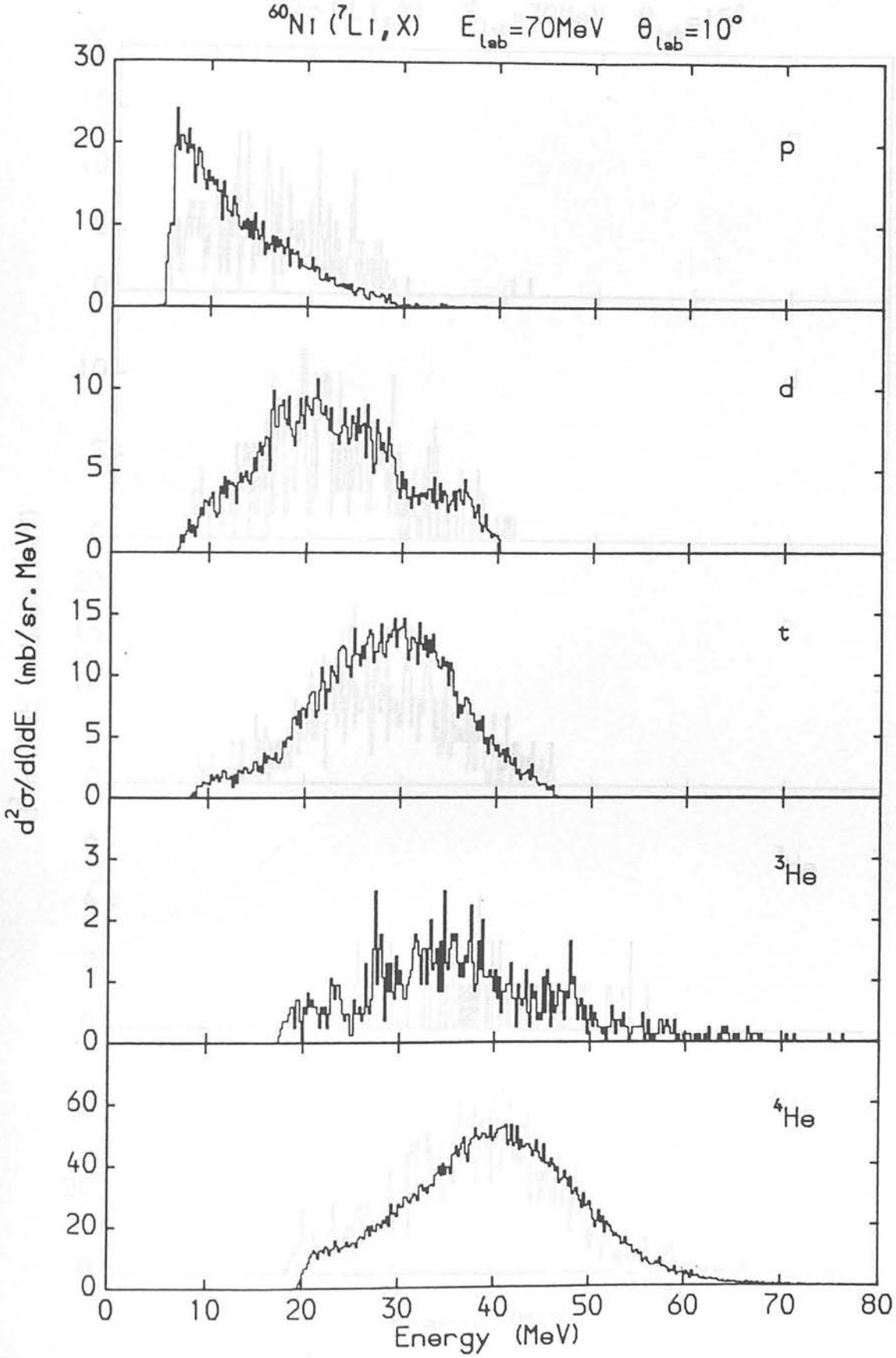

FIGURE 3.2: Inclusive energy spectra of outgoing charged particles from the reaction 70 MeV ^{7}Li + ^{60}Ni at forward angles.

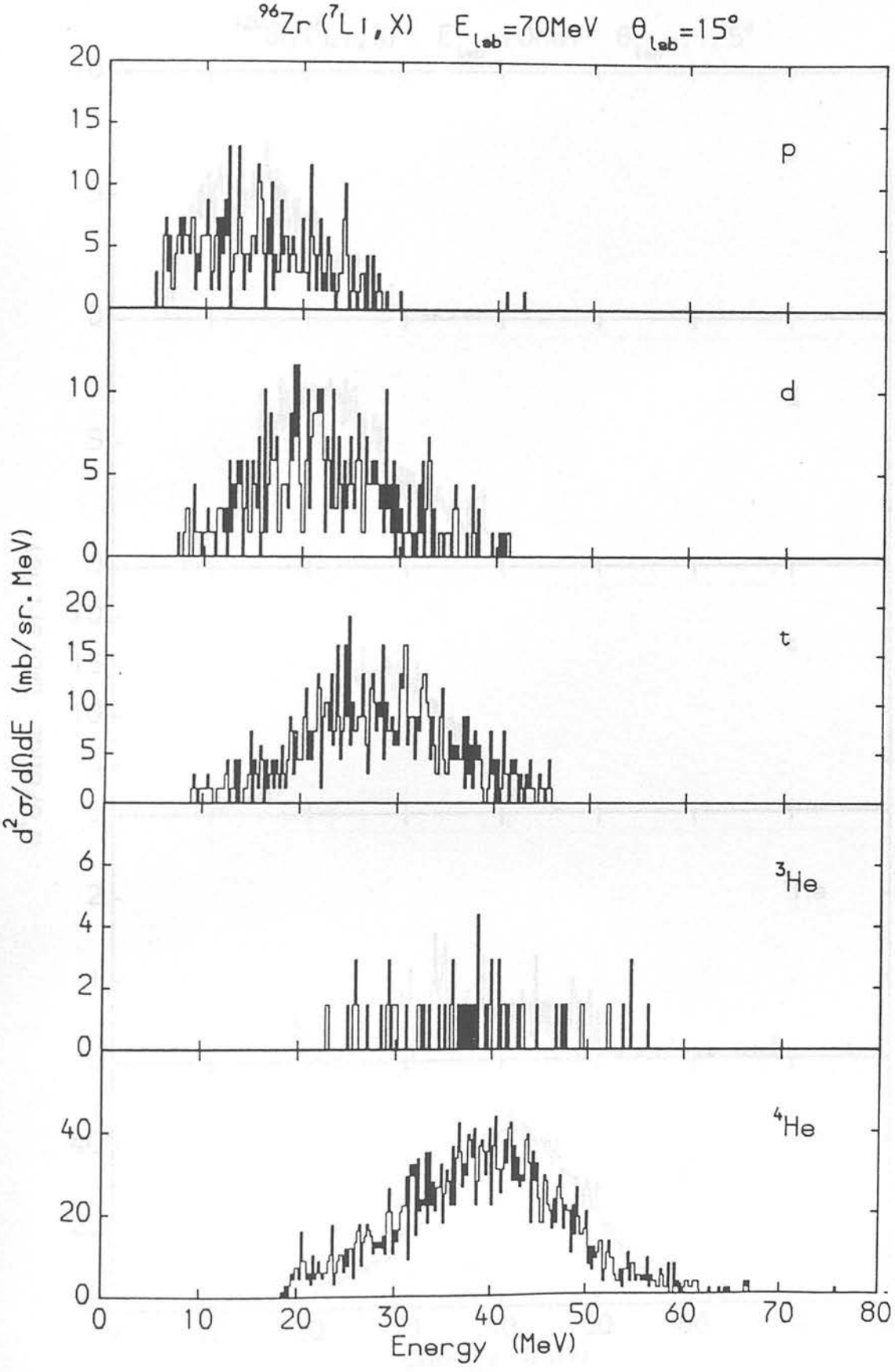

FIGURE 3.3: Inclusive energy spectra of outgoing charged particles from the reaction 70 MeV ^{7}Li + ^{96}Zr at forward angles.

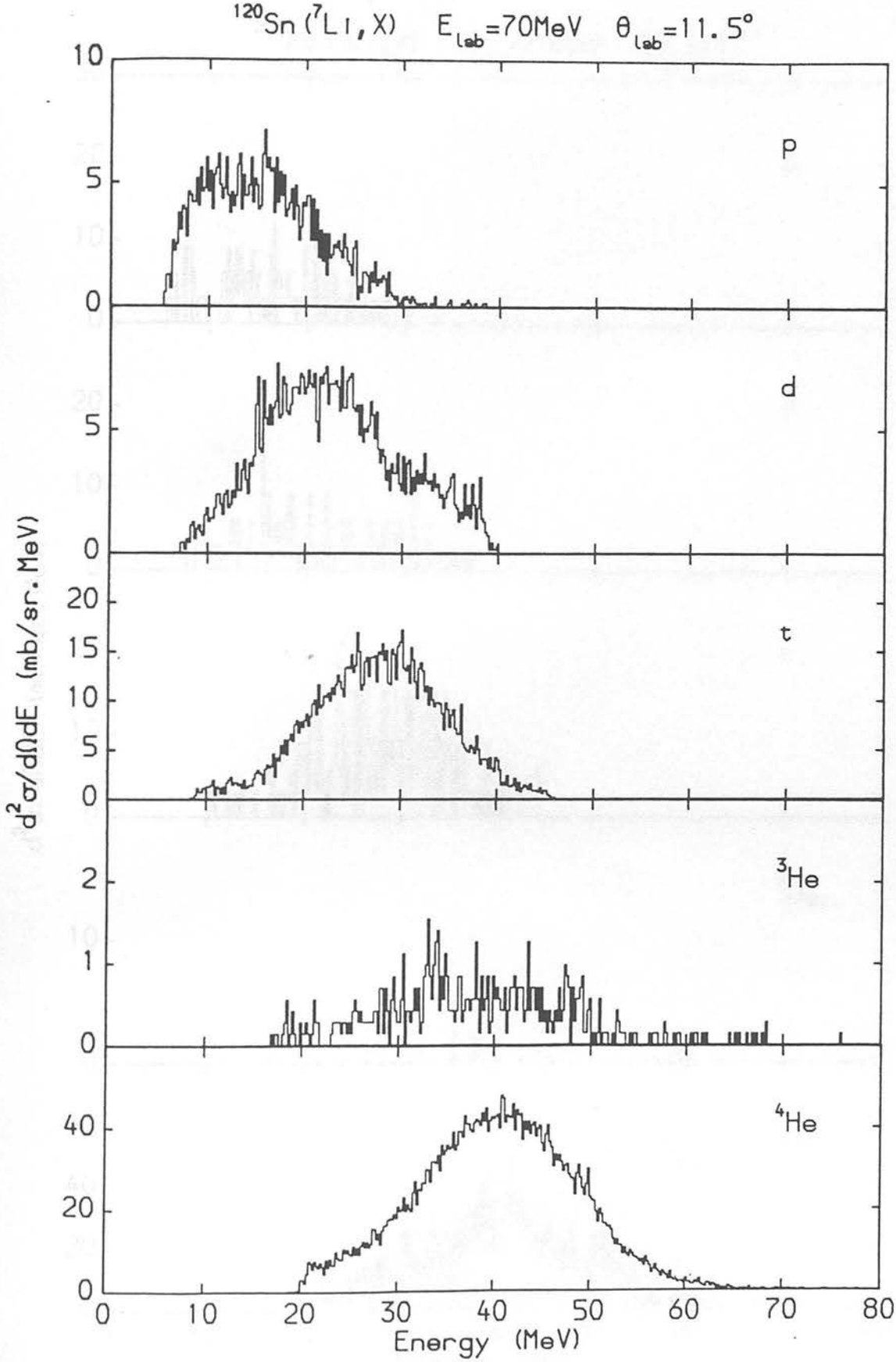

FIGURE 3.4: Inclusive energy spectra of outgoing charged particles for the reaction 70 MeV ^{7}Li + ^{120}Sn at forward angles.

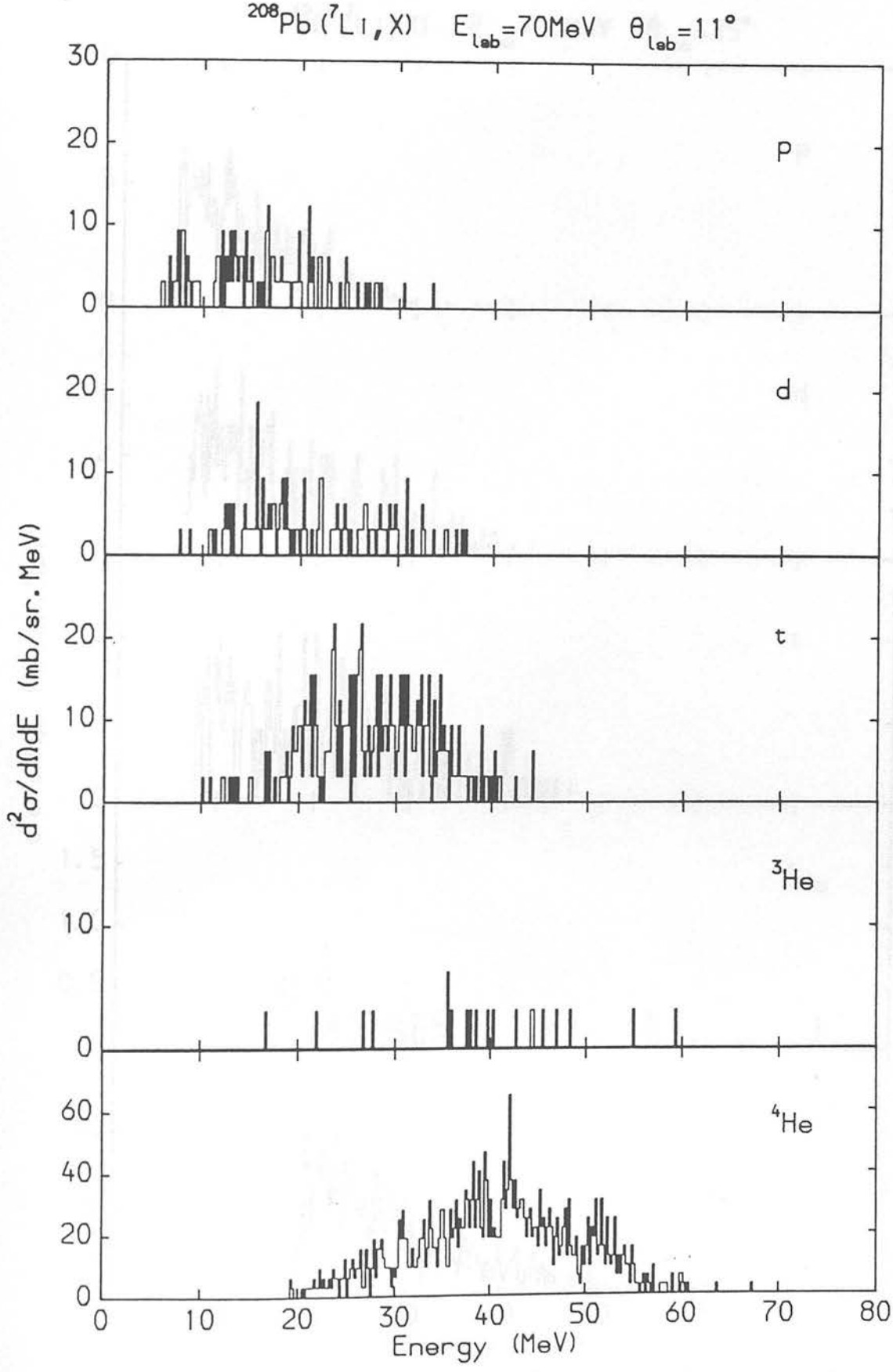

FIGURE 3.5: Inclusive energy spectra of outgoing charged particles from the reaction 70 MeV ^{7}Li + ^{208}Pb at forward angles.

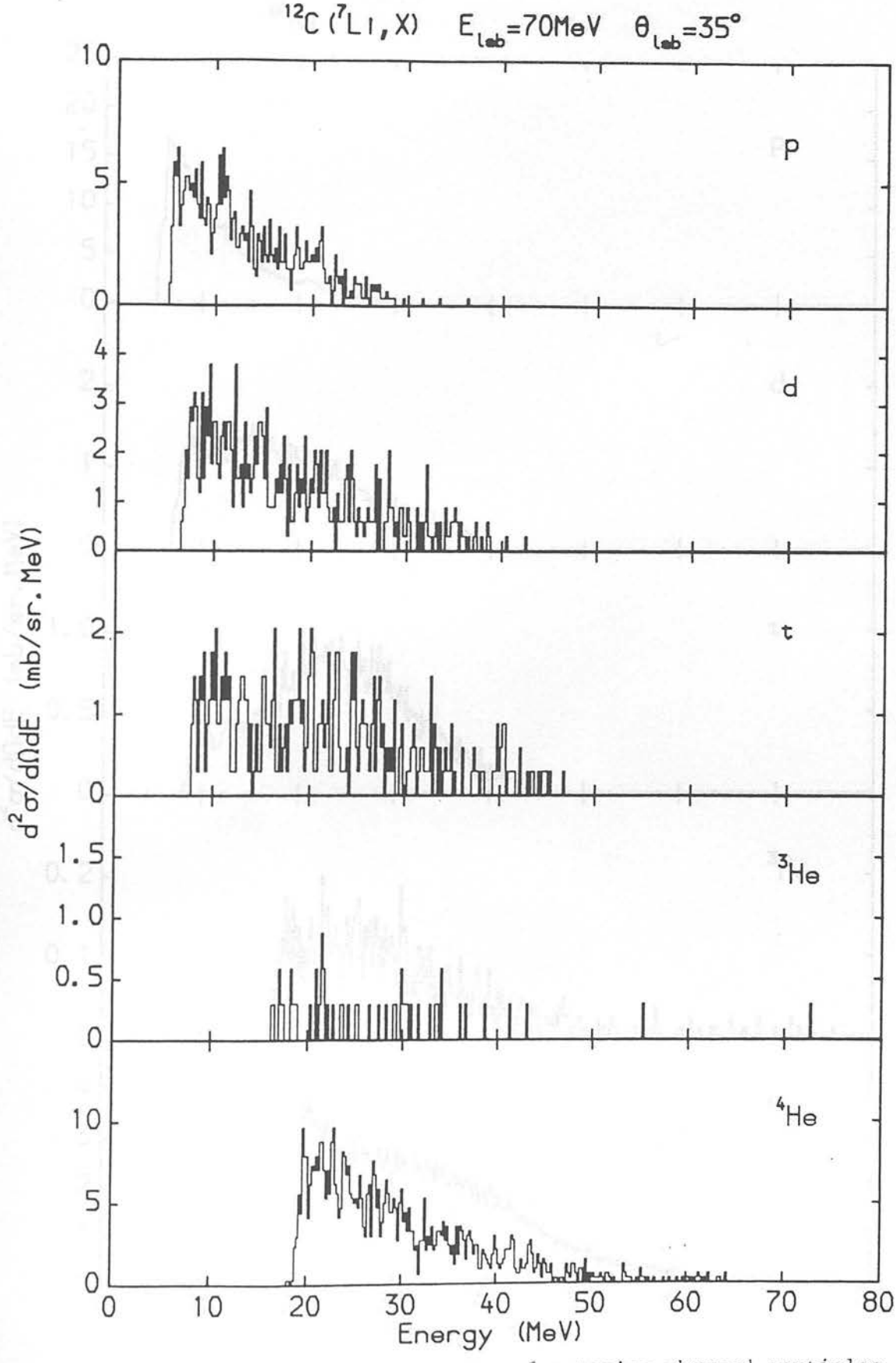

FIGURE 3.6: Inclusive energy spectra of outgoing charged particles from the reaction 70 MeV ^{7}Li + ^{12}C at backward angles.

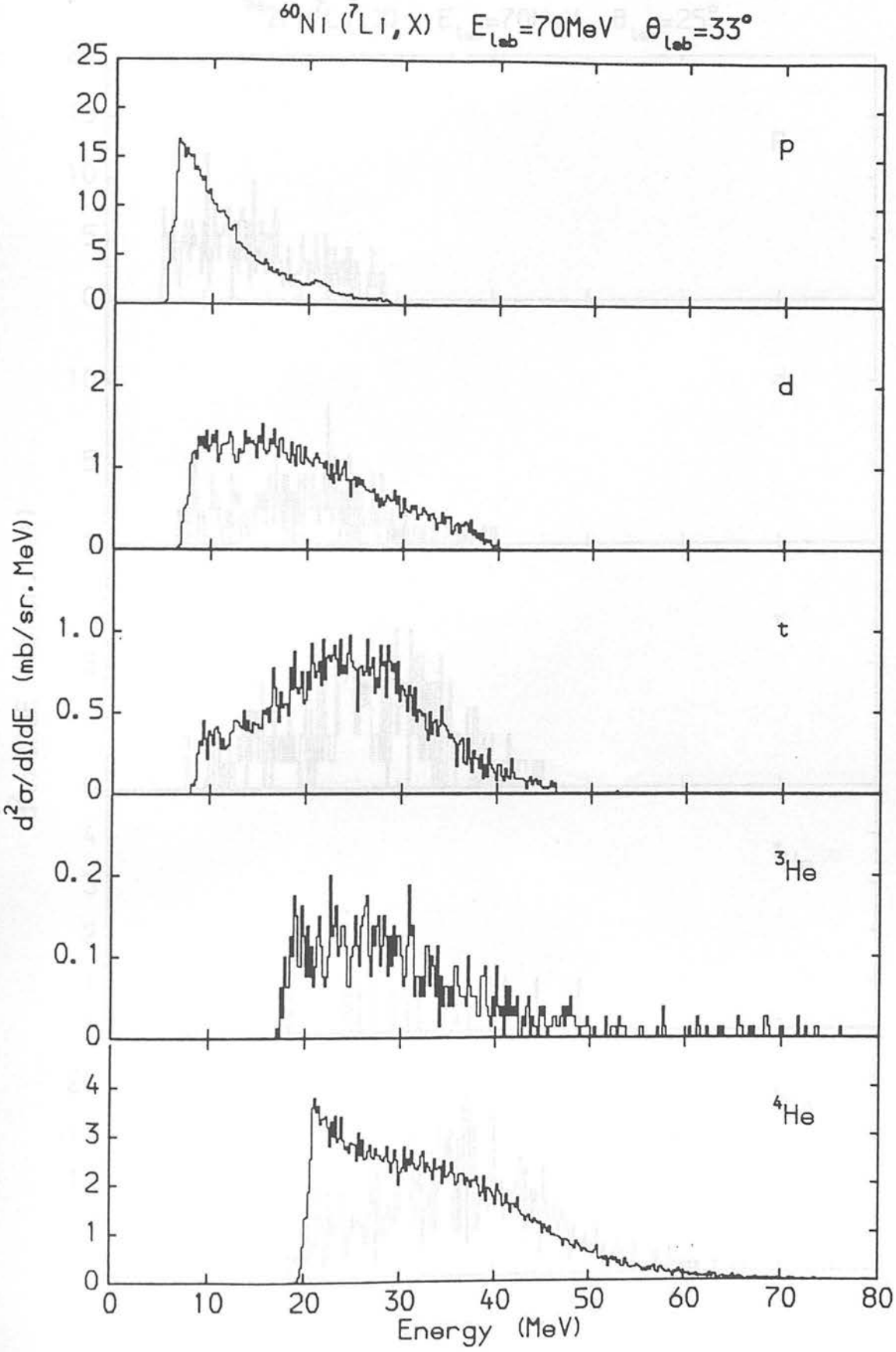

FIGURE 3.7: Inclusive energy spectra of outgoing charged particles from the reaction 70 MeV ^{7}Li + ^{60}Ni at backward angles.

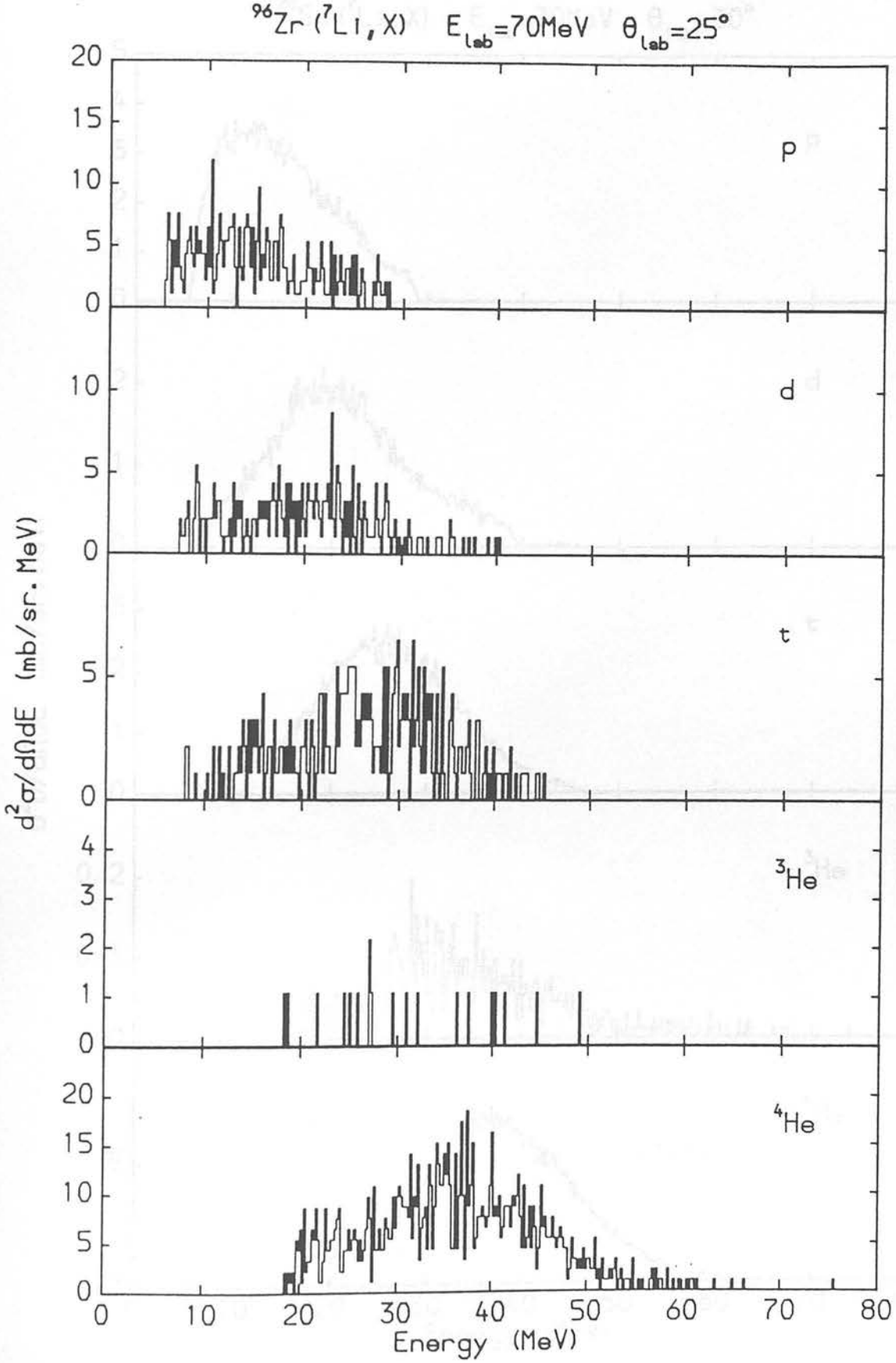

FIGURE 3.8 Inclusive energy spectra of outgoing charged particles from the reaction 70 MeV ^{7}Li + ^{96}Zr at backward angles.

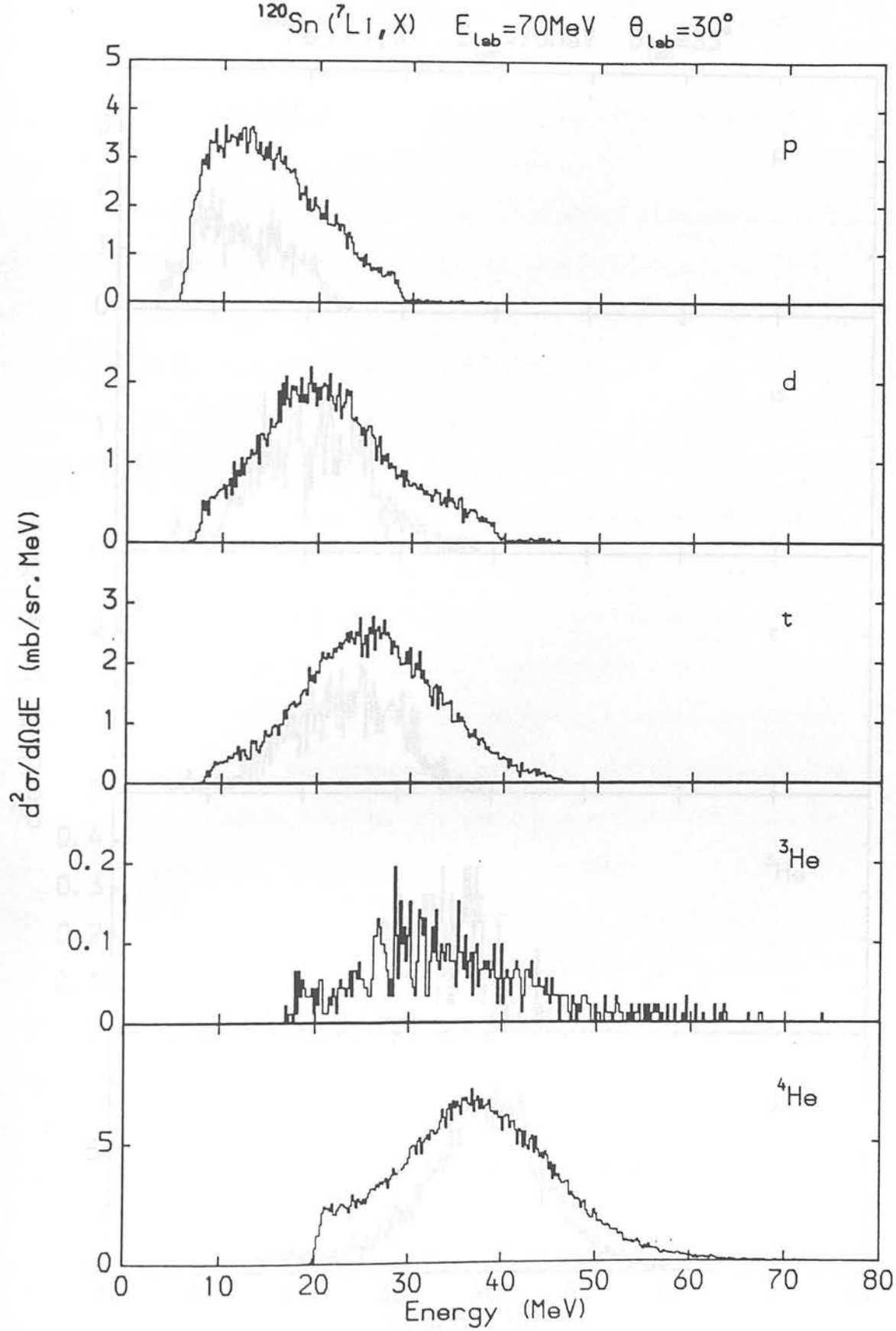

FIGURE 3.9 Inclusive energy spectra of outgoing charged particles from the reaction 70 MeV ^{7}Li + ^{120}Sn at backward angles.

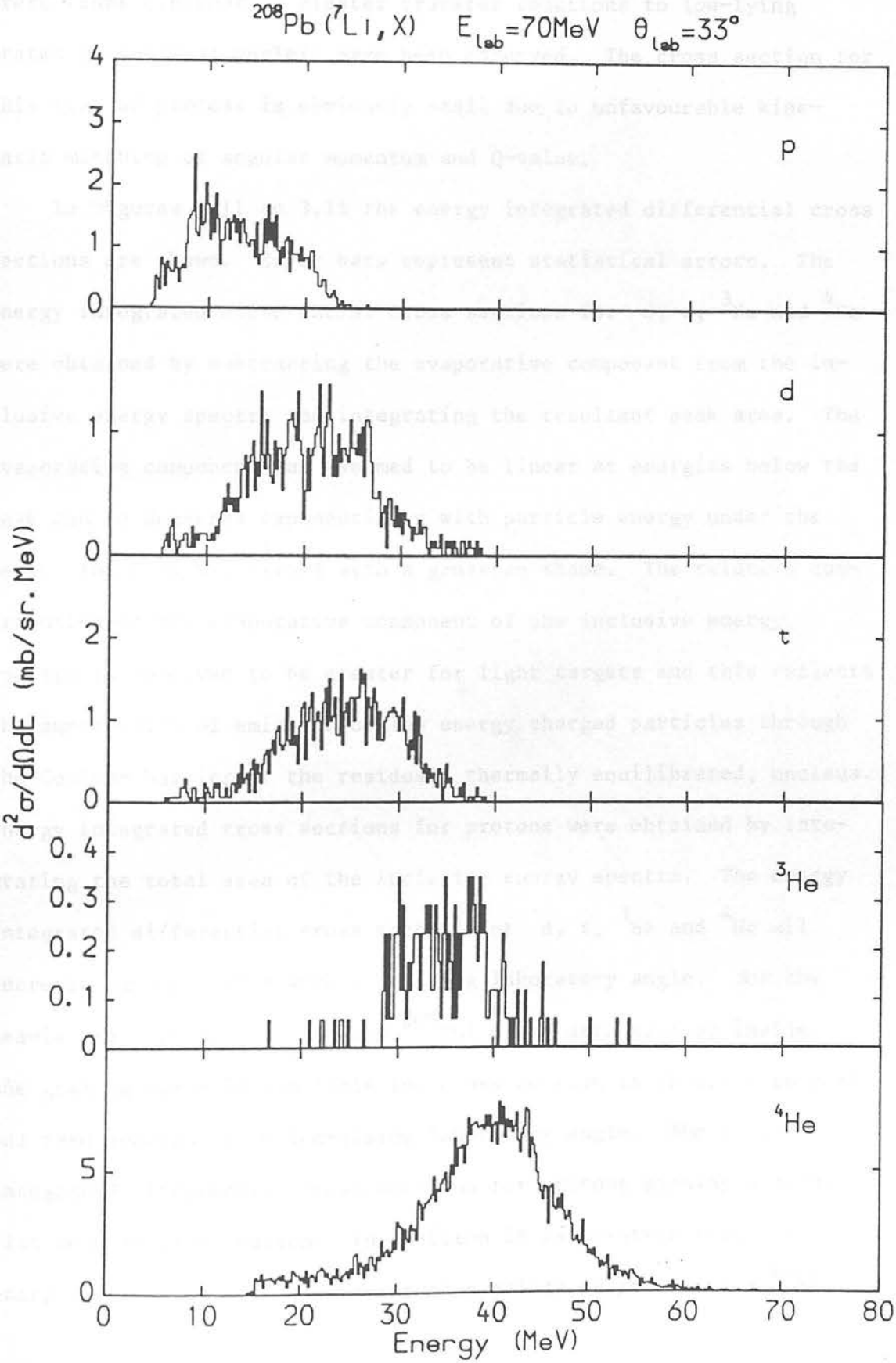

FIGURE 3.10: Inclusive energy spectra of outgoing charged particles from the reaction 70 MeV ^{7}Li + ^{208}Pb at backward angles.

the yield would seem to be entirely evaporative in origin. No discrete lines (indicating cluster transfer reactions to low-lying states of residual nuclei) have been observed. The cross section for this type of process is obviously small due to unfavourable kinematic matching of angular momentum and Q-value.

In Figures 3.11 to 3.15 the energy integrated differential cross sections are shown. Error bars represent statistical errors. The energy integrated differential cross sections for d, t, ^{3}He and ^{4}He were obtained by subtracting the evaporative component from the inclusive energy spectra and integrating the resultant peak area. The evaporative component was assumed to be linear at energies below the peak and to decrease exponentially with particle energy under the peak. The peak was fitted with a gaussian shape. The relative contribution of the evaporative component of the inclusive energy spectra is observed to be greater for light targets and this reflects the suppression of emission of low energy charged particles through the Coulomb barrier of the residual, thermally equilibrated, nucleus. Energy integrated cross sections for protons were obtained by integrating the total area of the inclusive energy spectra. The energy integrated differential cross section for d, t, ^{3}He and ^{4}He all decrease exponentially with increasing laboratory angle. For the heavier targets (i.e. ^{120}Sn and ^{208}Pb) where data near or inside the grazing angle is available the cross section is observed to peak and then decrease with decreasing laboratory angle. The energy integrated differential cross sections for protons display a rather flat angular distribution. In addition it is observed that the energy integrated differential cross sections of protons for ^{60}Ni,

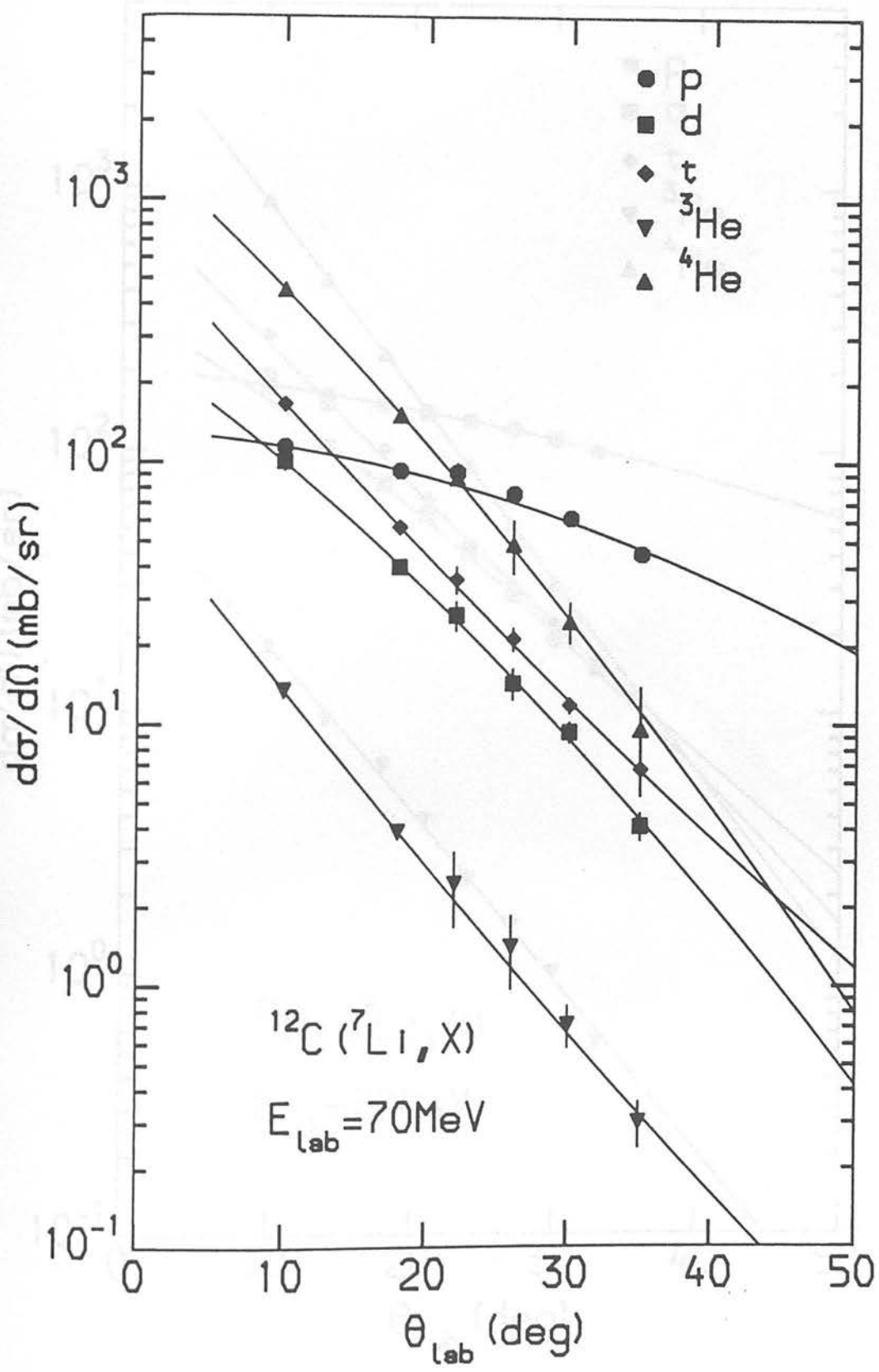

FIGURE 3.11: Angular distributions of outgoing charged particles from the reaction 70 MeV ^{7}Li + ^{12}C.

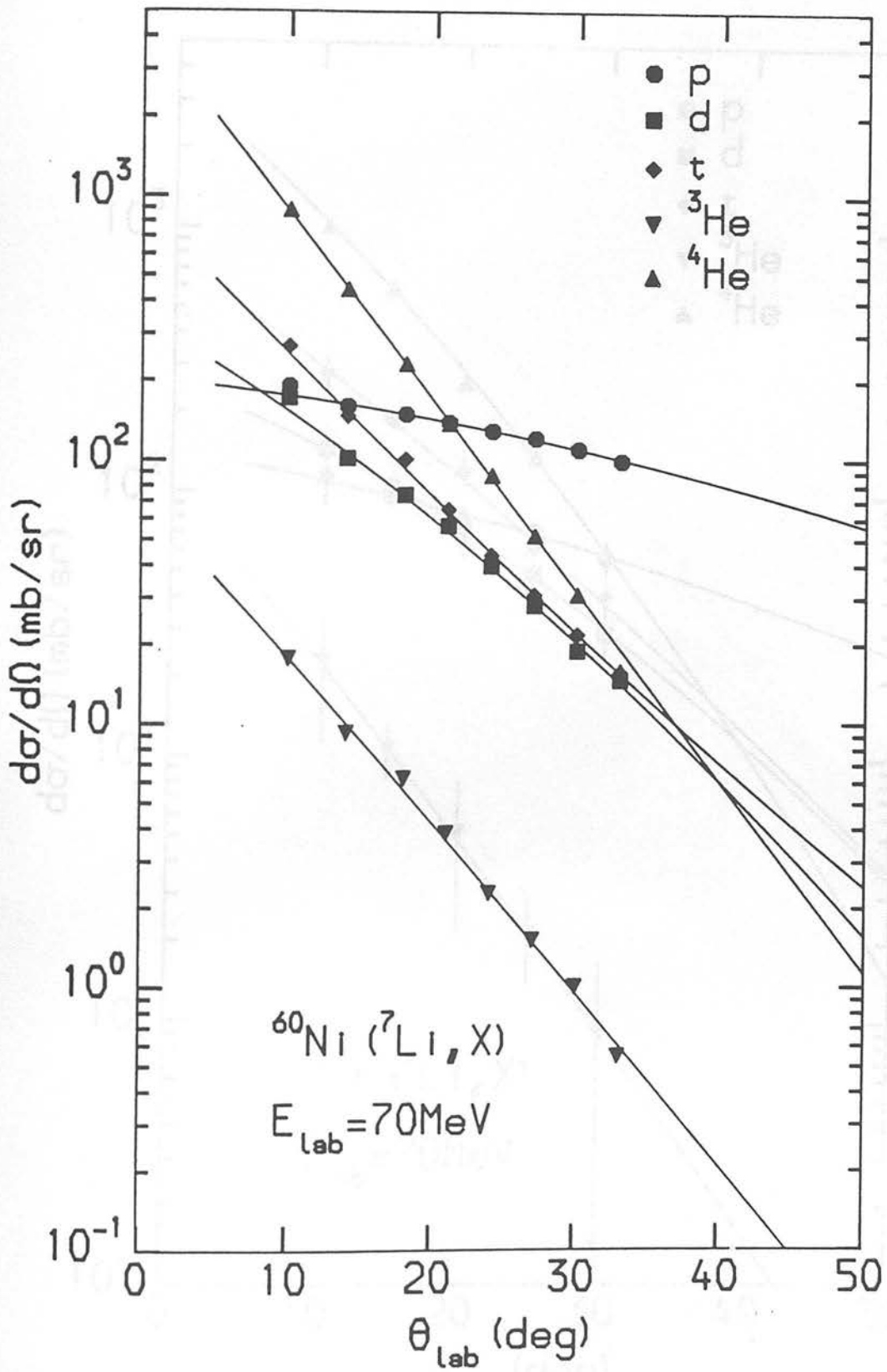

FIGURE 3.12: Angular distributions of outgoing charged particles from the reaction 70 MeV ^{7}Li + ^{60}Ni.

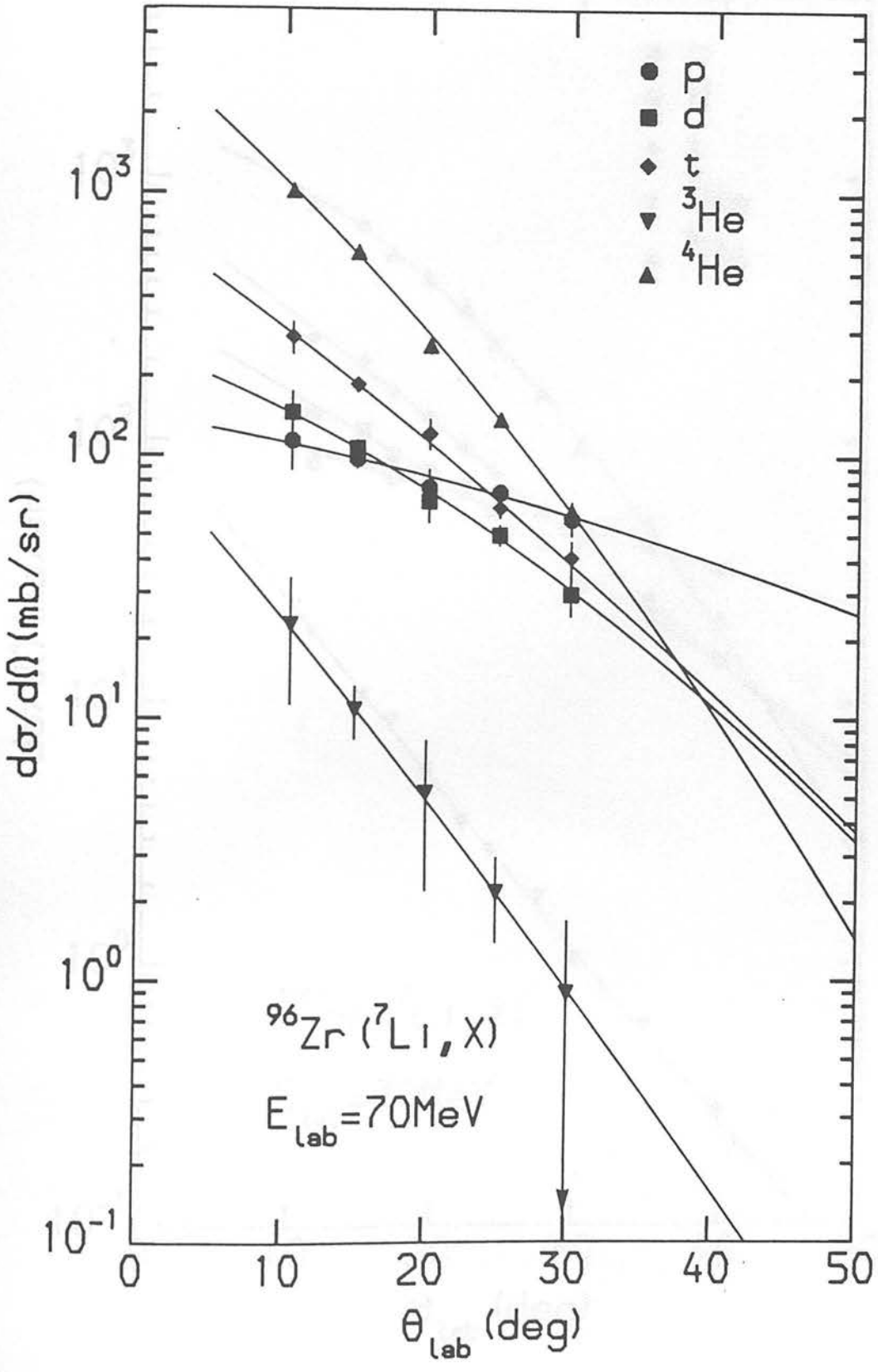

FIGURE 3.13: Angular distributions of outgoing charged particles from the reaction 70 MeV ^{7}Li + ^{96}Zr.

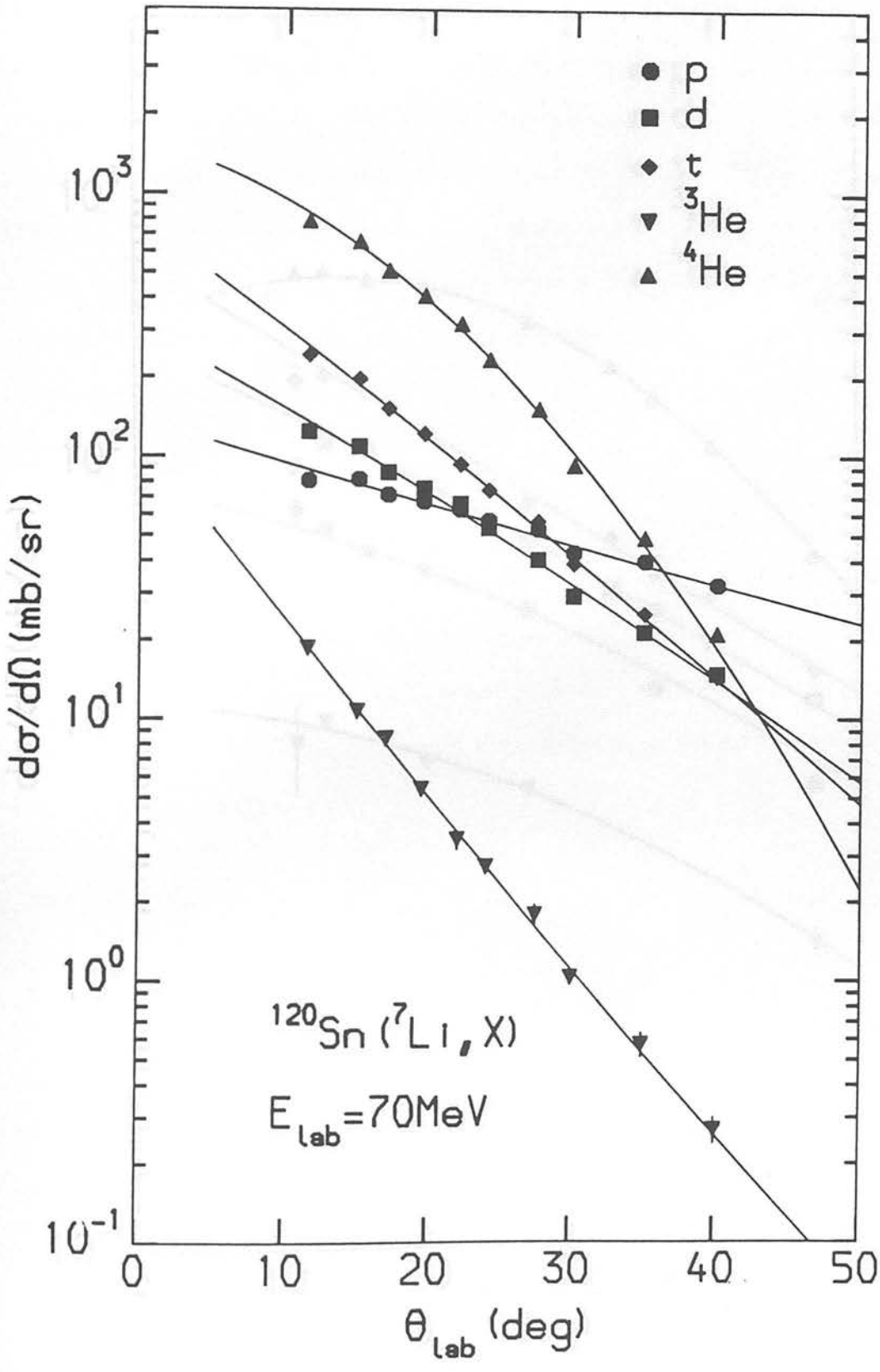

FIGURE 3.14: Angular distributions of outgoing charged particles from the reaction 70 MeV ^{7}Li + ^{120}Sn.

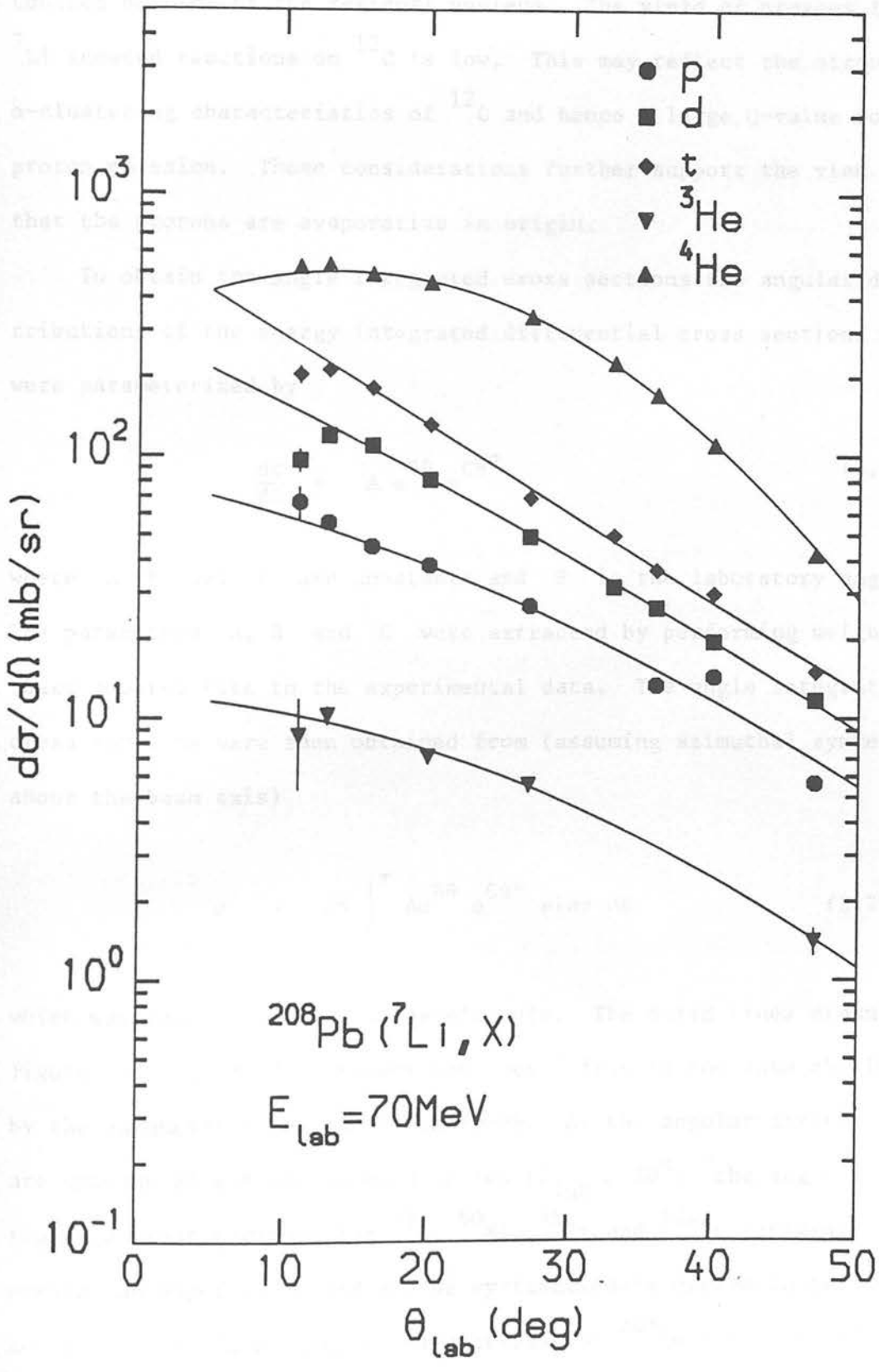

FIGURE 3.15: Angular distributions of outgoing charged particles from the reaction 70 MeV ^{7}Li + ^{208}Pb.

^{96}Zr, ^{120}Sn and ^{208}Pb decrease with increasing target charge, indicating the suppression of low energy proton emission by the Coulomb barrier of the residual nucleus. The yield of protons from ^{7}Li induced reactions on ^{12}C is low. This may reflect the strong α-clustering characteristics of ^{12}C and hence a large Q-value for proton emission. These considerations further support the view that the protons are evaporative in origin.

To obtain the angle integrated cross sections the angular distributions of the energy integrated differential cross sections were parameterized by

$$\frac{d\sigma}{d\Omega} = A\, e^{B\theta}\, e^{C\theta^2} \qquad (3.1)$$

where A, B and C are constants and θ is the laboratory angle. The parameters A, B and C were extracted by performing weighted least squares fits to the experimental data. The angle integrated cross sections were then obtained from (assuming azimuthal symmetry about the beam axis)

$$\sigma = 2\pi \int_0^{\pi} Ae^{B\theta}\, e^{C\theta^2} \sin\theta\, d\theta \qquad (3.2)$$

which was evaluated using Simpson's rule. The solid lines drawn in Figures 3.11 to 3.15 represent the 'best' fits to the data obtained by the parametrisation described above. As the angular distributions are unknown at extreme forward angles ($\theta_{lab} < 10^{o}$) the angle integrated cross sections for ^{12}C, ^{60}Ni, ^{96}Zr and ^{120}Sn certainly represent an upper limit and may be systematically overestimated by up to 30%. Angle integrated cross sections for ^{208}Pb are more reliable since maxima near the grazing angle are observed and reproduced by the weighted least squares fit.

The angle integrated cross sections are tabulated in Table 3.1. For comparison the reaction cross sections are presented also and it can be seen that the fast outgoing charged particles represent a significant fraction of the reaction cross section. Figure 3.16 displays the angle integrated cross sections as a function of the atomic mass number A_T of the target. Solid lines drawn through the data represent weighted least squares fits to the data. The d, t, ^{3}He and ^{4}He cross sections show an approximately $A_T^{1/3}$ dependence. This is characteristic of a surface peaked production mechanism and indicates that the reactions occur in a peripheral region characterized by the overlap of target and projectile. Figure 3.17 shows the yields of d, t and ^{3}He relative to the ^{4}He yield as a function of A_T. Little or no systematic dependence on A_T can be observed and it is concluded that charged particle production is more a reflection of the structure of the projectile than of the target.

3.2 Particle-Particle Correlations

In this section measurements of particle-particle correlations from ^{7}Li induced reactions on ^{12}C, ^{60}Ni, ^{96}Zr, ^{120}Sn, ^{208}Pb at 10 MeV/A are presented. Particle-particle coincidence measurements were performed with a pair of $\Delta E - E$ telescopes at a fixed separation angle and arranged vertically about the reaction plane. The experimental setup is described in detail in Section 2.3. As indicated in Sections 1.4 and 2.3 the detection geometry is designed to maximise the efficiency of detection of the unbound PLF's and specifically the sequential break-up of PLF's via states near particle threshold.

TABLE 3.1 Total Inclusive Cross Sections

Target	$\sigma_d(b)^2$	$\sigma_t(b)^2$	$\sigma_{^3He}(b)^2$	$\sigma_\alpha(b)^2$	$\sigma_R(b)^3$
^{12}C	0.042 ± 0.007	0.07 ± 0.01	0.005 ± 0.001	0.17 ± 0.03	0.99
^{60}Ni	0.07 ± 0.01	0.11 ± 0.016	0.007 ± 0.0014	0.31 ± 0.05	1.63
^{96}Zr	0.09 ± 0.03	0.15 ± 0.03	0.009 ± 0.005	0.42 ± 0.07	1.88
^{120}Sn	0.10 ± 0.015	0.15 ± 0.02	0.009 ± 0.0014	0.42 ± 0.06	1.94
^{208}Pb	0.12 ± 0.02	0.19 ± 0.03	0.011 ± 0.002	0.53 ± 0.08	2.00

1) Values quoted include estimates of systematic and statistical errors.

2) Beam velocity particles only

3) Total reaction cross section calculated from strong absorption model $\sigma_R = \pi R_C^2(1 - V_C/E)$ where $V_C = Z_p Z_T e^2/R_C$ and $R_C = 1.4(A_p^{1/3} + A_T^{1/3})$.

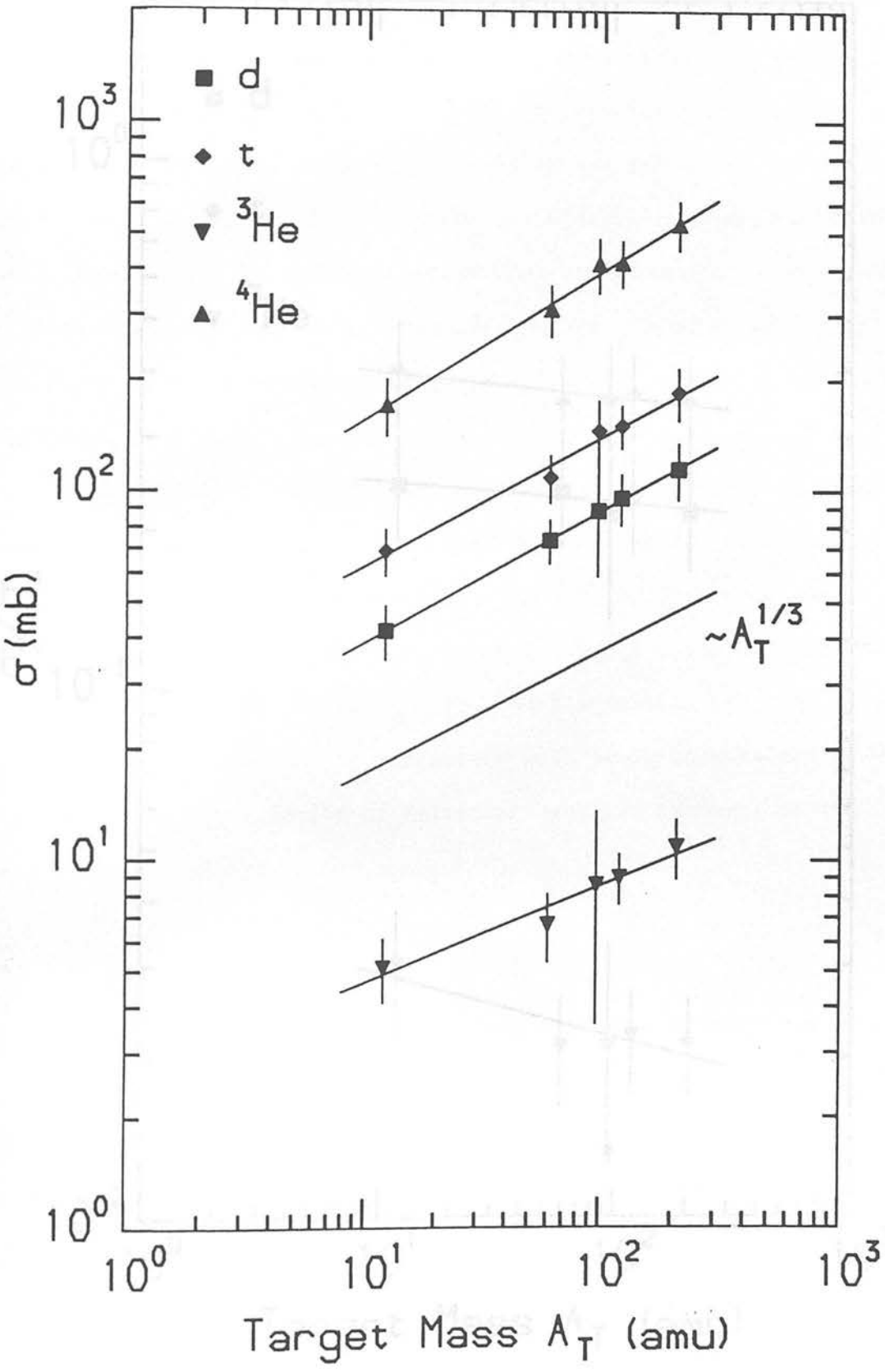

Figure 3.16: Total inclusive cross sections of outgoing charged particles as a function of A_T the mass number of the target.

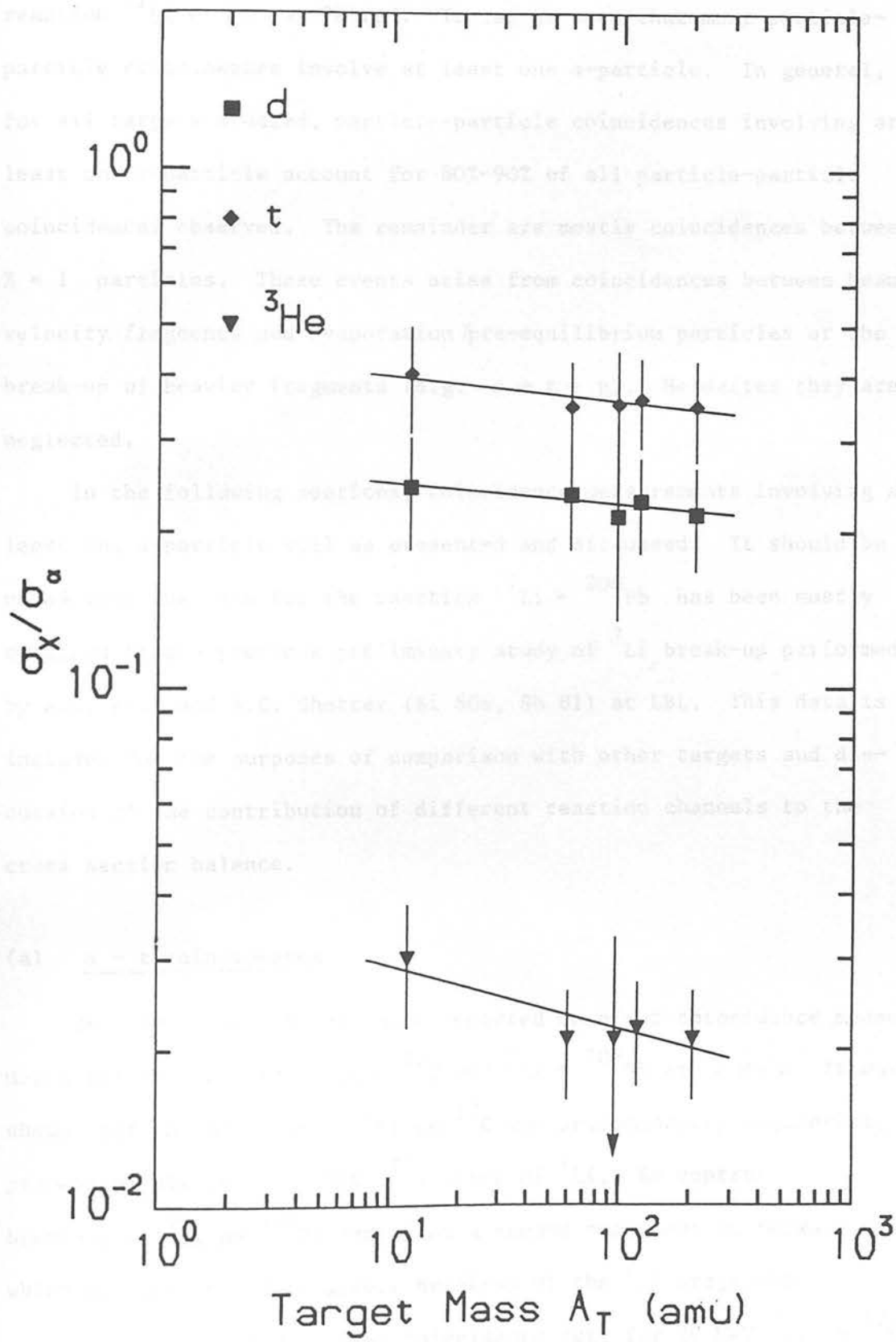

3.17: Ratio of total inclusive cross sections of deuterons, tritons and helions to the total inclusive cross section of α-particles as a function of A_T .

Figure 3.18 shows the particle-particle correlations from the reaction $^{7}Li + ^{12}C$ at 70 MeV. It can be seen that most particle-particle coincidences involve at least one α-particle. In general, for all targets studied, particle-particle coincidences involving at least one α-particle account for 80%-90% of all particle-particle coincidences observed. The remainder are mostly coincidences between Z = 1 particles. These events arise from coincidences between beam velocity fragments and evaporation/pre-equilibrium particles or the break-up of heavier fragments (e.g. $\alpha \rightarrow t + p$). Hereafter they are neglected.

In the following sections, coincidence measurements involving at least one α-particle will be presented and discussed. It should be noted that the data for the reaction $^{7}Li + ^{208}Pb$ has been mostly obtained from a previous preliminary study of ^{7}Li break-up performed by A.N. Bice and A.C. Shotter (Bi 80a, Sh 81) at LBL. This data is included for the purposes of comparison with other targets and discussion of the contribution of different reaction channels to the cross section balance.

(a) α - t coincidences

Shotter et al. (Sh 81) have reported on α - t coincidence measurements for the reactions $^{7}Li + ^{12}C$ and $^{7}Li + ^{208}Pb$ at 70 MeV. It was shown that the break-up of ^{7}Li on ^{12}C was predominantly sequential, proceeding via the 4.63 MeV ($\frac{7}{2}^{-}$) state of ^{7}Li. By contrast, the break-up of ^{7}Li on ^{208}Pb exhibited a second component at forward angles which was attributed to direct break-up of the ^{7}Li projectile.

Figures 3.19 - 3.23 show coincidence data for 70 MeV ^{7}Li on ^{12}C,

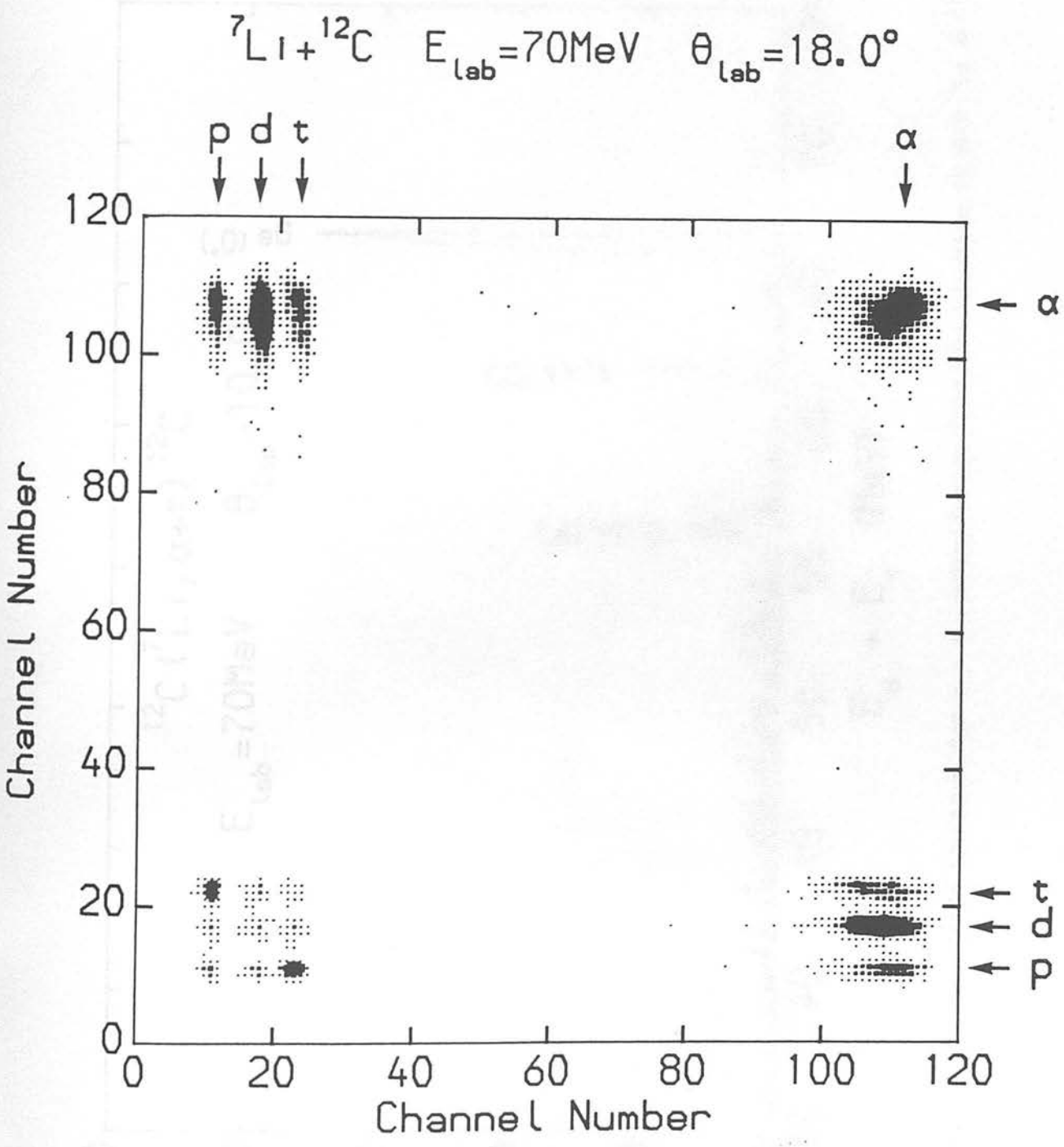

Figure 3.18: Two-dimensional particle-particle correlation spectrum for the reaction 70 MeV ^{7}Li + ^{12}C.

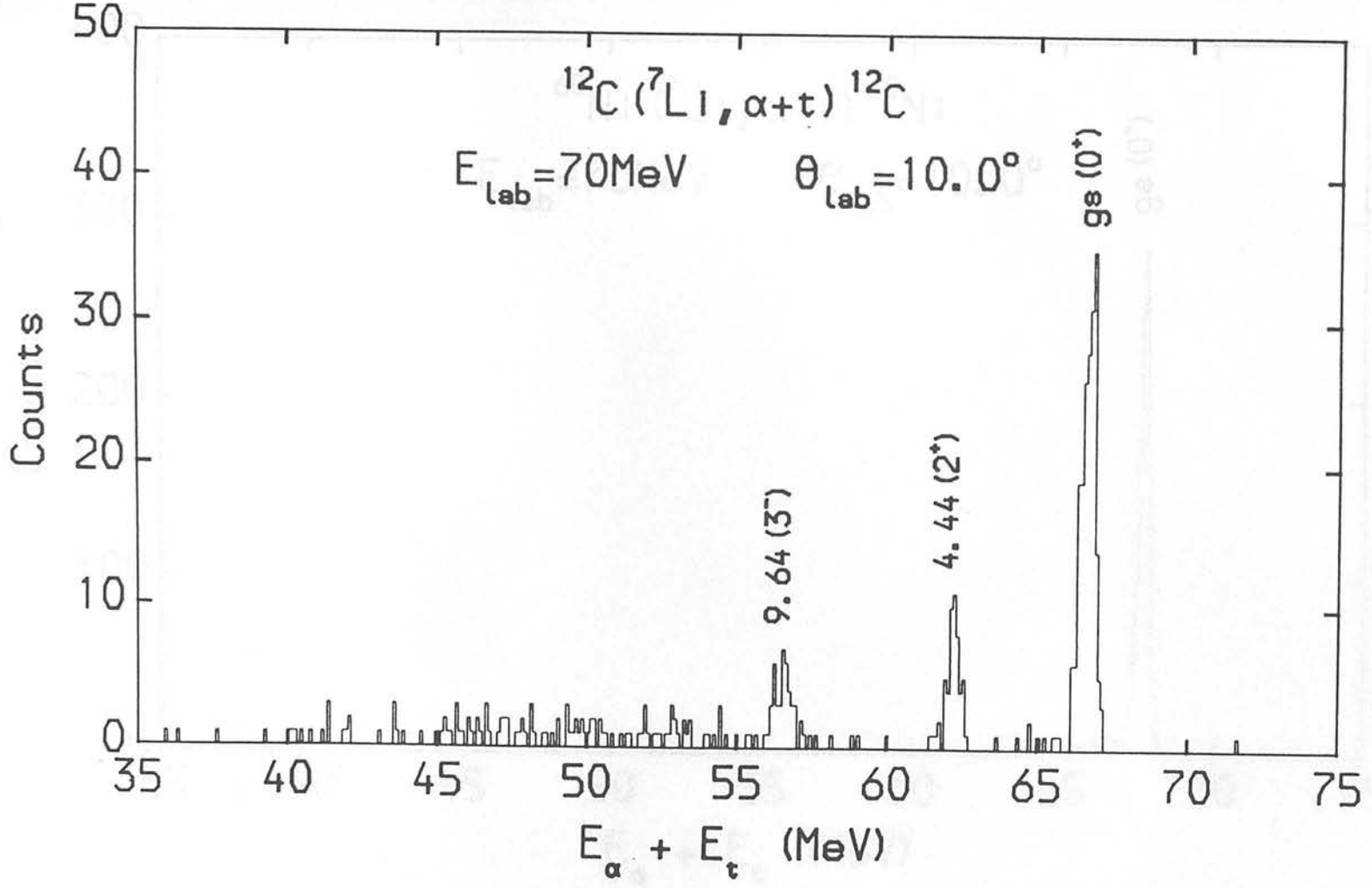

Figure 3.19: Summed energy spectrum for α - t coincidences from the reaction 70 MeV $^{7}Li + ^{12}C$.

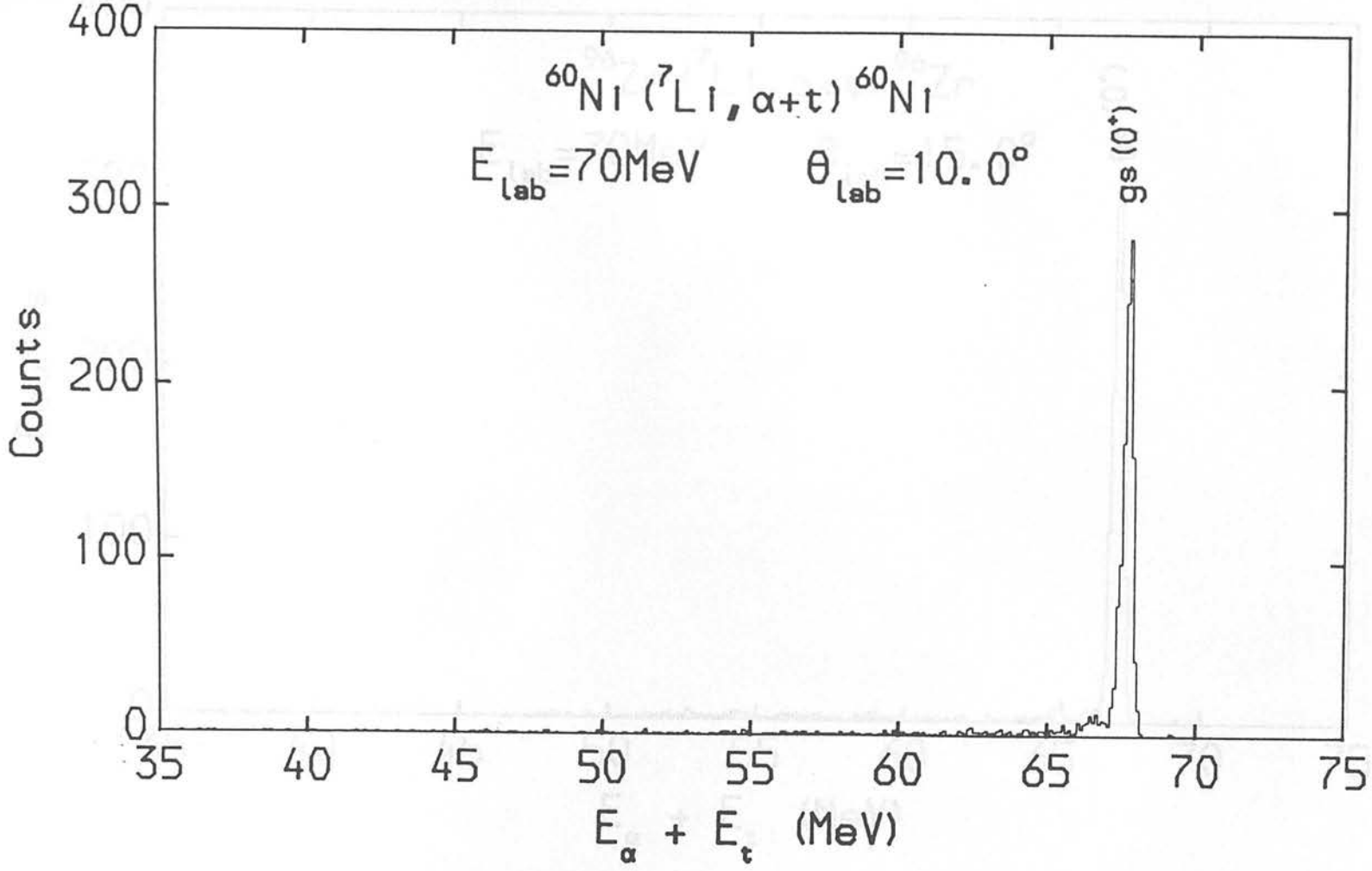

Figure 3.20: Summed energy spectrum for α - t coincidences from the reaction 70 MeV ^{7}Li + ^{60}Ni.

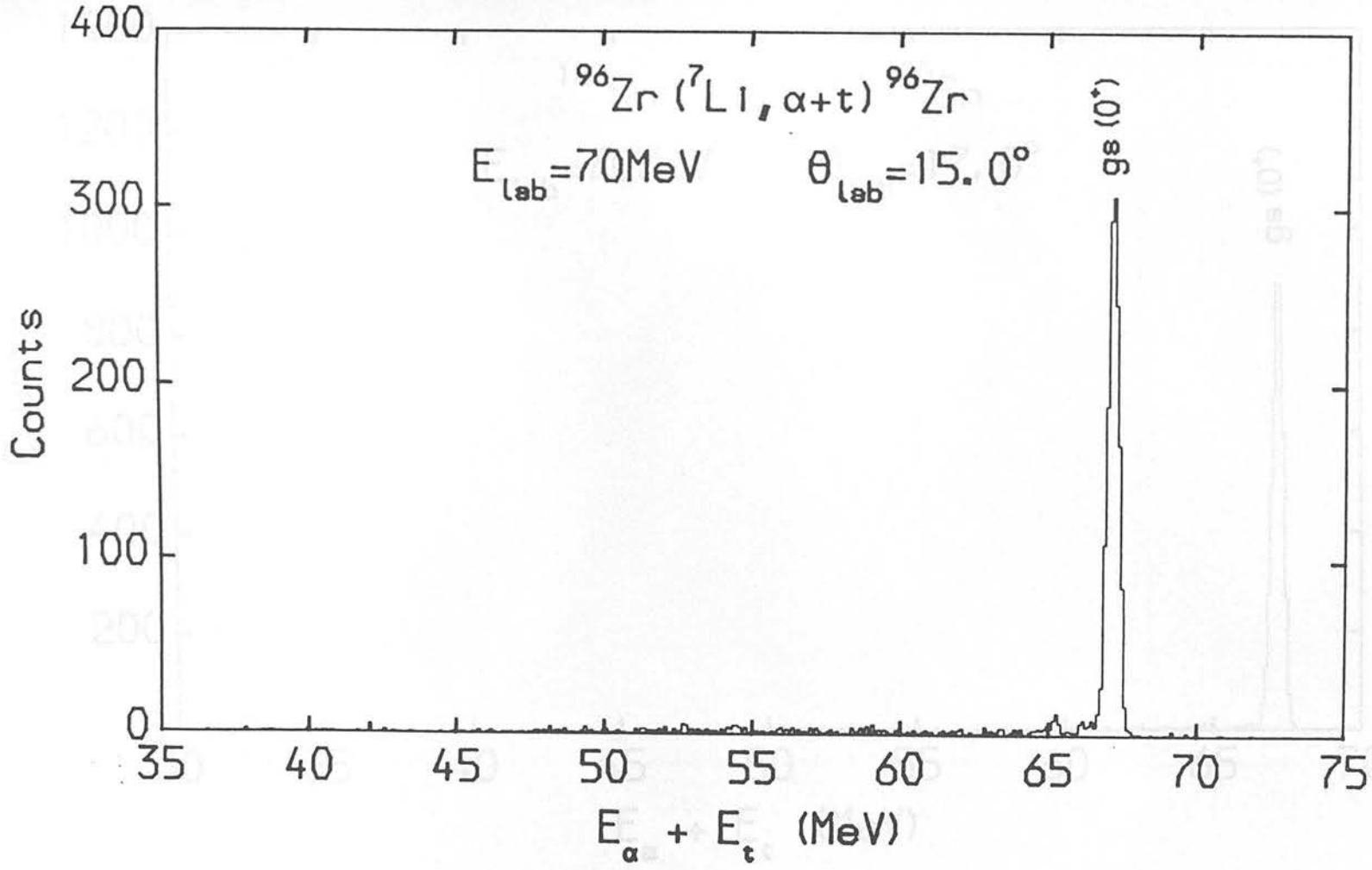

Figure 3.21: Summed energy spectrum for α - t coincidences from the reaction 70 MeV ^{7}Li + ^{96}Zr.

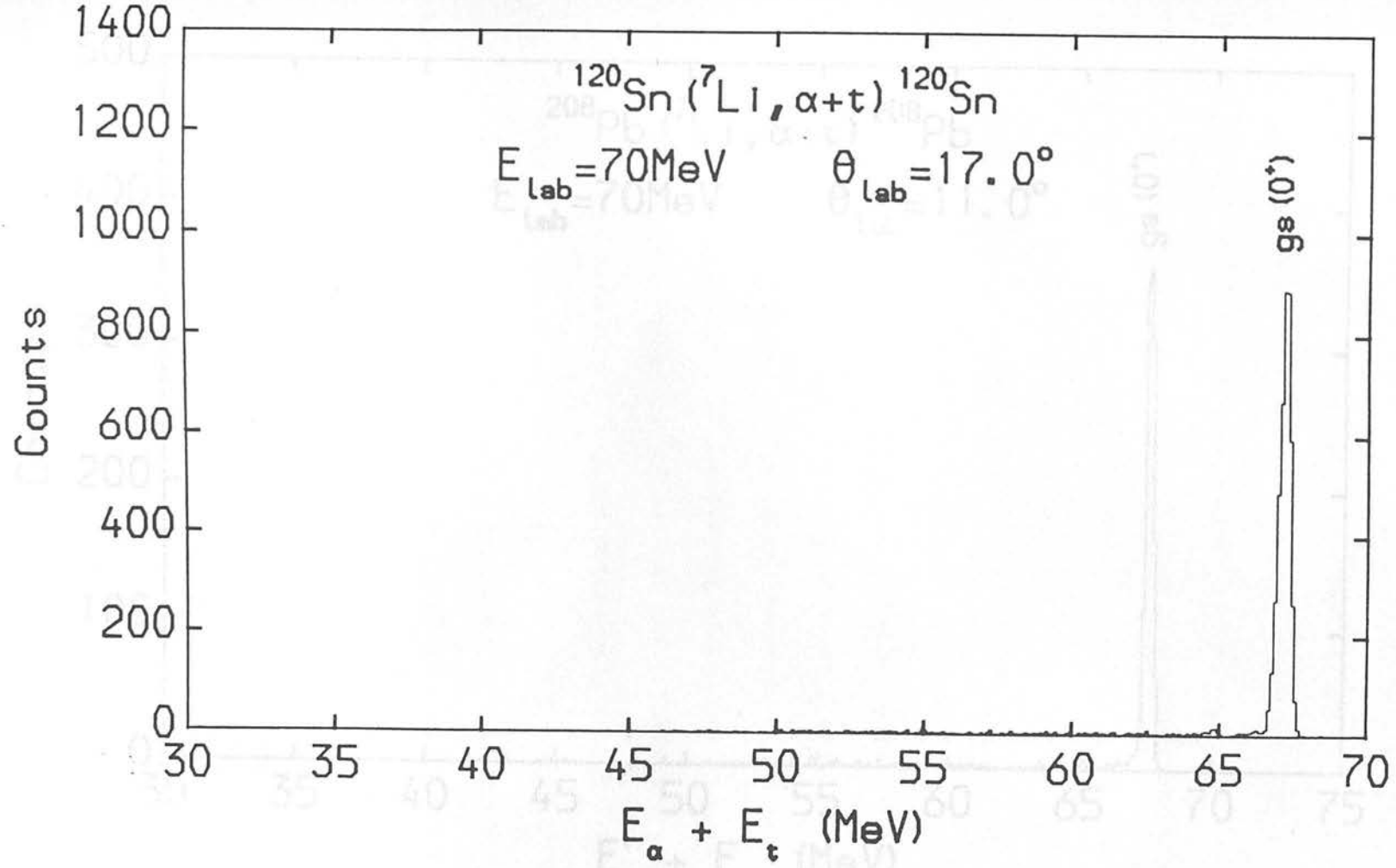

Figure 3.22: Summed energy spectrum for α - t coincidences from the reaction 70 MeV ^{7}Li + ^{120}Sn.

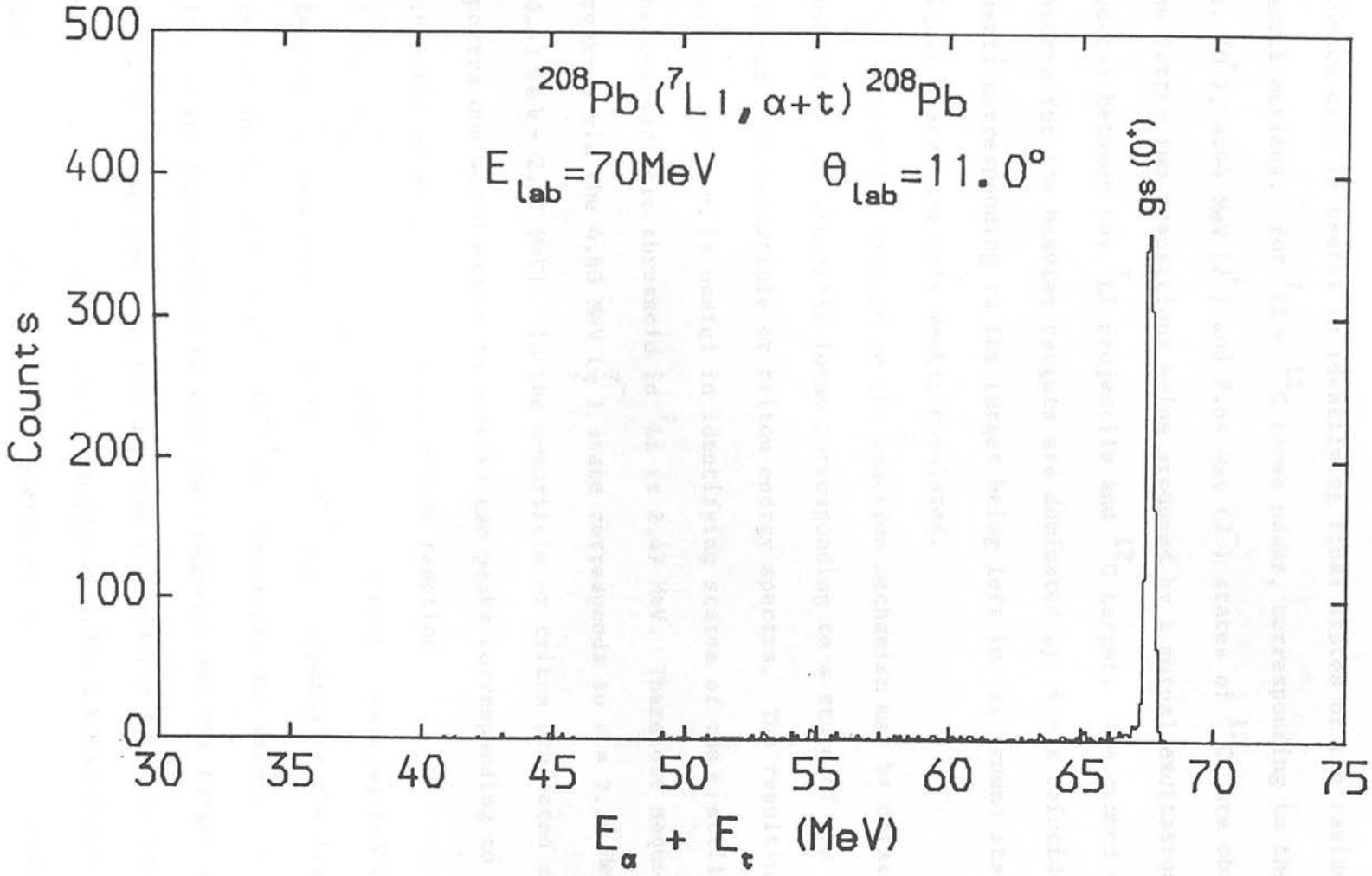

Figure 3.23: Summed energy spectrum for α - t coincidences from the reaction 70 MeV ^{7}Li + ^{208}Pb.

^{60}Ni, ^{96}Zr, ^{120}Sn and ^{208}Pb at forward angles. The summed energy of coincidence events is displayed with the requirement that an α-particle be recorded in one telescope and a triton in the other telescope. As indicated in Section 1.4, this type of presentation of coincidence data is useful in identifying final states of the residual/recoil nucleus. For $^{7}Li + {}^{12}C$ three peaks, corresponding to the gs. (0^+), 4.44 MeV (2^+) and 9.64 MeV (3^-) states of ^{12}C are observed, the latter two transitions being produced by a mutual excitation process between the ^{7}Li projectile and ^{12}C target. The summed energy spectra for the heavier targets are dominated by α - t coincidence events corresponding to the target being left in its ground state. Higher states are only weakly populated.

Further information on the reaction mechanism may be obtained by projecting the kinematic locus corresponding to a state of the recoil nucleus into α-particle or triton energy spectra. The resulting projection spectrum is useful in identifying states of the ejectile. The α-t particle threshold in ^{7}Li is 2.47 MeV. Therefore sequential break-up via the 4.63 MeV ($\frac{7}{2}^-$) state corresponds to ε = 2.16 MeV (4.63 MeV - 2.47 MeV). In the α-particle or triton projected energy spectra one would expect to observe two peaks corresponding to the kinematic solutions for the three-body reaction $X(^{7}Li, {}^{7}Li^{*}_{4.63} \rightarrow \alpha + t)X_{gs}$ with ε = 2.16 MeV. The 4.63 MeV ($\frac{7}{2}^-$) state of ^{7}Li has a mean life of $\sim 10^{-20}$s as compared to the transit time of the projectile of $\sim 10^{-22}$s. Therefore, one expects that final state interactions between the fragments and the target will not be important and that the momentum correlation from the break-up reaction will not be distorted. In Figure 3.24a a Monte Carlo simulation of the projected α-particle energy spectrum for the reaction

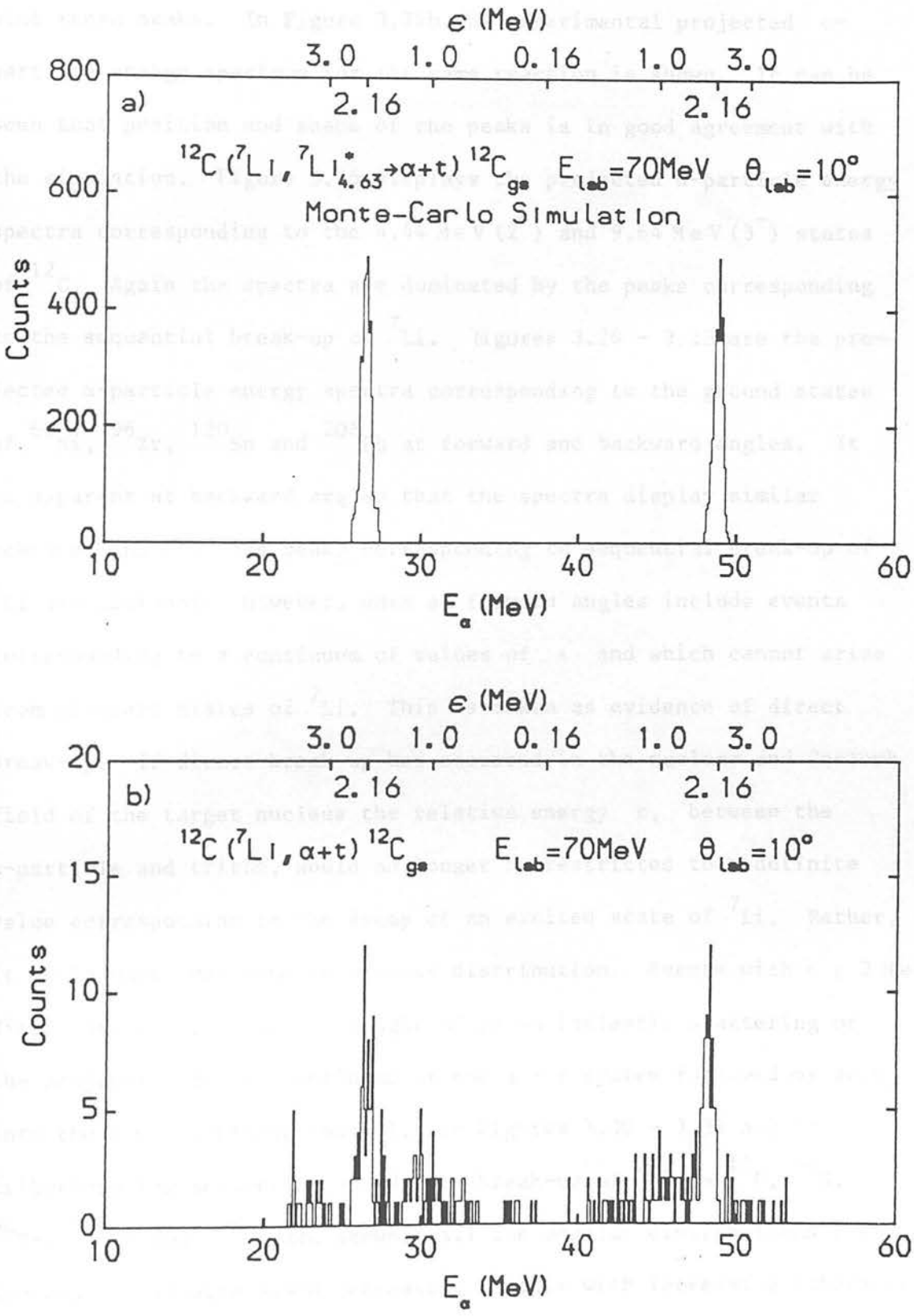

Figure 3.24: a) Monte-Carlo simulation of projected α energy spectrum for the reaction $^{12}C(^{7}Li, ^{7}Li^{*}_{4.63} \rightarrow \alpha+t)^{12}C_{gs}$.

b) Projected α energy spectrum for α-t coincidences corresponding to the ground state of ^{12}C.

$^{12}C(^{7}Li^{*}_{4.63} \rightarrow \alpha + t)^{12}C_{gs}$ is displayed. Events from the sequential break-up of ^{7}Li are located in two peaks. No events are observed outside these peaks. In Figure 3.24b the experimental projected α-particle energy spectrum for the same reaction is shown. It can be seen that position and shape of the peaks is in good agreement with the simulation. Figure 3.25 displays the projected α-particle energy spectra corresponding to the 4.44 MeV (2^{+}) and 9.64 MeV (3^{-}) states of ^{12}C. Again the spectra are dominated by the peaks corresponding to the sequential break-up of ^{7}Li. Figures 3.26 - 3.29 are the projected α-particle energy spectra corresponding to the ground states of ^{60}Ni, ^{96}Zr, ^{120}Sn and ^{208}Pb at forward and backward angles. It is apparent at backward angles that the spectra display similar features and that the peaks corresponding to sequential break-up of ^{7}Li are dominant. However, data at forward angles include events corresponding to a continuum of values of ε and which cannot arise from discrete states of ^{7}Li. This is taken as evidence of direct break-up. If direct break-up has occurred in the nuclear and Coulomb field of the target nucleus the relative energy ε, between the α-particle and triton, would no longer be restricted to a definite value corresponding to the decay of an excited state of ^{7}Li. Rather, it would vary over some continuous distribution. Events with $\varepsilon \lesssim 2$ MeV, direct break-up, might be thought of as an inelastic scattering of the projectile to the continuum of the α - t system followed by decay into the α + t particle channel. In Figures 3.30 - 3.34 angular distributions for sequential and direct break-up of ^{7}Li on ^{12}C, ^{60}Ni, ^{96}Zr, ^{120}Sn and ^{208}Pb are shown. All the angular distributions are forward peaked with yield decreasing rapidly with increasing laboratory angle.

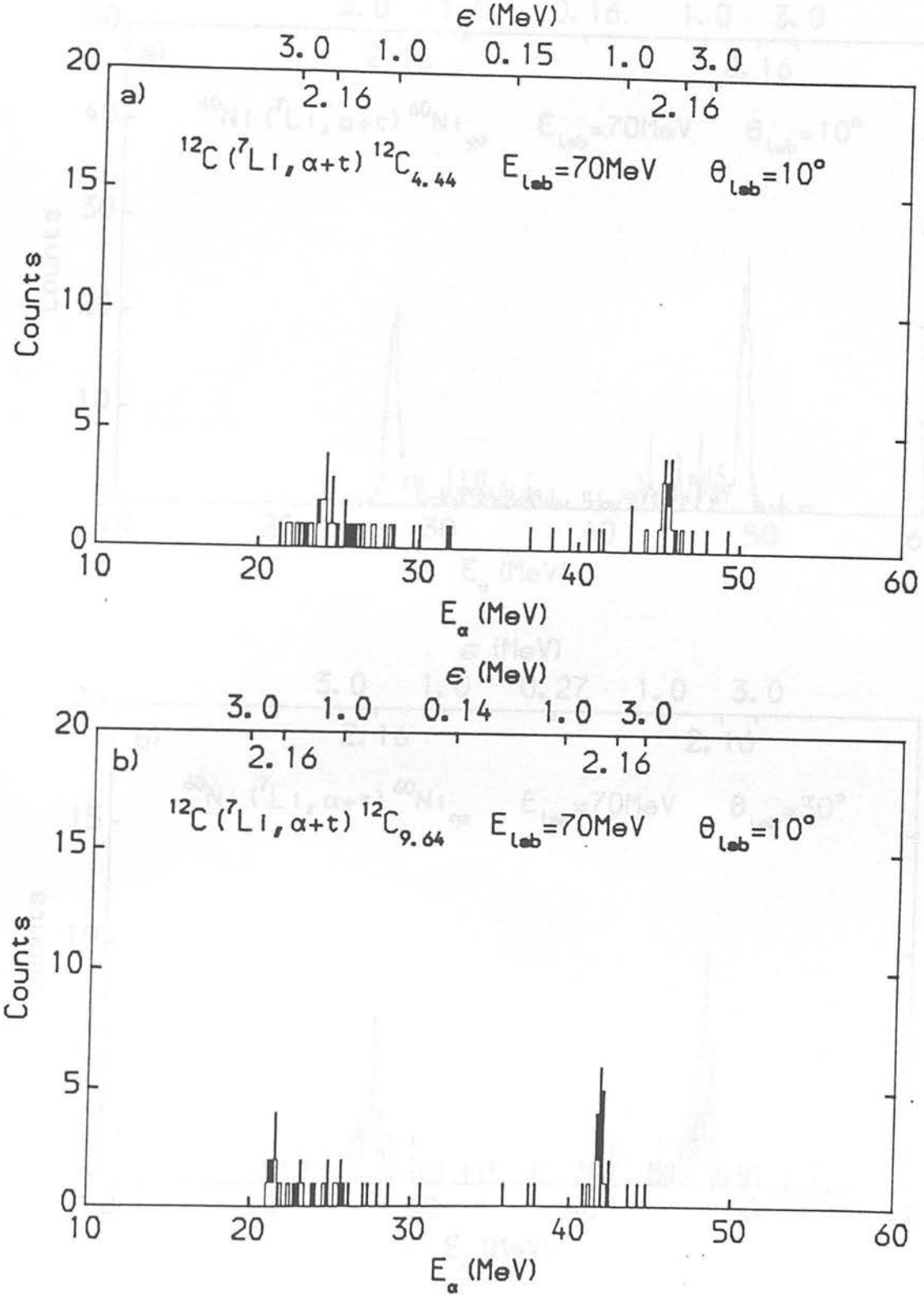

Figure 3.25: a) Projected α energy spectrum for α-t coincidences corresponding to the 4.44 MeV(2^+) state of ^{12}C.

b) Projected α energy spectrum for α-t coincidences corresponding to the 9.64 MeV(3^-) state of ^{12}C.

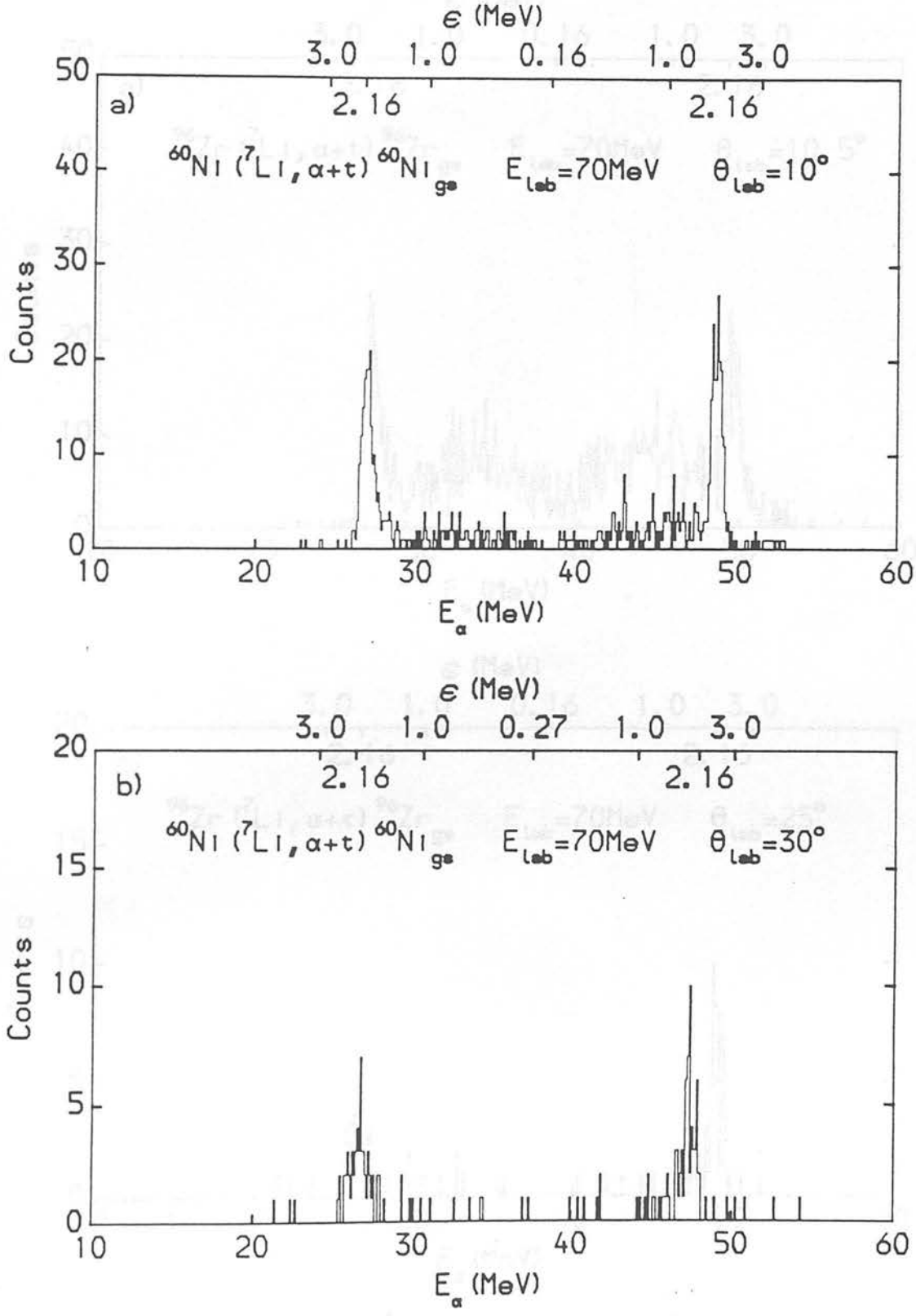

Figure 3.26: a) Projected α energy spectrum for α-t coincidences corresponding to the ground state of ^{60}Ni at $\theta_{lab} = 10°$,

b) Projected α energy spectrum for α-t coincidences corresponding to the ground state of ^{60}Ni at $\theta_{lab} = 30°$.

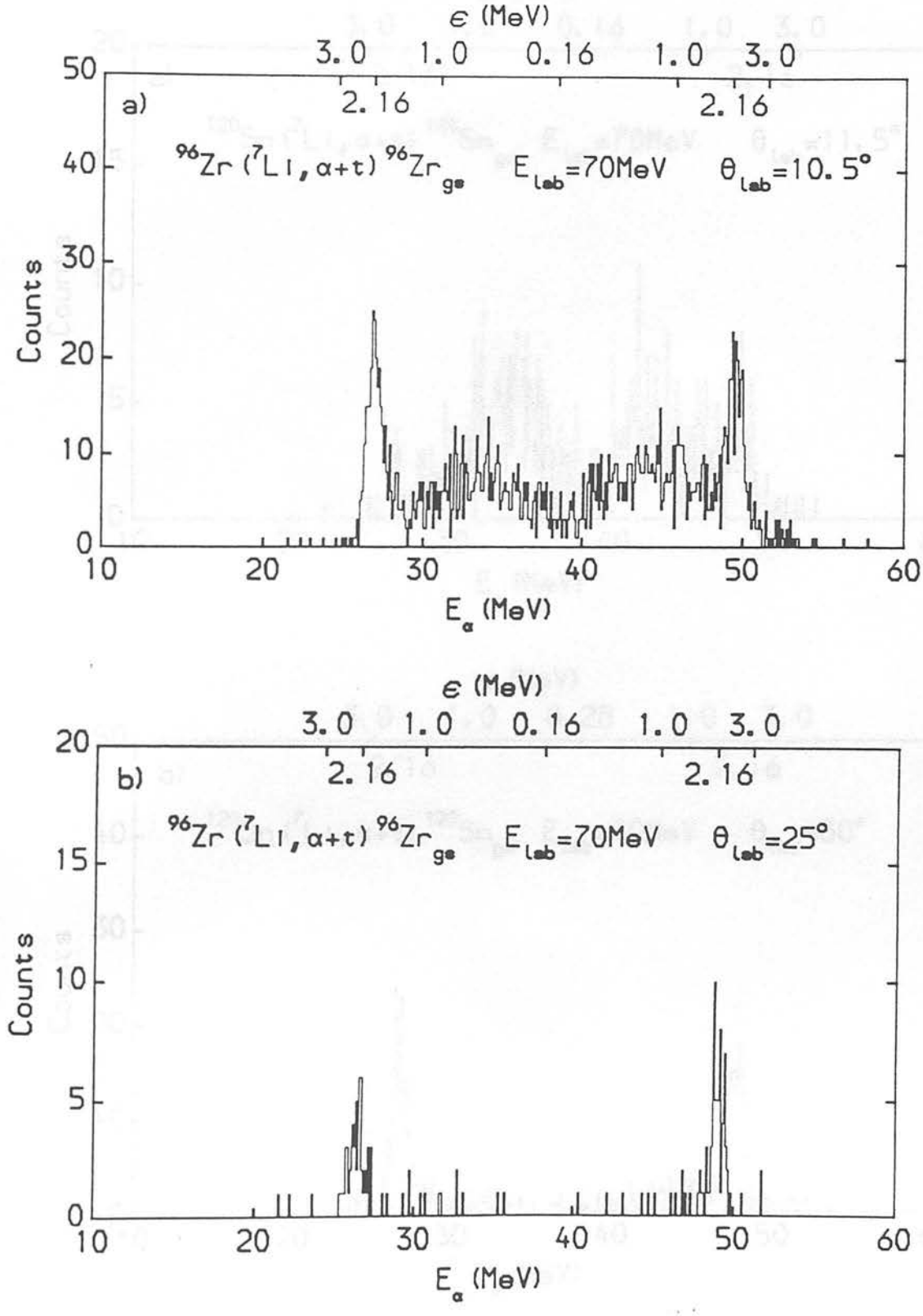

Figure 3.27: a) Projected α energy spectrum for α-t coincidences corresponding to the ground state of ^{96}Zr at $\theta_{lab} = 10.5°$,
b) Projected α energy spectrum for α-t coincidences corresponding to the ground state of ^{96}Zr at $\theta_{lab} = 25°$.

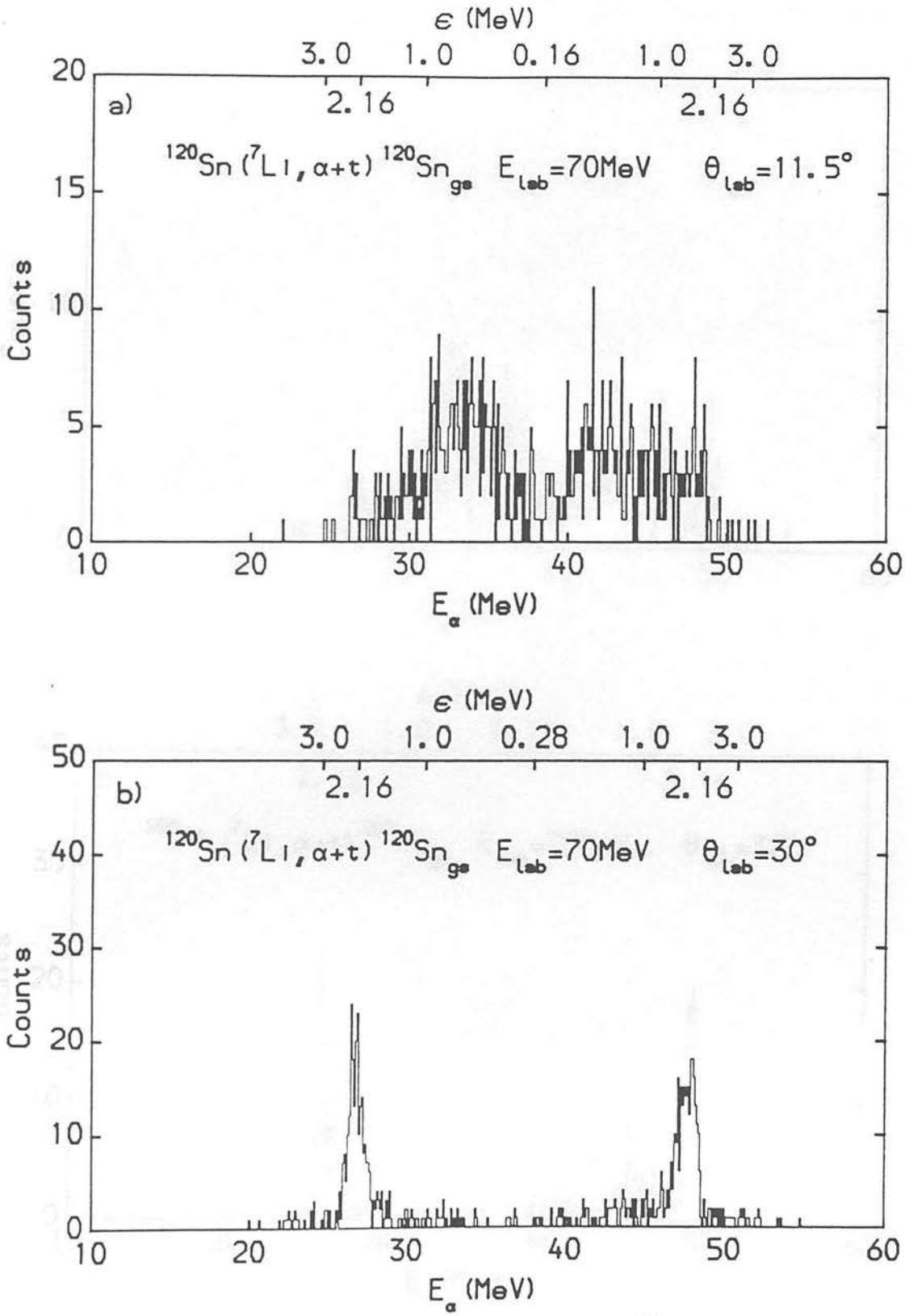

Figure 3.28: a) Projected α energy spectrum for α-t coincidences corresponding to the ground state of ^{120}Sn at θ_{lab} = 11.5°.
b) Projected α energy spectrum for α-t coincidences corresponding to the ground state of ^{120}Sn at θ_{lab} = 30°.

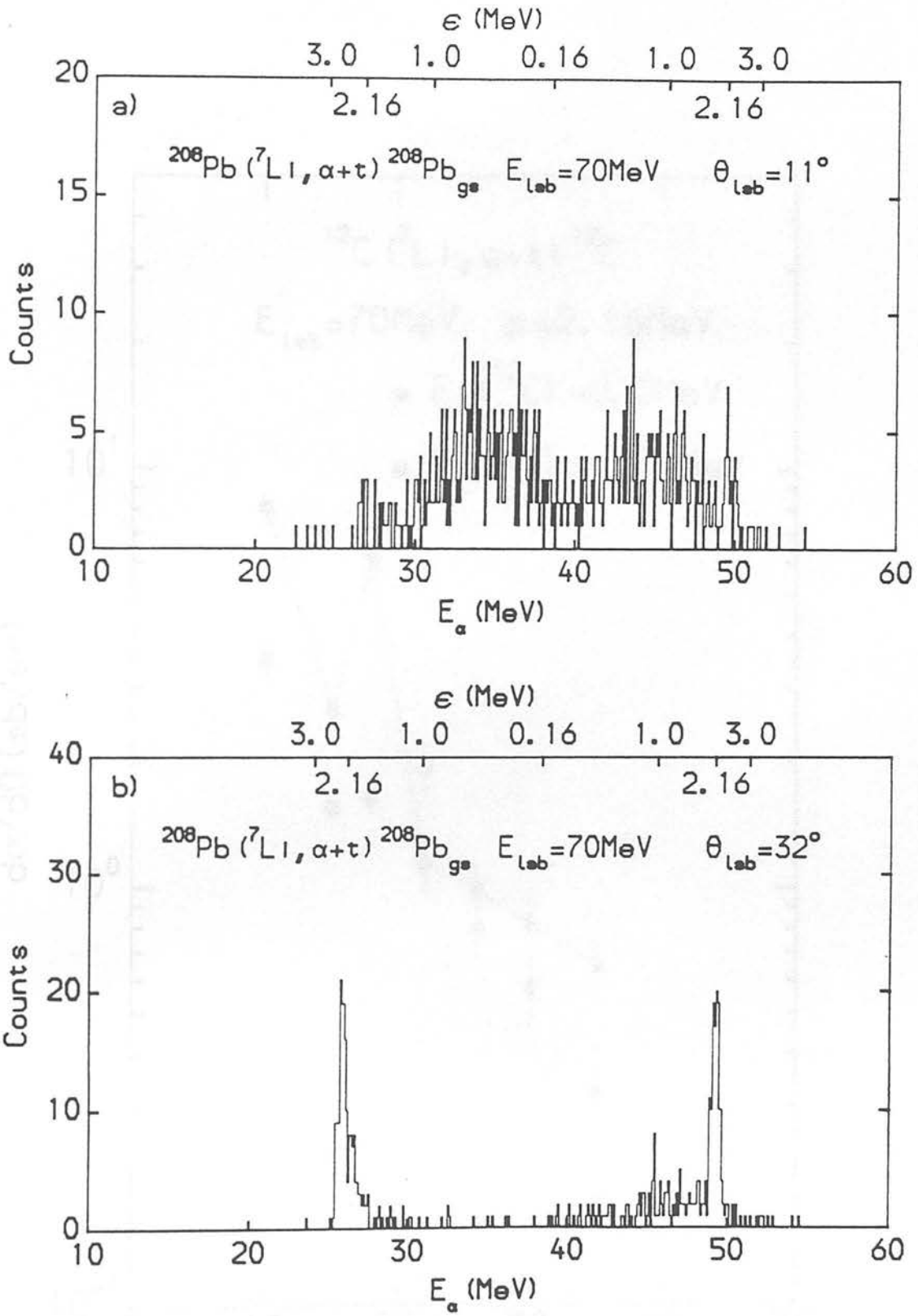

Figure 3.29: a) Projected α energy spectrum for α-t coincidences corresponding to the ground state of ^{208}Pb at $\theta_{lab} = 11°$.

b) Projected α energy spectrum for α-t coincidences corresponding to the ground state of ^{208}Pb at $\theta_{lab} = 32°$.

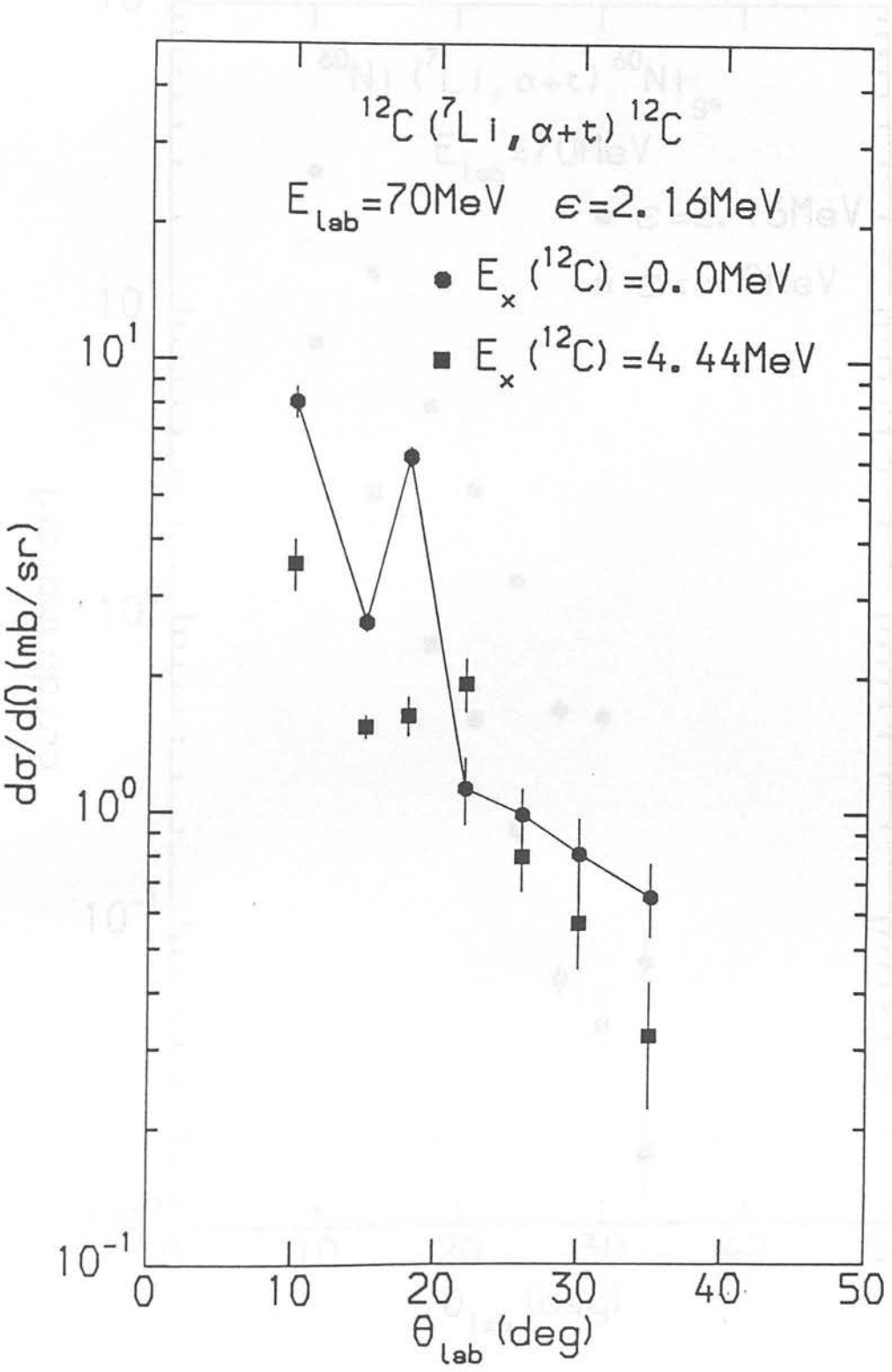

Figure 3.30: Angular distribution for the sequential reaction $^{12}C(^{7}Li, ^{7}Li^{*}_{4.63} \rightarrow \alpha+t)$.

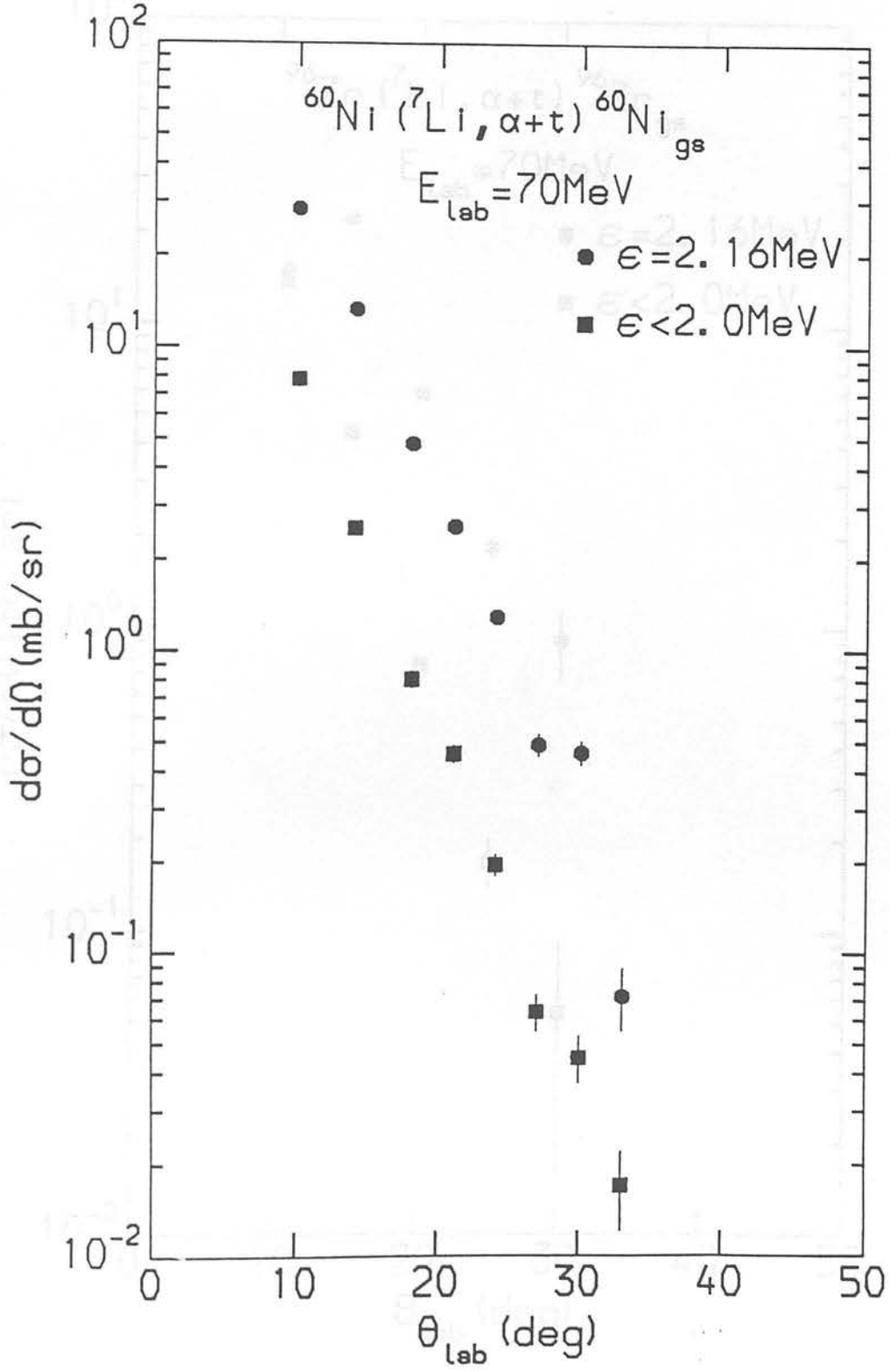

Figure 3.31: Angular distributions for the sequential reaction $^{60}Ni(^{7}Li, {}^{7}Li^{*}_{4.63} \rightarrow \alpha+t)^{60}Ni_{gs}$ and the non-sequential reaction $^{60}Ni(^{7}Li, \alpha+t)^{60}Ni_{gs}$.

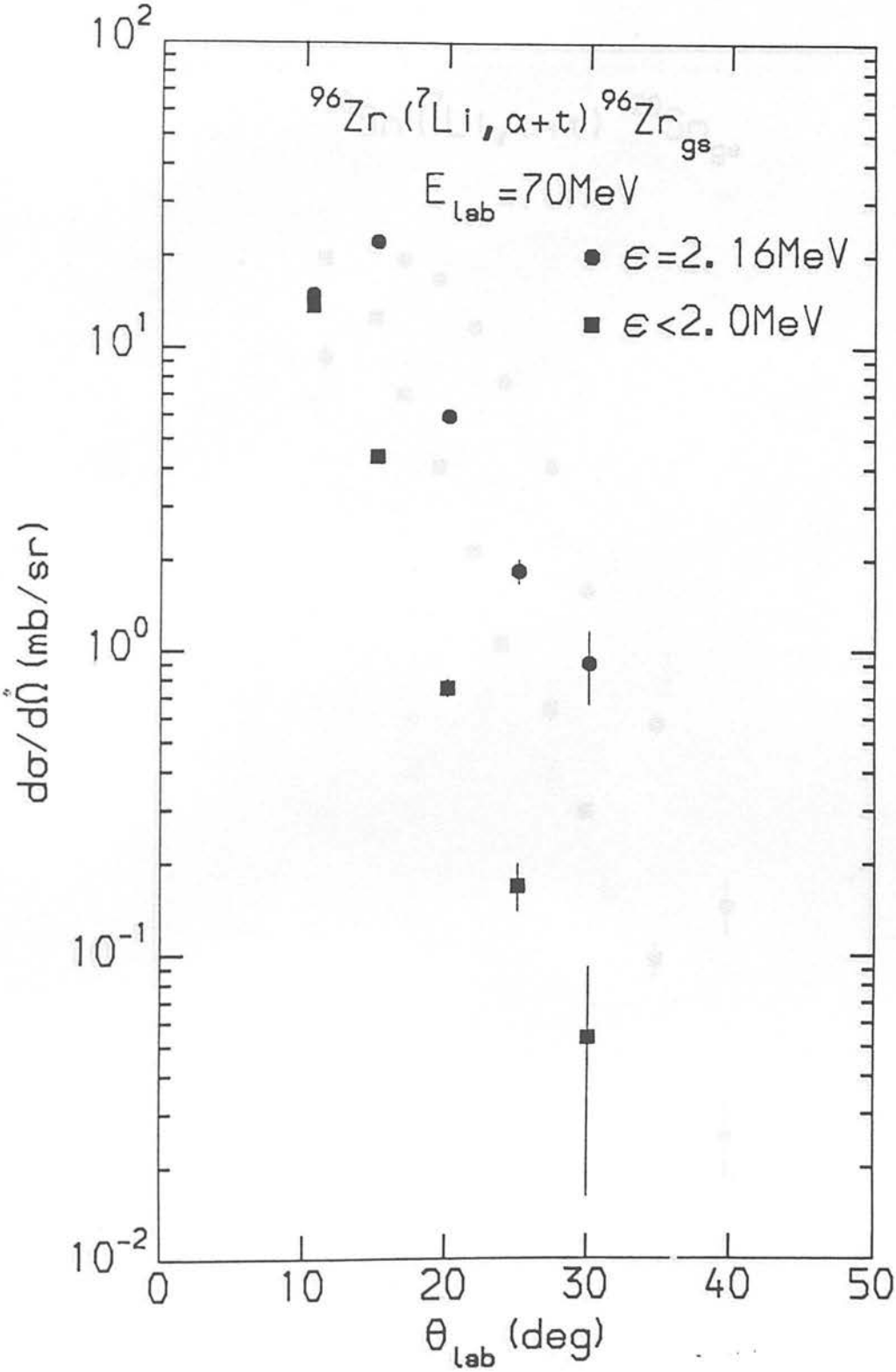

Figure 3.32: Angular distributions for the sequential reaction $^{96}Zr(^{7}Li, ^{7}Li^{*}_{4.63} \rightarrow \alpha+t)^{96}Zr_{gs}$ and the non-sequential reaction $^{96}Zr(^{7}Li, \alpha+t)^{96}Zr_{gs}$.

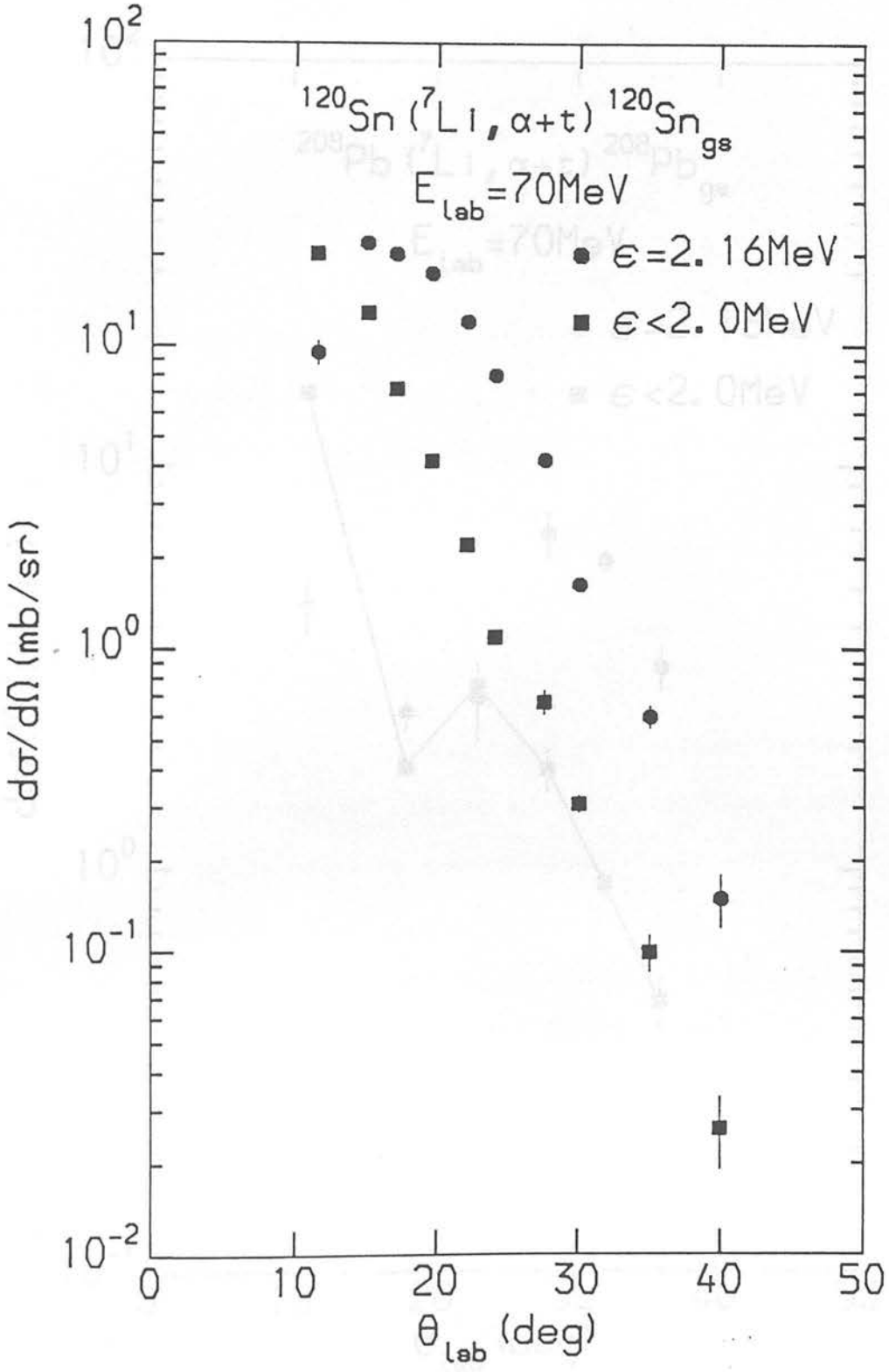

Figure 3.33: Angular distributions for the sequential reaction $^{120}Sn(^{7}Li, ^{7}Li^{*}_{4.63} \rightarrow \alpha+t)^{120}Sn_{gs}$ and the non-sequential reaction $^{120}Sn(^{7}Li, \alpha+t)^{120}Sn_{gs}$.

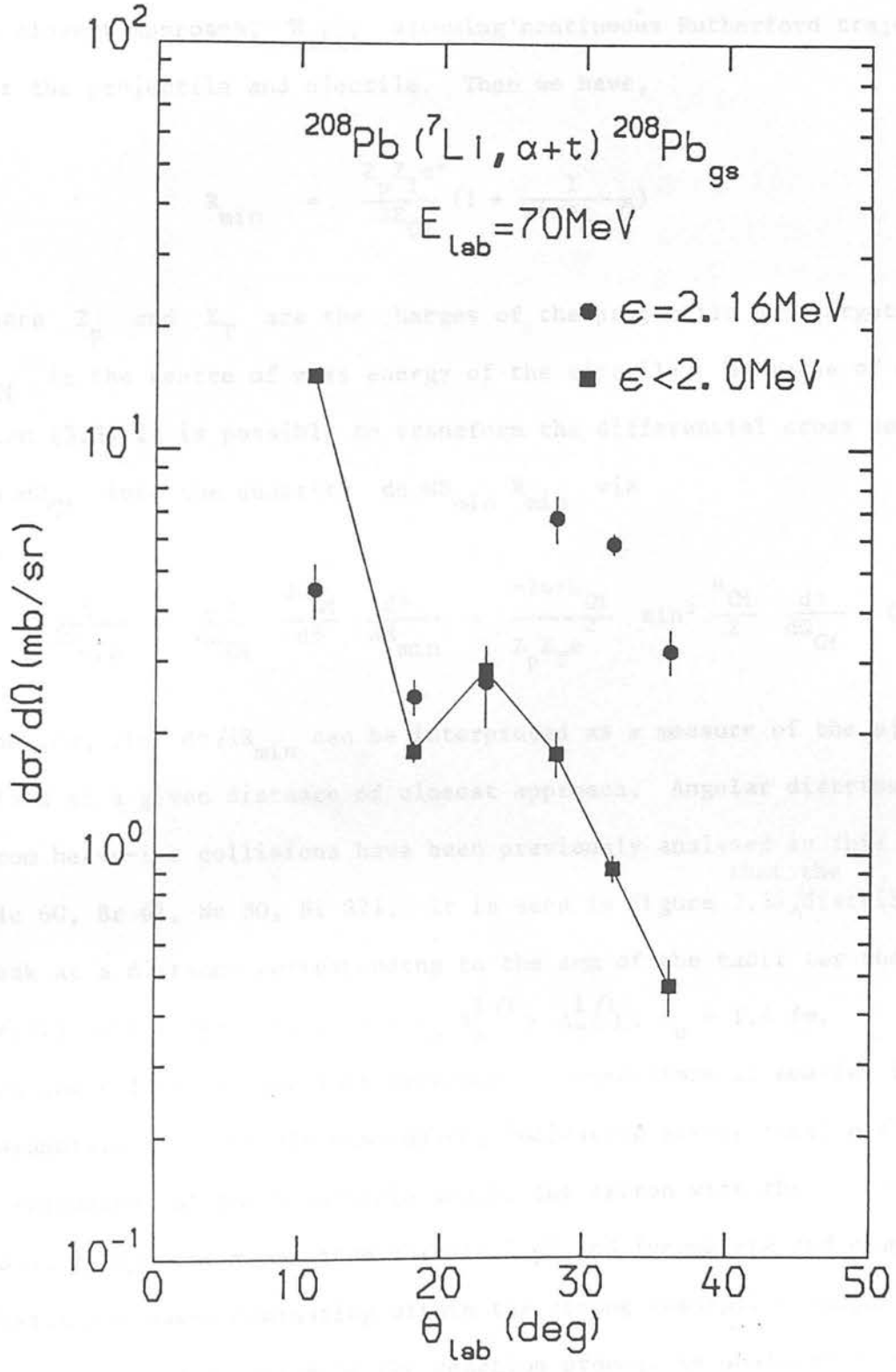

Figure 3.34: Angular distributions for the sequential reaction $^{208}Pb(^{7}Li, ^{7}Li^{*}_{4.63} \rightarrow \alpha+t)^{208}Pb$ and the non-sequential reaction $^{208}Pb(^{7}Li, \alpha+t)^{208}Pb_{gs}$.

Further information can be obtained from the shapes of the angular distributions. For reactions where the Sommerfeld parameter $\eta >> 1$, it is possible to correlate the emission angle θ_{CM} with the distance of closest approach, R_{min}, assuming continuous Rutherford trajectories for the projectile and ejectile. Then we have,

$$R_{min} = \frac{Z_p Z_T e^2}{2E_{CM}} \left(1 + \frac{1}{\sin\theta_{CM}/2}\right) \qquad (3.3)$$

where Z_p and Z_T are the charges of the projectile and target and E_{CM} is the centre of mass energy of the ejectile. By means of equation (3.3) it is possible to transform the differential cross section $d\sigma/d\Omega_{CM}$ into the quantity $d\sigma/dR_{min}$ R_{min} via

$$\frac{d\sigma}{dR_{min}} = \frac{d\sigma}{d\Omega_{CM}} \frac{d\Omega_{CM}}{d\theta} \frac{d\theta}{dR_{min}} = \frac{-16\pi E_{CM}}{Z_p Z_T e^2} \sin^3 \frac{\theta_{CM}}{Z} \frac{d\sigma}{d\Omega_{CM}} \qquad (3.4)$$

The quantity $d\sigma/dR_{min}$ can be interpreted as a measure of the ejectile yield at a given distance of closest approach. Angular distributions from heavy-ion collisions have been previously analysed in this manner (Mc 60, Br 61, Ne 80, Bi 82). It is seen in Figure 3.35 that the distributions peak at a distance corresponding to the sum of the radii for the projectile and target, i.e. $R = r_o(A_p^{1/3} + A_T^{1/3})$: $r_o = 1.4$ fm. Grazing collisions are most probable. Interactions at smaller impact parameters are strongly suppressed, indicating strong final state interactions of the α-particle and/or the triton with the target (which would remove their momentum correlation) and incomplete and complete fusion processes dominating within the strong absorption radius. This peripheral localisation of the reaction process is qualitatively confirmed by the calculations of Sakuragi et al. (Sa 83b) for the reaction

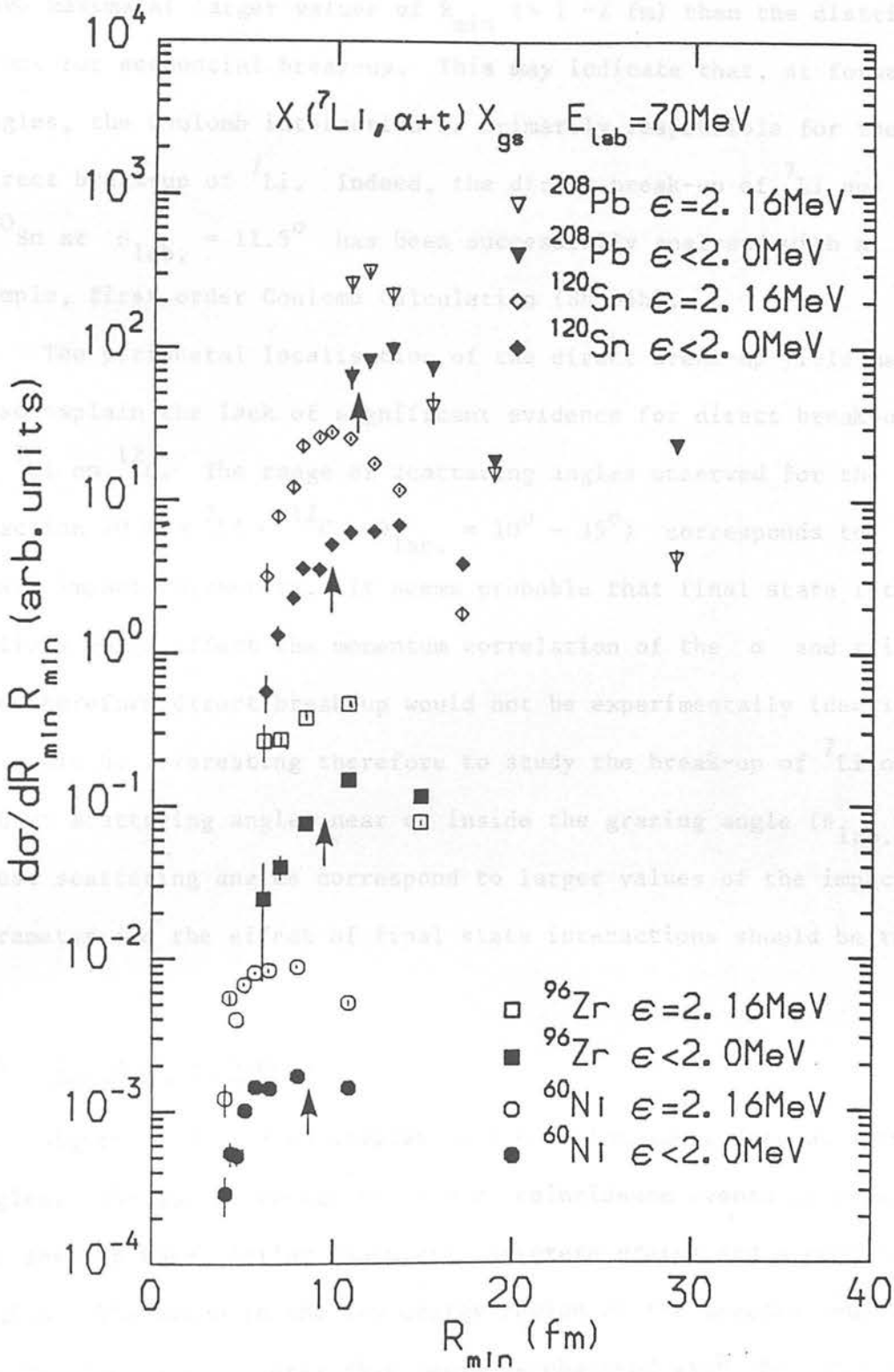

Figure 3.35: $d\sigma/dR_{min}R_{min}$ as a function of R_{min}. The arrows indicate the sum of the radii for the projectile and target.

$^{6}Li + {}^{28}Si$ at 99 MeV.

It is noticeable that the distributions for direct break-up have maxima at larger values of $R_{min.}$ ($\sim$ 1 -2 fm) than the distributions for sequential break-up. This may indicate that, at forward angles, the Coulomb interaction is primarily responsible for the direct break-up of ^{7}Li. Indeed, the direct break-up of ^{7}Li on ^{120}Sn at $\theta_{lab.} = 11.5^{o}$ has been successfully analysed with a simple, first order Coulomb calculation (Sh 84b).

The peripheral localisation of the direct break-up yield may also explain the lack of significant evidence for direct break-up of ^{7}Li on ^{12}C. The range of scattering angles observed for the reaction 70 MeV $^{7}Li + {}^{12}C$ ($\theta_{lab.} = 10^{o} - 35^{o}$) corresponds to small impact parameters. It seems probable that final state interactions would affect the momentum correlation of the α and triton, and therefore direct break-up would not be experimentally identified. It would be interesting therefore to study the break-up of ^{7}Li on ^{12}C at scattering angles near or inside the grazing angle ($\theta_{lab.} \sim 2^{o}$) These scattering angles correspond to larger values of the impact parameter and the effect of final state interactions should be reduced.

(b) α - d coincidences

Figures 3.36 - 3.40 display α - d coincidence data at forward angles. The summed energy of α - d coincidence events is shown. The spectra have similar features: discrete states and a continuum region. The arrow in the low energy region of the spectra indicates the minimum α + d energy that could be observed with the ΔE - E telescopes used in this study. The discrete states are identifiable

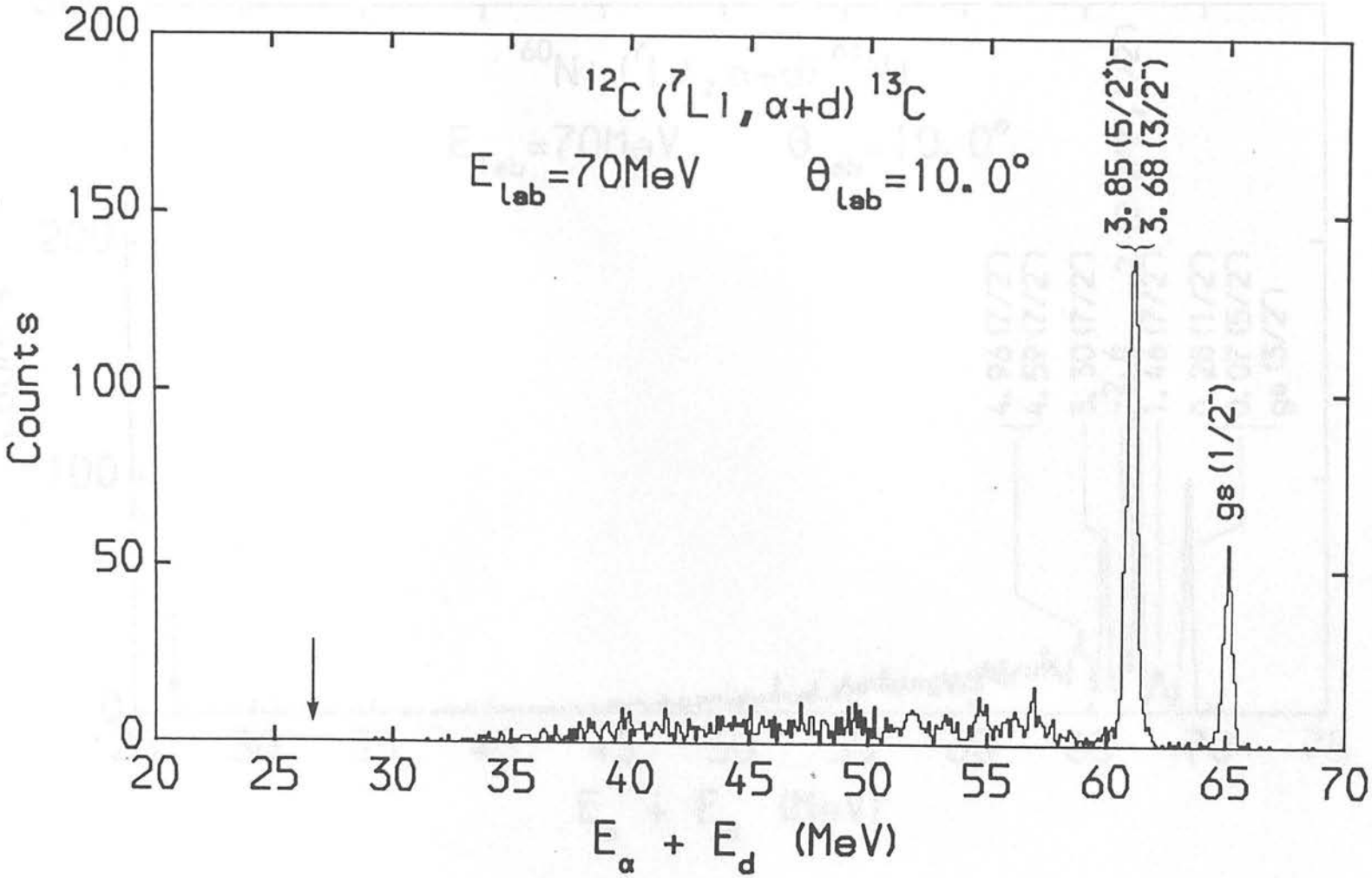

Figure 3.36: Summed energy spectrum for α-d coincidences from the reaction 70 MeV ^{7}Li + ^{12}C.

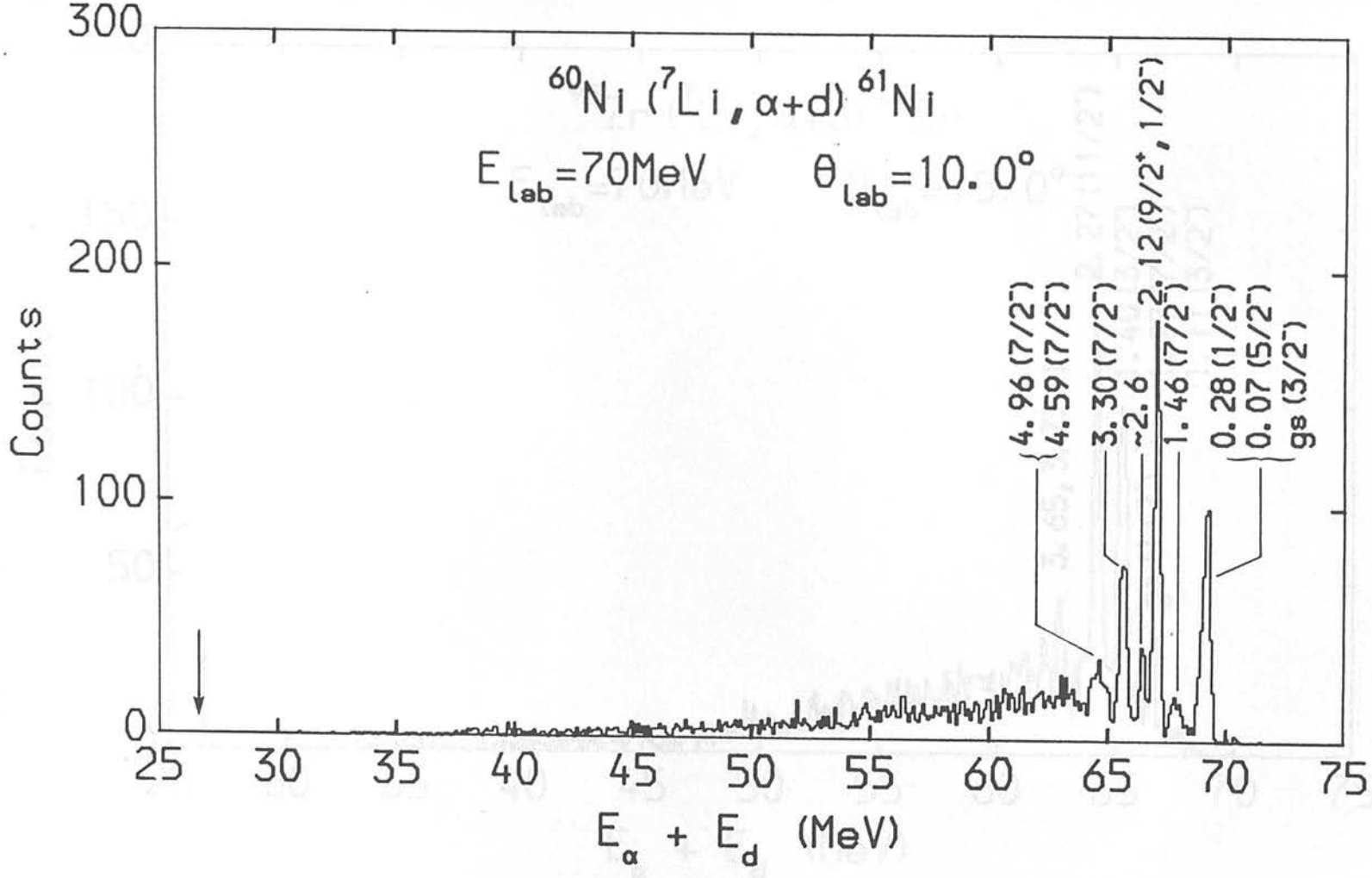

Figure 3.37: Summed energy spectrum for α-d coincidences from the reaction 70 MeV ^{7}Li + ^{60}Ni.

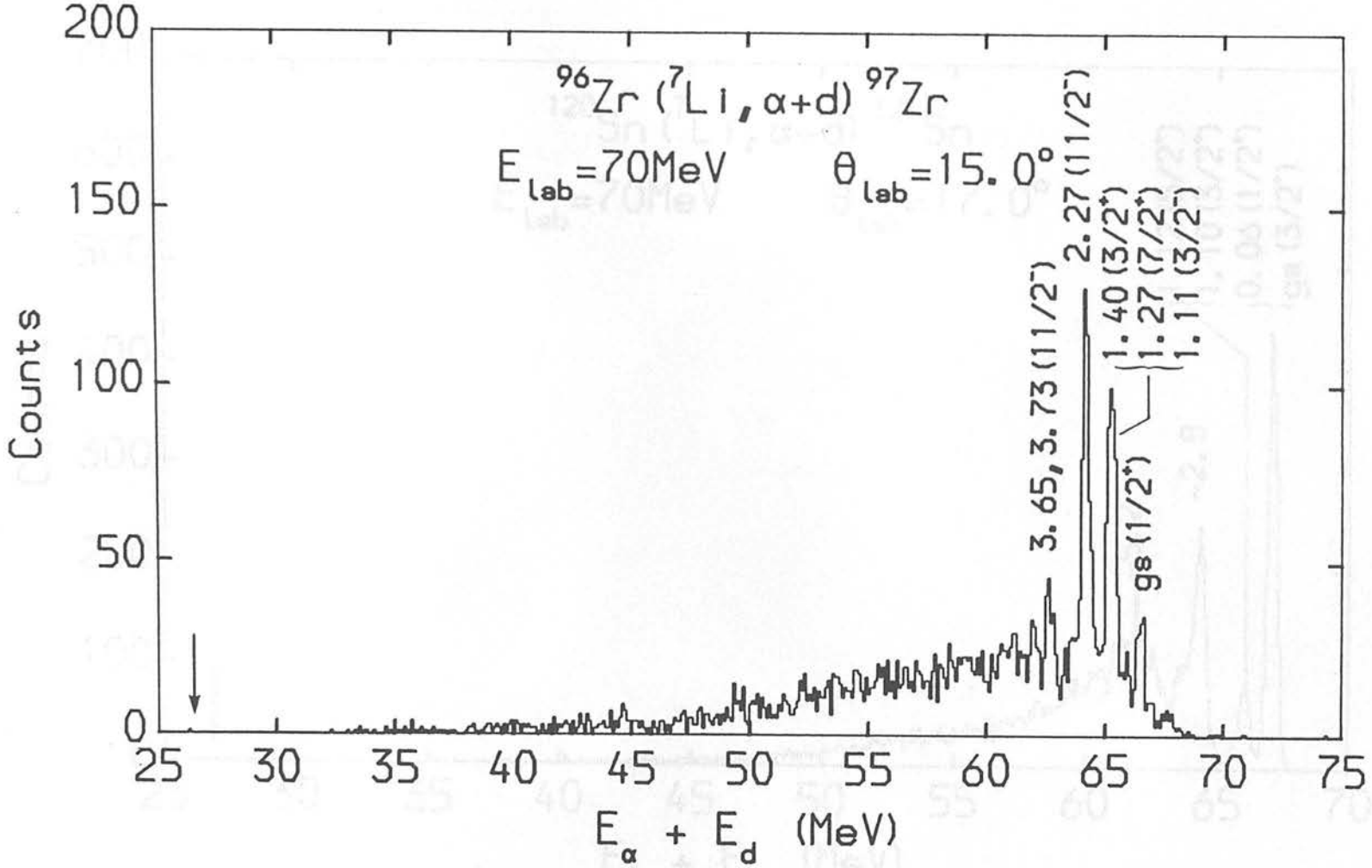

Figure 3.38: Summed energy spectrum for α-d coincidences from the reaction 70 MeV ^{7}Li + ^{96}Zr.

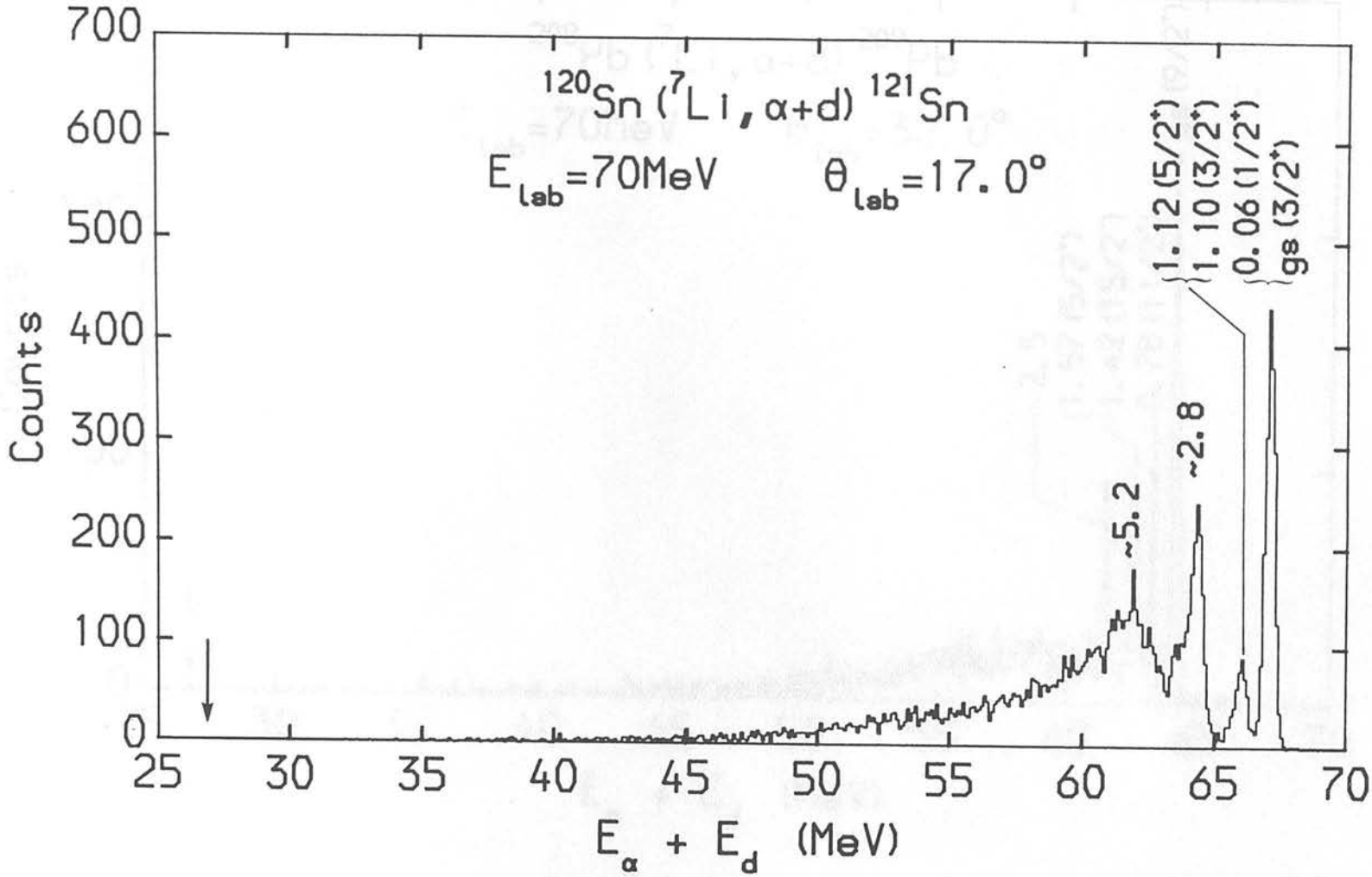

Figure 3.39: Summed energy spectrum for α-d coincidences from the reaction 70 MeV ^{7}Li + ^{120}Sn.

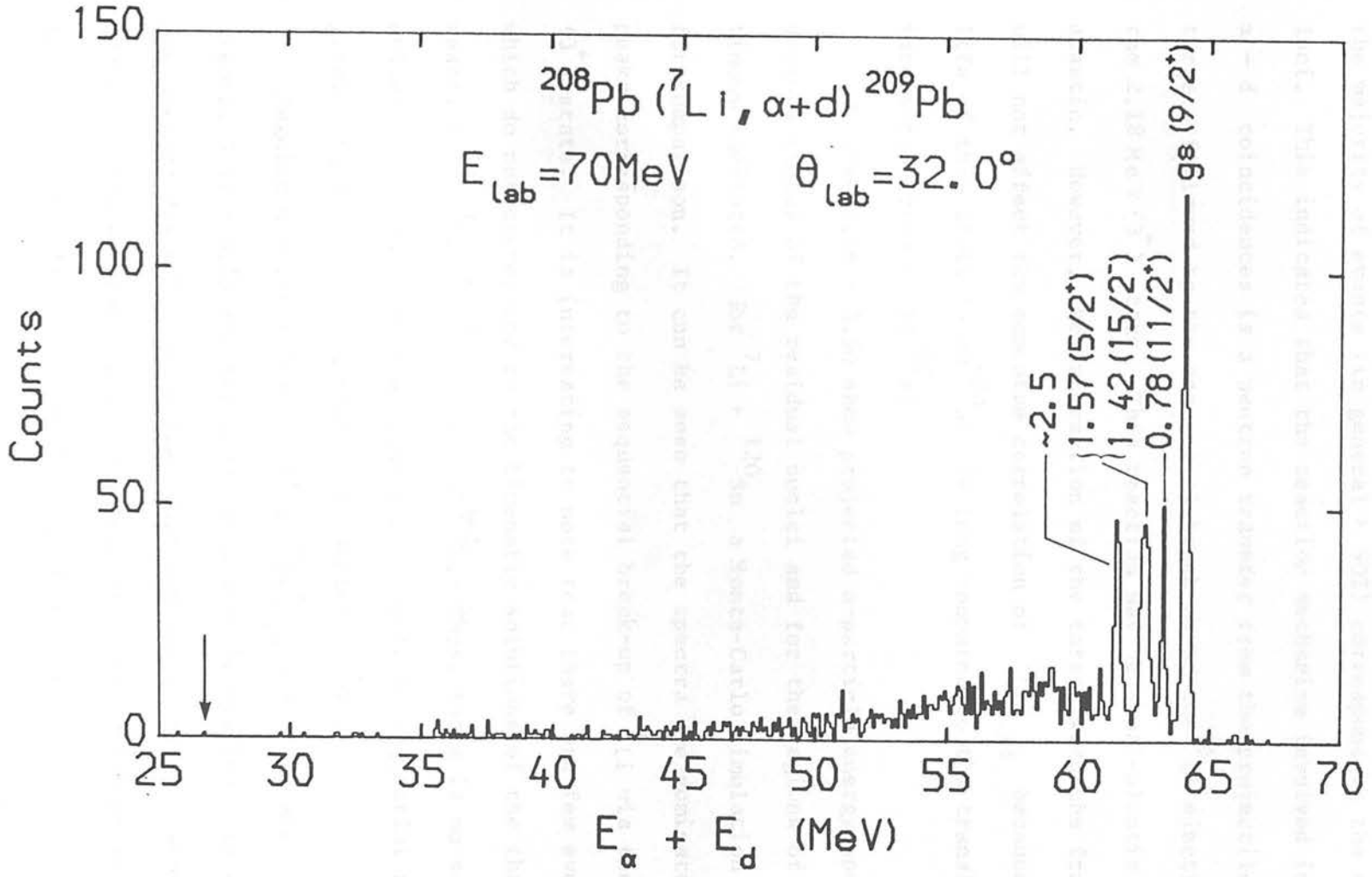

Figure 3.40: Summed energy spectrum for α-d coincidences from the reaction 70 MeV ^{7}Li + ^{208}Pb.

assuming a neutron transfer from the projectile to the target. Further information on the reaction mechanism and the origin of the continuum region of the spectra may be obtained by examination of the α - d correlation spectra shown in Figures 3.41 - 3.45. It can be seen that the majority of events (in general > 90%) correspond to the ε = 0.71 MeV loci. This indicates that the reaction mechanism involved in producing α - d coincidences is a neutron transfer from the projectile to the target, followed by the sequential break-up of the ^{6}Li ejectile via the 2.18 MeV (3^{+}) state. This reaction may be quasi-elastic or inelastic. However, the interaction of the target with the fragments will not affect the momentum correlation of $^{6}Li^{*}_{2.18}$ because the mean life of this state ($\sim 10^{-20}$s) is long compared to the transit or interaction time ($\sim 10^{-22}$s).

Figures 3.46 - 3.50 show projected α-particle energy spectra for various states of the residual nuclei and for the regions of the continuum indicated. For ^{7}Li + ^{120}Sn a Monte-Carlo simulation is shown for comparison. It can be seen that the spectra are dominated by the peaks corresponding to the sequential break-up of ^{6}Li via the 2.18 MeV (3^{+}) state. It is interesting to note that there are few events which do not correspond to the kinematic solutions of the three-body reaction $^{A}X(^{7}Li, ^{6}Li^{*}_{2.18} \rightarrow \alpha + d)^{A+1}X$. Thus, there is no significant evidence for non-sequential reaction channels or sequential reactions proceeding via the broad high-lying states of ^{6}Li.

Angular distributions for $(^{7}Li, ^{6}Li^{*}_{2.18} \rightarrow \alpha + d)$ are shown in Figures 3.51 - 3.55 for the discrete states identified. In addition the angular distribution of the continuum region is also shown. The cross section was calculated by integrating the continuum region and folding in the efficiency of $^{6}Li^{*}_{2.18}$ detection as a function of

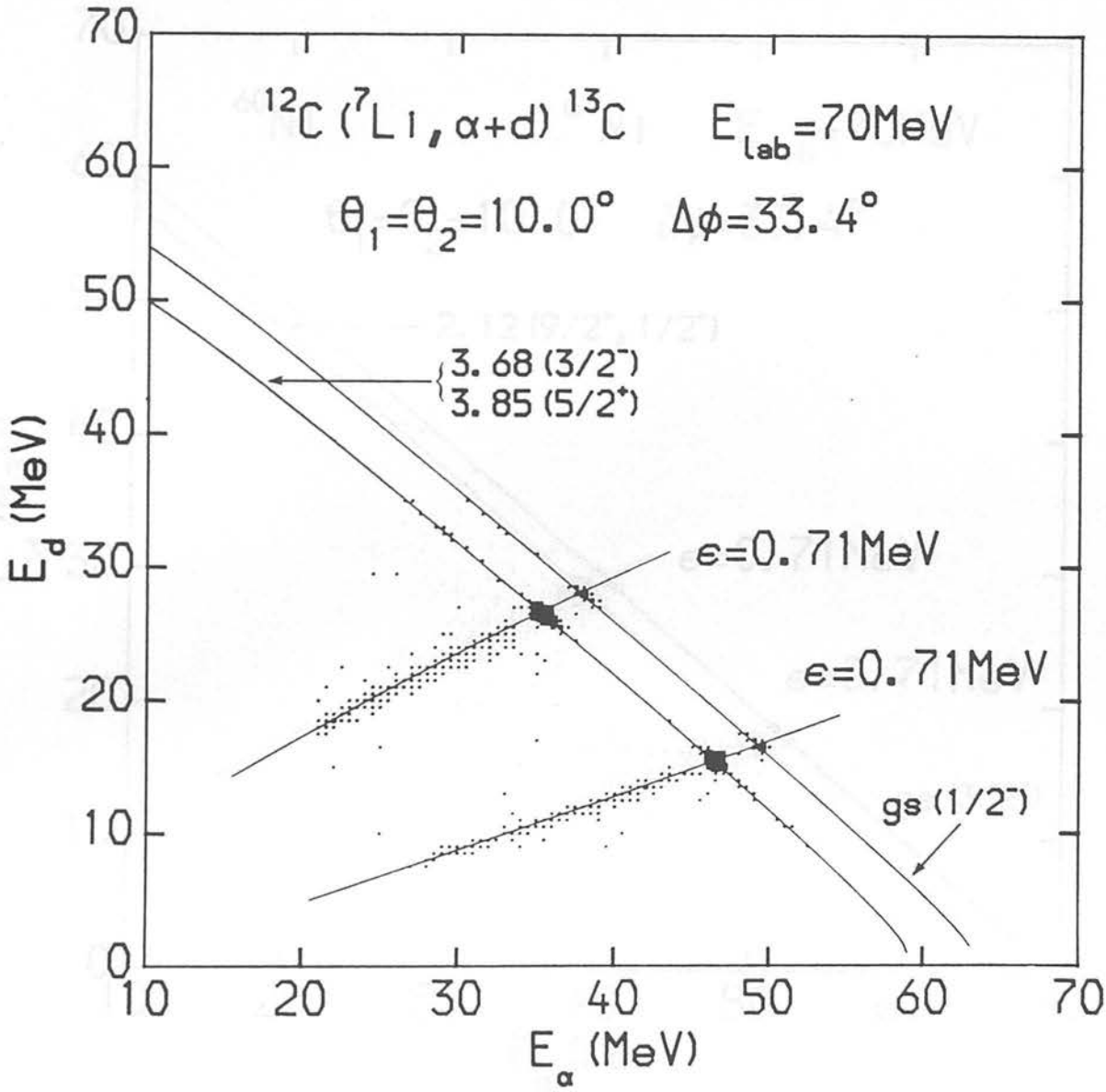

Figure 3.41: Two-dimensional energy correlation spectrum for α-d coincidences from the reaction 70 MeV ^{7}Li + ^{12}C. Loci corresponding to ε = 0.71 MeV are shown.

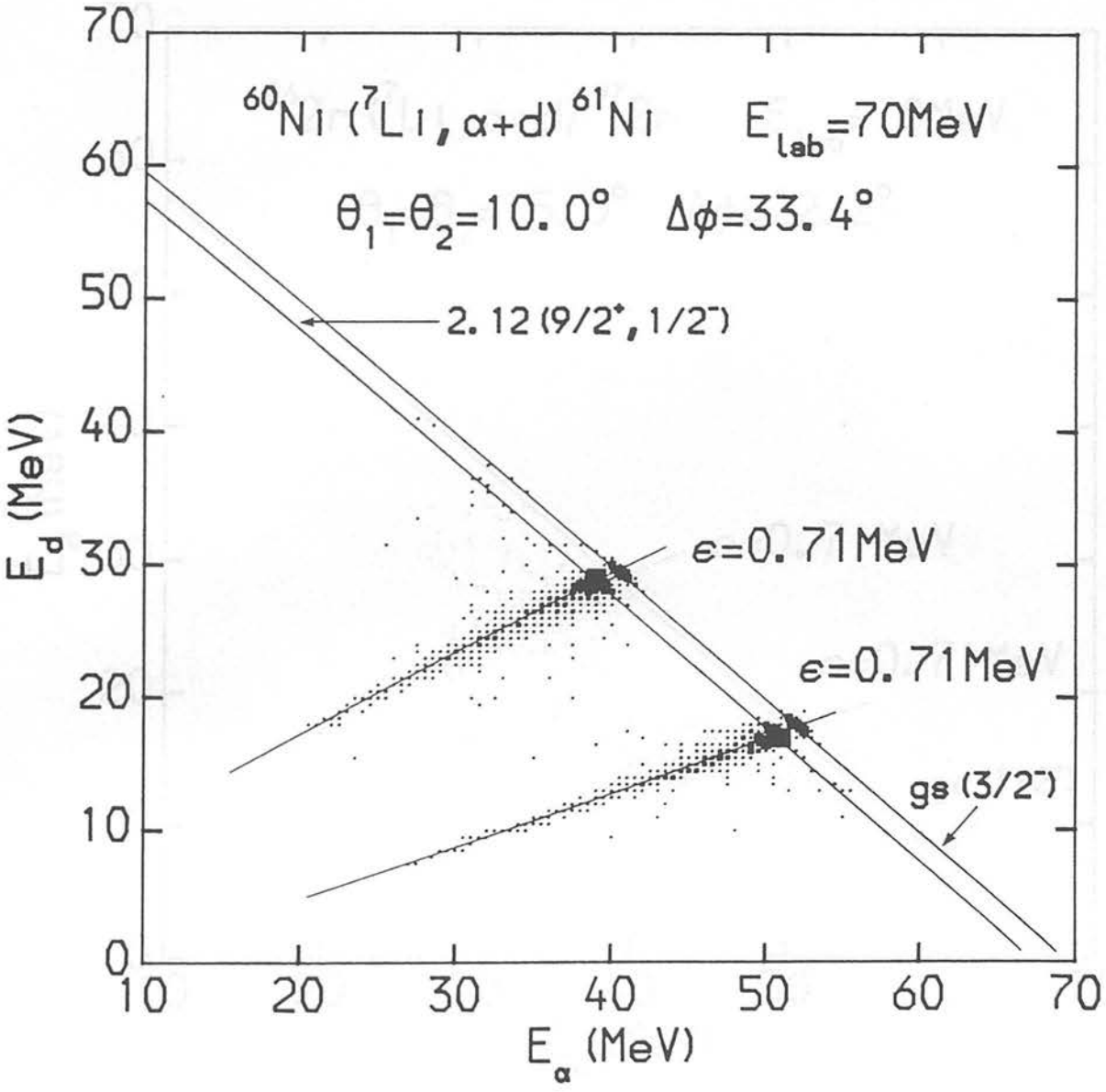

Figure 3.42: Two-dimensional energy correlation spectrum for α-d coincidences from the reaction 70 MeV ^{7}Li + ^{60}Ni. Loci corresponding to ε = 0.71 MeV are shown.

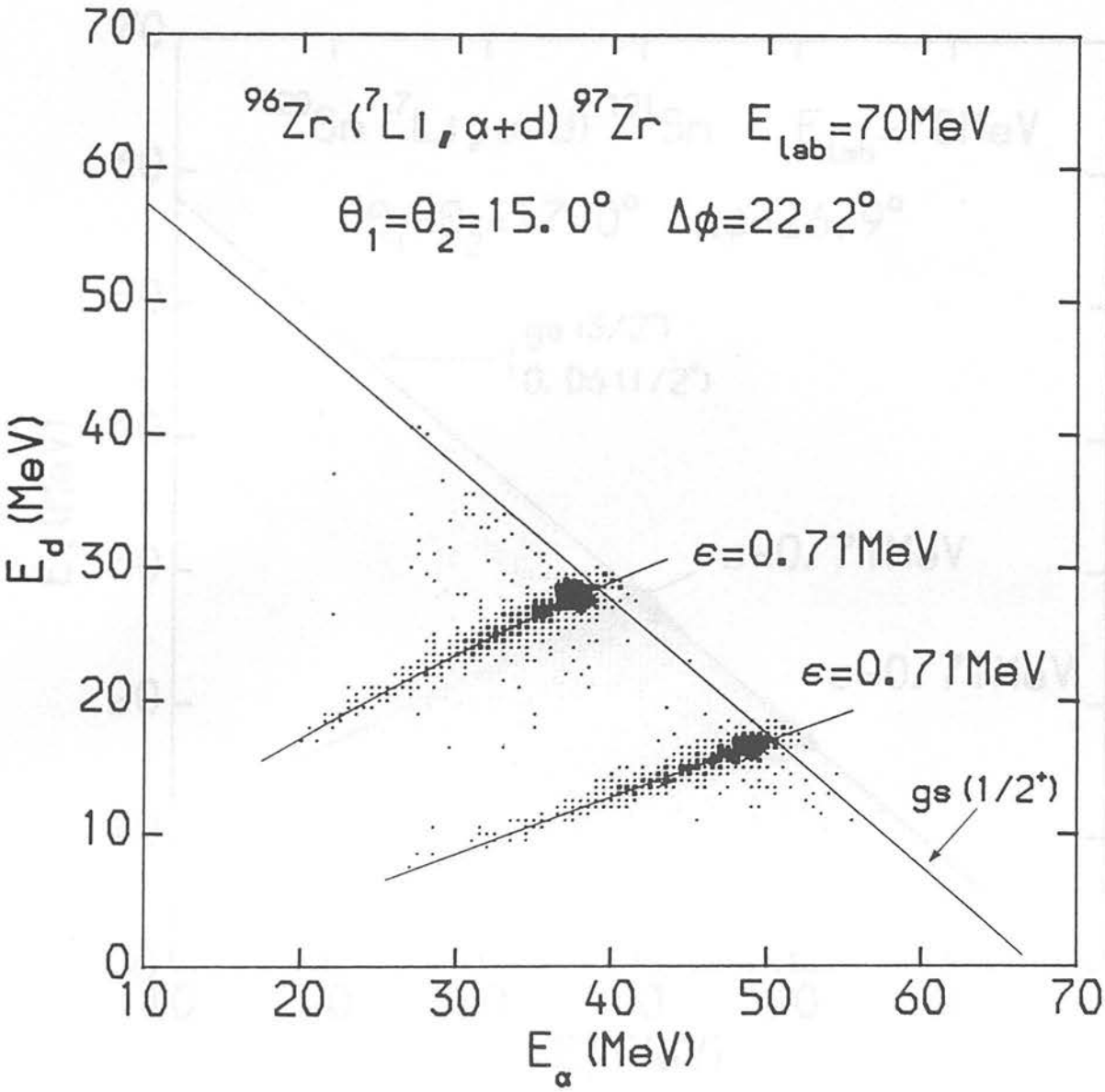

Figure 3.43: Two-dimensional energy correlation spectrum for α-d coincidences from the reaction 70 MeV ^{7}Li + ^{96}Zr. Locii corresponding to ε = 0.71 MeV are shown.

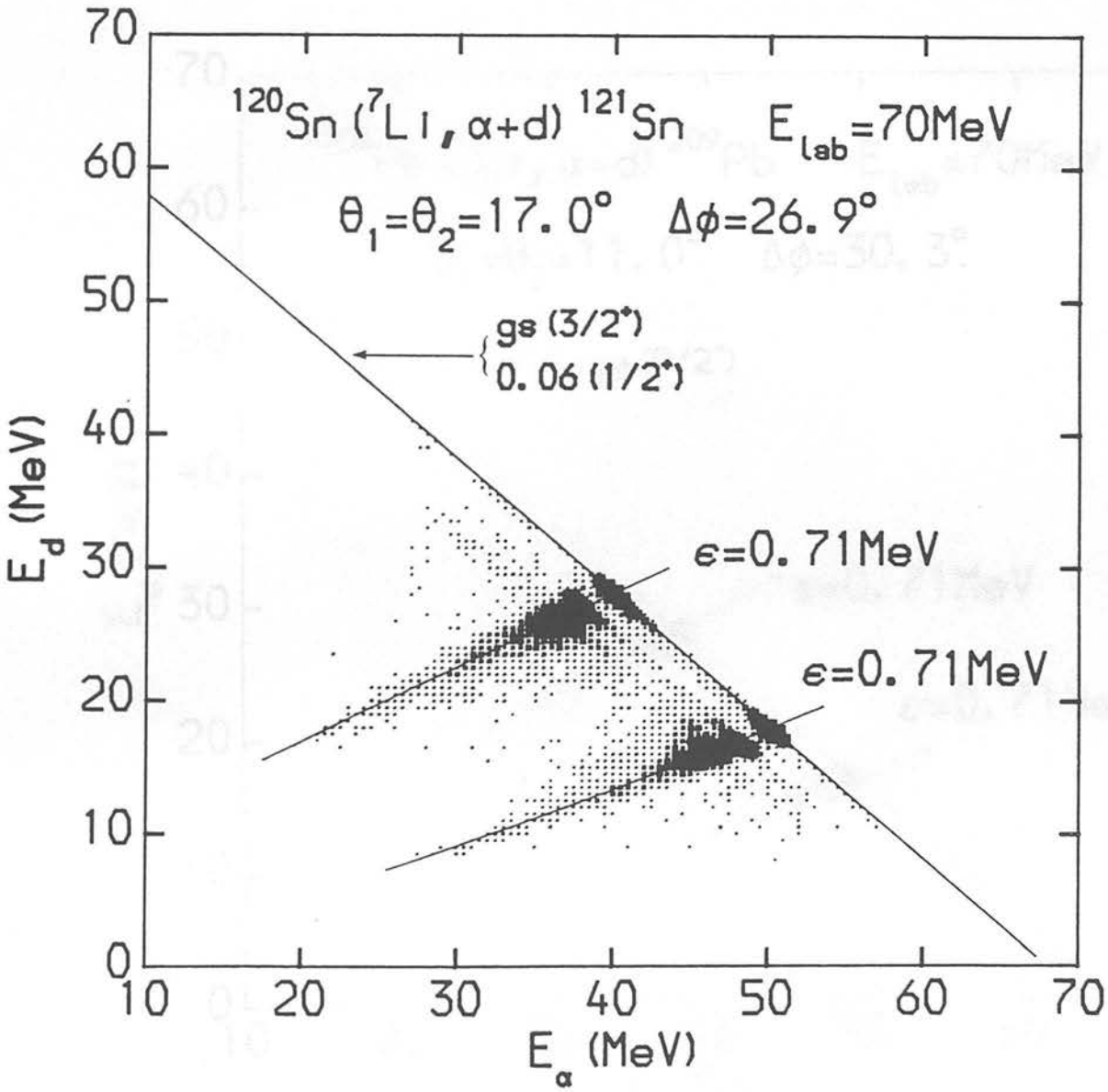

Figure 3.44: Two dimensional energy correlation spectrum for α-d coincidences from the reaction 70 MeV ^{7}Li + ^{120}Sn. Locii corresponding to ε = 0.71 MeV are shown.

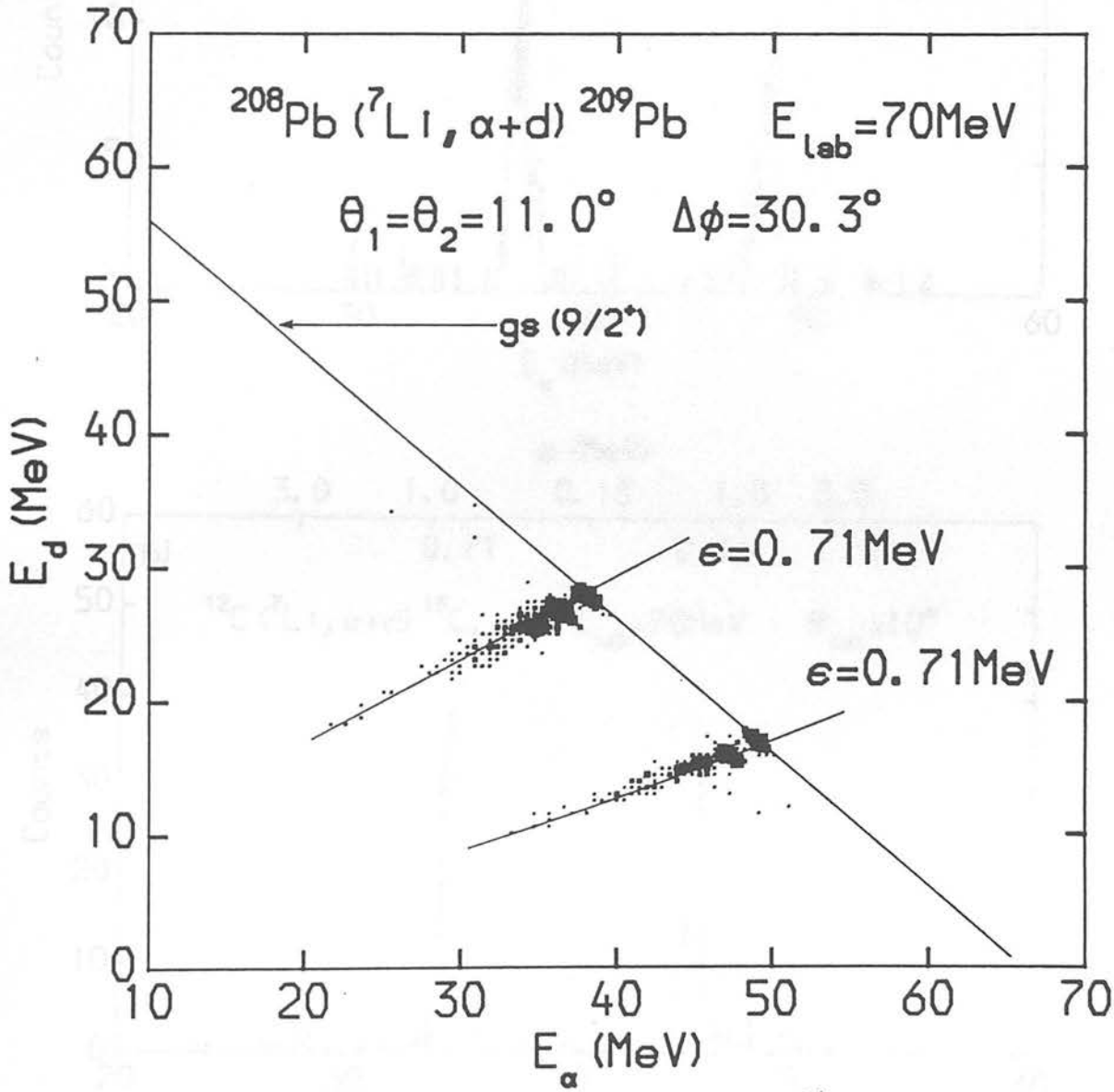

Figure 3.45: Two-dimensional energy correlation spectrum for α-d coincidences from the reaction 70 MeV ^{7}Li + ^{208}Pb. Locii corresponding to ε = 0.71 MeV are shown.

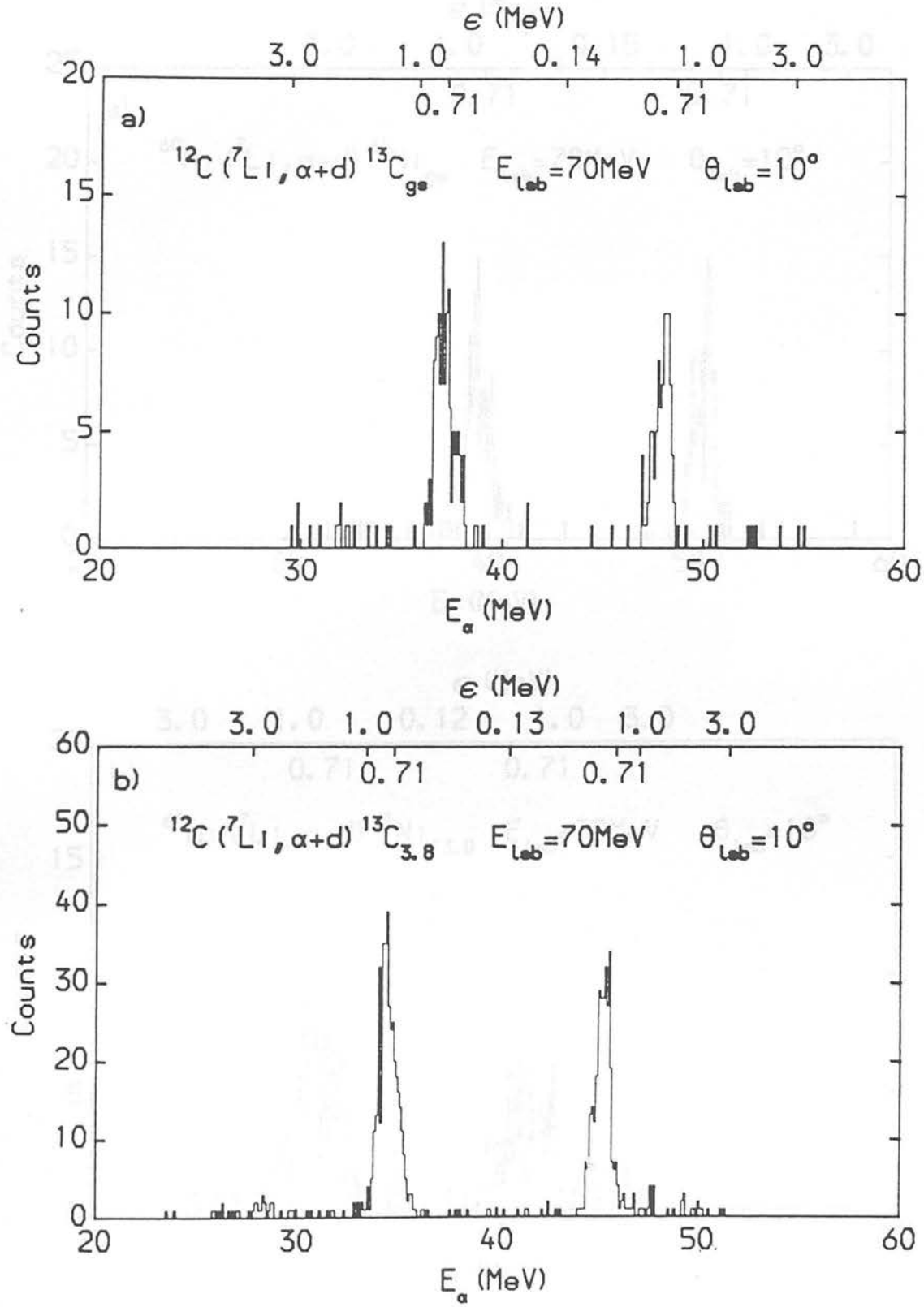

Figure 3.46: Projected α energy spectra for α-d coincidences corresponding to

a) the ground state of ^{13}C

b) 3.68 MeV ($\frac{3^-}{2}$) and 3.85 MeV ($\frac{5^+}{2}$) states of ^{13}C.

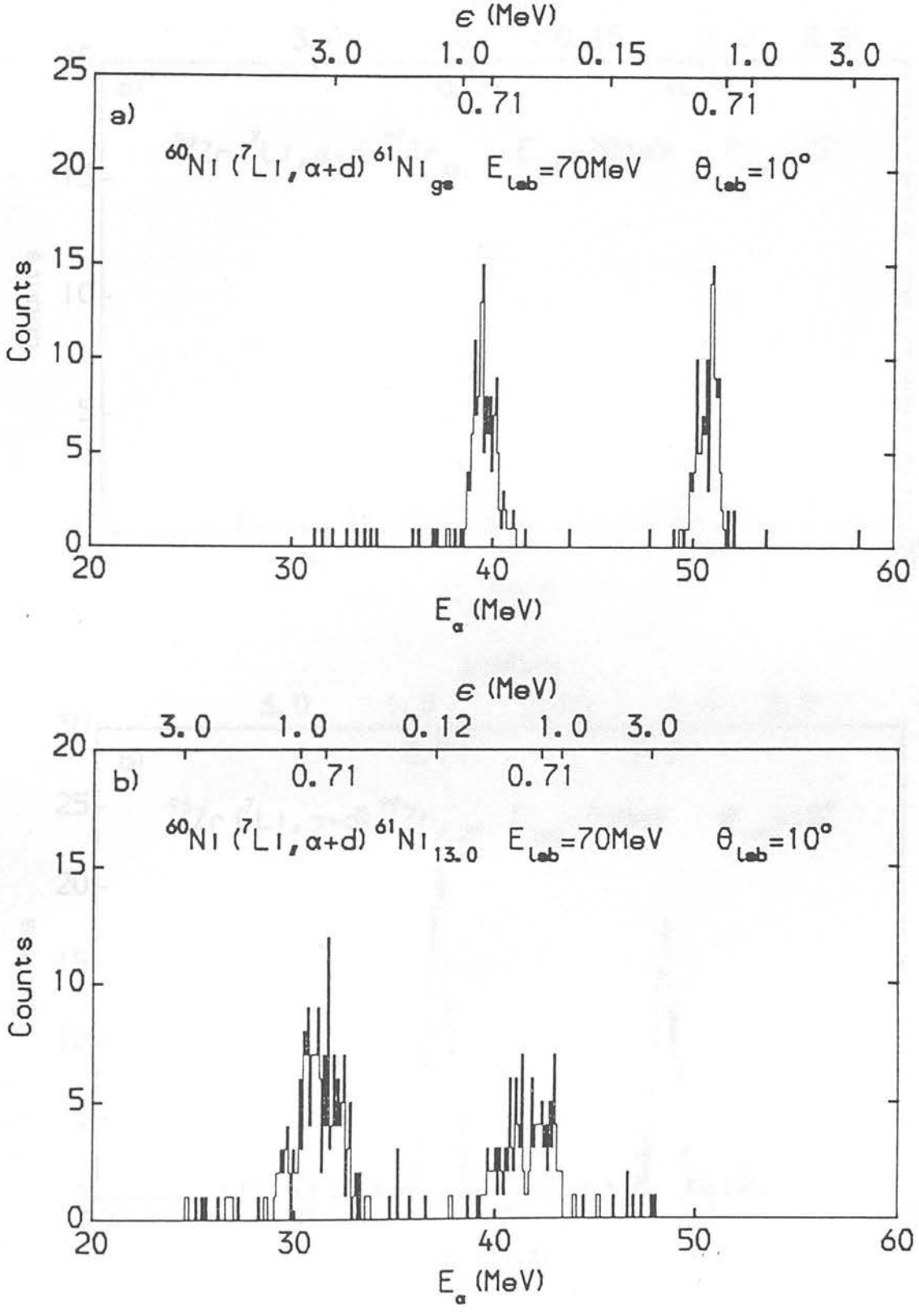

Figure 3.47: Projected α energy spectra for α-d coincidences corresponding to

a) the ground state of ^{61}Ni and

b) 52 MeV $\lesssim E_\alpha + E_d \lesssim$ 57 MeV $- E_x(^{61}\text{Ni}) \sim$ 13 MeV.

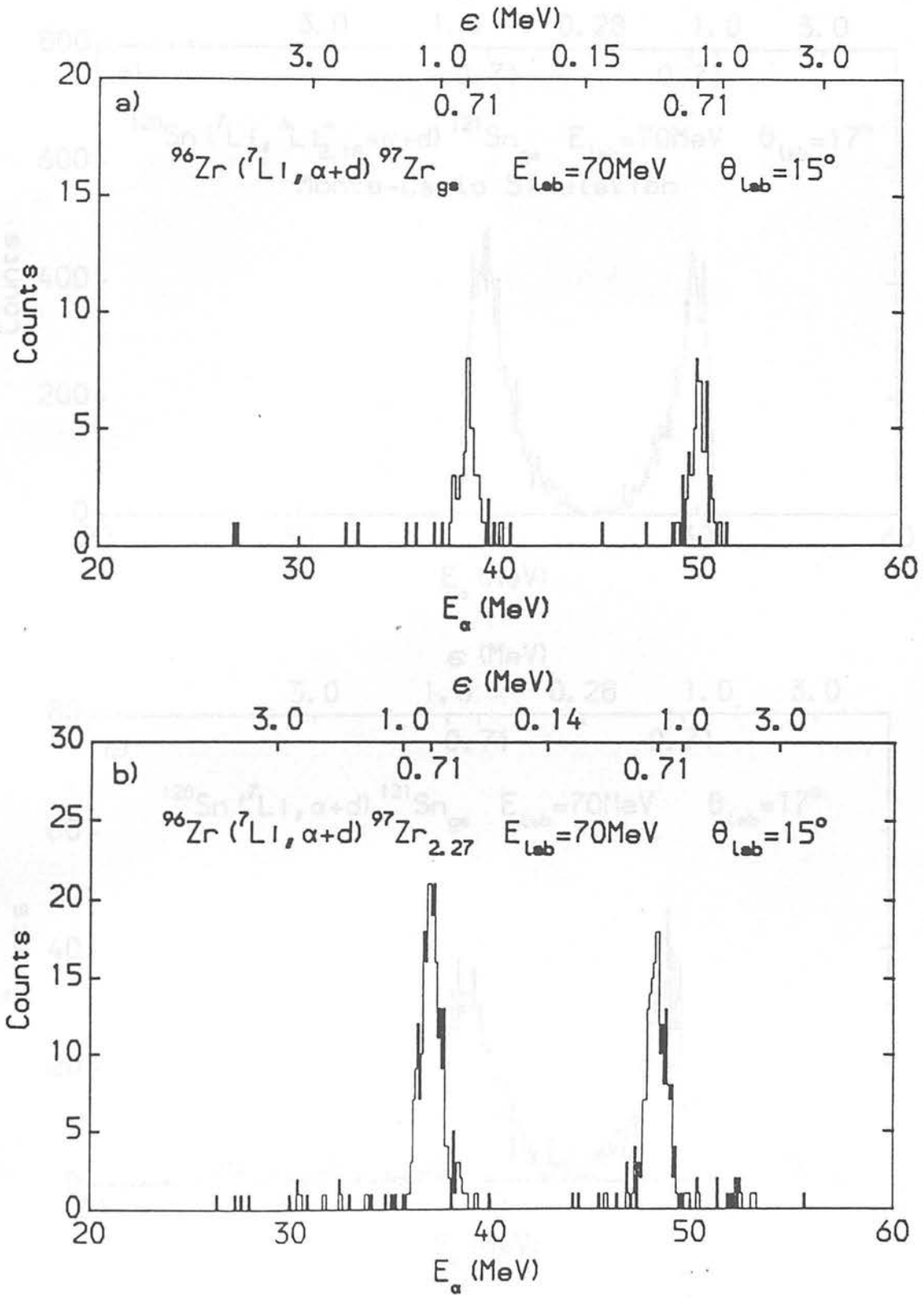

Figure 3.48: Projected α energy spectra for α-d coincidences corresponding to

a) the ground state of ^{97}Zr and,

b) 2.27 ($\frac{11^-}{2}$) state of ^{97}Zr.

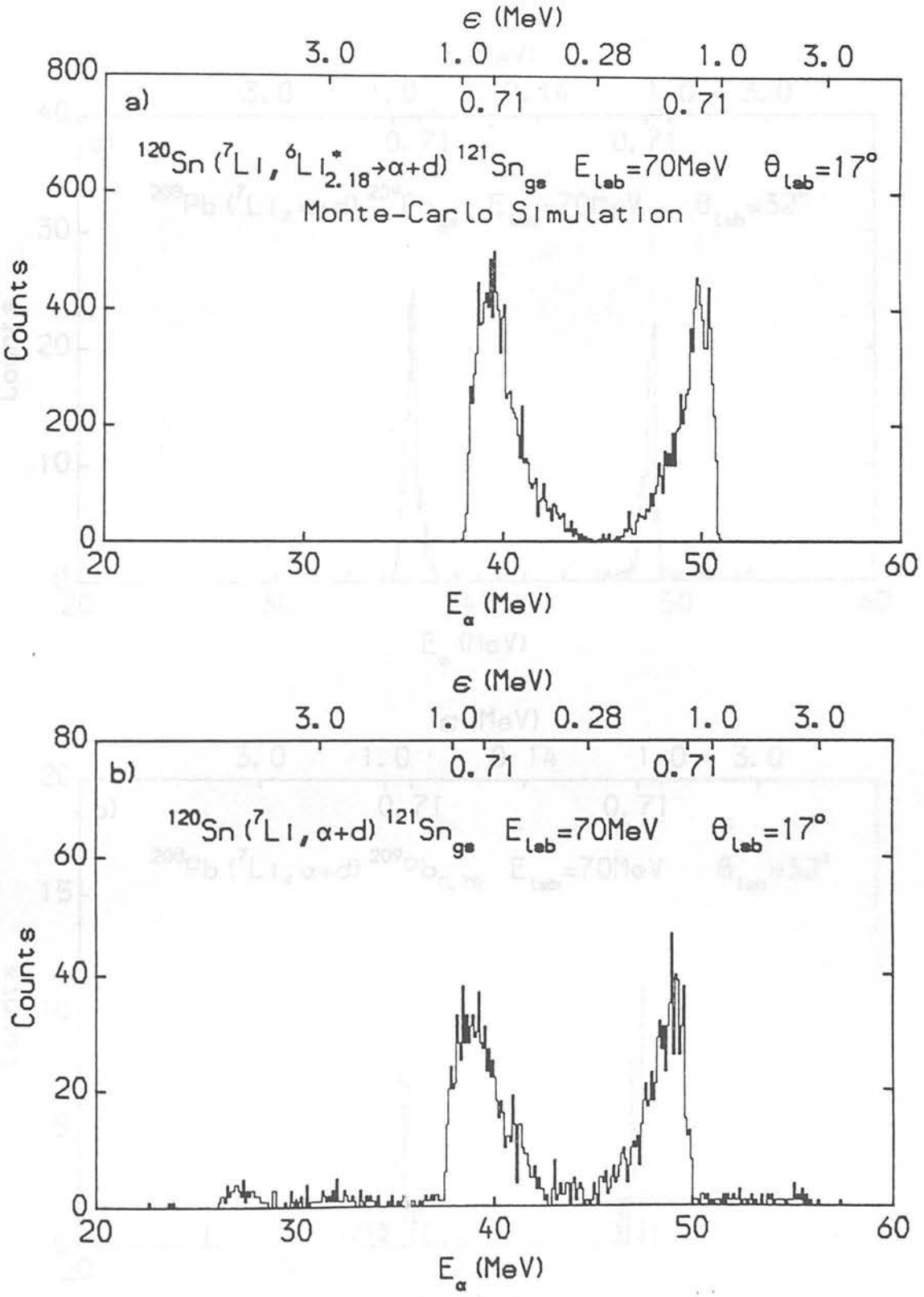

Figure 3.49: a) Monte Carlo simulation of projected α energy spectrum for the reaction $^{120}Sn(^{7}Li, ^{6}Li^{*}_{2.18} \rightarrow \alpha+d)^{121}Sn_{gs}$.

b) Projected α energy spectrum for α-d coincidences corresponding to the ground state of ^{121}Sn.

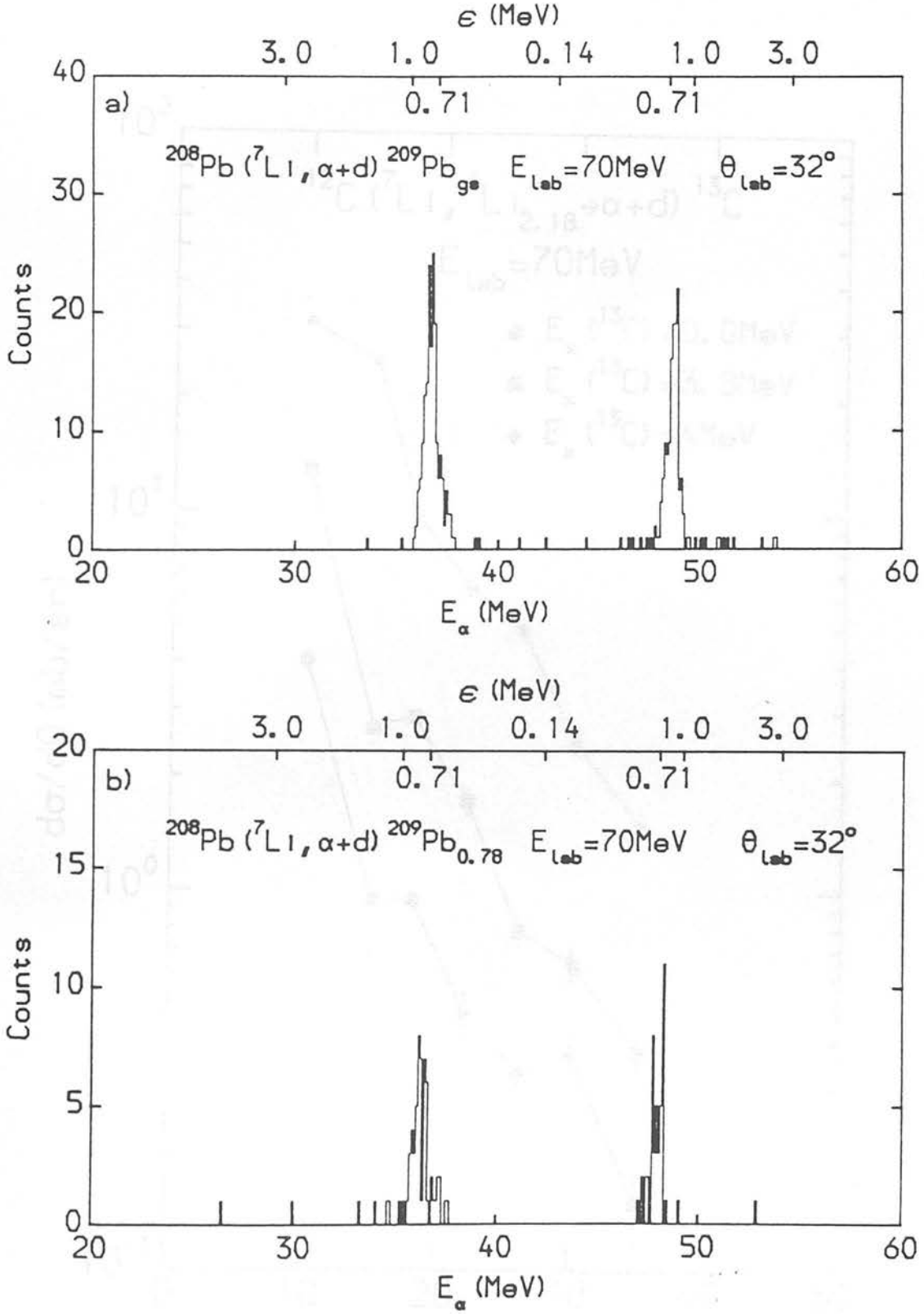

Figure 3.50: Projected α energy spectra for α-d coincidences corresponding to

a) the ground state of ^{209}Pb and,

b) 0.78 MeV ($\frac{11}{2}^-$) state of ^{209}Pb.

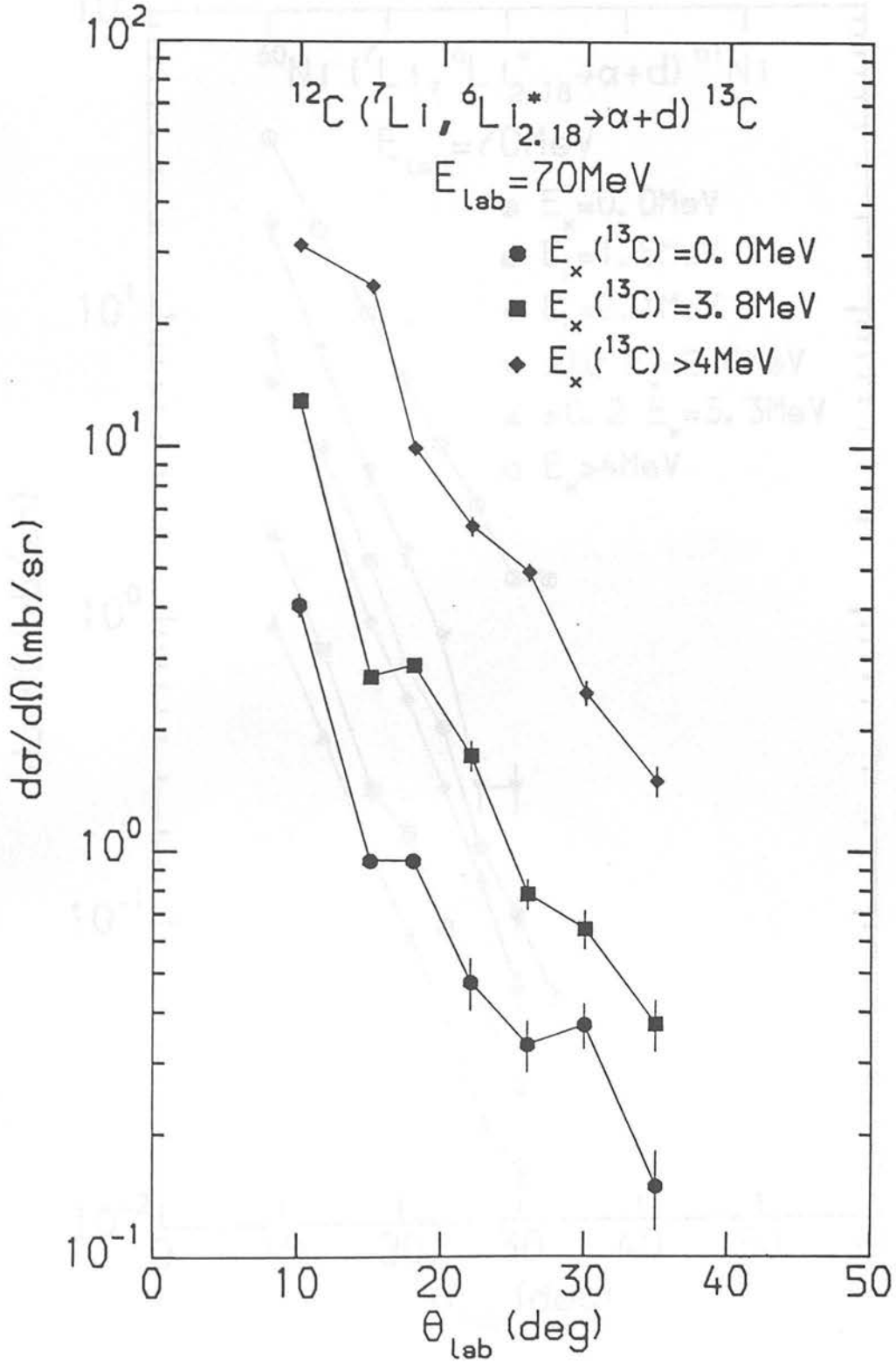

Figure 3.51: Angular distributions for the sequential reaction $^{12}C(^{7}Li, ^{6}Li^{*}_{2.18} \rightarrow \alpha+d)^{13}C$.

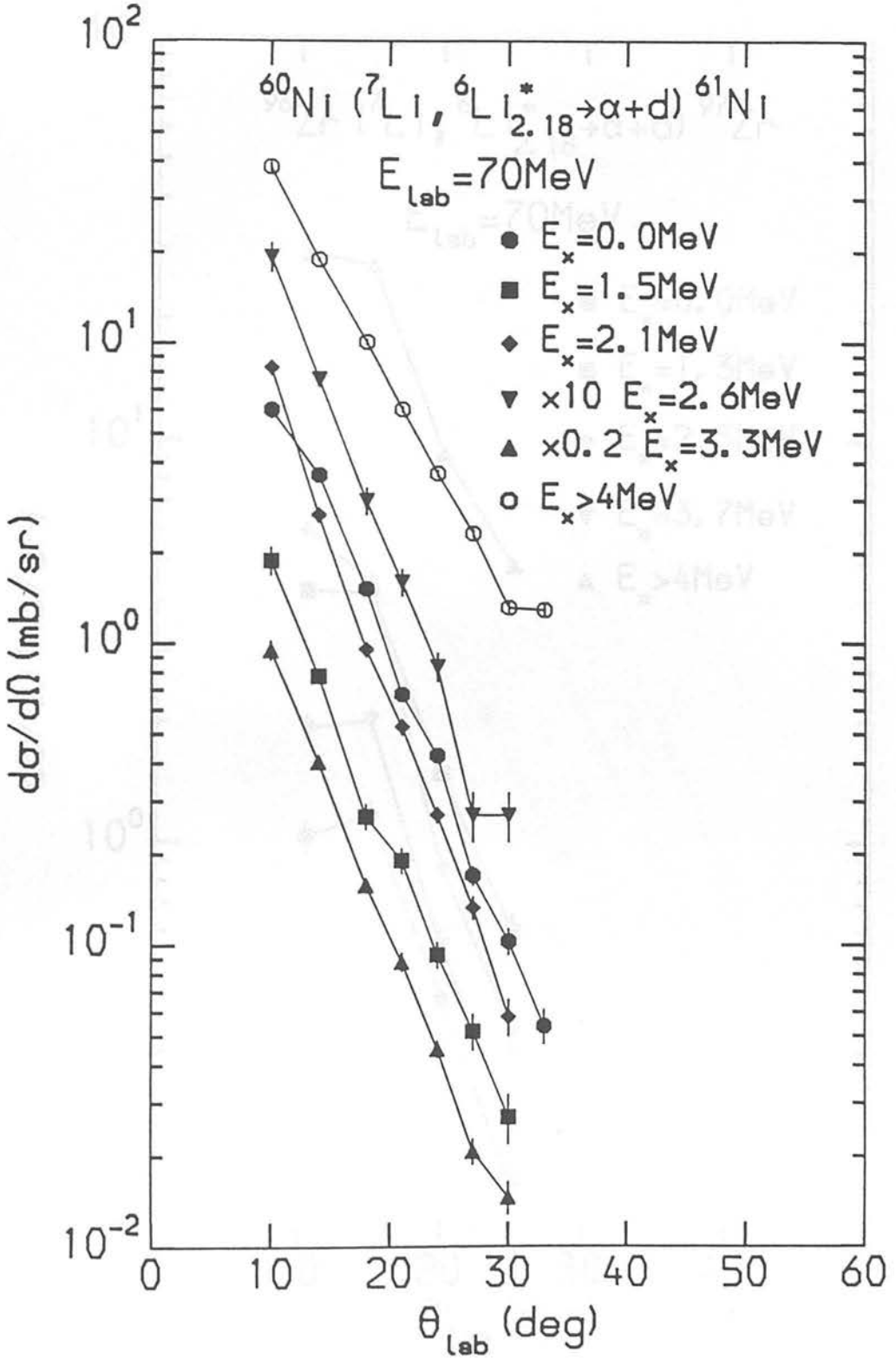

Figure 3.52: Angular distributions for the sequential reaction ^{60}Ni(^{7}Li, ^{6}Li$^{*}_{2.18}$ → α+d)^{61}Ni.

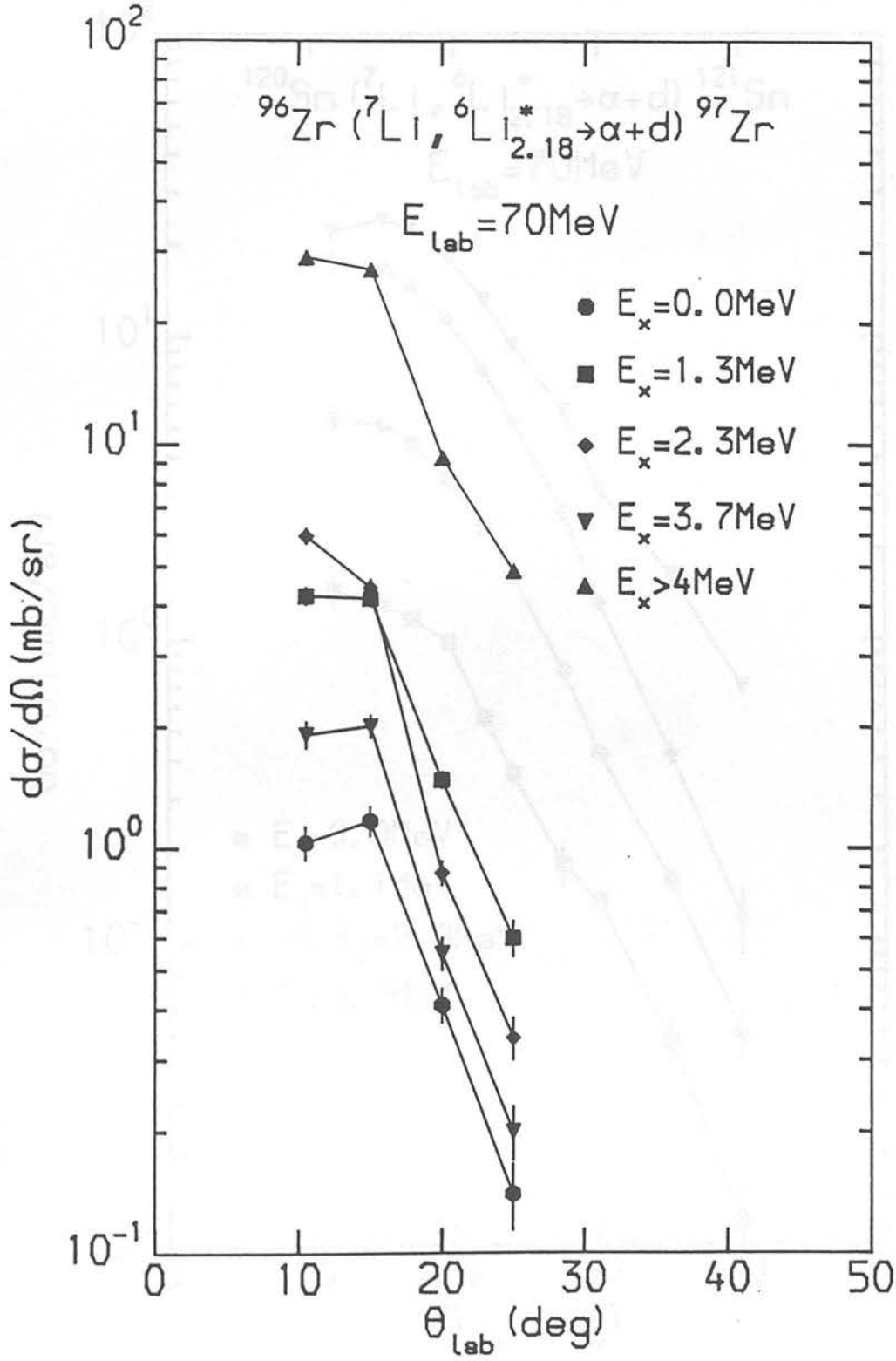

Figure 3.53: Angular distributions for the sequential reaction $^{96}Zr(^{7}Li, ^{6}Li^{*}_{2.18} \rightarrow \alpha+d)^{97}Zr$.

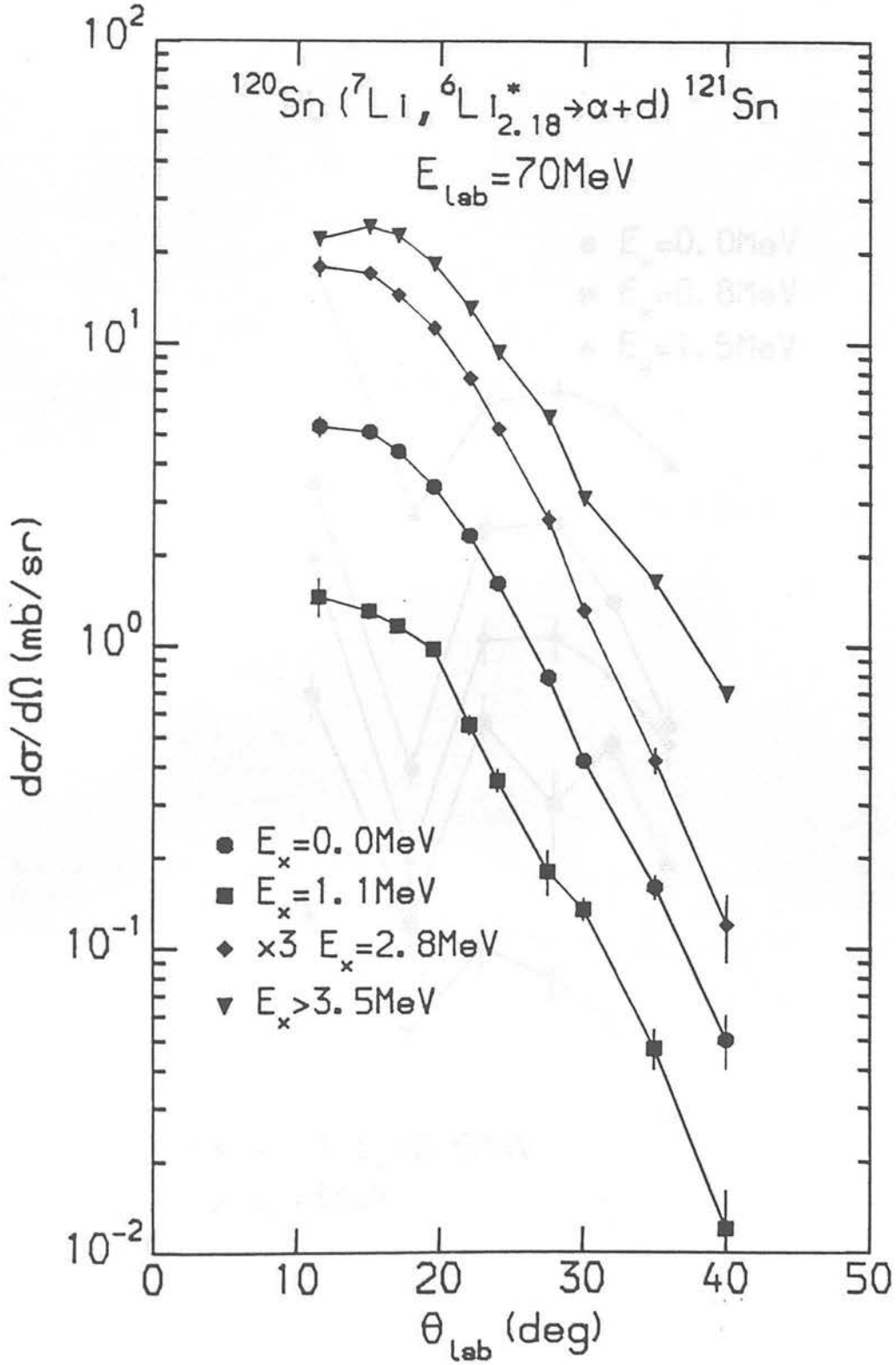

Figure 3.54: Angular distributions for the sequential reaction ^{120}Sn(^{7}Li, ^{6}Li$^{*}_{2.18}$ → α+d)^{121}Sn.

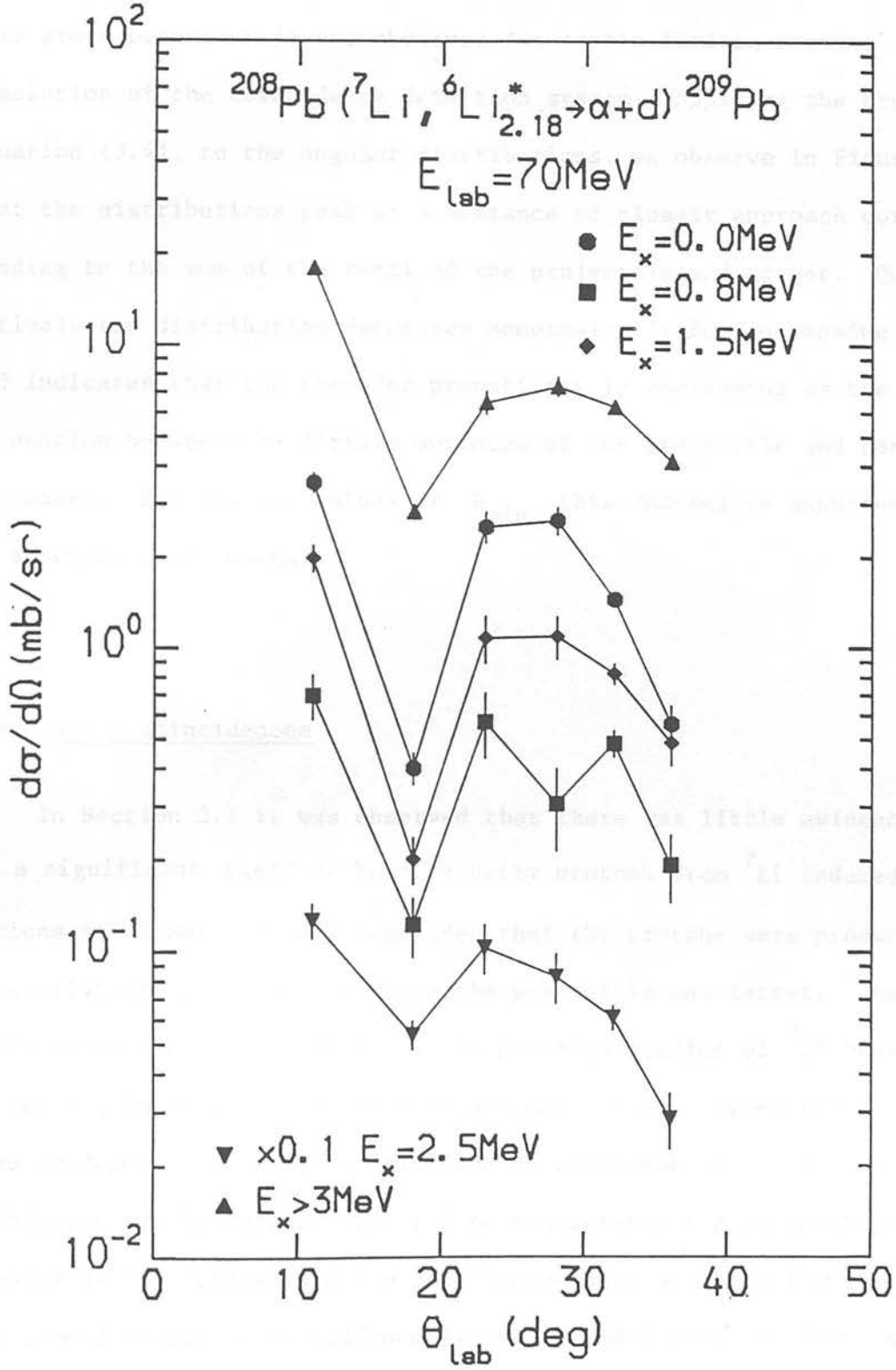

Figure 3.55: Angular distributions for the sequential reaction $^{208}Pb(^{7}Li, ^{6}Li^{*}_{2.18} \rightarrow \alpha+d)^{209}Pb$.

ejectile energy. The angular distributions are peaked around the grazing angle, a feature typical of nucleon transfer in heavy-ion induced reactions. However, any oscillatory structure superimposed on this gross behaviour is not observed due to the limited angular resolution of the coincidence detection system. Applying the transform, equation (3.4), to the angular distributions, we observe in Figure 3.56, that the distributions peak at a distance of closest approach corresponding to the sum of the radii of the projectile and target. Qualitatively the distribution decreases monotonically for increasing R_{min} and indicates that the transfer probability is decreasing as the degree of overlap between the diffuse surfaces of the projectile and target decreases. For smaller values of R_{min} this channel is suppressed by absorptive processes.

(c) α - p coincidences

In Section 3.1 it was observed that there was little evidence for a significant yield of beam velocity protons from ^{7}Li induced reactions at 70 MeV. It was concluded that the protons were produced in equilibrated processes between the projectile and target. These conclusions are broadly supported in previous studies of ^{7}Li break-up (Ut 83, Pa 84b), except that at extreme forward angles there is some evidence of a small contribution to the break-up yield. This conclusion may be further explored by examining α - p correlations. Figures 3.57 - 3.61 show α - p coincidence data at forward angles. The summed energy of coincidence events is displayed. Statistics are poor but a continuum region is identifiable for all targets.

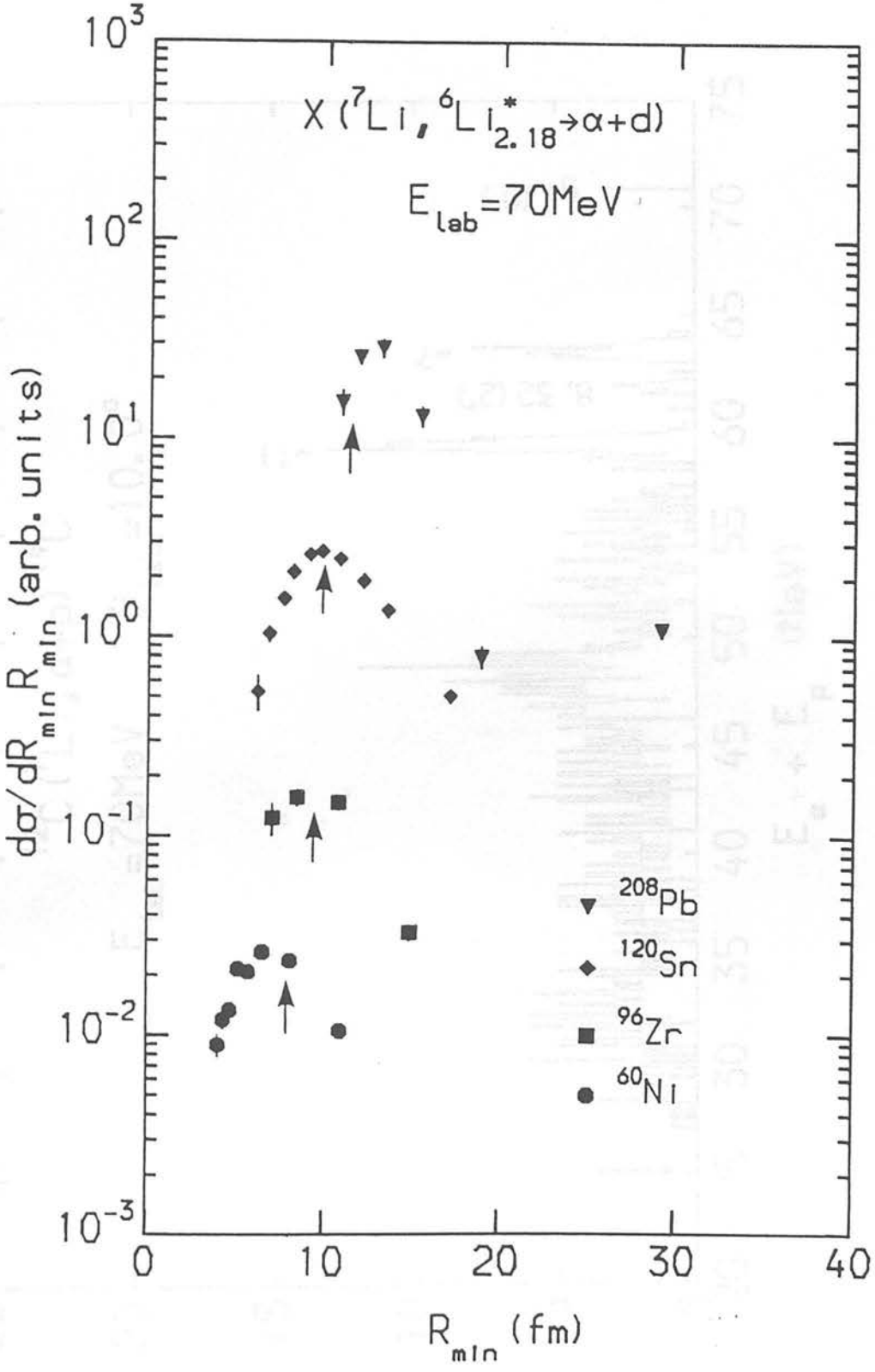

Figure 3.56: $d\sigma/dR_{min}\ R_{min}$ as a function of R_{min}. The arrows indicate the sum of the radii for the projectile and target.

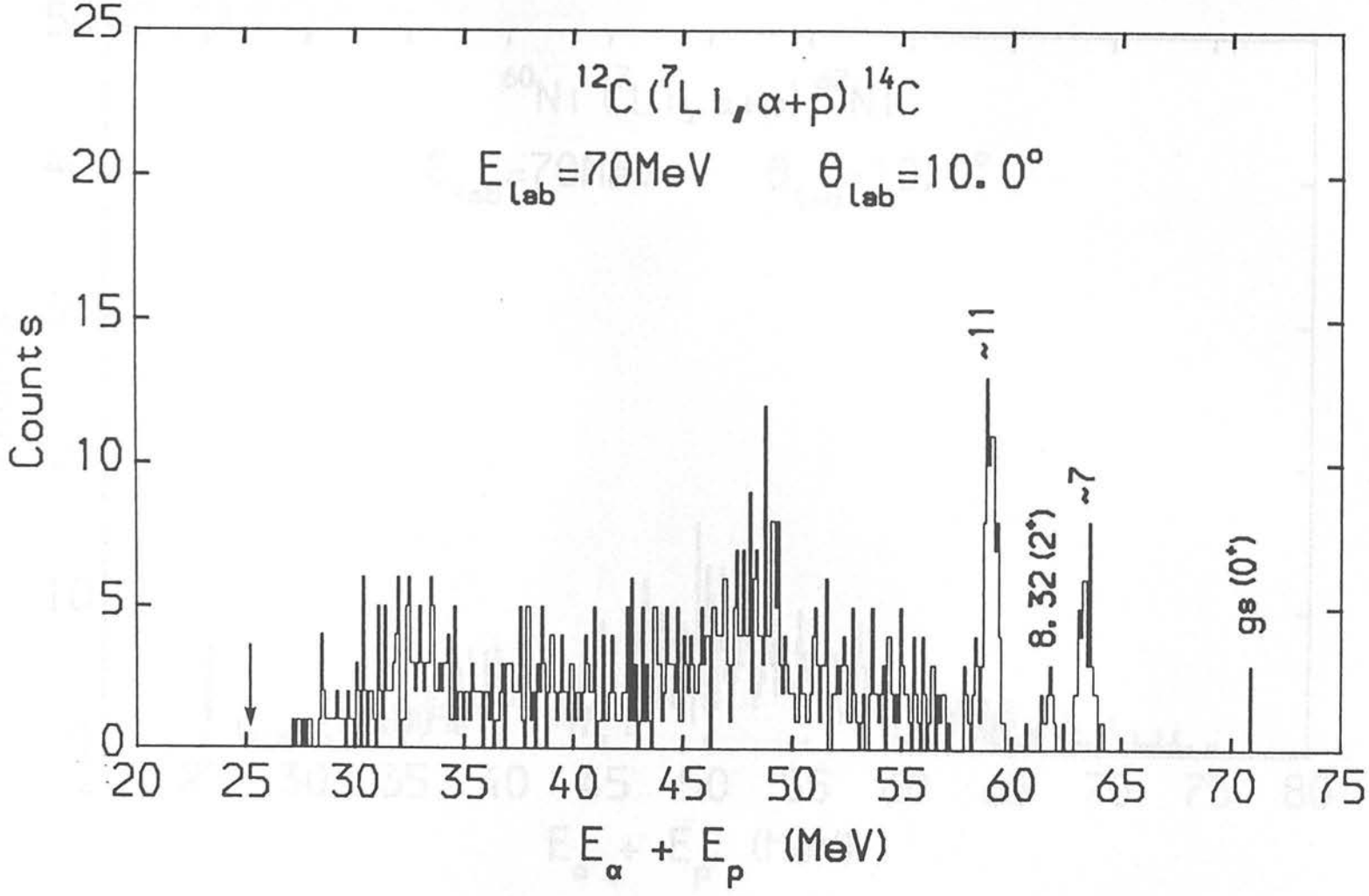

Figure 3.57: Summed energy spectrum for α-p coincidences from the reaction 70 MeV ^{7}Li + ^{12}C.

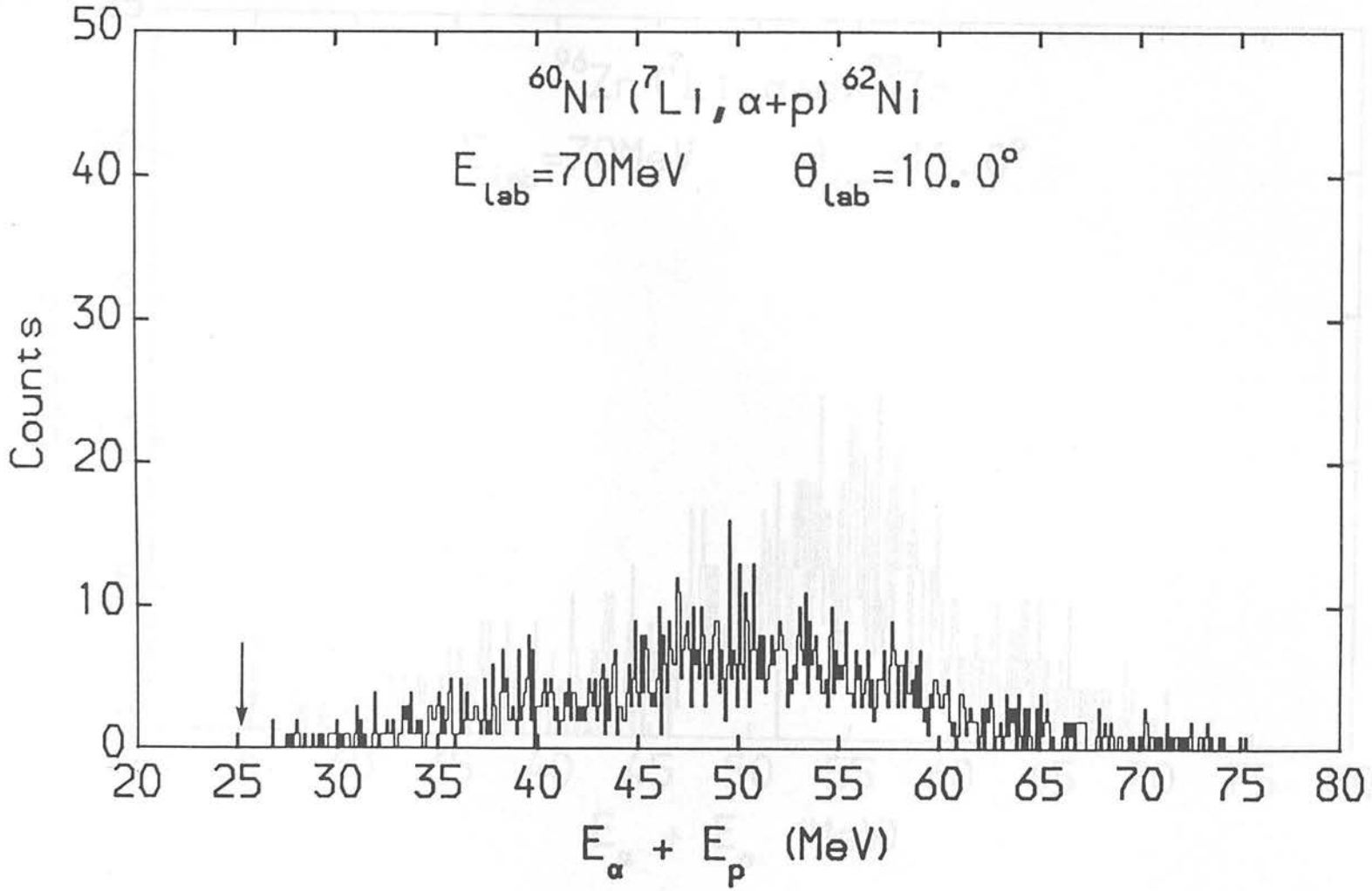

Figure 3.58: Summed energy spectrum for α-p coincidences from the reaction 70 MeV ^{7}Li + ^{60}Ni.

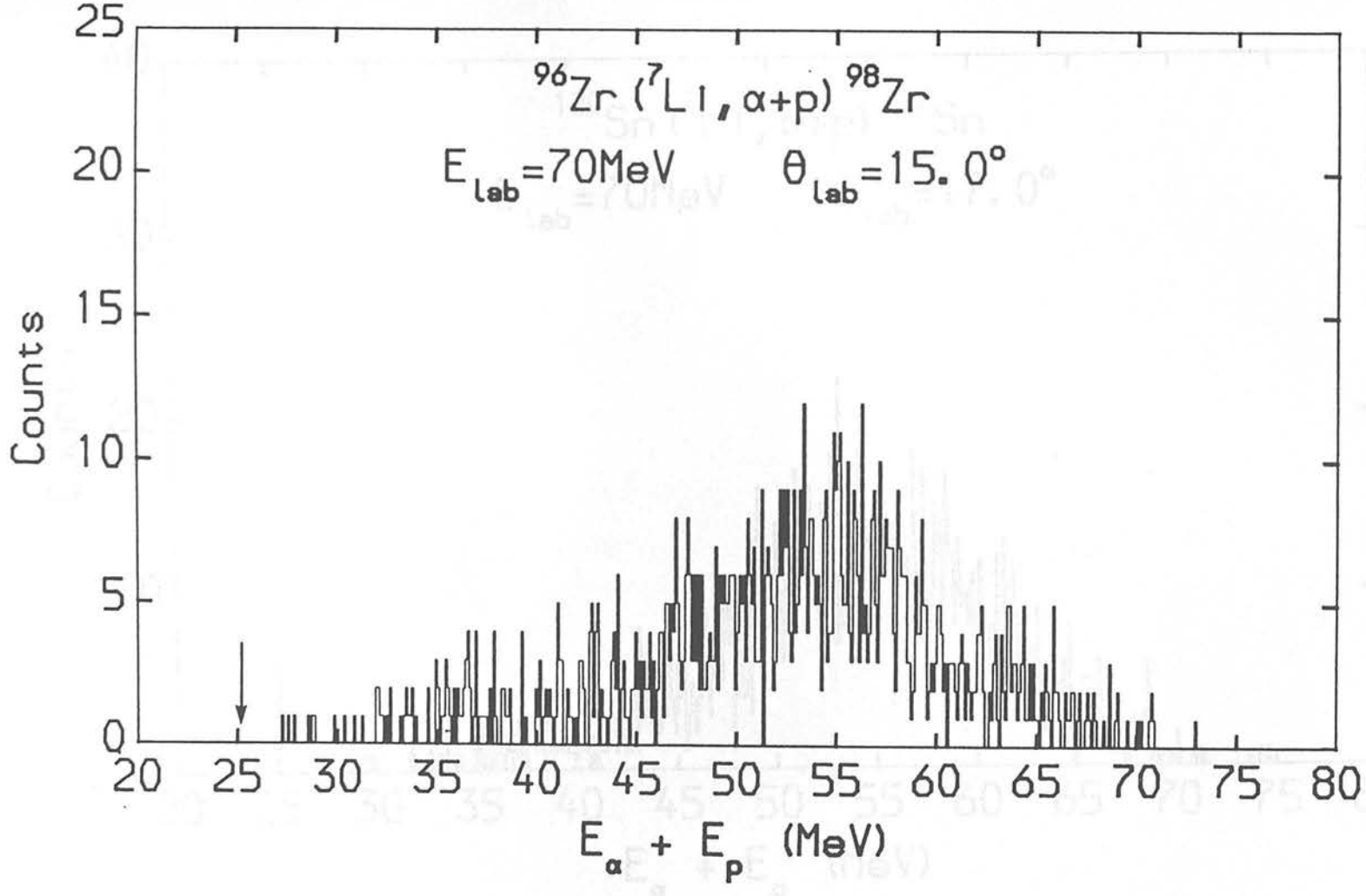

Figure 3.59: Summed energy spectrum for α-p coincidences from the reaction 70 MeV ^{7}Li + ^{96}Zr.

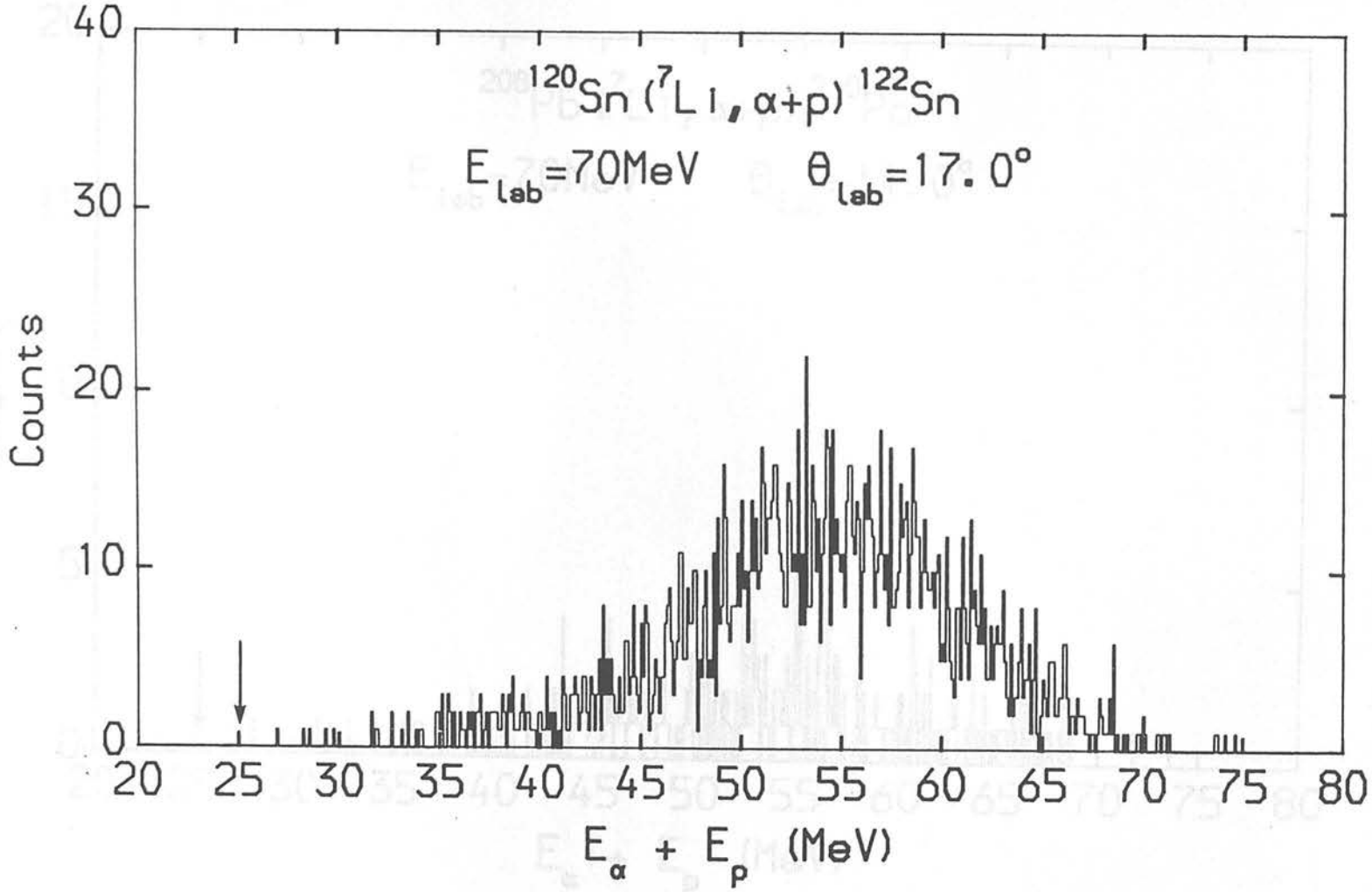

Figure 3.60: Summed energy spectrum for α-p coincidences from the reaction 70 MeV ^{7}Li + ^{120}Sn.

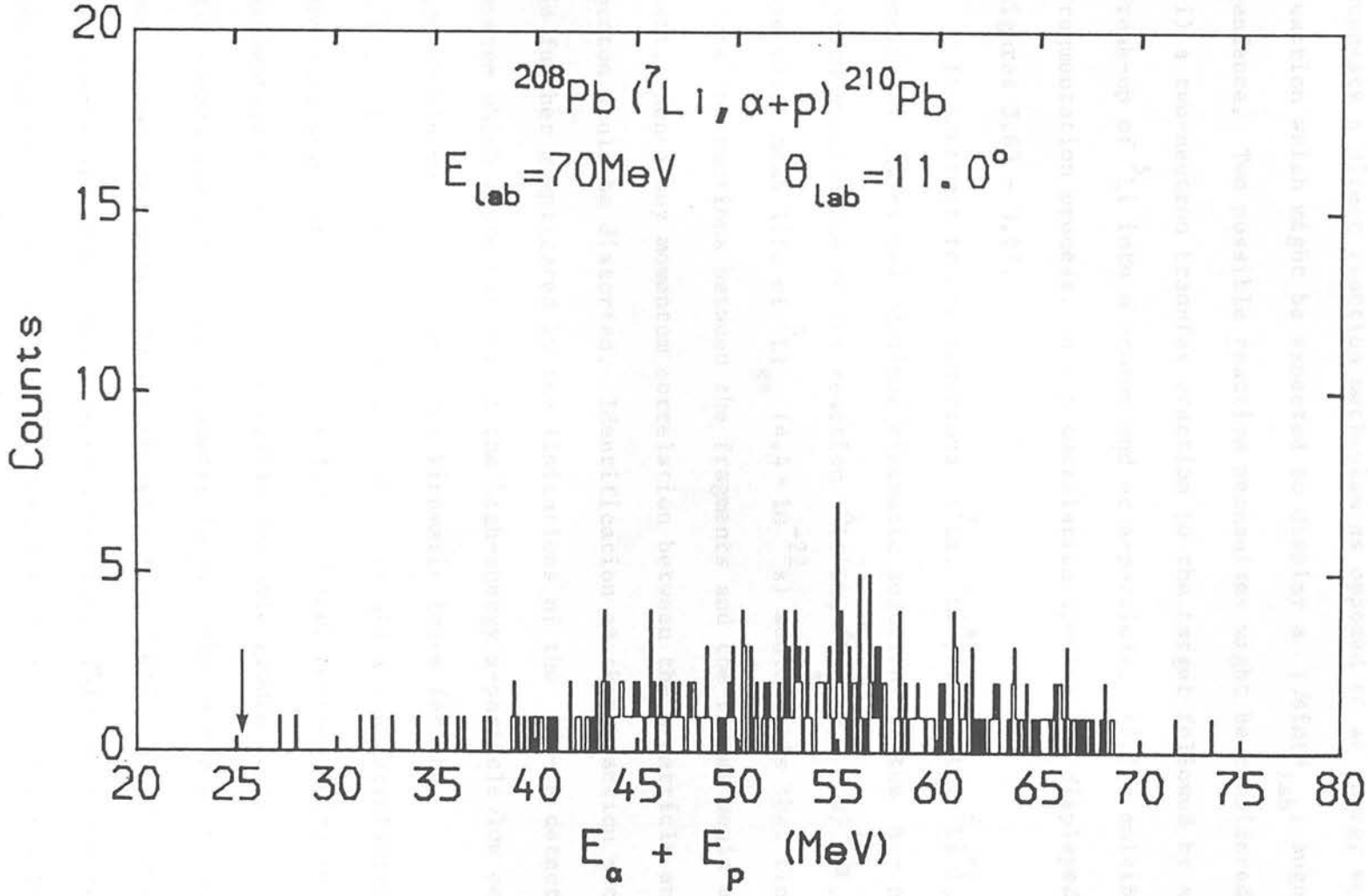

Figure 3.61: Summed energy spectrum for α-p coincidences from the reaction 70 MeV ^{7}Li + ^{208}Pb.

Discrete states were only identified for the reaction $^{7}Li + ^{12}C$ at $\theta_{lab.} = 10^{o}$. The angular distributions of the energy integrated double differential cross sections are shown in Figure 3.62 for all targets. Yield falls off exponentially with increasing laboratory angle. This suggests a direct reaction mechanism as opposed to an energy equilibrated reaction which might be expected to display a $1/\sin(\theta_{lab})$ angular dependence. Two possible reaction mechanisms might be considered: (i) a two-neutron transfer reaction to the target followed by sequential break-up of ^{5}Li into a proton and an α-particle, (ii) a multibody fragmentation process. α - p correlation spectra are displayed in Figures 3.63 - 3.67.

In contrast to the reactions $(^{7}Li, ^{7}Li^{*})$ and $(^{7}Li, ^{6}Li^{*})$, one would not expect well defined kinematic solutions in the α - p correlation spectra due to the reaction $^{A}X(^{7}Li, ^{5}Li_{gs} \rightarrow \alpha + p)^{A+2}X$, since the short mean life of $^{5}Li_{gs}$ $(4.4 \times 10^{-22}s)$ would imply that final state interactions between the fragments and the target would be important. Hence any momentum correlation between the α-particle and the proton would be distorted. Identification of this reaction mechanism is further complicated by the limitations of the ΔE - E detection system which could not detect the high-energy α-particle/low energy proton kinematic solution. The kinematic locus for the $(^{7}Li, ^{5}Li_{gs} \rightarrow \alpha + p)$ reaction is shown in all α - p correlation spectra, together with the $\varepsilon = 1.97$ MeV loci corresponding to the sequential break-up of the particle unstable ground state of ^{5}Li. All events are within the kinematic locus. The α - p coincidence events observed appear to lie on the $\varepsilon = 1.97$ MeV locus although the events are widely distributed in energy. This is consistent with the expectation of strong final state interactions affecting the

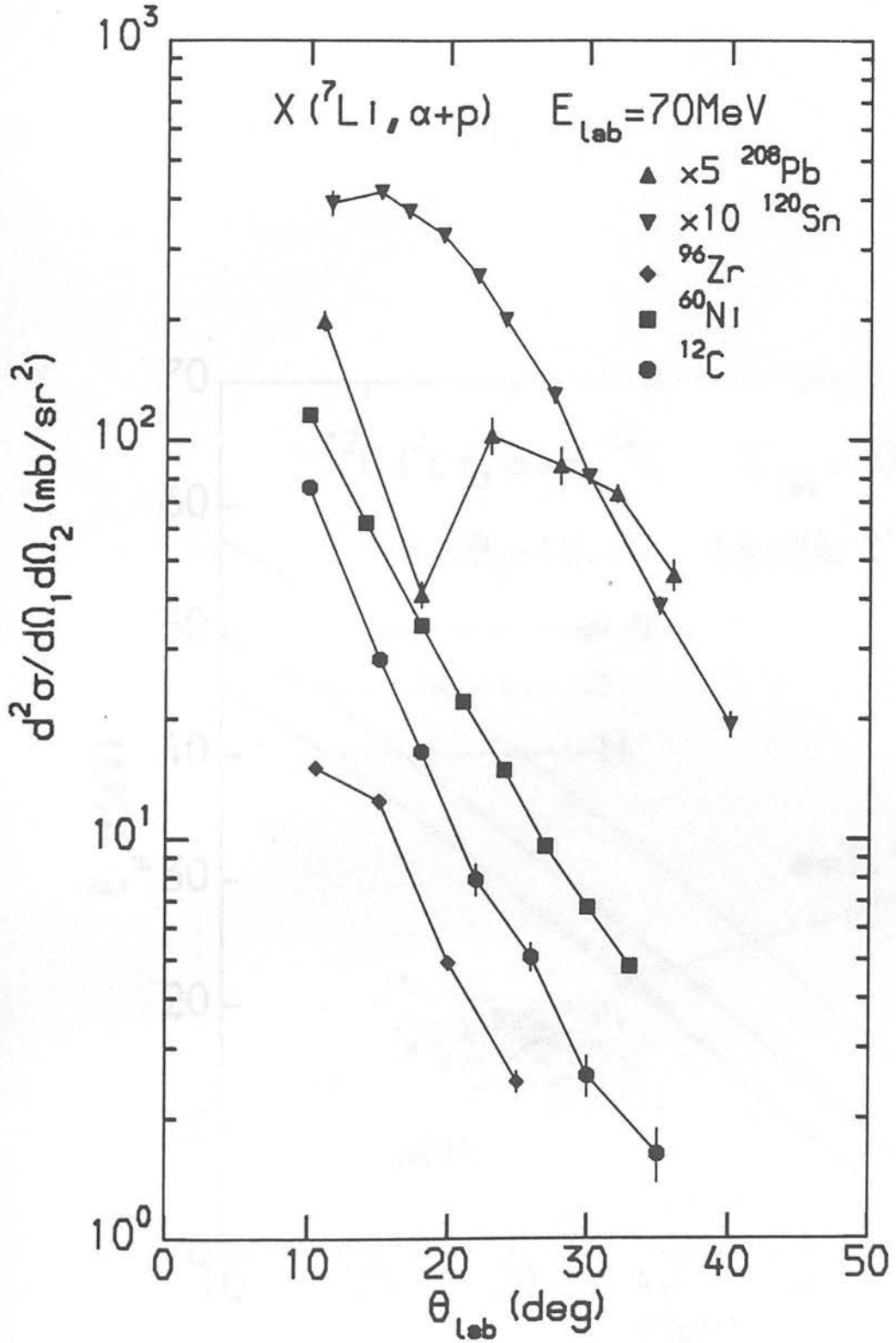

Figure 3.62: Angular distributions for α-p coincidences from 70 MeV ^{7}Li on ^{12}C, ^{60}Ni, ^{96}Zr, ^{120}Sn and ^{208}Pb.

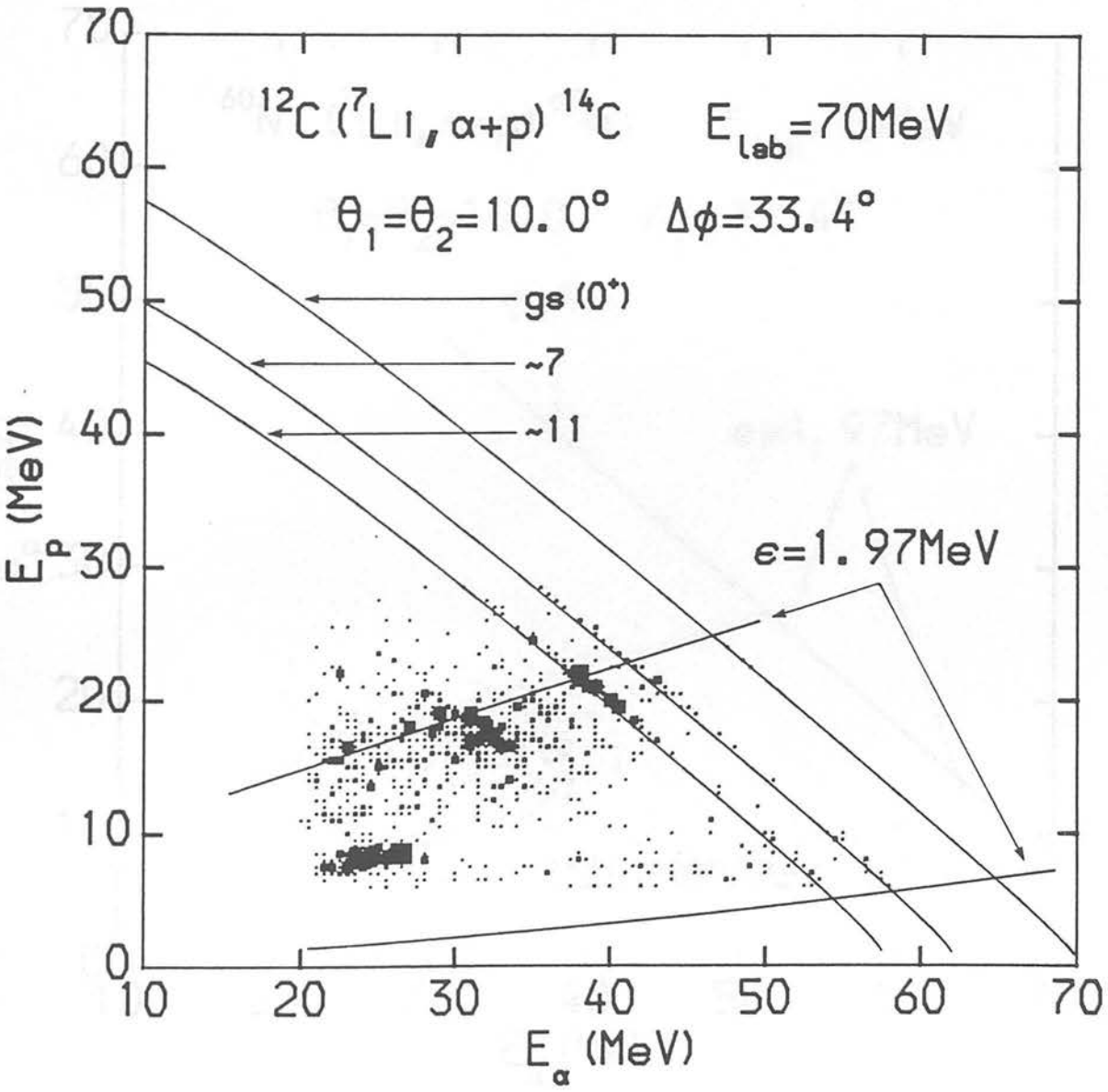

Figure 3.63: Two dimensional energy correlation spectrum for α-p coincidences from the reaction 70 MeV ^{7}Li + ^{12}C. The kinematic locus for the ground state of ^{14}C is shown. Locii corresponding to ϵ = 1.97 MeV are also shown.

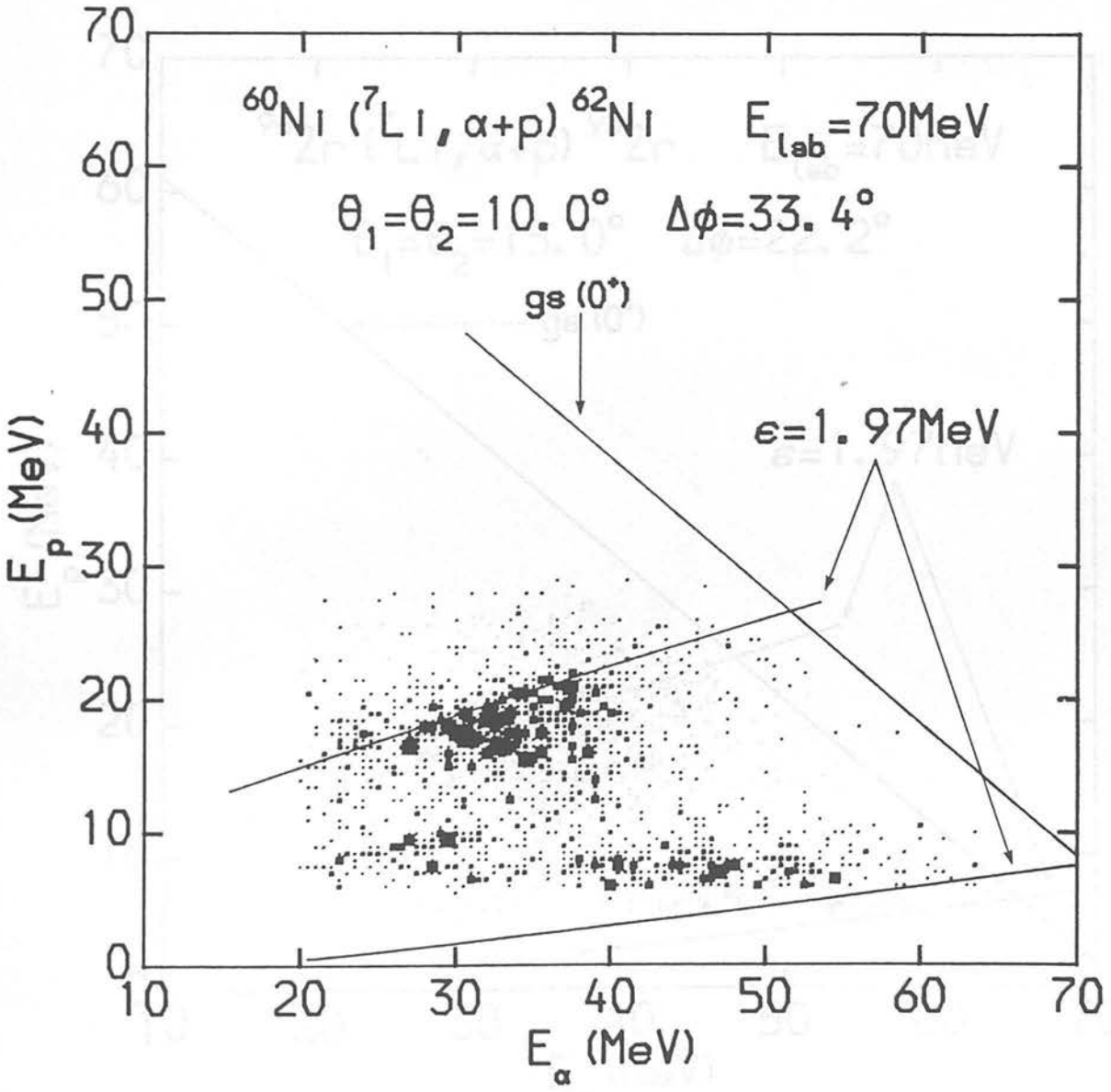

Figure 3.64: Two dimensional energy correlation spectrum for α-p coincidences from the reaction 70 MeV ^{7}Li + ^{60}Ni. The kinematic locus for the ground state of ^{62}Ni is shown. Locii corresponding to ε = 1.97 MeV are also shown.

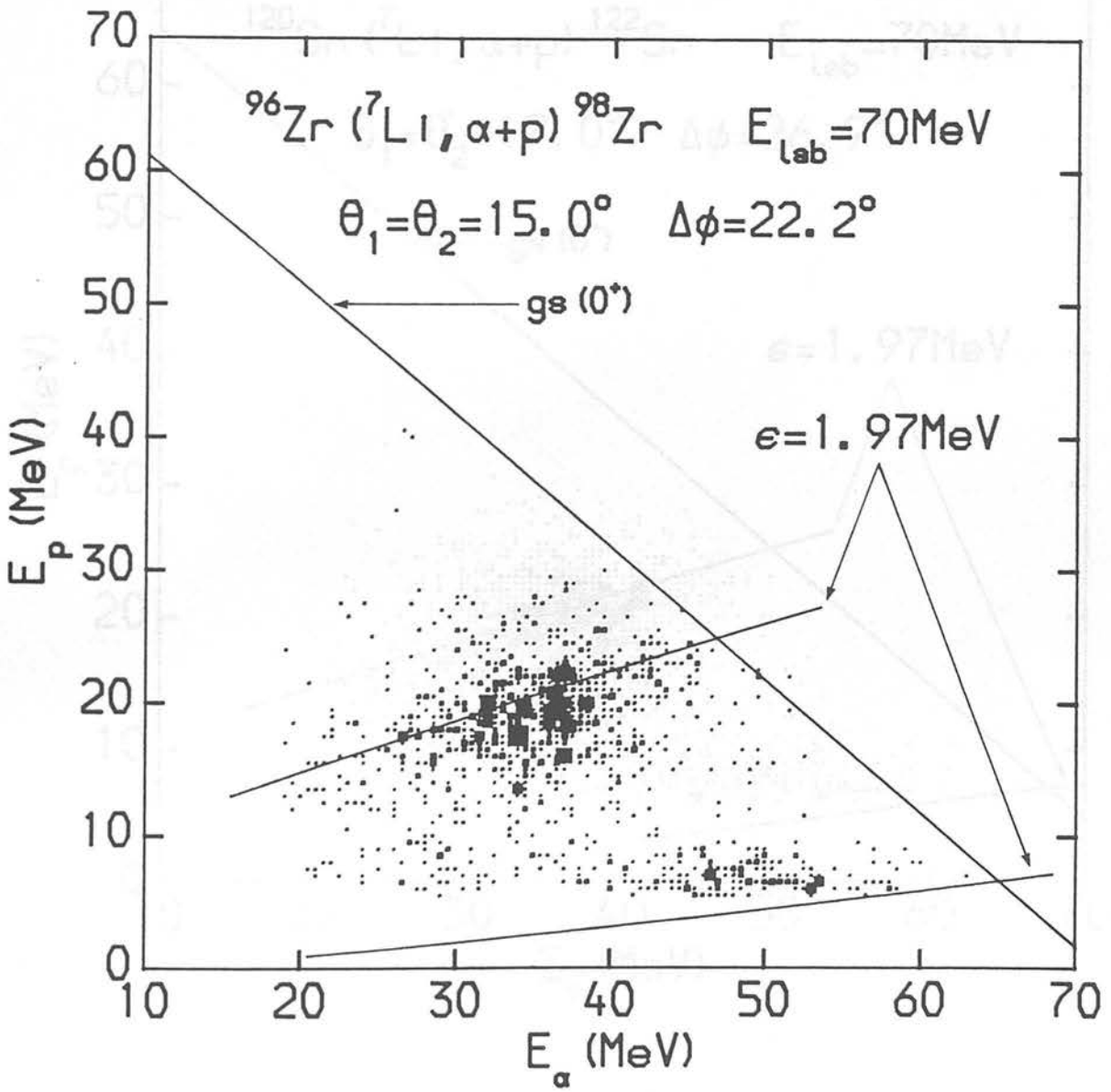

Figure 3.65: Two-dimensional energy correlation spectrum for α-p coincidences from the reaction 70 MeV ^{7}Li + ^{96}Zr. The kinematic locus for the ground state of ^{98}Zr is shown. Locii corresponding to ε = 1.97 MeV are also shown.

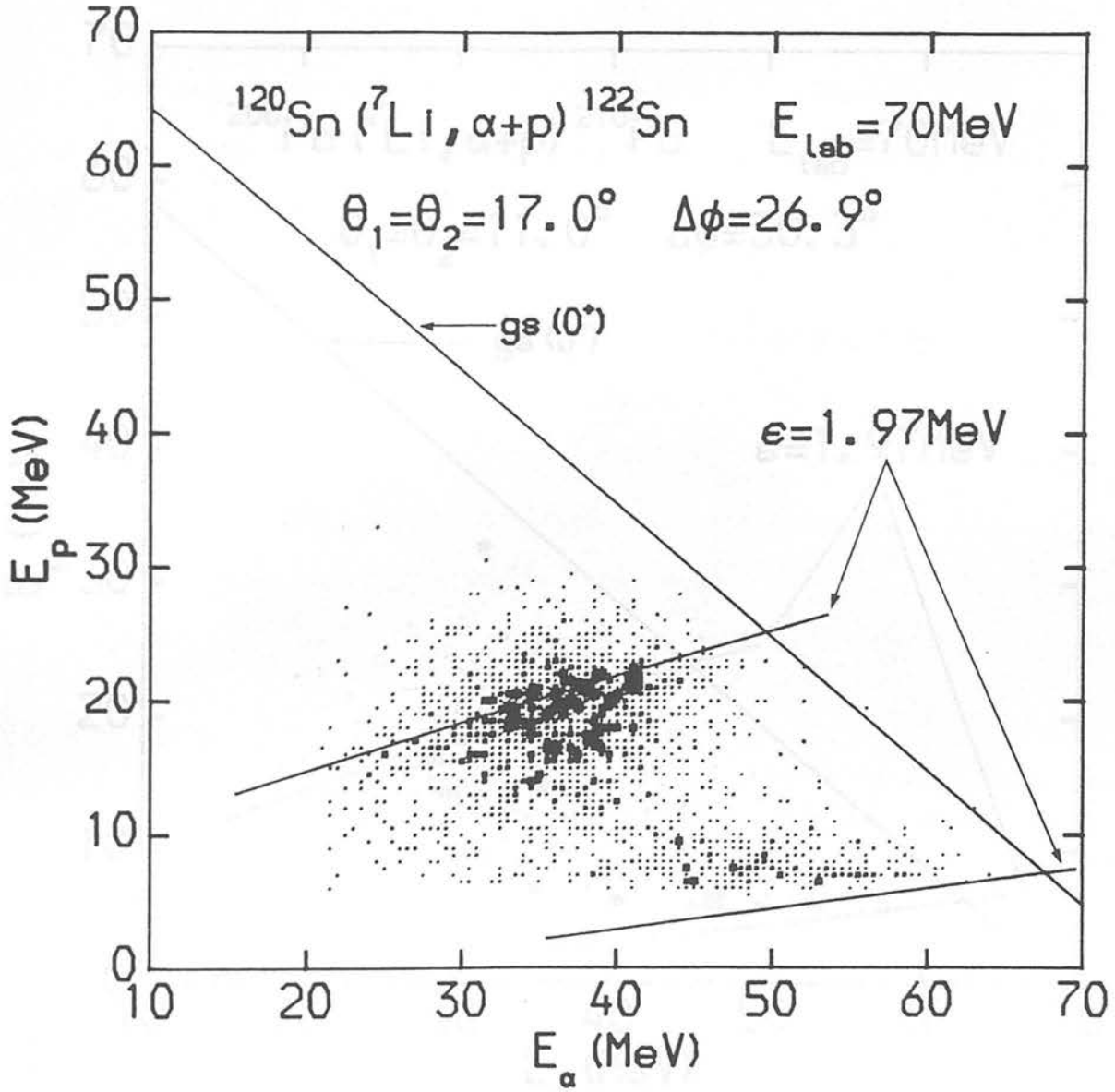

Figure 3.66: Two-dimensional energy correlation spectrum for α-p coincidences from the reaction 70 MeV ^{7}Li + ^{120}Sn. The kinematic locus for the ground state of ^{122}Sn is shown. Loci corresponding to ε = 1.97 MeV are also shown.

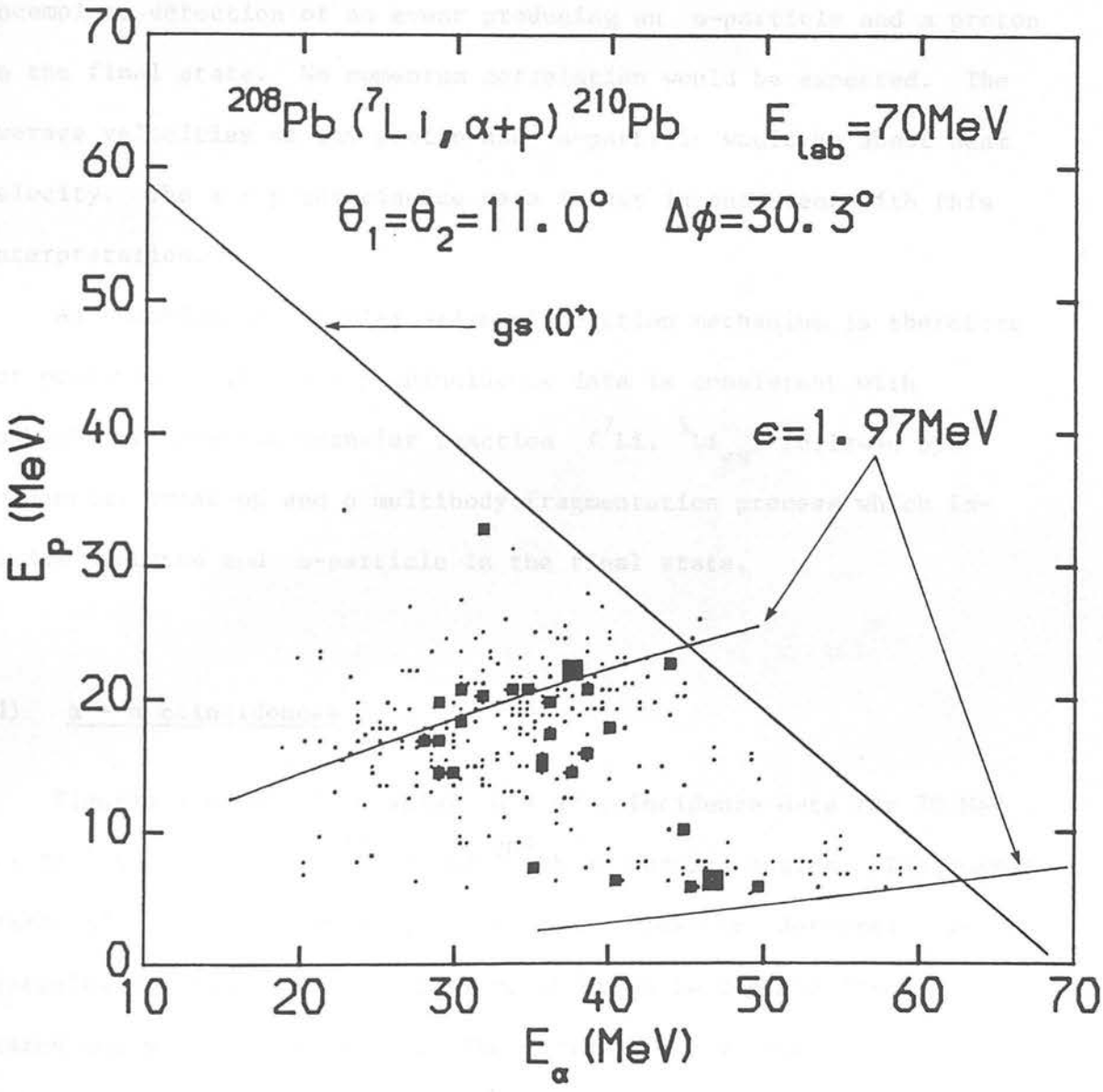

Figure 3.67: Two-dimensional energy correlation spectrum for α-p coincidences from the reaction 70 MeV ^{7}Li + ^{208}Pb. The kinematic locus for the ground state of ^{210}Pb is shown. Locii corresponding to ε = 1.97 MeV are also shown.

momentum correlation of the sequential reaction process. The absence of discrete transitions probably reflects kinematic effects. Optimum transfer probability being associated with Q-values corresponding to high excitation energies in the residual nucleus where the density of states is high and individual states are not resolved.

A multibody fragmentation process would result in the kinematically incomplete detection of an event producing an α-particle and a proton in the final state. No momentum correlation would be expected. The average velocities of the proton and α-particle would be about beam velocity. The α - p coincidence data is not inconsistent with this interpretation.

An unambiguous identification of reaction mechanism is therefore not possible. The α - p coincidence data is consistent with both the two neutron transfer reaction (^{7}Li, ^{5}Li$_{gs}$) followed by sequential break-up and a multibody fragmentation process which includes a proton and α-particle in the final state.

(d) α - α coincidences

Figures 3.68 - 3.72 display α - α coincidence data for 70 MeV ^{7}Li on ^{12}C, ^{60}Ni, ^{96}Zr, ^{120}Sn and ^{208}Pb at forward angles. The summed energy of coincident events in which both telescopes detected α-particles is shown. All spectra are observed to contain discrete states and a continuum region. The minimum α + α energy observable with the ΔE - E telescopes used in this study is indicated by the arrows in the low energy region of each spectrum. The discrete states are identifiable as states of a recoil nucleus following proton transfer to the projectile, i.e. $^{A}_{Z}X(^{7}Li, ^{8}Be \rightarrow \alpha + \alpha)^{A+1}_{Z+1}X$. α - α correlation

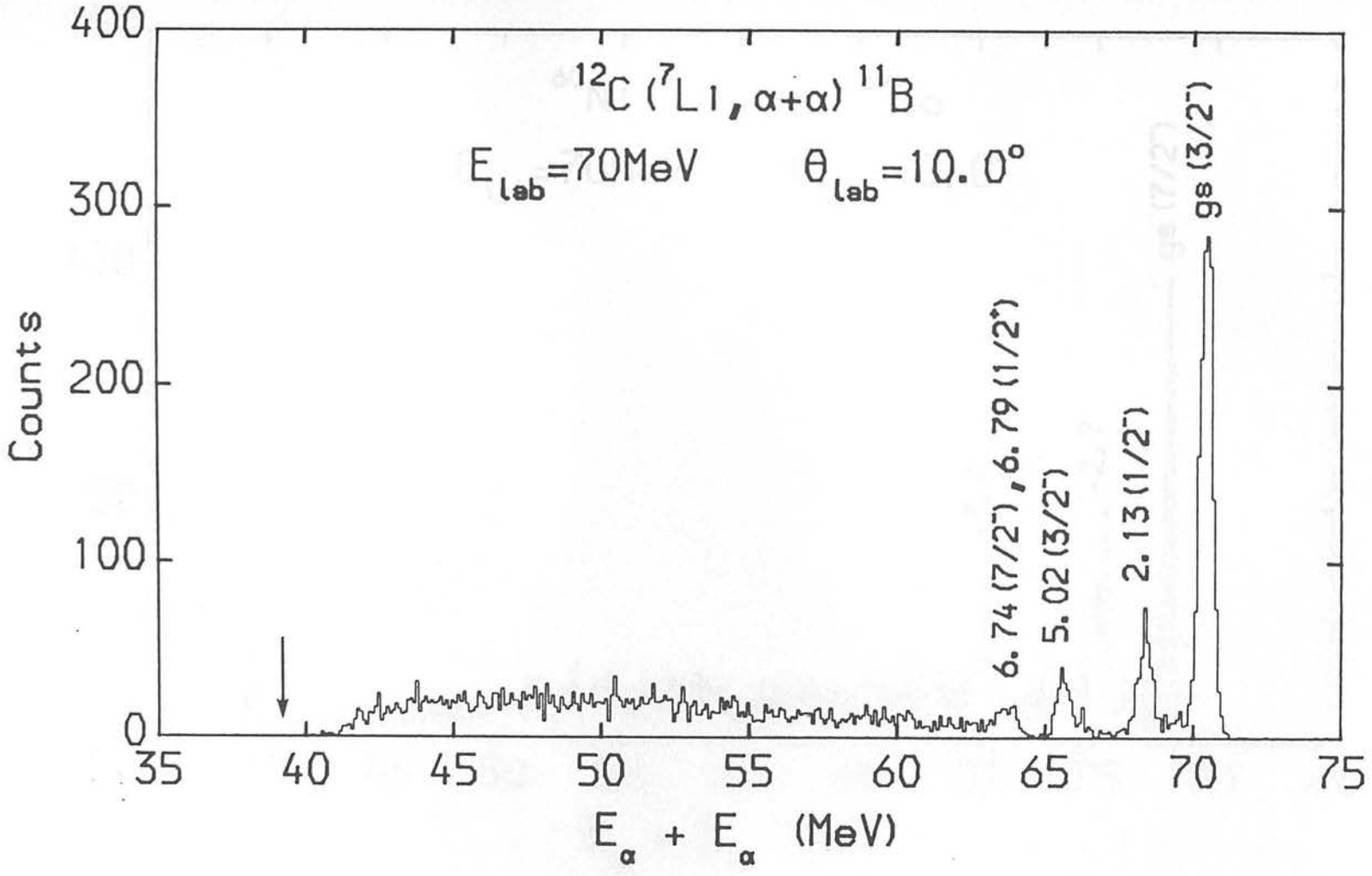

Figure 3.68: Summed energy spectrum for α-α coincidences from the reaction 70 MeV ^{7}Li + ^{12}C.

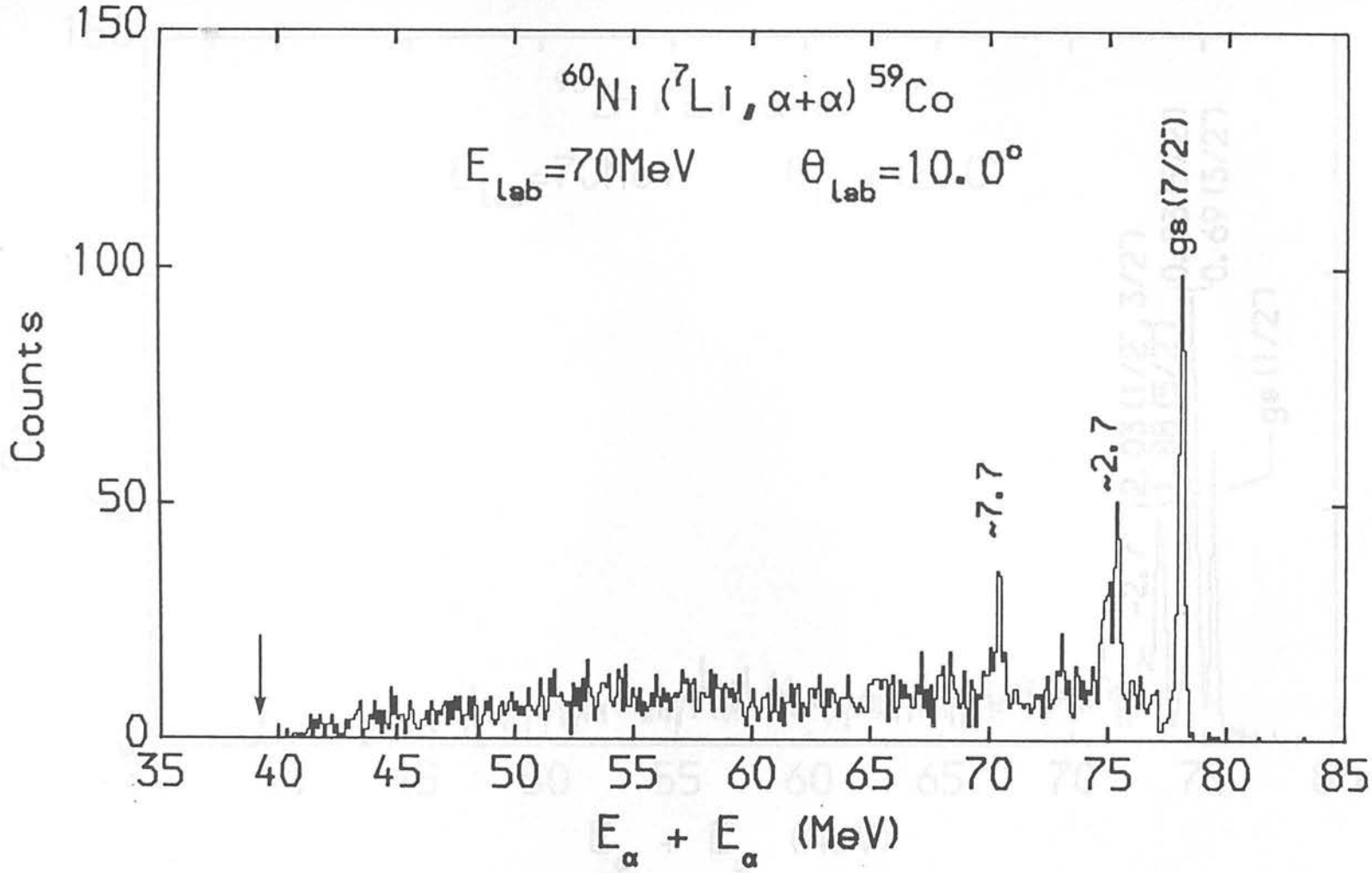

Figure 3.69: Summed energy spectrum for α-α coincidences from the reaction 70 MeV ^{7}Li + ^{60}Ni.

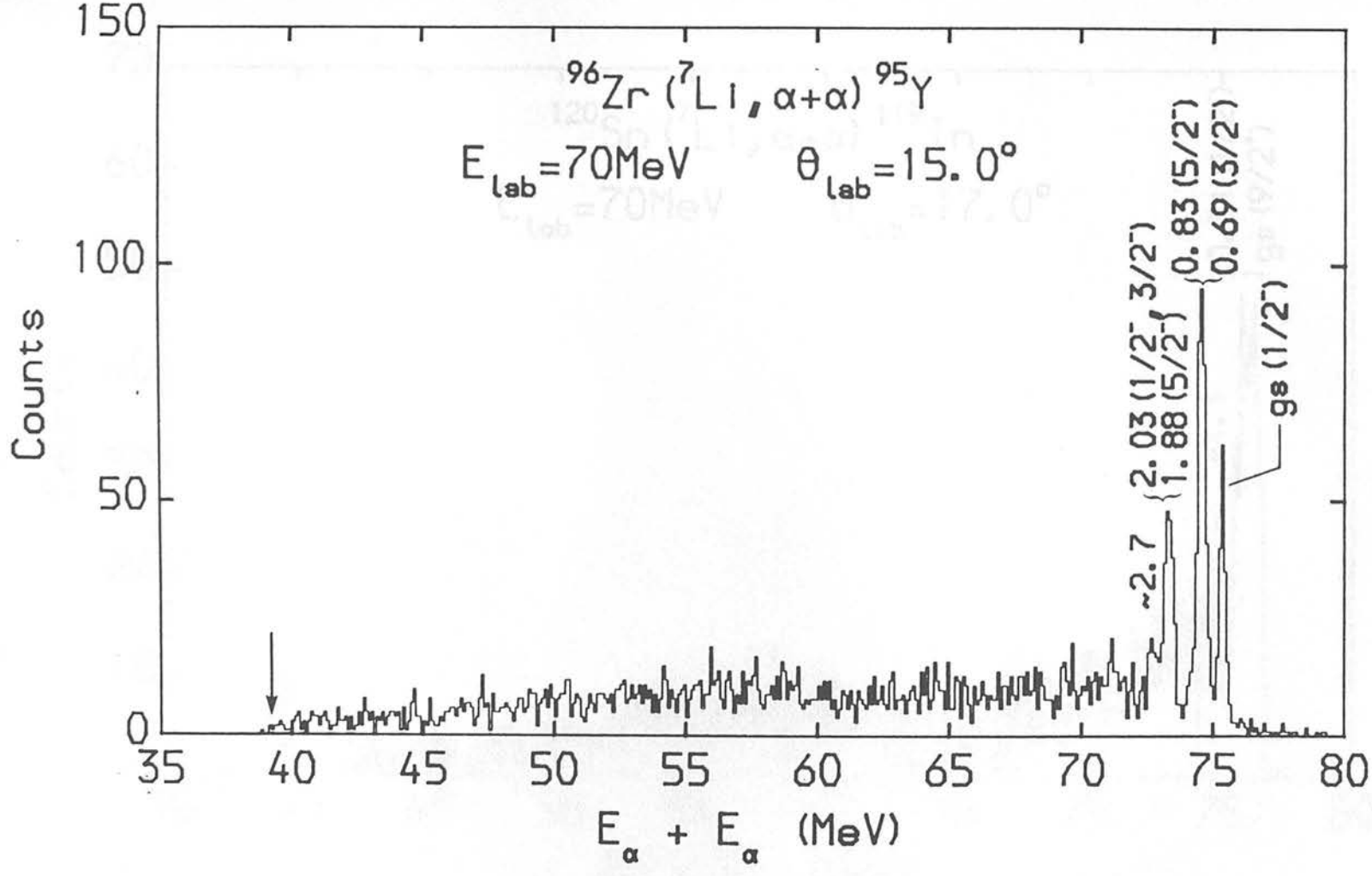

Figure 3.70: Summed energy spectrum for α-α coincidences from the reaction 70 MeV ^{7}Li + ^{96}Zr.

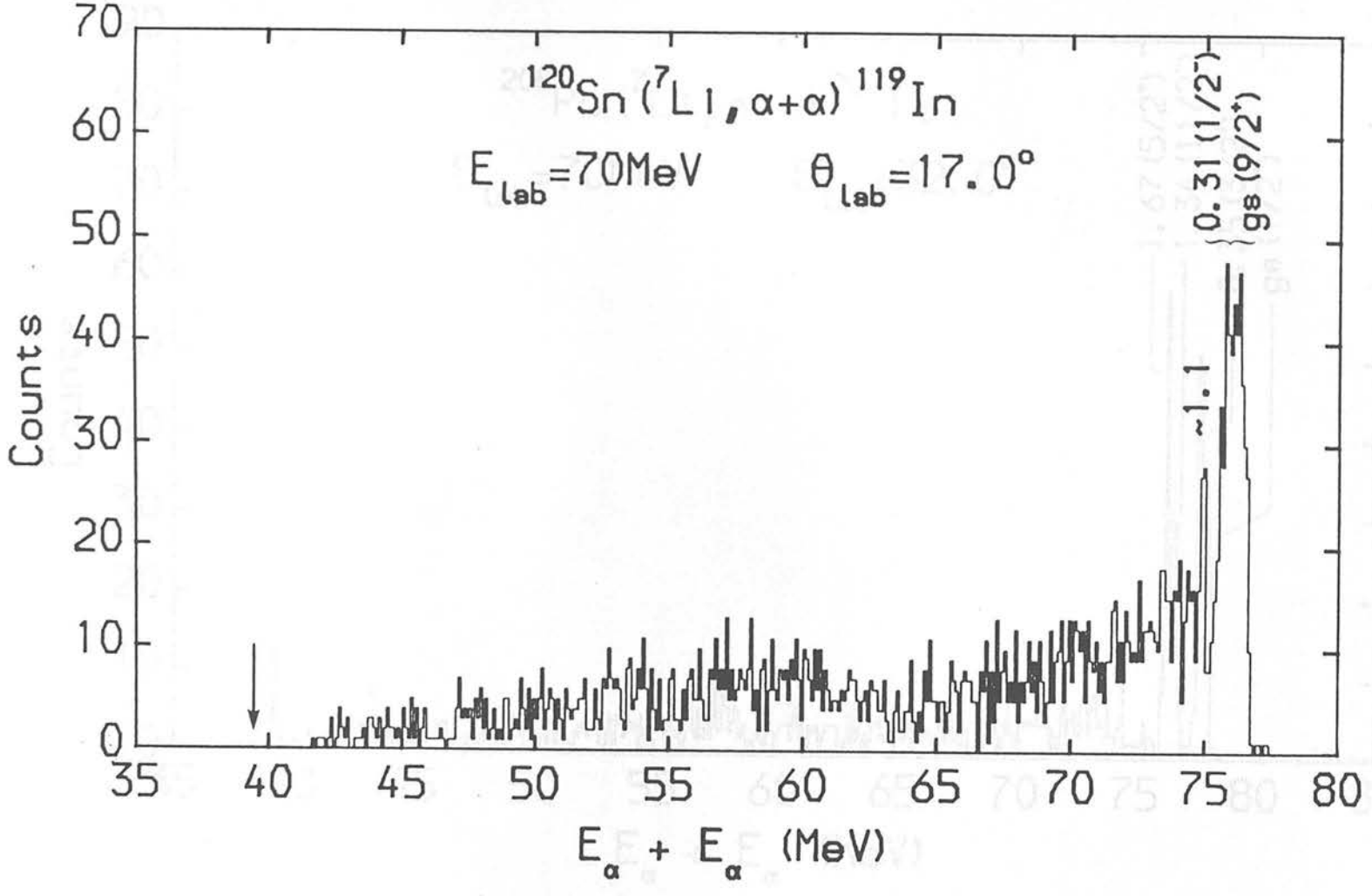

Figure 3.71: Summed energy spectrum for α-α coincidences from the reaction 70 MeV ^{7}Li + ^{120}Sn.

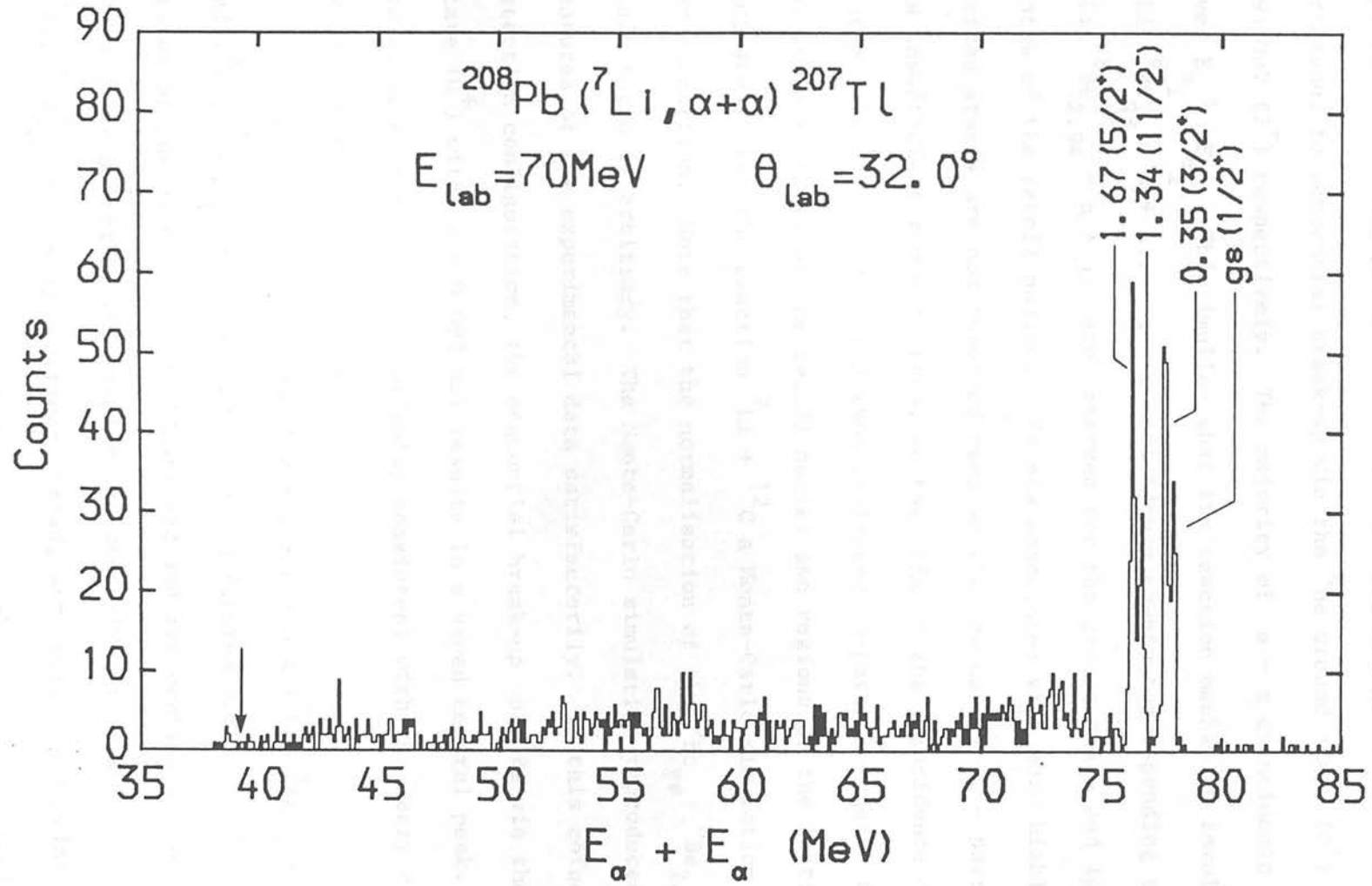

Figure 3.72: Summed energy spectrum for α-α coincidences from the reaction 70 MeV ^{7}Li + ^{208}Pb.

spectra are shown in Figures 3.73 - 3.77. The kinematic loci for the reaction (^{7}Li, ^{8}Be $\rightarrow \alpha + \alpha$) are shown for each target. In addition, the loci for ε = 0.092 MeV and ε = 3.03 MeV are shown. These values of ε correspond to sequential break-up via the ^{8}Be ground state (0^+) and 2.94 MeV (2^+) respectively. The majority of $\alpha - \alpha$ coincidence events have $E_{\alpha_1} \approx E_{\alpha_2}$. This implies that the reaction mechanism involved is (^{7}Li, ^{8}Be$_{gs} \rightarrow \alpha + \alpha$). $\alpha - \alpha$ coincidence events corresponding to (^{7}Li, ^{8}Be$_{2.94} \rightarrow \alpha + \alpha$) are observed for the ground state and low-lying states of the recoil nucleus. Events associated with more highly excited states are not observed because the low energy α - particle has insufficient range to traverse the ΔEs of the coincidence detection system. Figures 3.78 - 3.82 show projected α-particle energy spectra for various states of the recoil nuclei and regions of the continuum indicated. For the reaction ^{7}Li + ^{12}C a Monte-Carlo simulation is shown for comparison. Note that the normalisation of the ^{8}Be$_{gs}$: ^{8}Be$_{2.94}$ yield ratio is arbitrary. The Monte-Carlo simulation reproduces the features of the experimental data satisfactorily. In this coincidence detection configuration, the sequential break-up of ^{8}Be via the ground state (0^+) with ε = 0.092 MeV results in a broad central peak. The broad, weak bumps are kinematically consistent with the decay of the broad 2.94 MeV (2^+) state of ^{8}Be.

The angular distributions for the reactions (^{7}Li, ^{8}Be$_{gs} \rightarrow \alpha + \alpha$) and (^{7}Li, ^{8}Be$^*_{2.94} \rightarrow \alpha + \alpha$) are shown in Figures 3.83 - 3.87 for the states of the recoil nucleus identified and the continuum. Qualitatively the angular distributions display features similar to the (^{7}Li, ^{6}Li$^*_{2.18} \rightarrow$ a + d) reaction: broad, structureless angular distributions peaked near the grazing angle. It should be noted that some angular distributions probably contain contributions from two or more

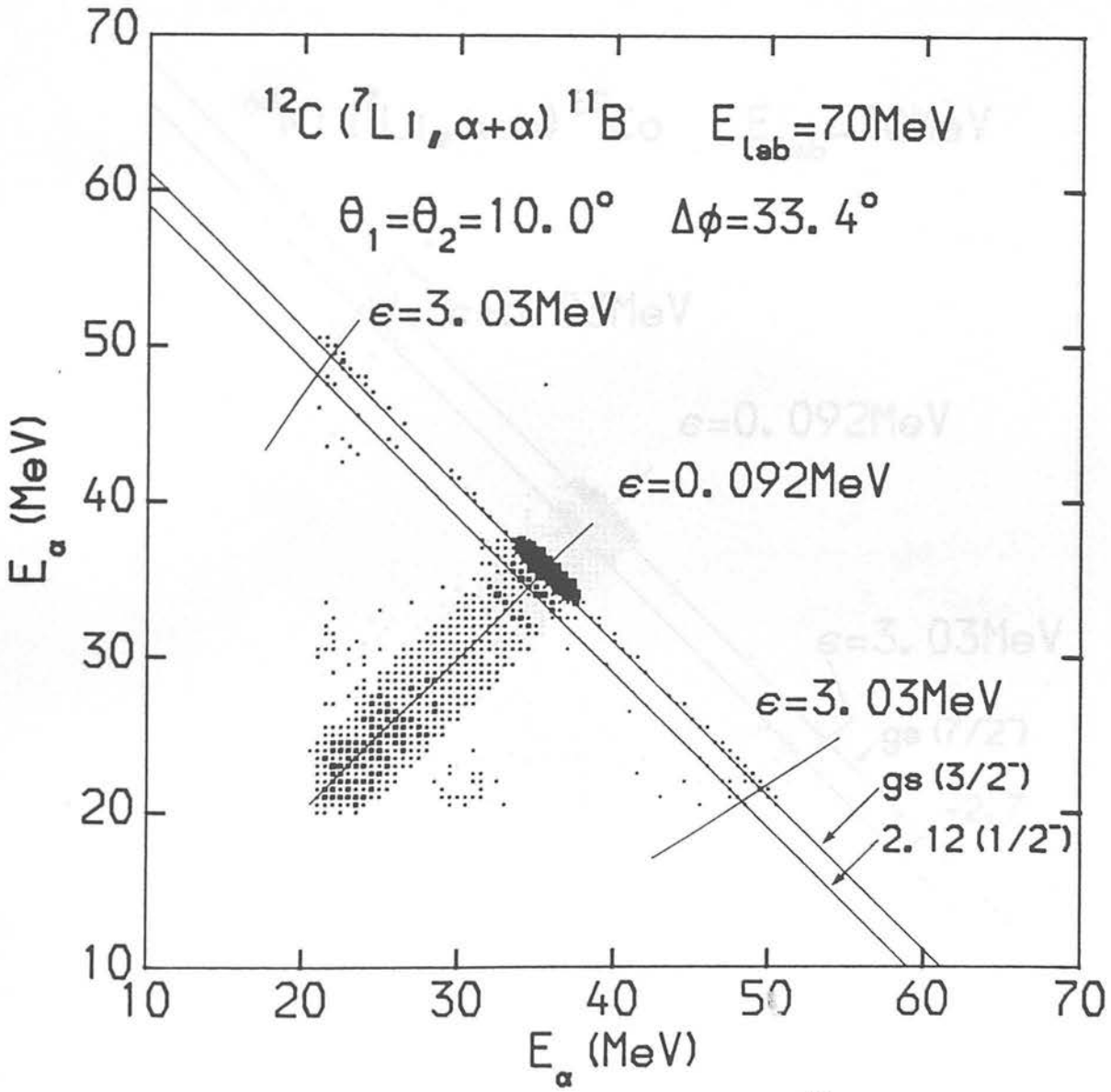

Figure 3.73: Two-dimensional energy correlation spectrum for α-α coincidences from the reaction 70 MeV ^{7}Li + ^{12}C. The kinematic locus for the ground state of ^{11}B is shown. Loci corresponding to ϵ = 0.092 MeV and ϵ = 3.03 MeV are also shown.

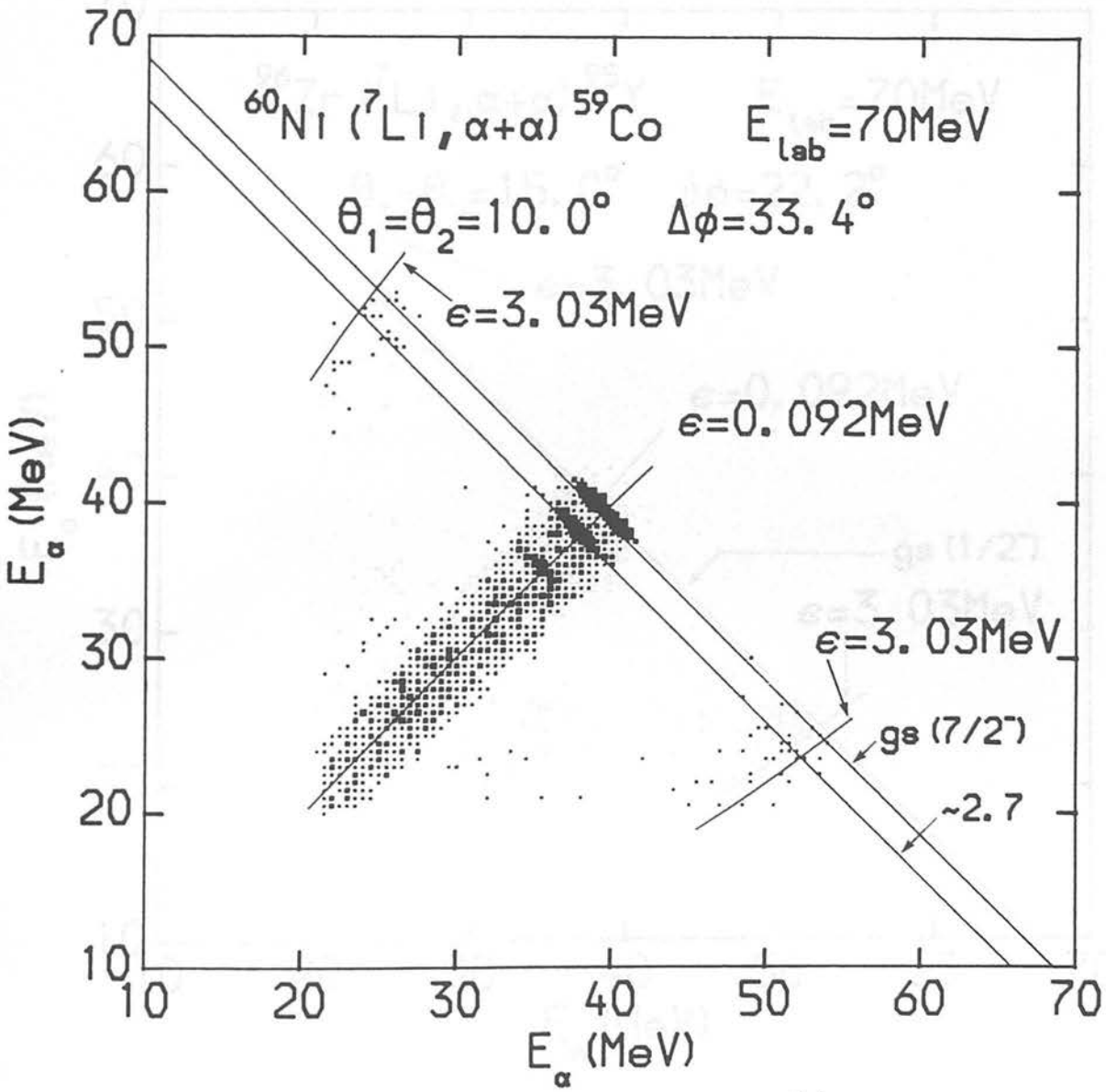

Figure 3.74: Two-dimensional energy correlation spectrum for α-α coincidences from the reaction 70 MeV ^{7}Li + ^{60}Ni. The kinematic locus for the ground state of ^{59}Co is shown. Loci corresponding to ε = 0.092 MeV and ε = 3.03 MeV are also shown.

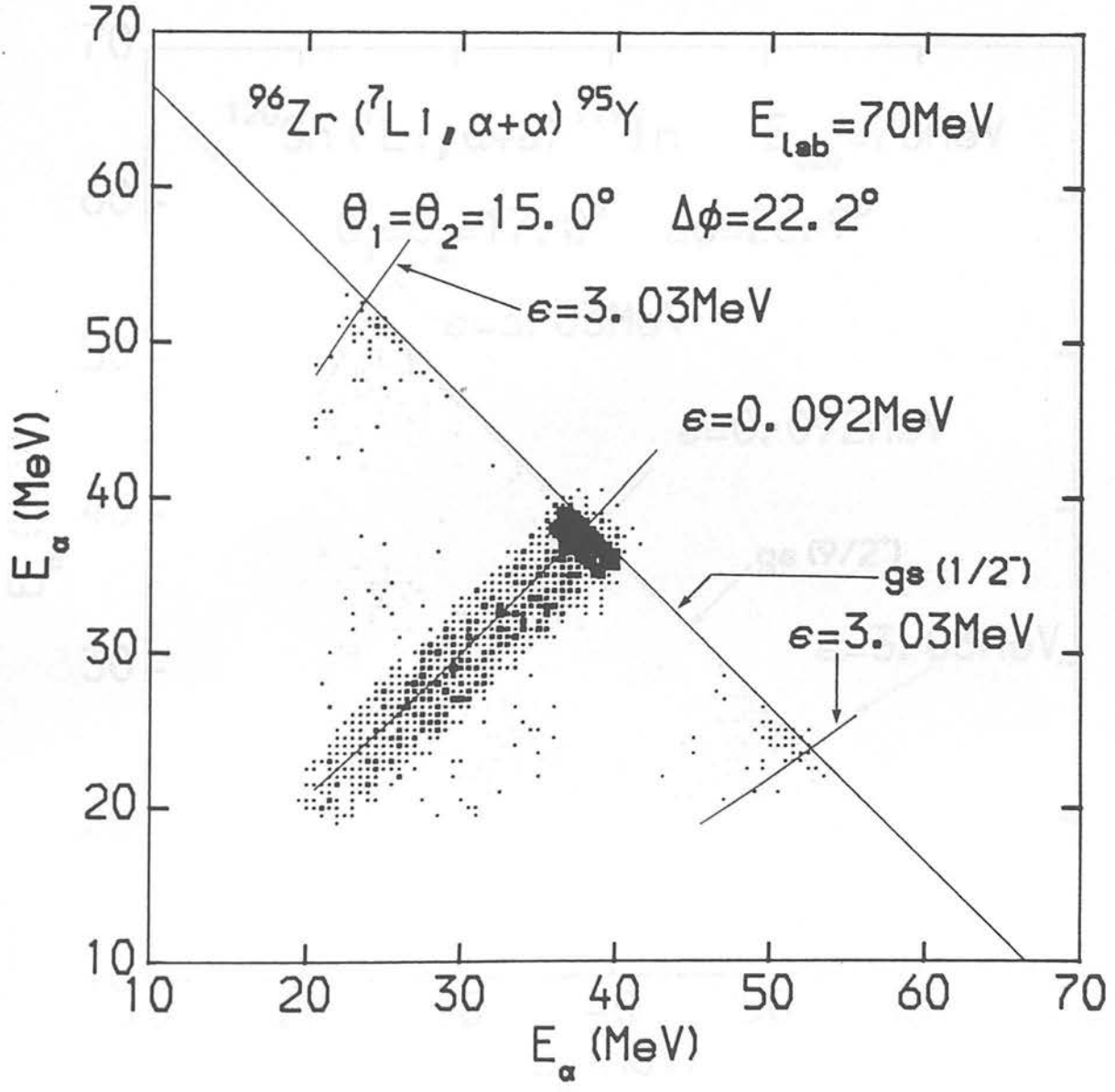

Figure 3.75: Two-dimensional energy correlations spectrum for α-α coincidences from the reaction 70 MeV ^{7}Li + ^{96}Zr. The kinematic locus for the ground state of ^{95}Y is shown. Locii corresponding to ε = 0.092 MeV and ε = 3.03 MeV are also shown.

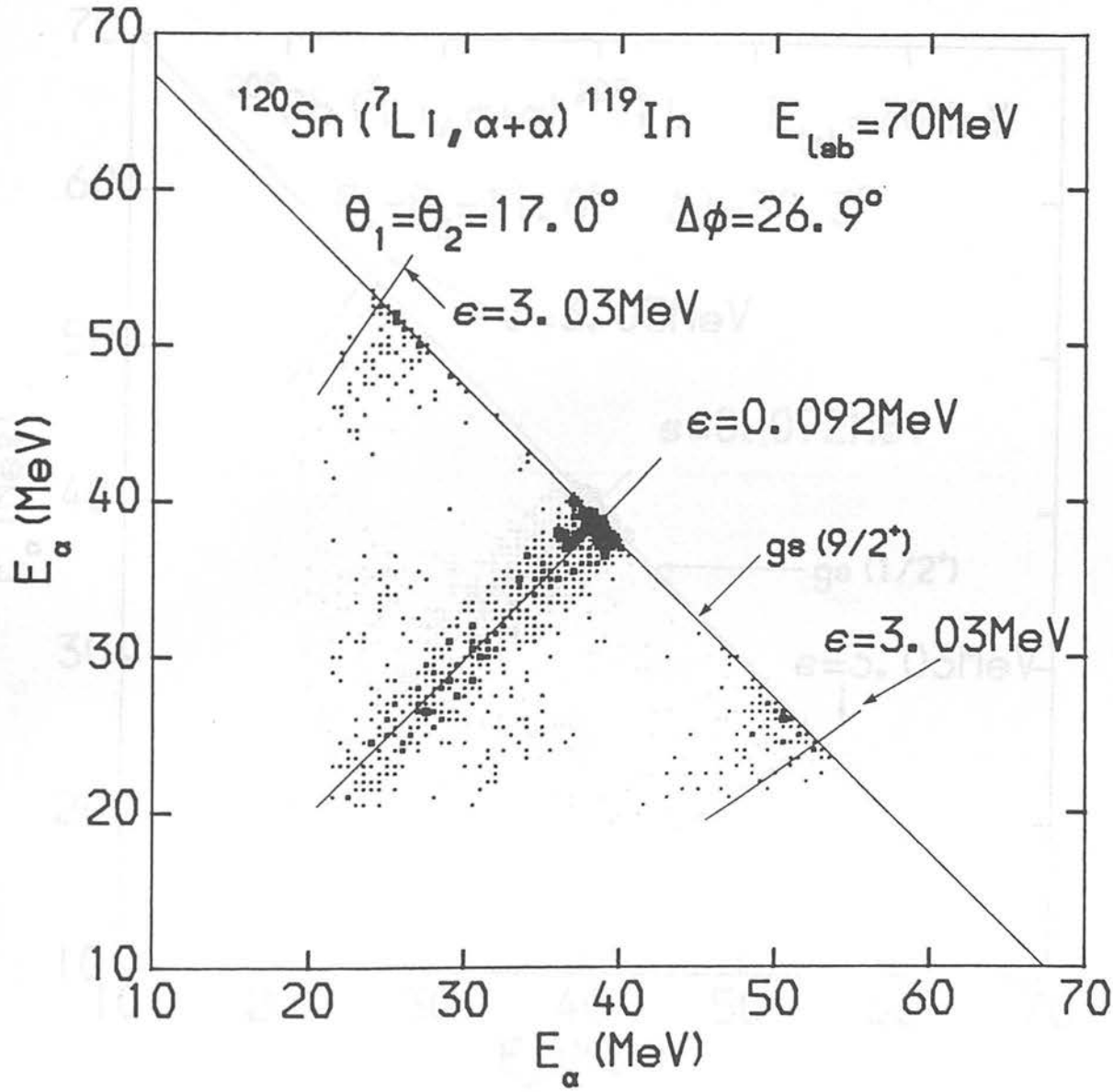

Figure 3.76: Two-dimensional and energy correlation spectrum for α-α coincidences from the reaction 70 MeV ^{7}Li + ^{120}Sn. The kinematic locus for the ground state of ^{119}In is shown. Locii corresponding to ε = 0.092 MeV and ε = 3.03 MeV are also shown.

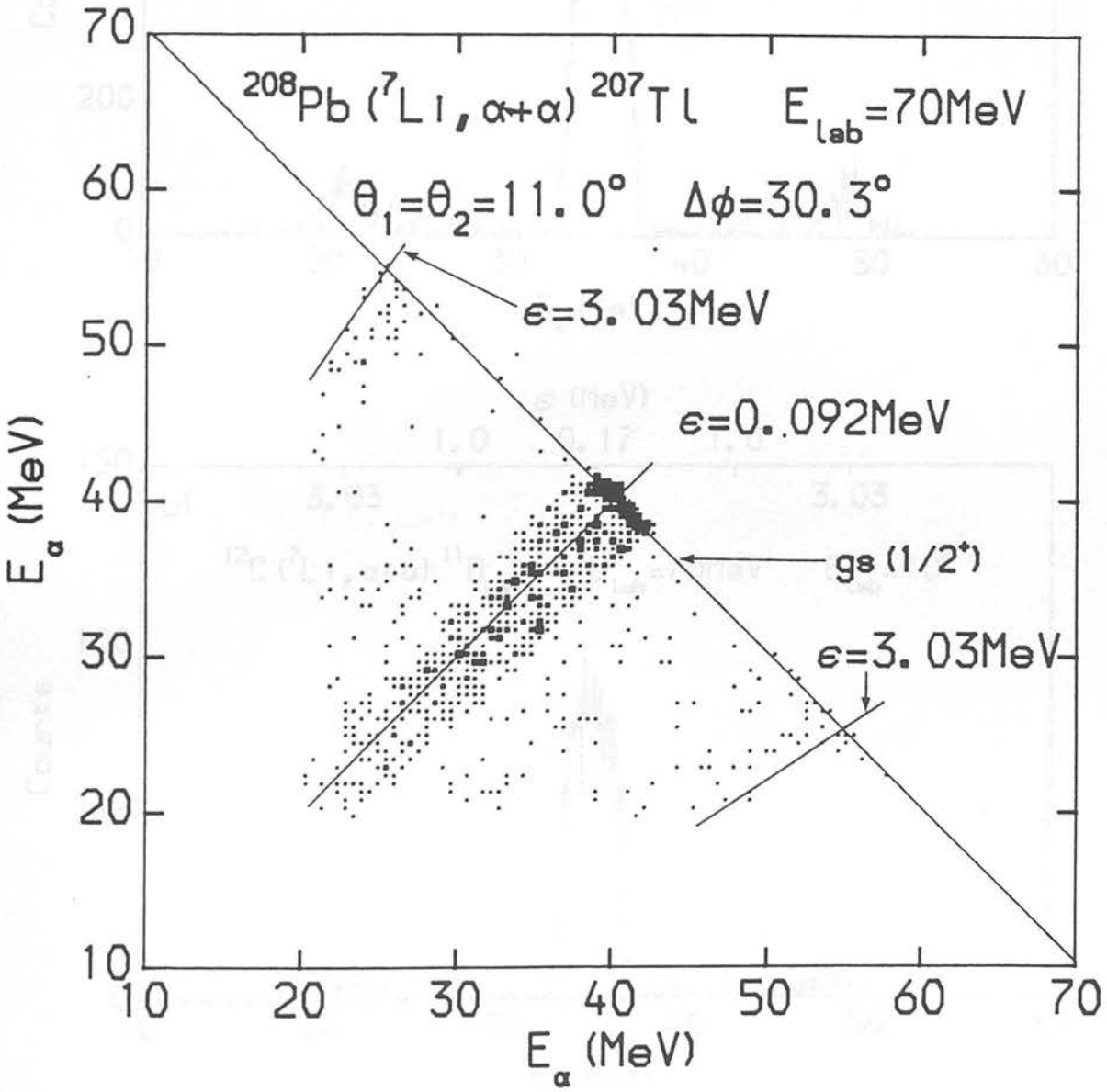

Figure 3.77: Two-dimensional energy correlation spectrum for α-α coincidences from the reaction 70 MeV ^{7}Li + ^{208}Pb. The kinematic locus for the ground state of ^{207}Tl is shown. Locii corresponding to ε = 0.092 MeV and ε = 3.03 MeV, are also shown.

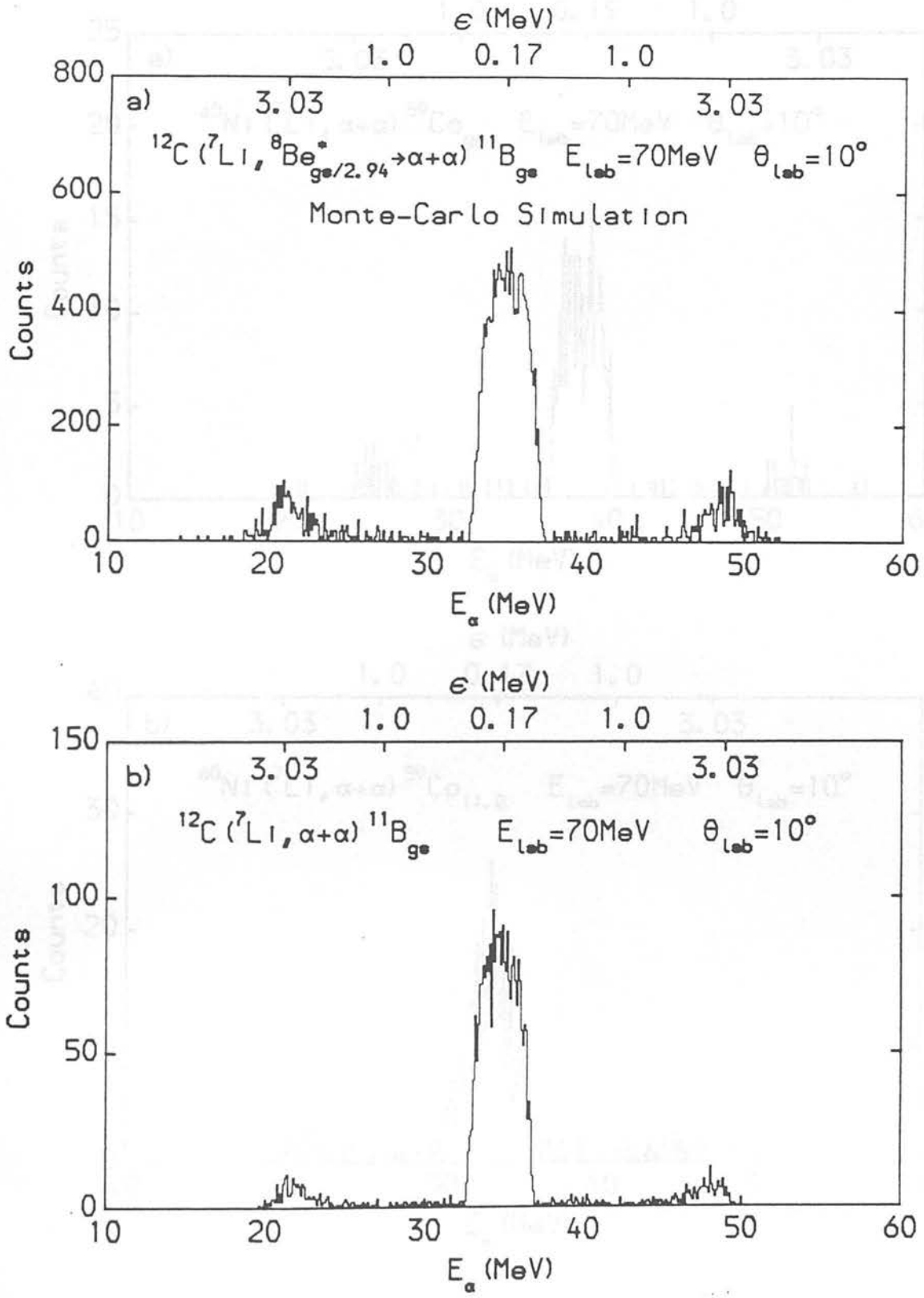

Figure 3.78: a) Monte-Carlo simulation of projected α energy spectrum for the reactions $^{12}C(^{7}Li, ^{8}Be_{gs} \rightarrow \alpha+\alpha)^{11}B_{gs}$ and $^{12}C(^{7}Li, ^{8}Be^{*}_{2.94} \rightarrow \alpha+\alpha)^{11}B_{gs}$.

b) Projected α energy spectrum for α+α coincidences corresponding to the ground state of ^{11}B.

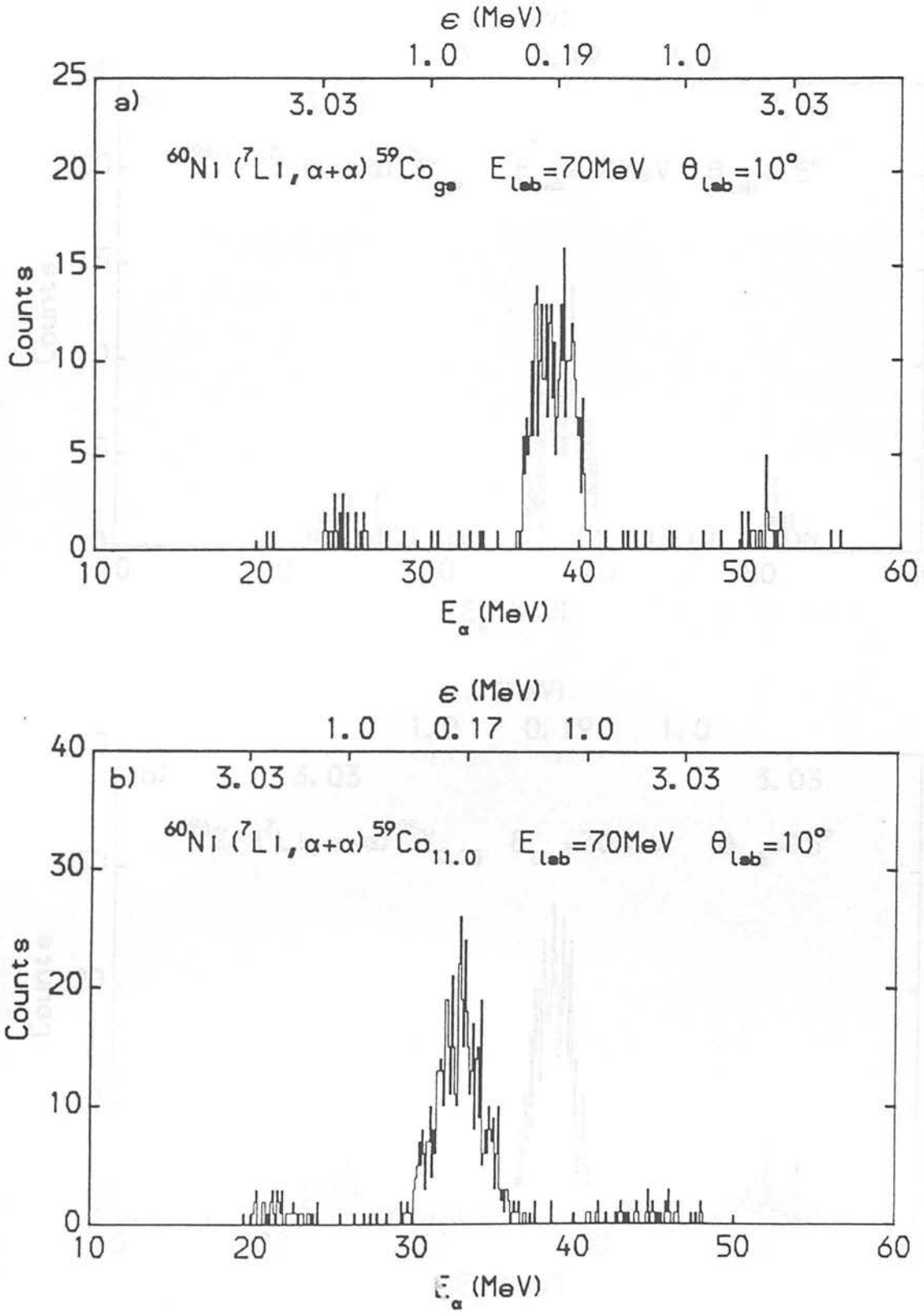

Figure 3.79: Projected α energy spectra for α-α coincidences corresponding to

a) the ground state of ^{59}Co and,

b) 63 MeV $\lesssim E_\alpha + E_\alpha \lesssim$ 68 MeV $- E_x$ (^{59}Co) $\sim$ 11 MeV.

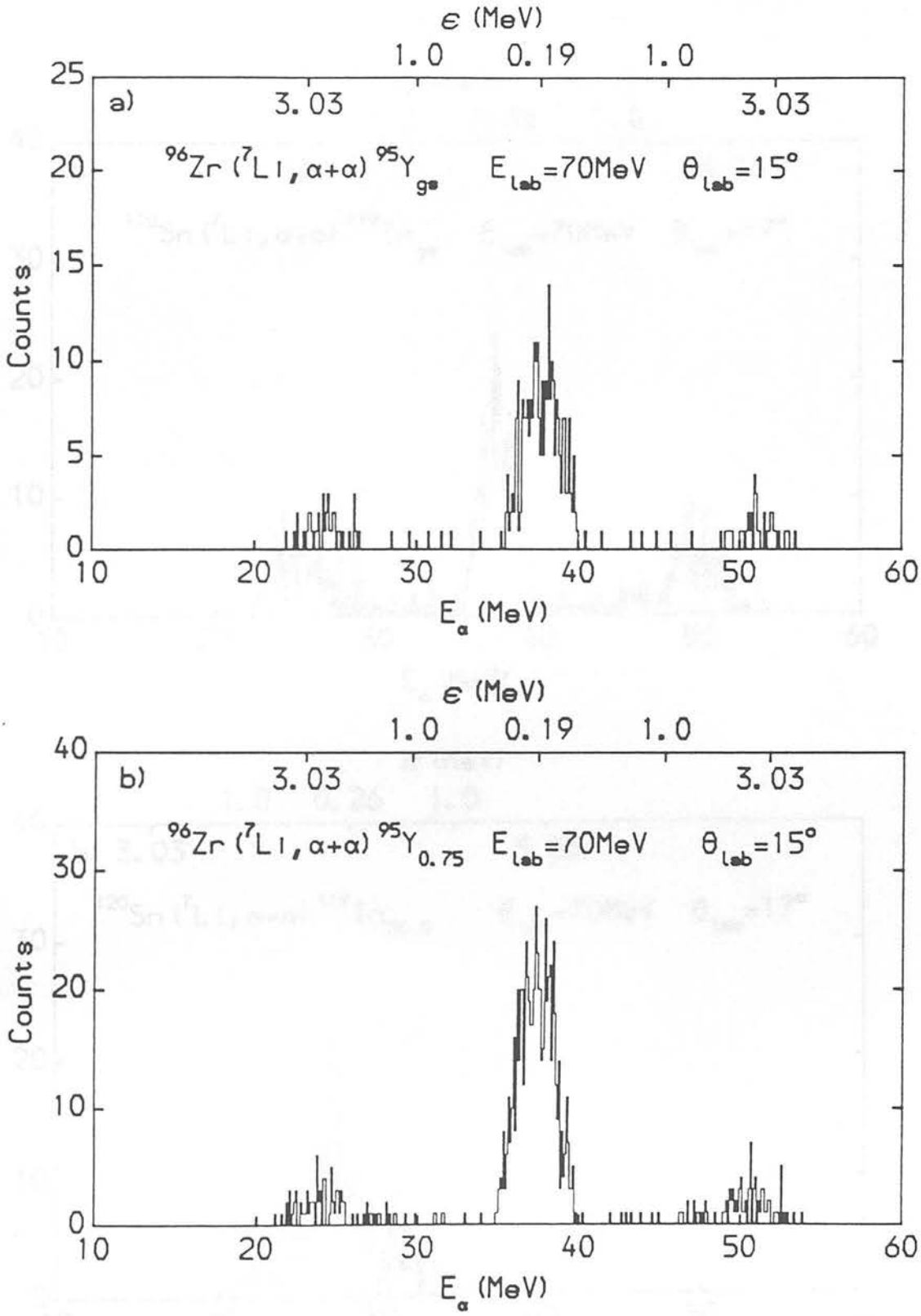

Figure 3.80: Projected α energy spectra for α-α coincidences corresponding to

a) the ground state of ^{95}Y and,

b) 0.69 ($\frac{3}{2}^-$) and 0.83 ($\frac{5}{2}^-$) states of ^{95}Y.

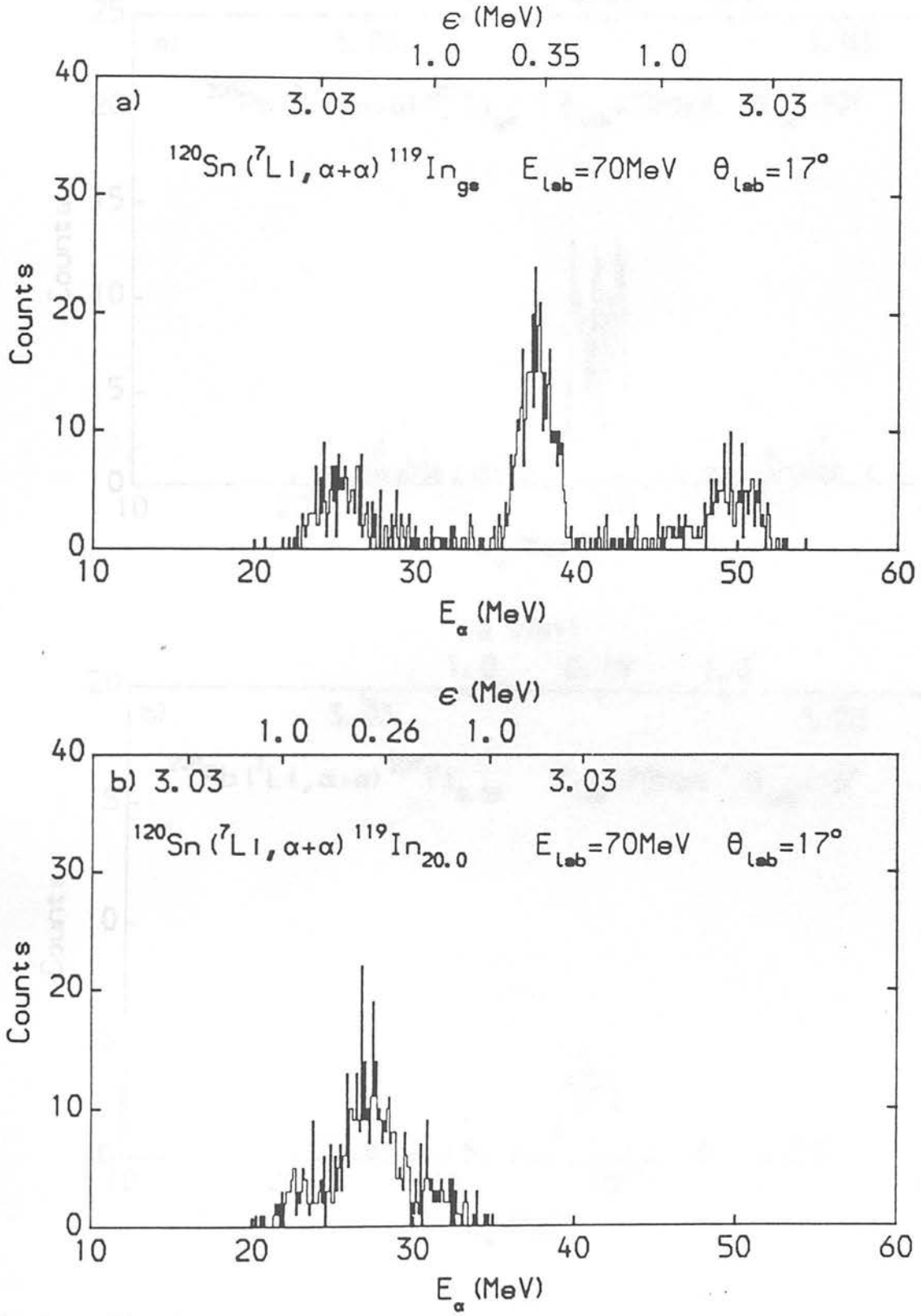

Figure 3.81: Projected α energy spectra for α-α coincidences corresding to

a) the gs($\frac{9}{2}^+$) and 0.31($\frac{11}{2}^-$) states of ^{119}In and,

b) 52 MeV $\lesssim E_\alpha + E_\alpha \lesssim$ 57 MeV - $E_x(^{119}\text{In}) \approx$ 20 MeV.

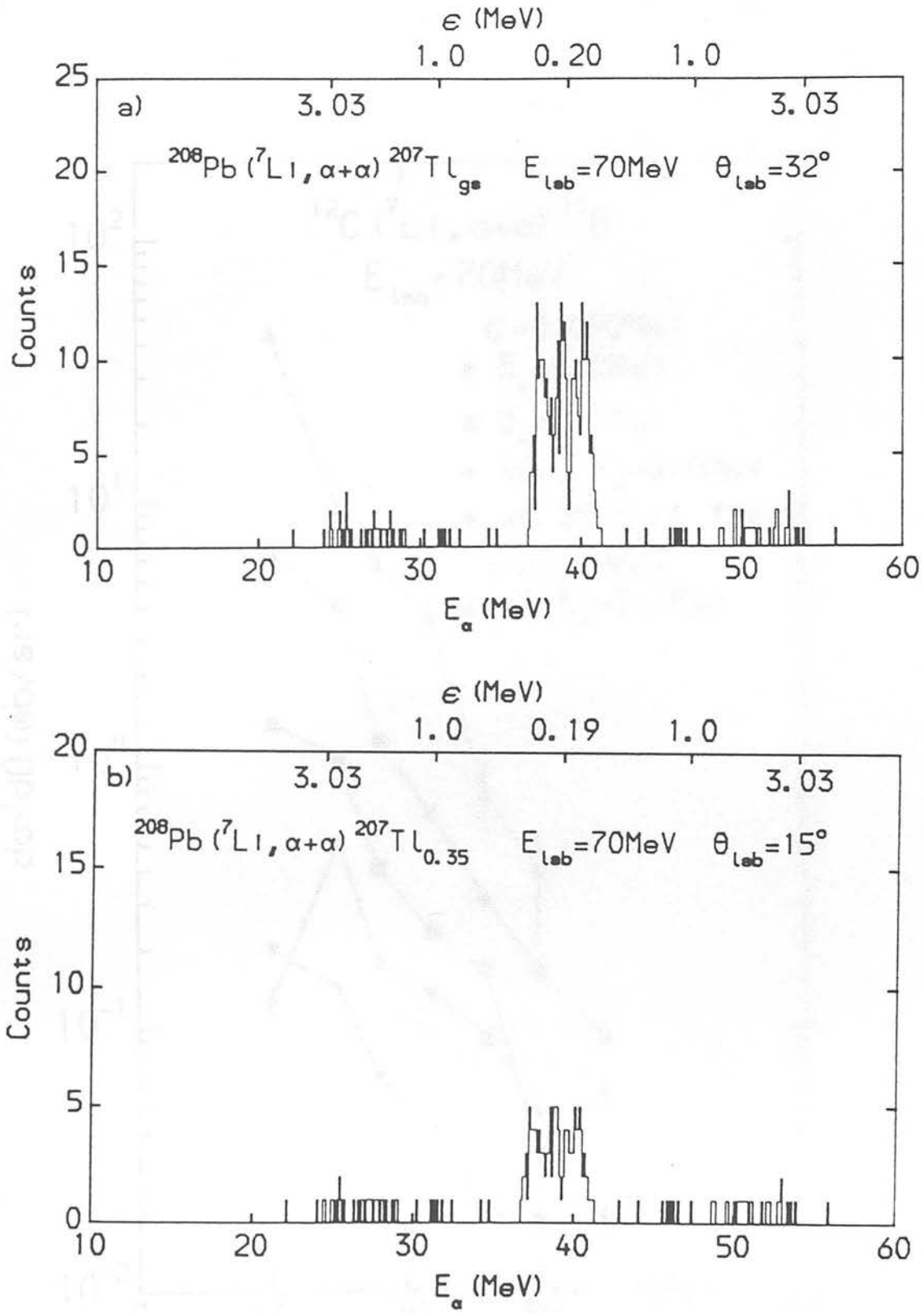

Figure 3.82: Projected α energy spectra for α-α coincidences corresponding to

a) the ground state of ^{207}Tℓ and,

b) 0.35 ($\frac{3^+}{2}$) state of ^{207}Tℓ.

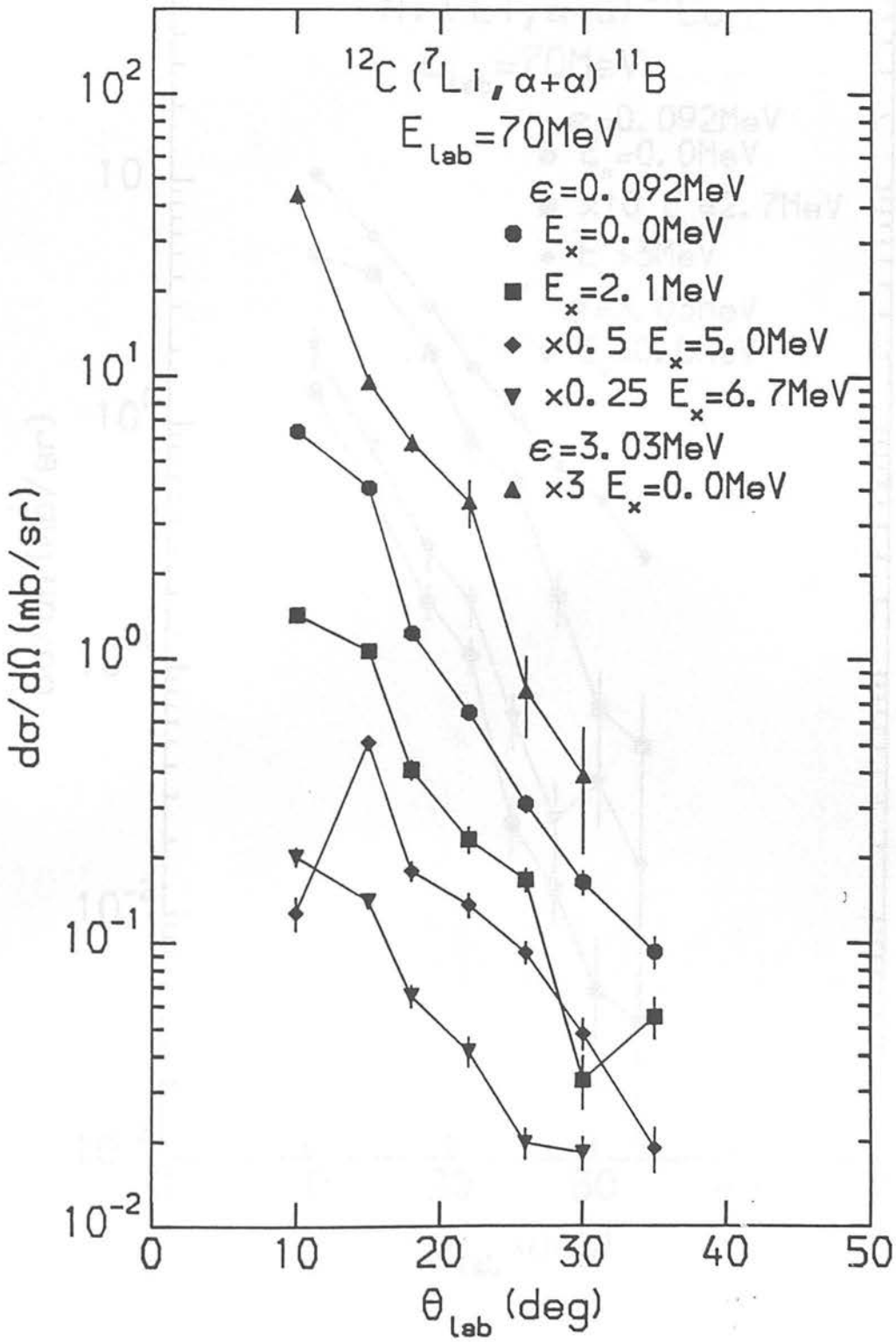

Figure 3.83: Angular distributions for the sequential reactions $^{12}C(^{7}Li, {}^{8}Be_{gs} \rightarrow \alpha+\alpha)^{11}B$ and $^{12}C(^{7}Li, {}^{8}Be^{*}_{2.94} \rightarrow \alpha+\alpha)^{11}B$.

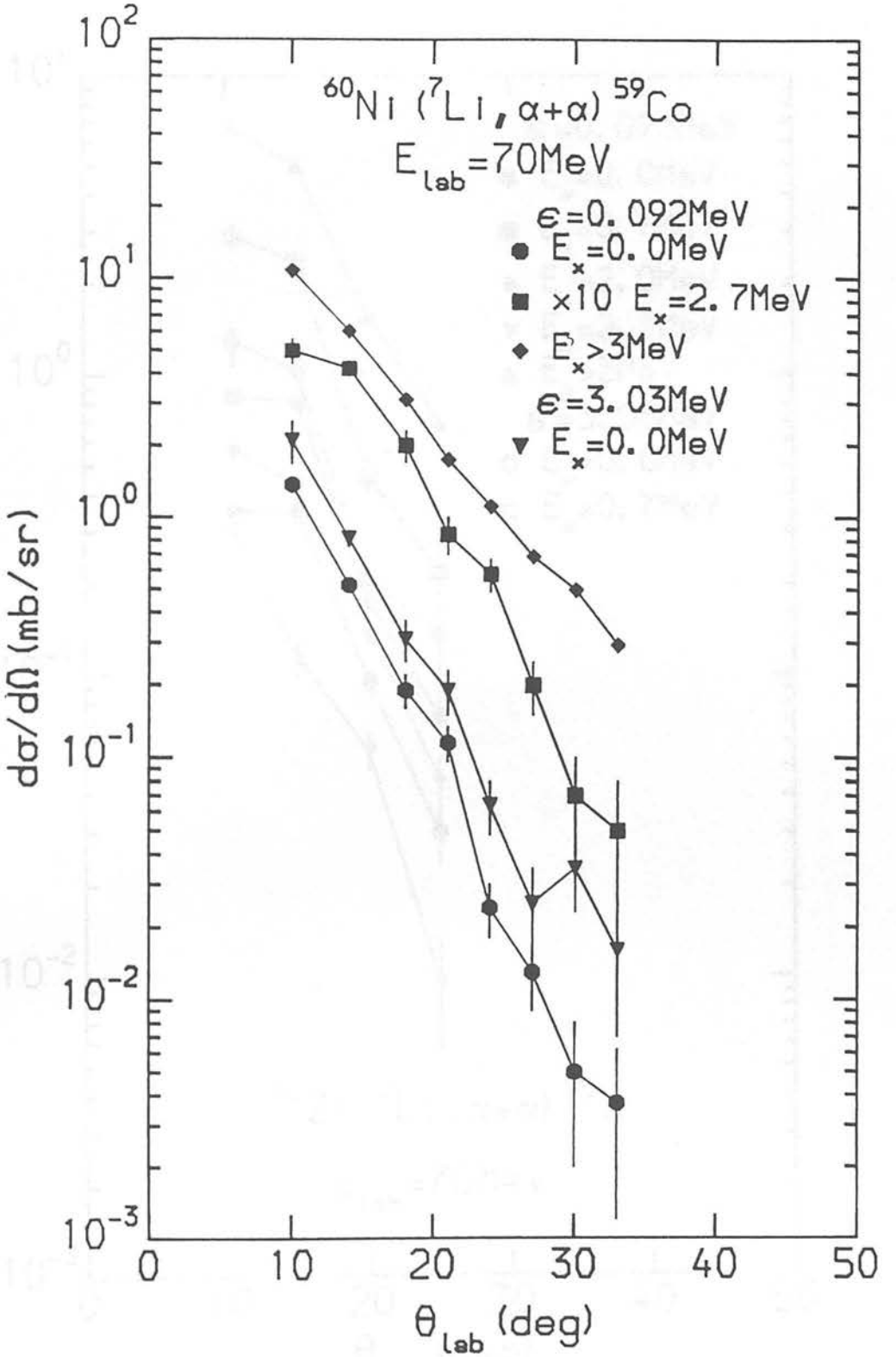

Figure 3.84: Angular distributions for the sequential reactions ^{60}Ni(^{7}Li, ^{8}Be$_{gs}$ → α+ α)^{59}Co and ^{60}Ni(^{7}Li, ^{8}Be$^{*}_{2.94}$ → α+α)^{59}Co.

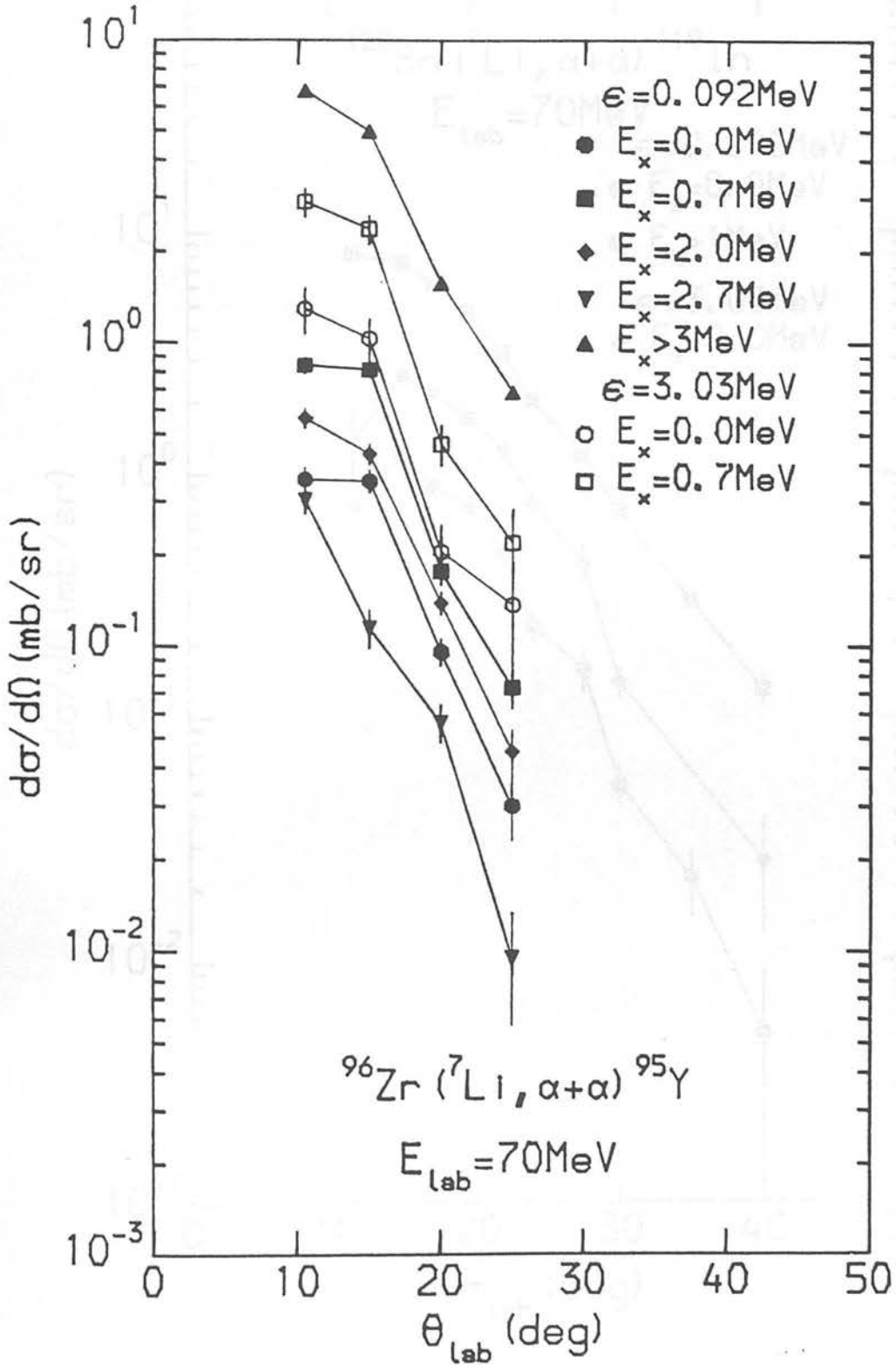

Figure 3.85: Angular distributions for the sequential reactions $^{96}Zr(^{7}Li, ^{8}Be_{gs} \rightarrow \alpha+\alpha)^{95}Y$ and $^{96}Zr(^{7}Li, ^{8}Be^{*}_{2.94} \rightarrow \alpha+\alpha)^{95}Y$.

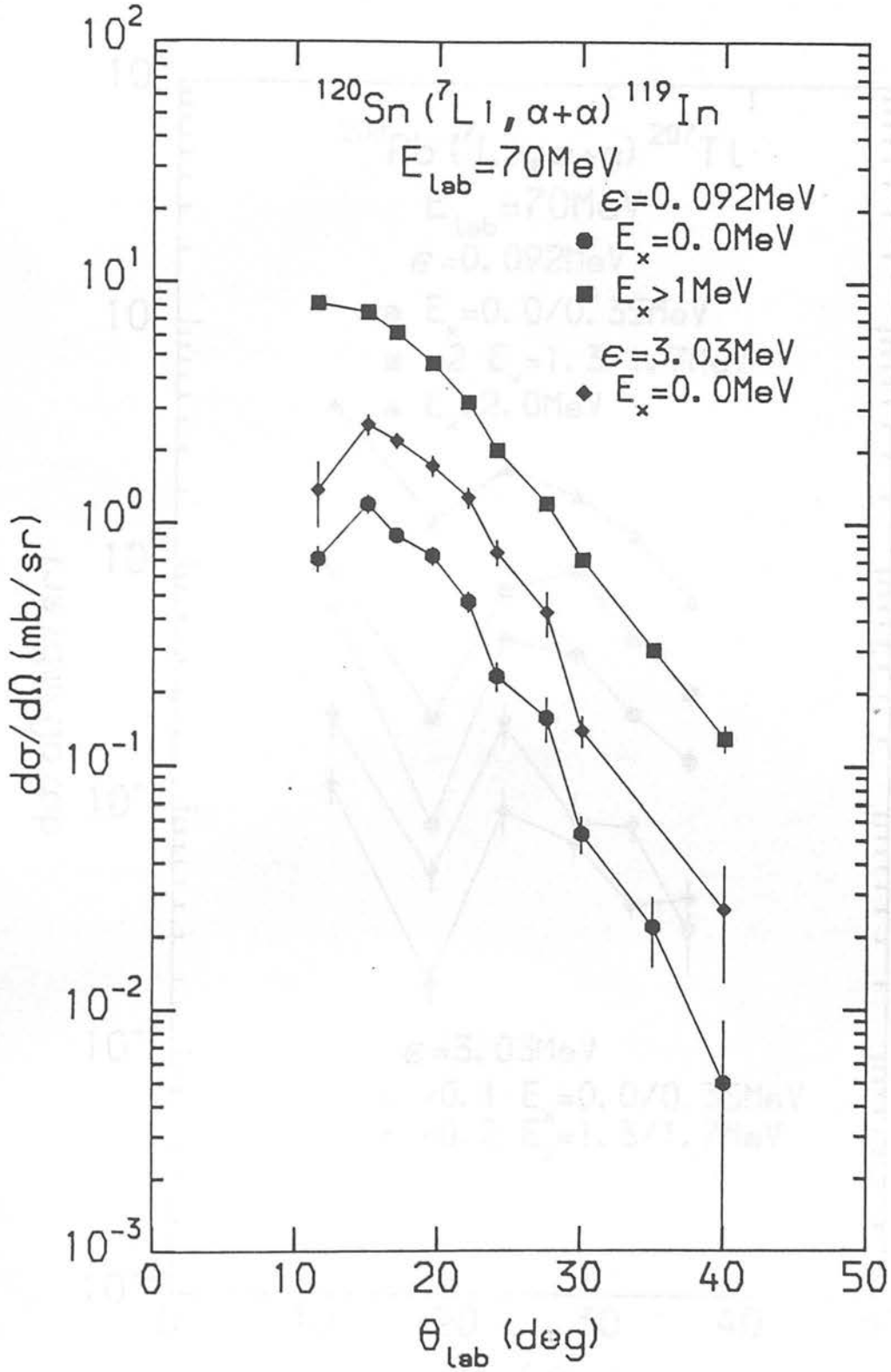

Figure 3.86: Angular distributions for the sequential reactions ^{120}Sn(^{7}Li, ^{8}Be$_{gs}$ → α+α)^{119}In and ^{120}Sn(^{7}Li, ^{8}Be$^{*}_{2.94}$ → α+α)^{119}In.

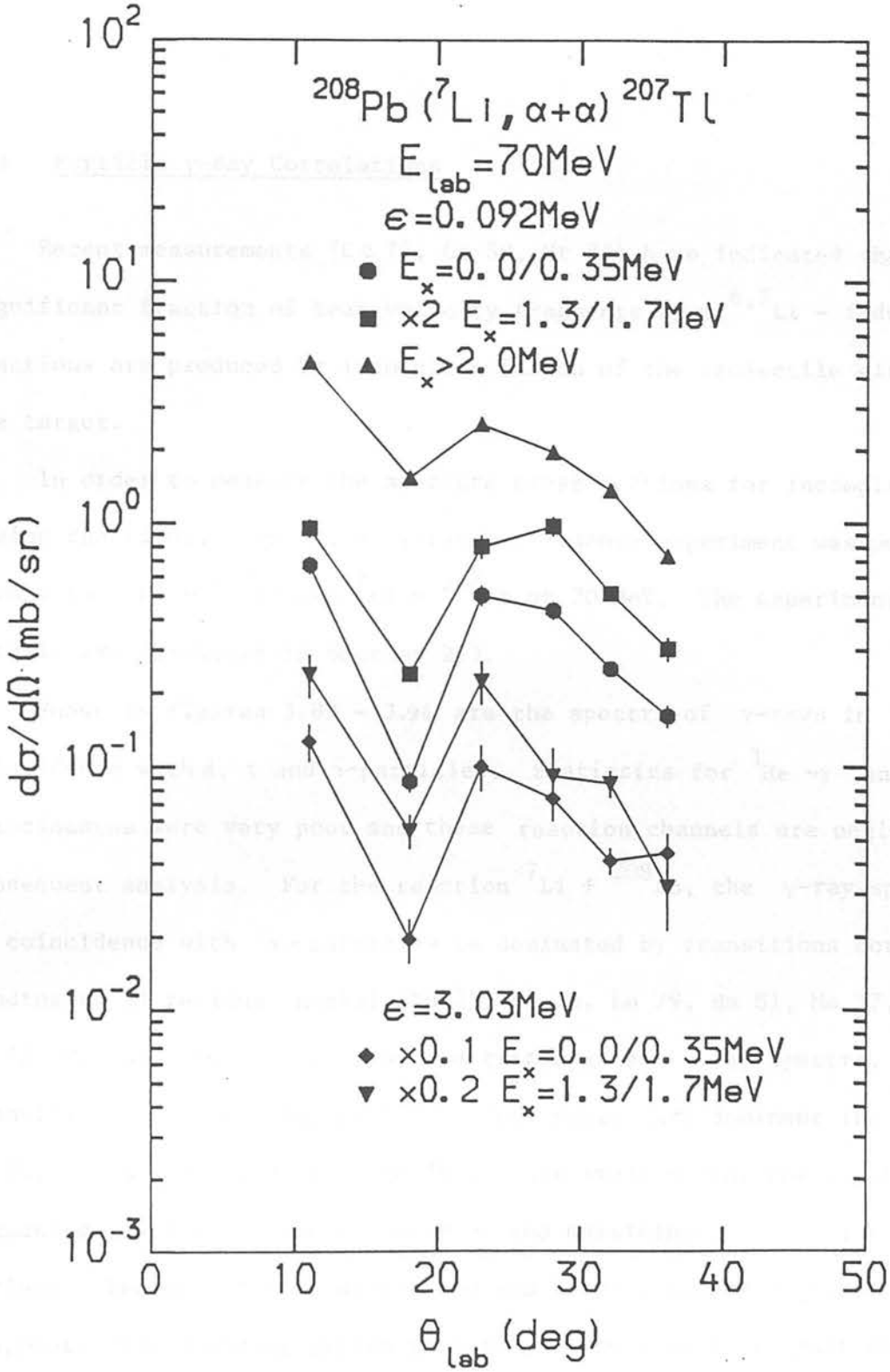

Figure 3.87: Angular distributions for the sequential reactions ^{208}Pb(^{7}Li, ^{8}Be$_{gs}$ → α+α)^{207}Tℓ and ^{208}Pb(^{7}Li, ^{8}Be$^{*}_{2.94}$ → α+α)^{207}Tℓ.

states of the recoil nucleus. The peripheral nature of these interactions is demonstrated in Figure 3.88.

3.3 Particle γ-Ray Correlations

Recent measurements (Ca 78, Ca 80, Ut 83) have indicated that a significant fraction of beam velocity fragments from ^{6,7}Li - induced reactions are produced by incomplete fusion of the projectile with the target.

In order to measure the absolute cross sections for incomplete fusion reactions, a particle γ-ray coincidence experiment was performed for ^{7}Li + ^{120}Sn and ^{7}Li + ^{208}Pb at 70 MeV. The experimental details are discussed in Section 2.3.

Shown in Figures 3.89 - 3.94 are the spectra of γ-rays in coincidence with d, t and α-particles. Statistics for ^{3}He -γ and p - γ coincidences were very poor and these reaction channels are neglected in subsequent analysis. For the reaction ^{7}Li + ^{208}Pb, the γ-ray spectrum in coincidence with α - particles is dominated by transitions corresponding to Bi residual nuclei (Do 75, Lo 78, Lo 79, Ha 81, Ma 77, Ma 83, Hu 72, Pr 73). In the deuteron and triton gated γ-ray spectra, transitions corresponding to Po residual nuclei are dominant (Ha 81, Ma 77, Su 85, Dr 82, Da 83b, Be 78). This implies that the reaction mechanism involved is the transfer of the participant to the target nucleus. The spectator is unaffected and is detected as a beam velocity fragment. The residual system thus formed would decay in part by emission of neutrons and γ-rays resembling a (projectile, xn) reaction. The reaction channels are then written as

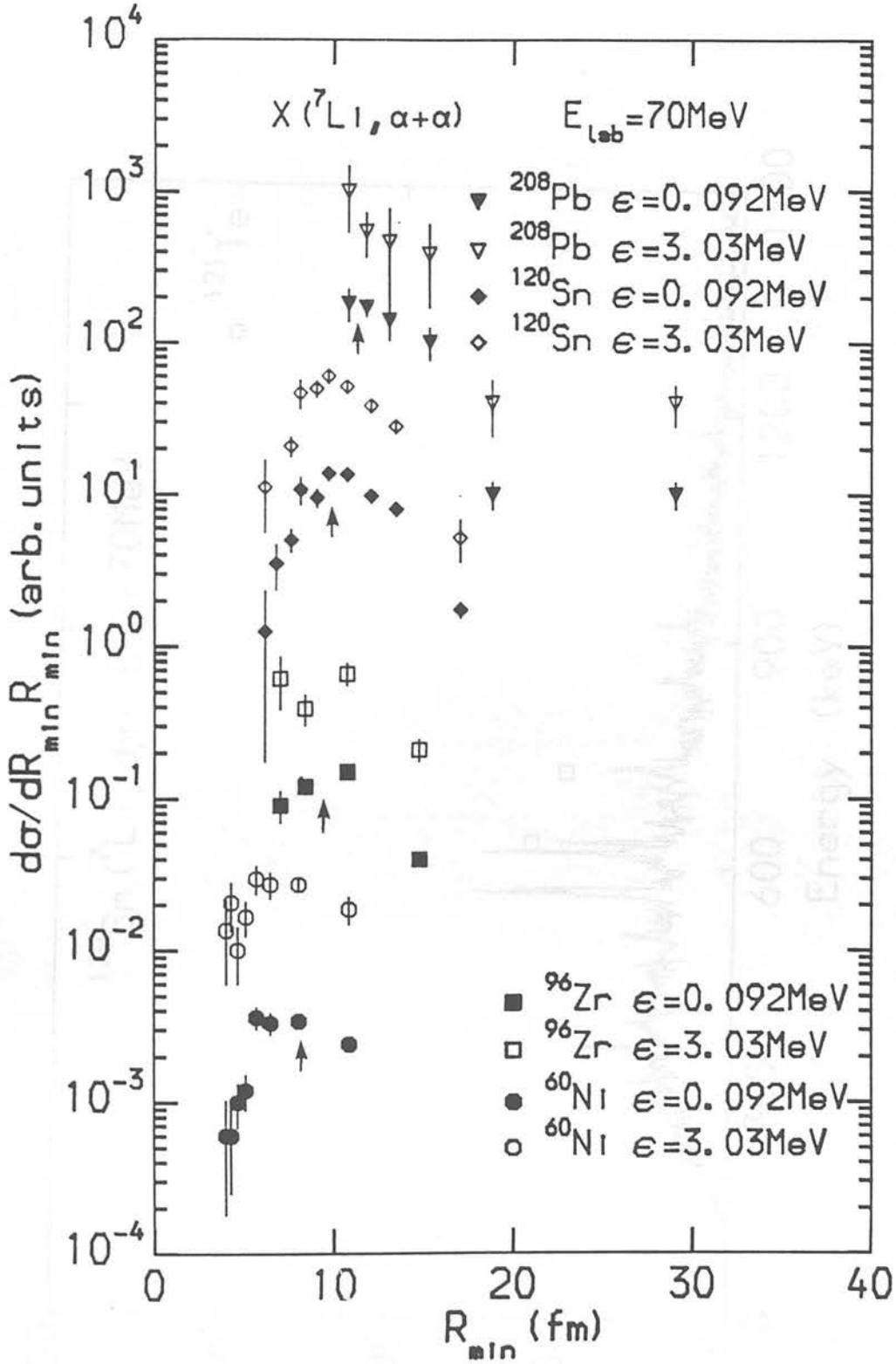

Figure 3.88: $d\sigma/dR_{min} R_{min}$ as a function of R_{min}. The arrows indicate the sum of radii for the projectile and target.

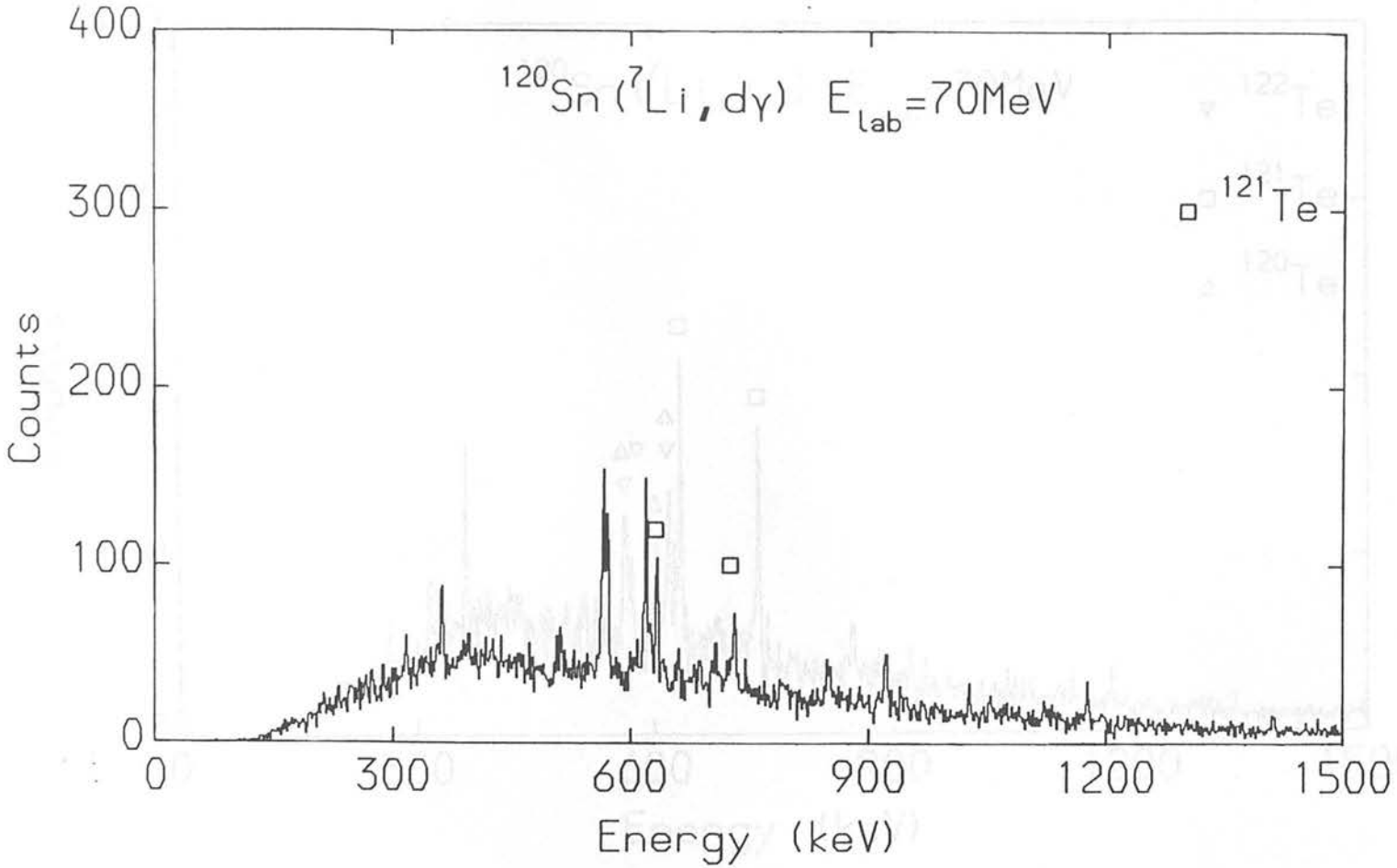

Figure 3.89: γ-ray spectrum in coincidence with deuterons from the reaction 70 MeV ^{7}Li + ^{120}Sn. Spectrum dispersion is approximately 1.5 keV per channel.

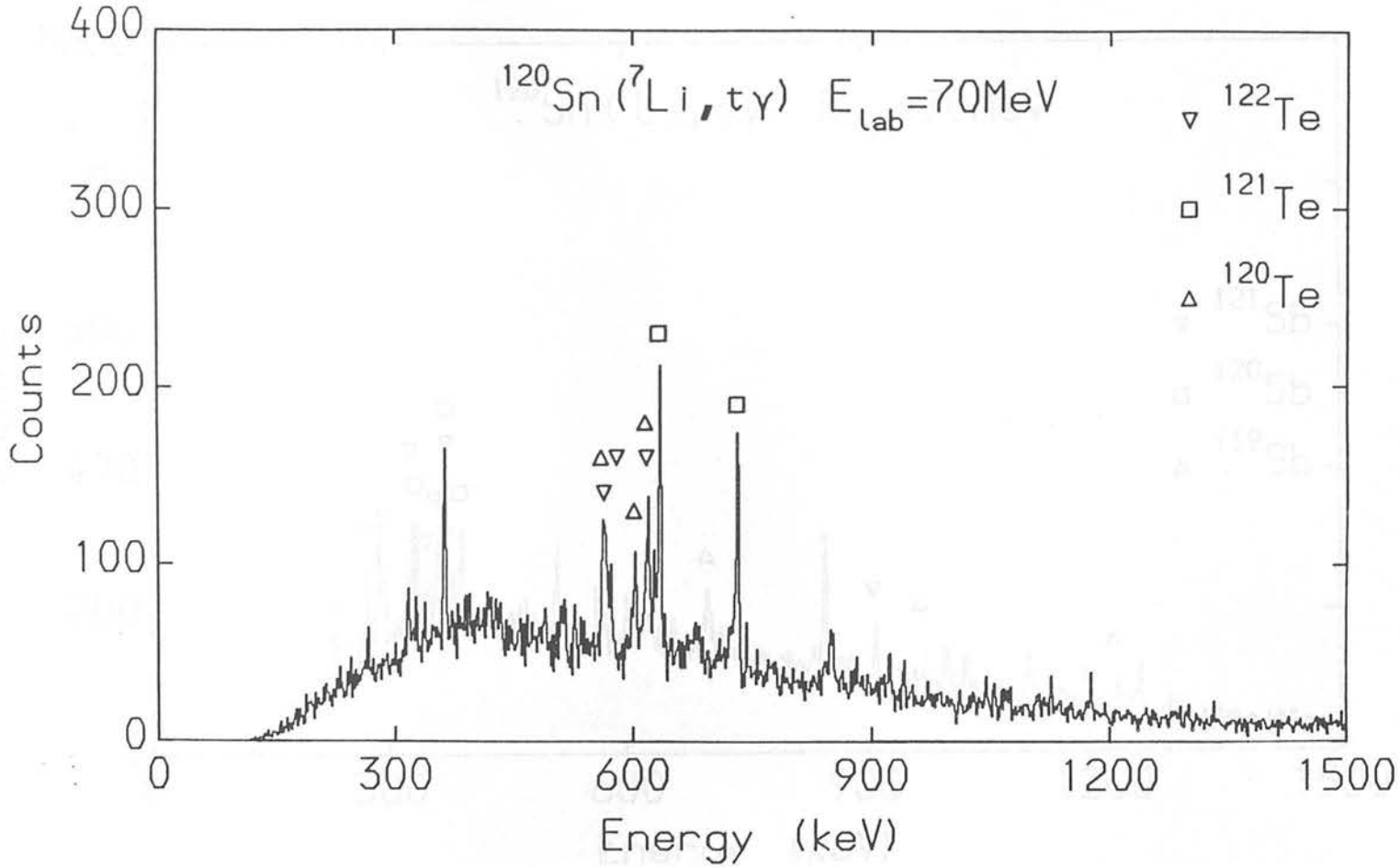

Figure 3.90: γ-ray spectrum in coincidence with tritons from the reaction 70 MeV ^{7}Li + ^{120}Sn. Spectrum dispersion is approximately 1.5 keV per channel.

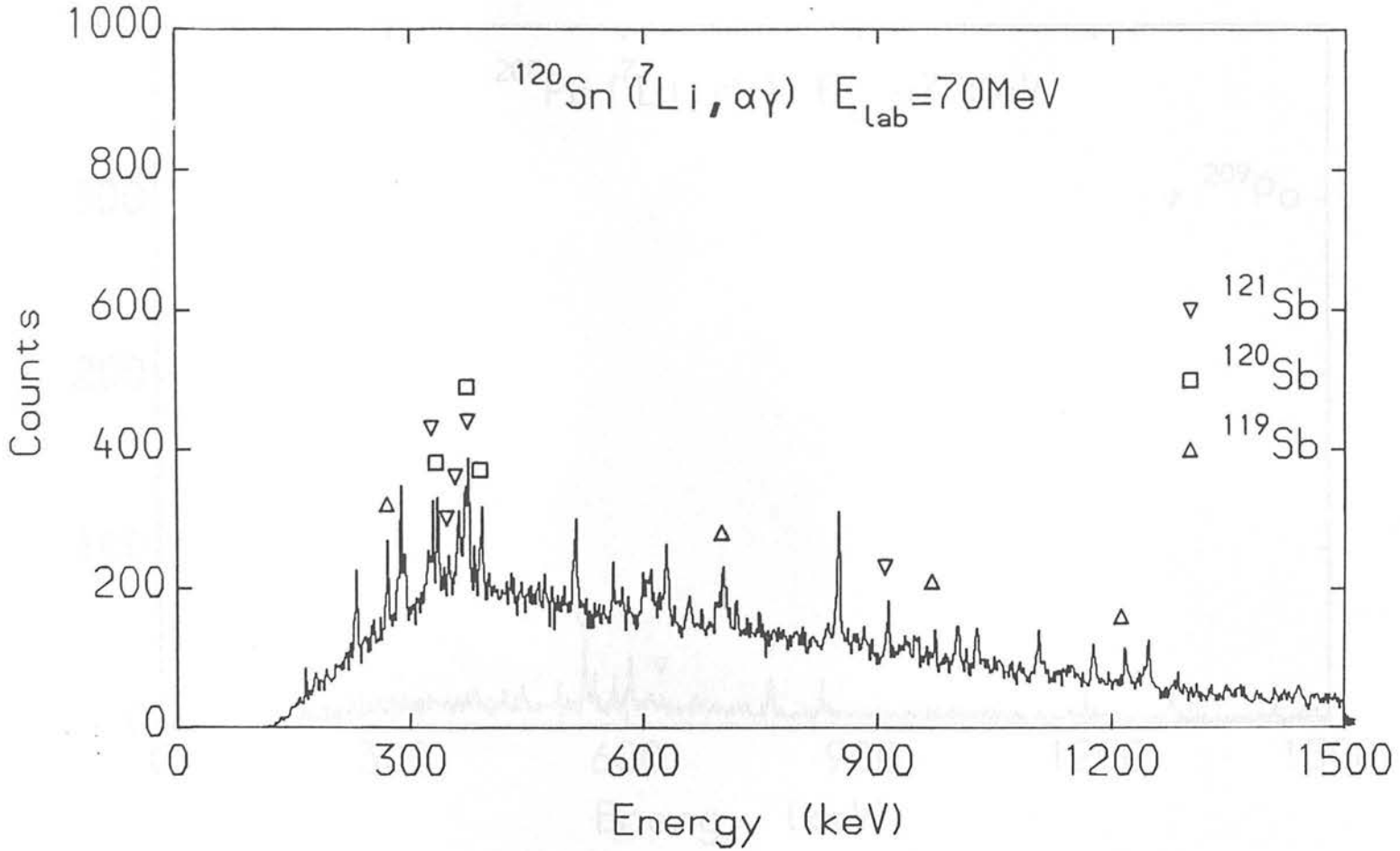

Figure 3.91: γ-ray spectrum in coincidence with α-particles from the reaction 70 MeV ^{7}Li + ^{120}Sn. Spectrum dispersion is approximately 1.5 keV per channel.

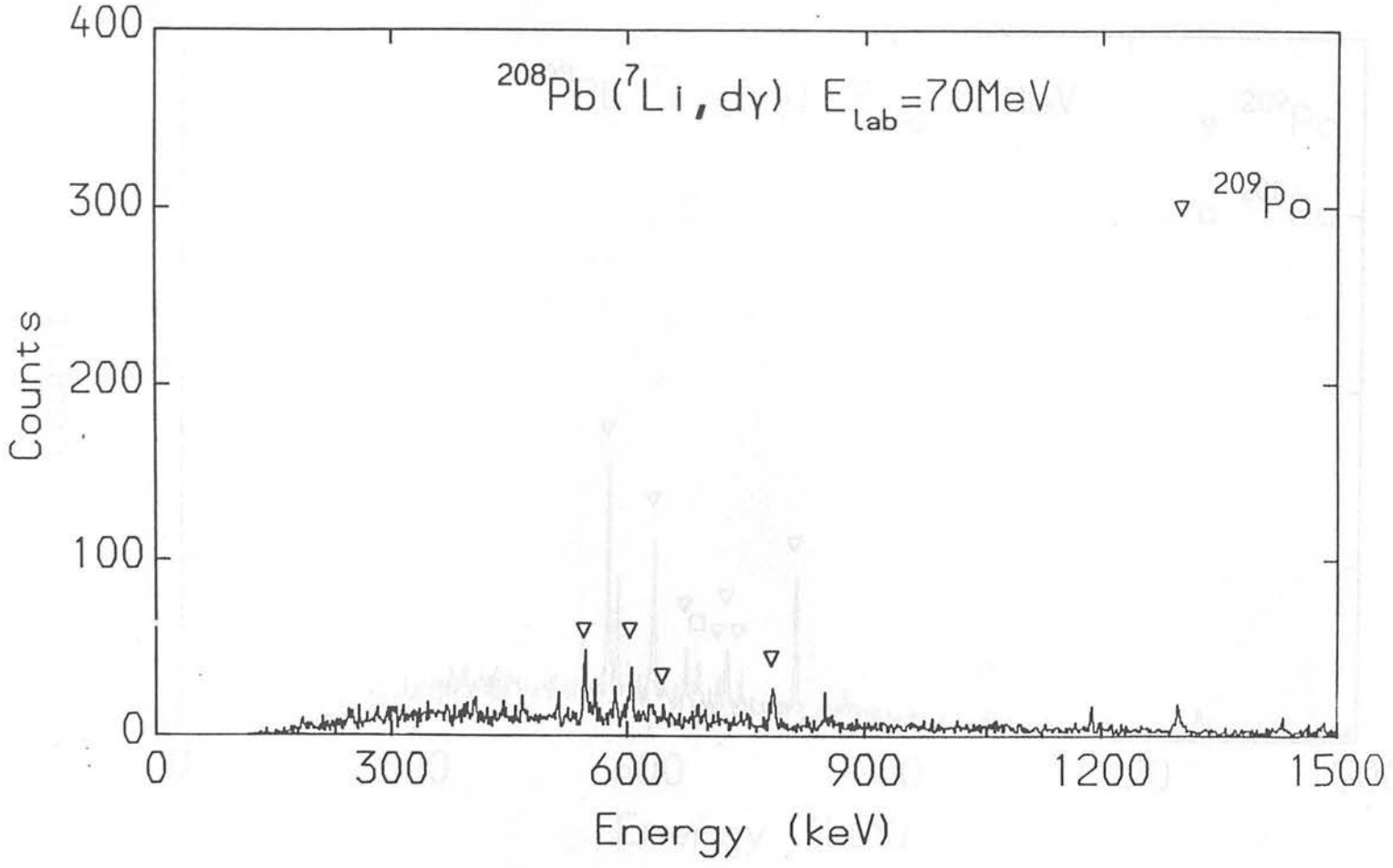

Figure 3.92: γ-ray spectrum in coincidence with deuterons from the reaction 70 MeV ^{7}Li + ^{208}Pb. Spectrum dispersion is approximately 1.5 keV per channel.

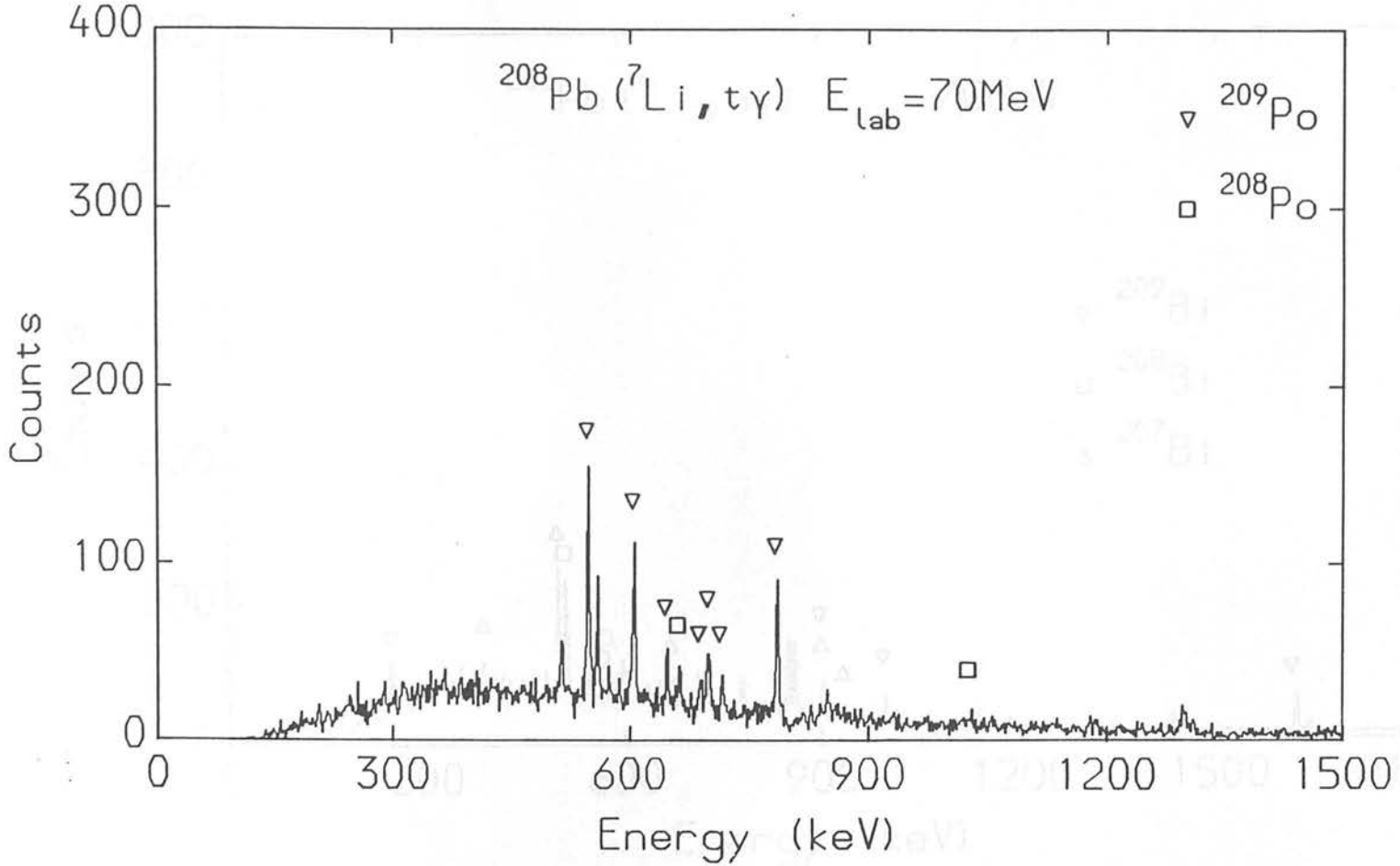

Figure 3.93: γ-ray spectrum in coincidence with tritons from the reaction 70 MeV ^{7}Li + ^{208}Pb. Spectrum dispersion is approximately 1.5 keV per channel.

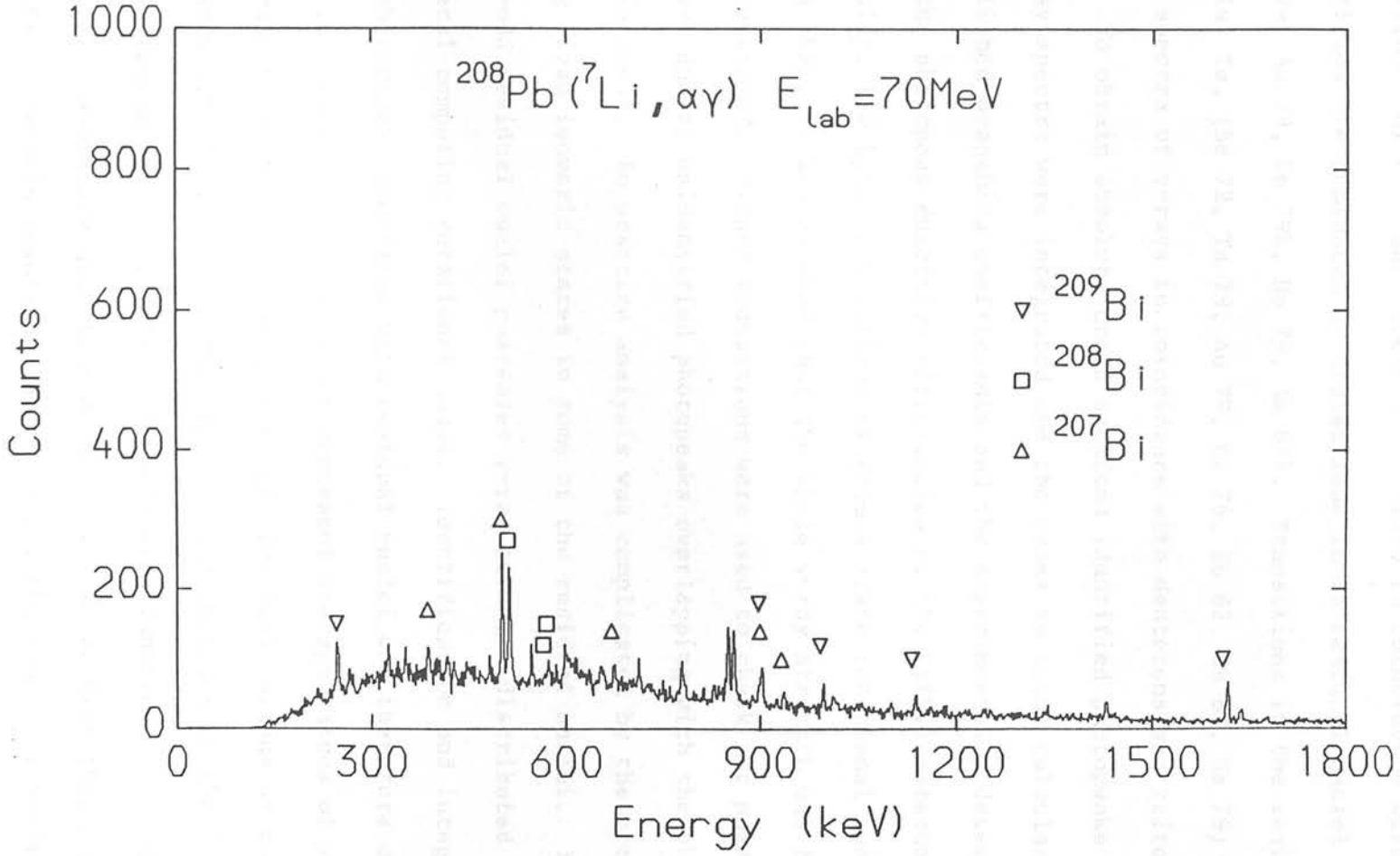

Figure 3.94: γ-ray spectrum in coincidence with α-particles from the reaction 70 MeV ^{7}Li + ^{208}Pb. Spectrum dispersion is approximately 1.5 keV per channel.

$^{208}Pb(^{7}Li,\alpha x n\gamma)^{211-x}Bi$ or $^{208}Pb(^{7}Li, txn\gamma)^{212-x}Po$ or $^{208}Pb(^{7}Li, dxn\gamma)^{213-x}Po$. Similar conclusions are reached for the reaction $^{7}Li + ^{120}Sn$. Spectra of γ-rays in coincidence with α-particles are dominated by transitions in Sb residual nuclei (Be 72, Ta 79, Au 79, Sn 79b, Ho 79, Va 83). Transitions in the residual nuclei Te, (Be 72, Ta 79, Au 79, Ko 76, Ru 82, Ch 82, Ha 79) dominated the spectra of γ-rays in coincidence with deuterons and tritons.

To obtain absolute cross sections identified photopeaks in the γ-ray spectra were integrated and the cross sections calculated using published branching coefficients and the experimentally determined values of the photopeak detection efficiencies of the Ge(Li) detectors. Ideally, low-lying transitions of ground state rotational bands were used where it was assumed that the whole γ-ray strength was finally concentrated. Higher transitions were used to check for possible errors due to unidentified photopeaks overlapping with the photopeak of interest. In practice analysis was complicated by the presence of long lived isomeric states in some of the residual nuclei. Further, odd-odd residual nuclei possessed γ-ray strength distributed over several competing rotational bands. Identification and integration of photopeaks associated with residual nuclei was therefore difficult. Partial reaction cross sections represent average values of yield for as many transitions in the appropriate residual nucleus as possible. Figures 3.95 - 3.100 show the angular distributions of the incomplete fusion partial reaction channels as a function of charged particle laboratory detection angle. It can be seen that partial reaction channels involving low x (i.e. the number of neutrons emitted from the residual nucleus) dominate at forward laboratory

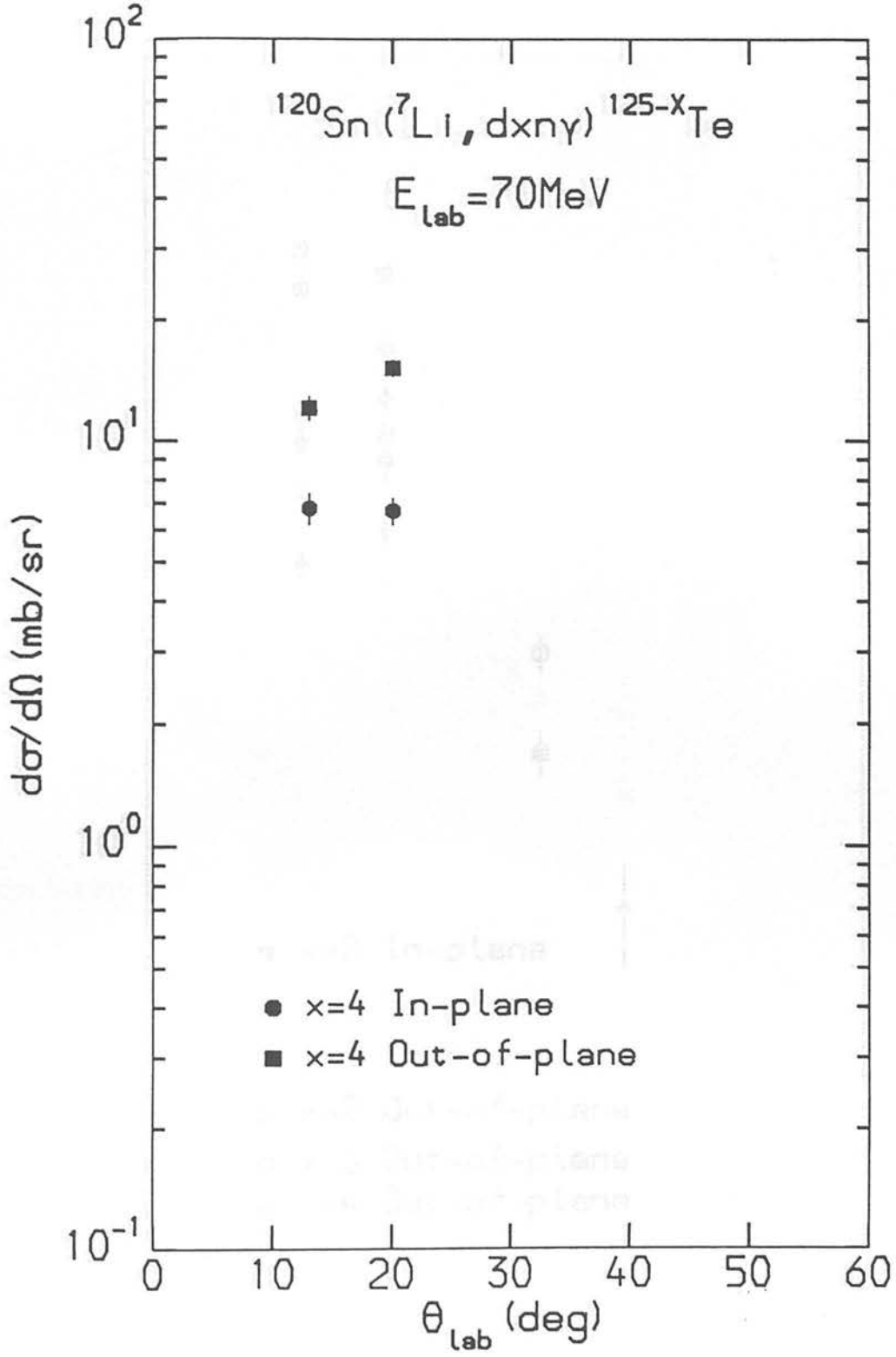

Figure 3.95: Angular distributions for the incomplete fusion reaction ^{120}Sn(^{7}Li, dxnγ).

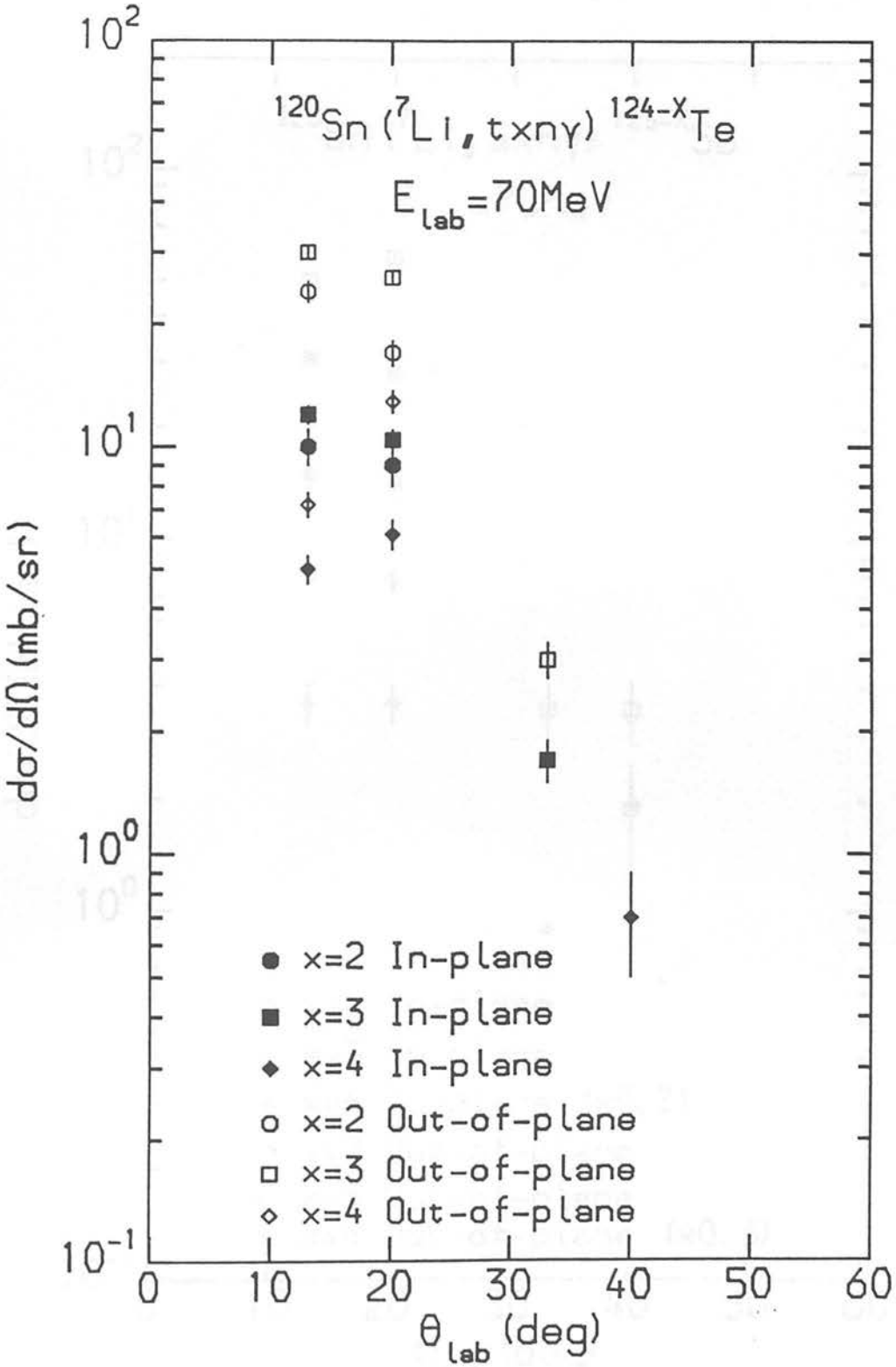

Figure 3.96: Angular distributions for the incomplete fusion reaction $^{120}Sn(^{7}Li, txn\gamma)$.

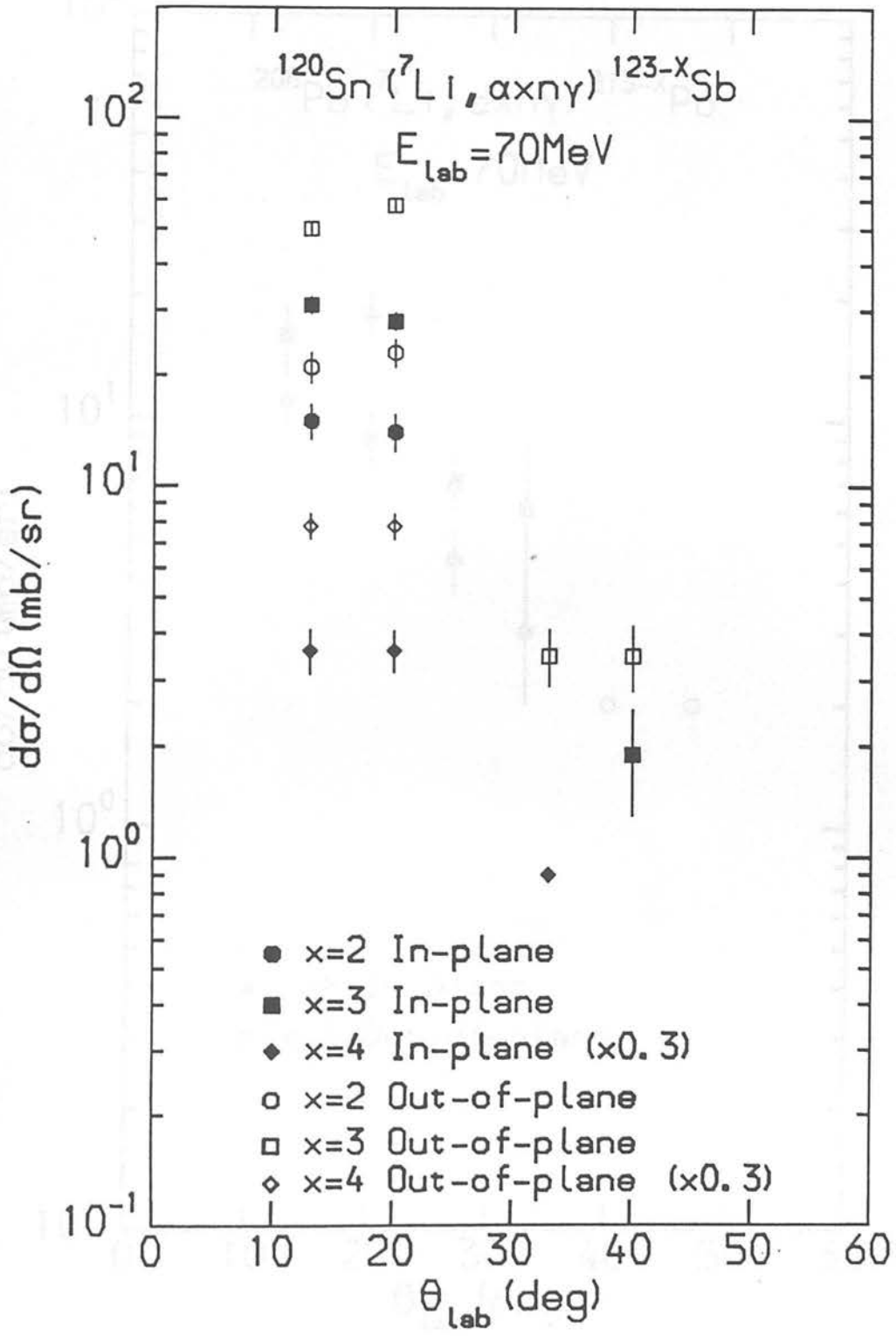

Figure 3.97: Angular distributions for the incomplete fusion reaction ^{120}Sn(^{7}Li, αxnγ).

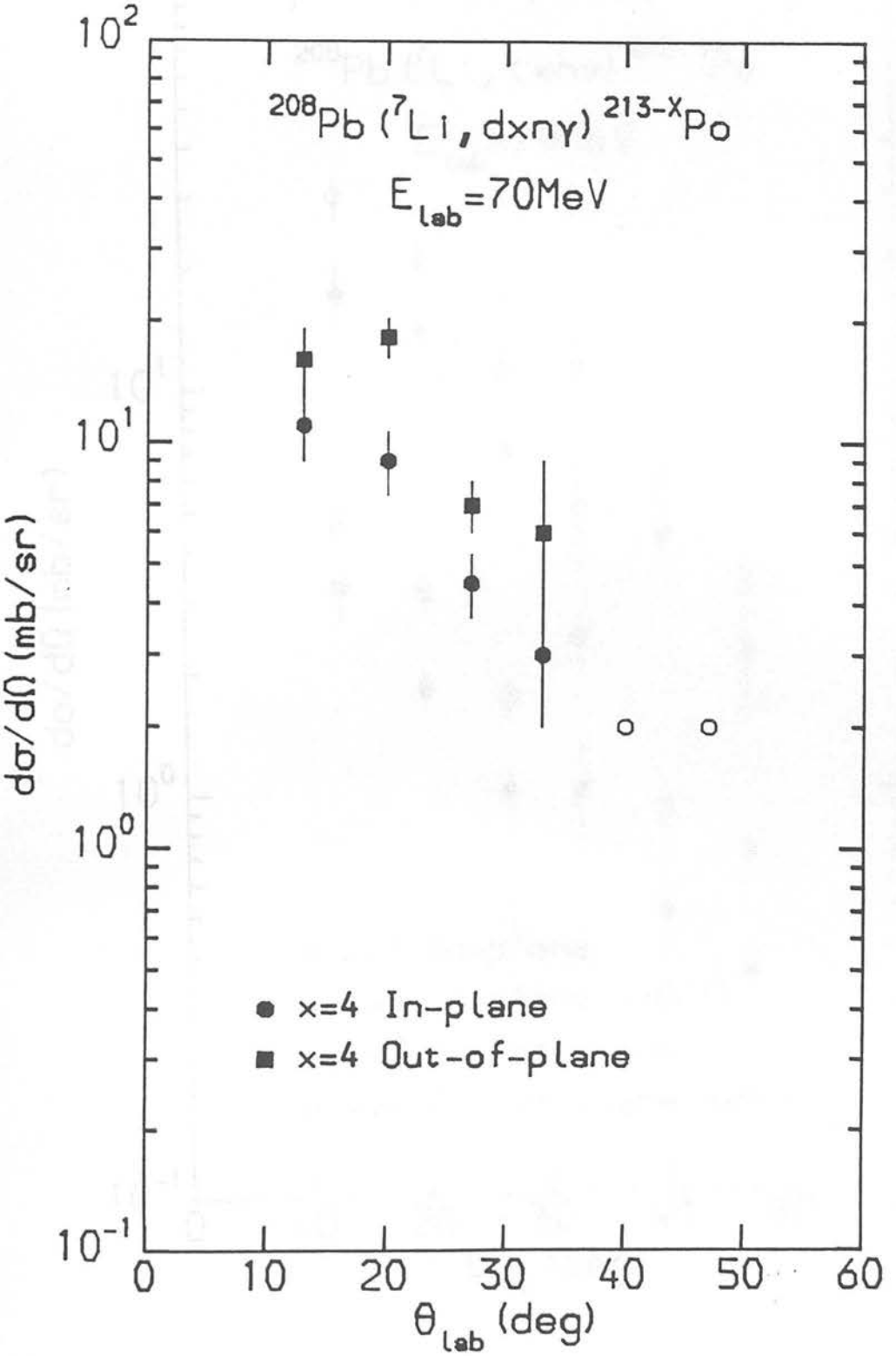

Figure 3.98: Angular distributions for the incomplete fusion reaction $^{208}Pb(^7Li, dx n\gamma)$.

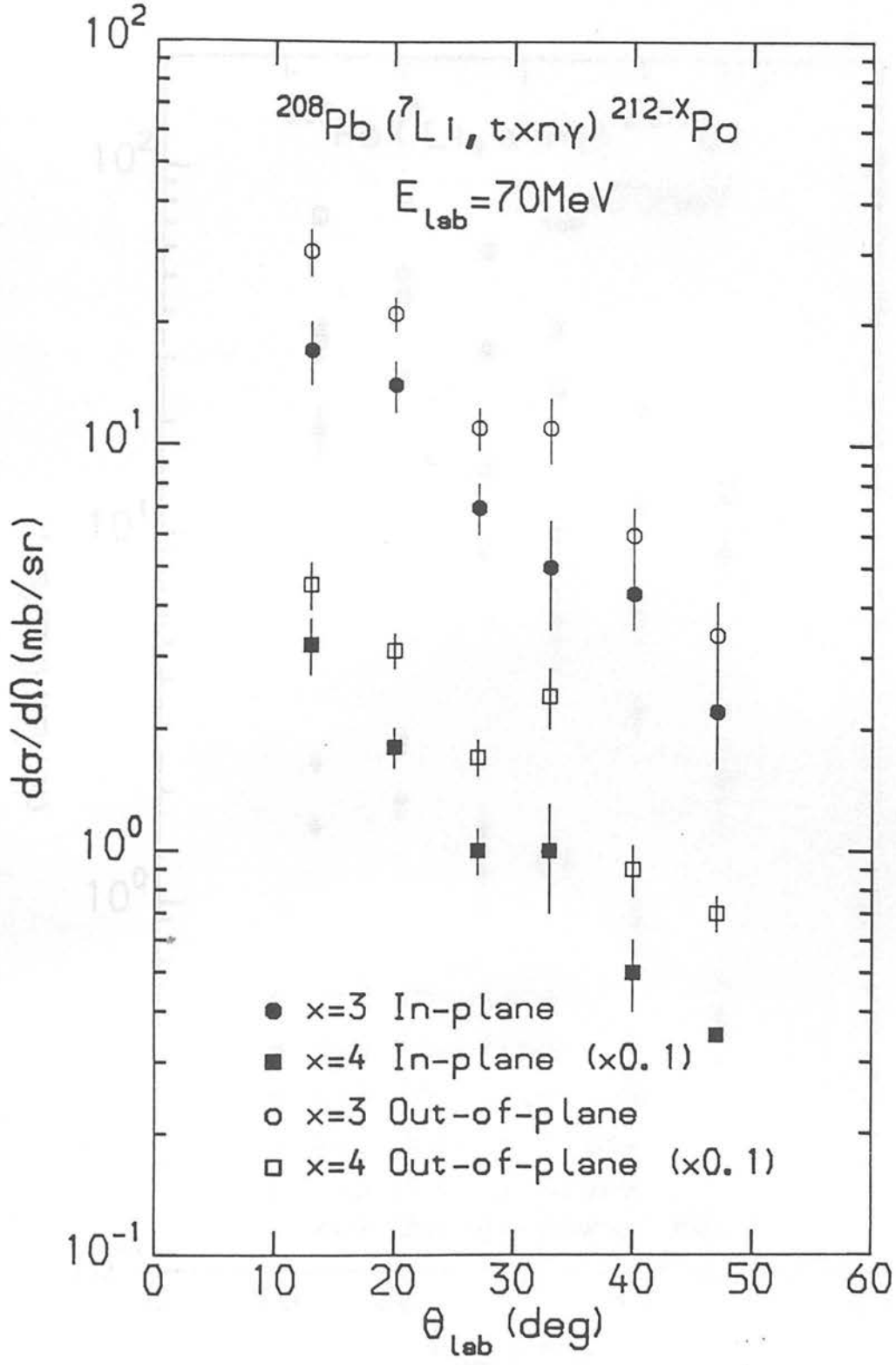

Figure 3.99: Angular distributions for the incomplete fusion reaction ^{208}Pb(^{7}Li, txnγ).

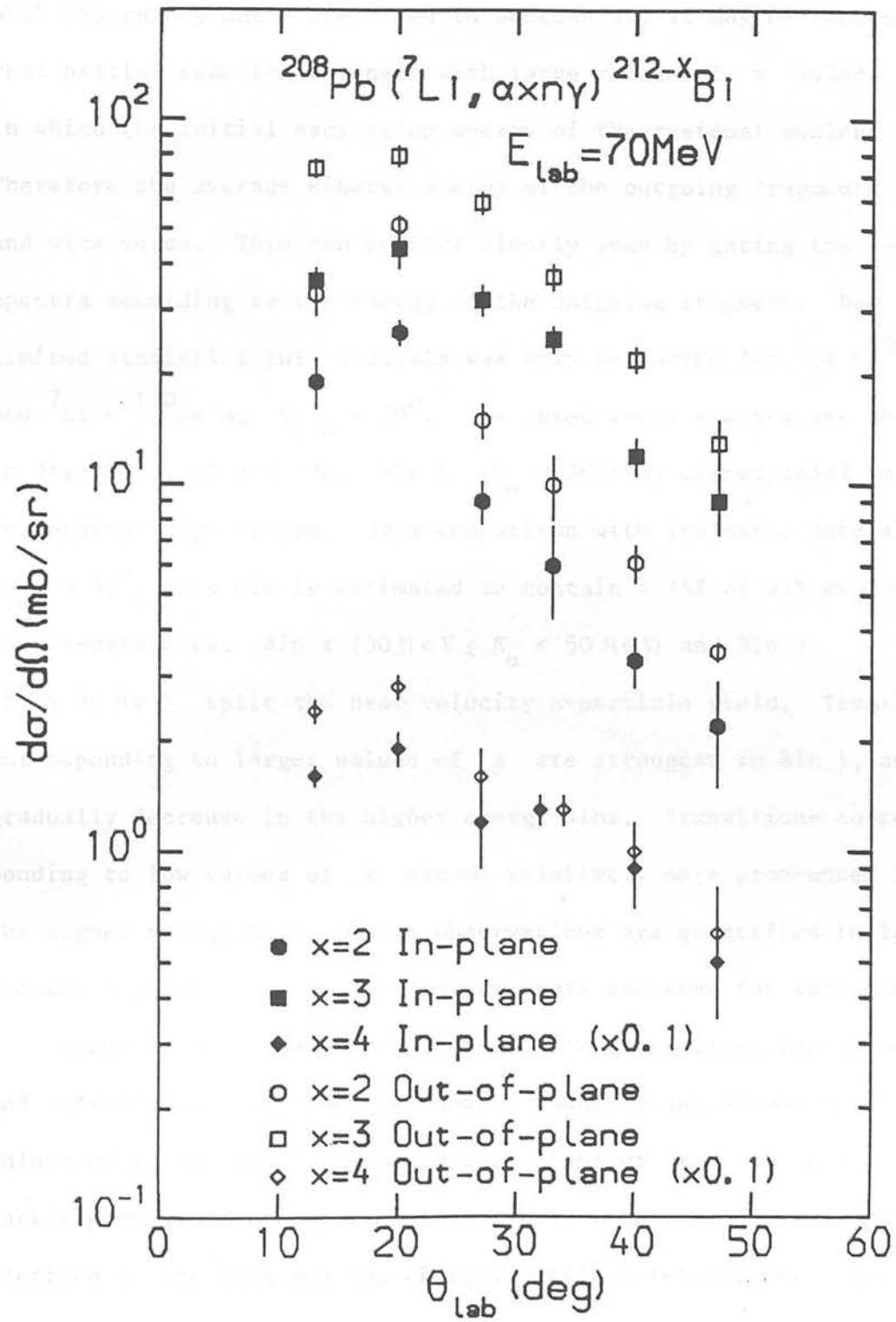

Figure 4.100: Angular distributions for the incomplete fusion reaction ^{208}Pb(^{7}Li, αxnγ).

angles. At backward angles, partial reaction channels involving larger values of x are relatively more important. Recalling the exponential decrease in the inclusive yield of beam velocity fragments with laboratory angle discussed in Section 3.1 it may be concluded that partial reaction channels with large values of x select channels in which the initial excitation energy of the residual nucleus is high. Therefore the average kinetic energy of the outgoing fragments is lower, and vice versa. This can be more clearly seen by gating the γ-ray spectra according to the energy of the outgoing fragment. Due to limited statistics this analysis was only performed for $^{7}Li + ^{208}Pb$ and $^{7}Li + ^{120}Sn$ at $\theta_{lab} = 20^{o}$. The gated γ-ray spectra are shown in Figures 3.101 - 3.102. Bin 1 ($E_{\alpha} < 30$ MeV) corresponded to evaporation α-particles. From comparison with inclusive data at $\theta_{lab} > 30^{o}$, this bin is estimated to contain > 75% of all evaporation α-particles. Bin 2 ($30 \text{ MeV} \lesssim E_{\alpha} < 50$ MeV) and Bin 3 ($E_{\alpha} \gtrsim 30$ MeV) split the beam velocity α-particle yield. Transitions corresponding to larger values of x are strongest in Bin 1, and gradually decrease in the higher energy bins. Transitions corresponding to low values of x become relatively more pronounced in the higher energy bins. These observations are quantified in Table 3.2 which gives the partial reaction cross sections for each bin.

Comparison of the partial reaction cross sections for in-plane and out-of-plane coincidences shows pronounced anisotropy for low values of x, and isotropy for larger values of x. Semi-classically the participant would be captured into orbits concentrated in the reaction plane defined by the beam and the charged-particle telescopes. In consequence

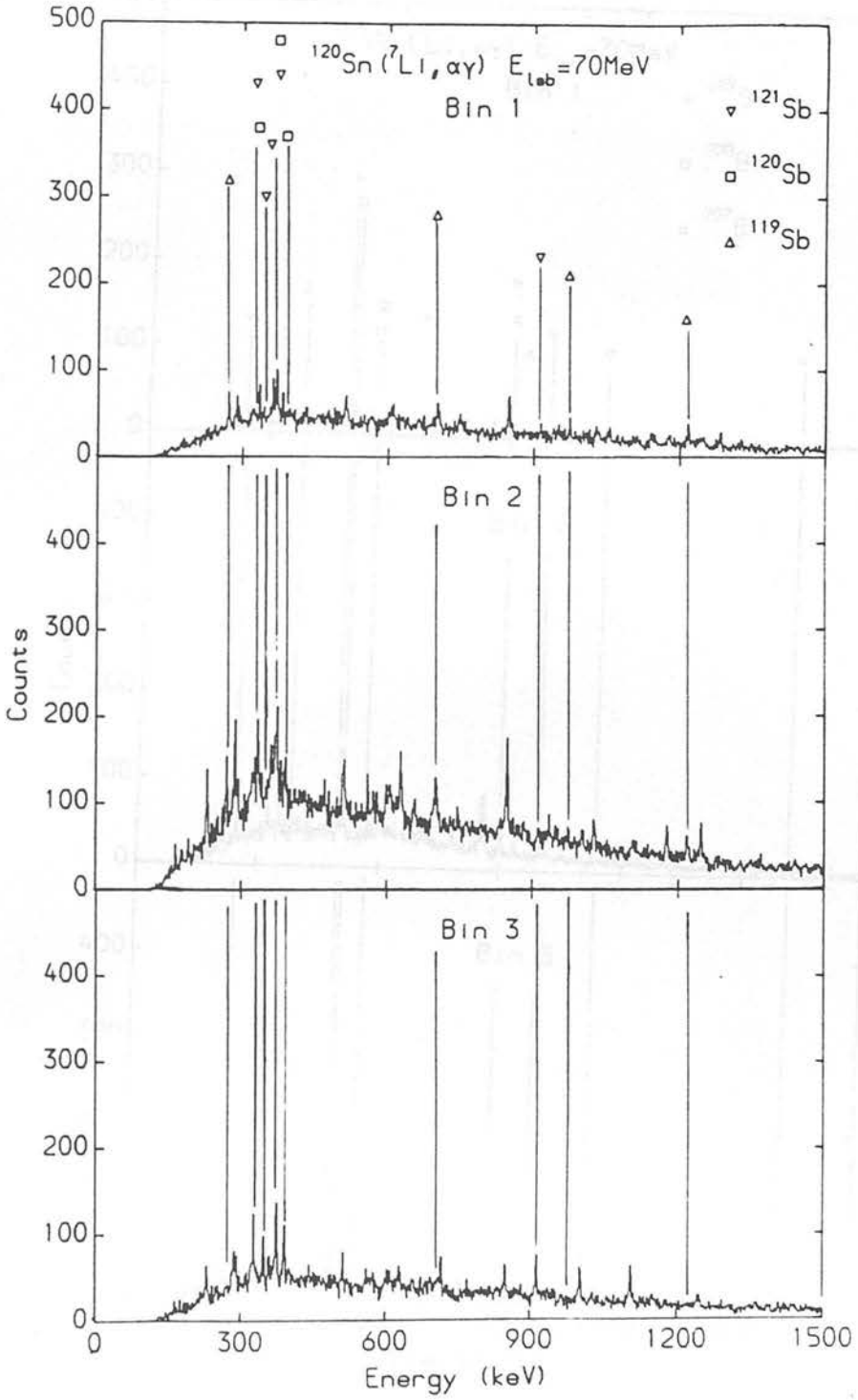

Figure 3.101: γ-ray spectra in coincidence with α-particles of energy E_α < 30 MeV, b) 30 MeV ≤ E_α < 50 MeV and c) E_α ≥ 50 MeV from the reaction 70 MeV ^{7}Li + ^{120}Sn.

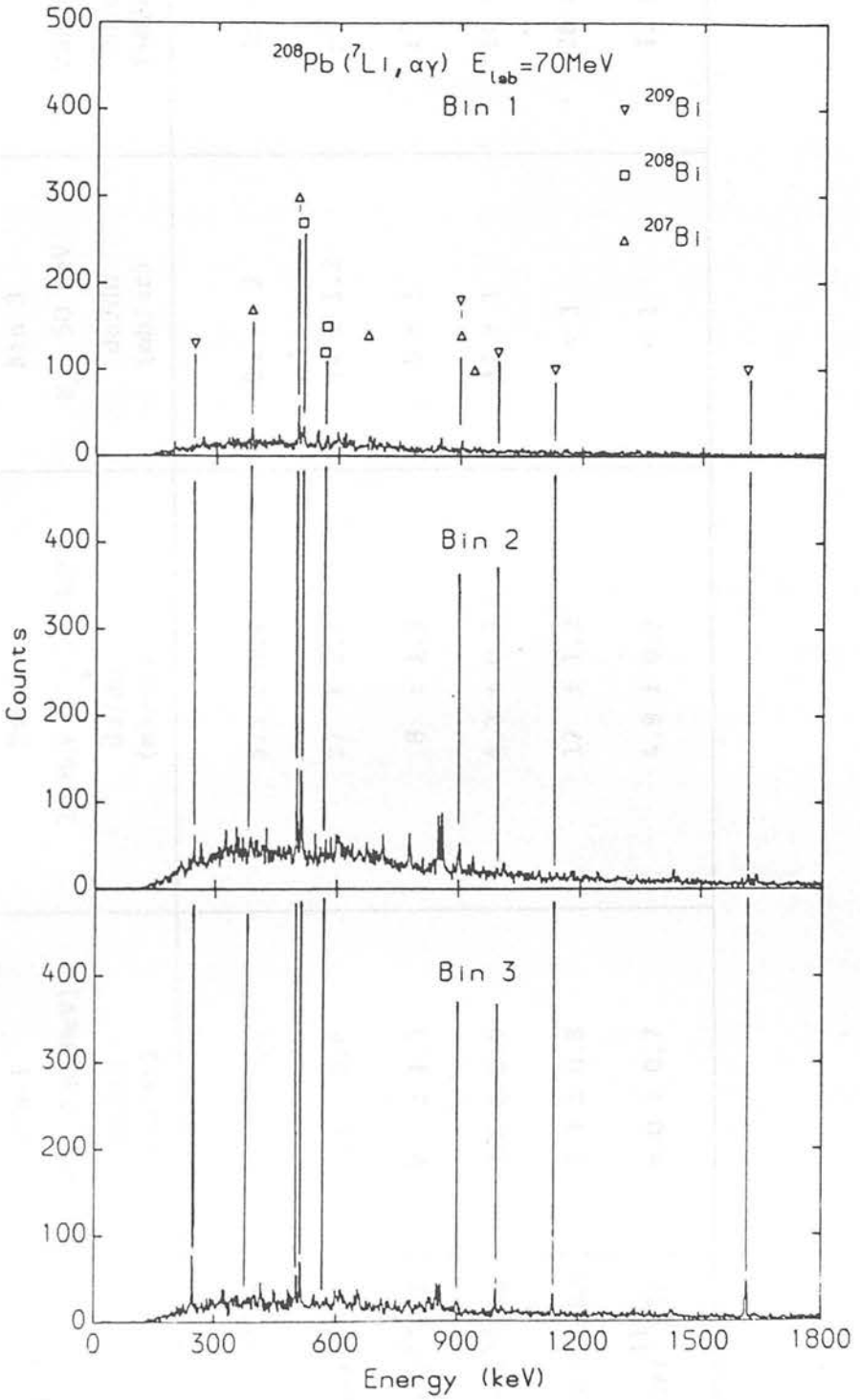

Figure 3.102: γ-ray spectra in coincidence with α-particles of energy a) E_α < 30 MeV, b) 30 MeV ≤ E_α < 50 MeV and c) E_α ≥ 50 MeV from the reaction 70 MeV ^{7}Li + ^{208}Pb.

TABLE 3.2: Partial Reaction Cross Sections as a Function of α Energy

Reaction	Bin 1 $4(E_\alpha < 30$ MeV) $d\sigma/d\Omega$ (mb/sr)	Bin 2 30 MeV $\leq E_\alpha < 50$ MeV $d\sigma/d\Omega$ (mb/sr)	Bin 3 $E_\alpha \geq 50$ MeV $d\sigma/d\Omega$ (mb/sr)	Ungated $d\sigma/d\Omega$ (mb/sr)
$^{208}Pb(^{7}Li, \alpha 2n\gamma)^{209}Bi$	1.2 ± 0.4	5.5 ± 0.9	23 ± 2	26 ± 2
$^{208}Pb(^{7}Li, \alpha 3n\gamma)^{208}Bi$	3.1 ± 0.6	27 ± 1.7	14 ± 1.2	44 ± 5
$^{208}Pb(^{7}Li, \alpha 4n\gamma)^{207}Bi$	9 ± 1.3	8 ± 1.3	5 ± 1	19 ± 2
$^{120}Sn(^{7}Li, \alpha 2n\gamma)^{120}Sn$	3.0 ± 0.6	4.3 ± 0.7	12 ± 1	14 ± 1.6
$^{120}Sn(^{7}Li, \alpha 3n\gamma)^{120}Sn$	7.3 ± 0.8	17 ± 1.2	< 3	28 ± 1.5
$^{120}Sn(^{7}Li, \alpha 4n\gamma)^{119}Sn$	6.0 ± 0.7	4.9 ± 0.7	< 1	12 ± 1.5

particle γ-ray correlations would arise from residual nuclei with angular momentum oriented perpendicular to the reaction plane. This would produce a uniform γ-ray intensity in the reaction plane but pronounced anisotropy out of plane. The anisotropy observed for low values of x indicates the spin alignment of the residual nucleus and is consistent with high-energy particles being produced in a direct reaction. The isotropy observed for larger values of x suggests little alignment of the residual nucleus and indicates that the low-energy particles observed arise from the decay of a compound nucleus.

It is interesting to note that the yield for (^{7}Li,αxnγ) reactions is greater than the total yield for (^{7}Li, txnγ) and (^{7}Li, dxnγ) reactions. That is, the incomplete fusion of a triton is much more probable than the incomplete fusion of an α-particle. There are several possible explanations of this: (i) the difference in ground state Q-values, (ii) the Coulomb interaction, (iii) difference in binding energy. The ^{208}Pb(^{7}Li,α) reaction has Q = 2.6 MeV, ^{208}Pb(^{7}Li,t) has Q =-11.4 MeV. Thus the reactions producing α-particles are generally more exoergic and since the density of nuclear states increases exponentially with excitation energy, there are more states open to the former than the latter. If one considers ^{7}Li as a bound α - t cluster system, the long-range Coulomb force will tend to align the axis of the approaching ^{7}Li projectile such that the triton is closer to the target. It would therefore be more probable that the triton acts as the participant and interacts strongly with the target. The binding energy of the α-particle is greater than the binding energy of a triton. In a strong interaction with the target fragmentation of the triton is more likely.

Additional reaction mechanisms considered involve the decay of the residual nucleus via charged particle emission and fission, e.g.

(^{7}Li, αxn.yppγ) and (^{7}Li, αf). It will be recalled from Section 3.1 that the inclusive yield of protons was greater for ^{7}Li + ^{120}Sn than ^{7}Li + ^{208}Pb and this reaction channel was initially examined to estimate its significance. An attempt was made to correlate prominent photopeaks with low lying transitions in residual nuclei from the reaction ^{120}Sn(^{7}Li, αxnypγ). No transitions were observed and it is concluded that this type of decay of the residual nucleus is not a significant contributor to the beam velocity yield of charged particles. Decay of the residual nucleus by fission would be more probable for the ^{7}Li + ^{208}Pb reaction and an attempt was made to correlate prominent photopeaks in γ-ray spectra with transitions in the mass region A = 90 - 120. No transitions were unambiguously identified for this type of reaction. Presumably this means that the γ-ray strength is distributed amongst a wide range of possible fission fragments and that there is insufficient statistics to identify any given transition. It is therefore difficult to reach any conclusion on the strength of this reaction channel

3.4 Discussion of Cross Section Balance

In the previous sections the following reaction mechanisms have been identified and discussed:

(i) Sequential break-up of PLF.

(ii) Direct break-up.

(iii) Incomplete fusion.

In this section the quantitative contributions of these processes to the inclusive yield is discussed.

It is appropriate to review the assumptions of such an approach and the limitations of the experimental study presented.

To obtain the differential cross sections from observed particle-particle coincidence yields it is necessary to calculate the effective solid angle for detection of the unbound, outgoing ejectile as indicated in Section 2.6 and equation (2.2). It is assumed that all sequential decays occur isotropically in the rest frame of the unbound particle. The angular correlation of fragments originating from the decay of an excited ejectile can be described by a summation of spherical harmonics

$$P(\theta,\phi) = \left| \sum_{\ell m} a_{\ell m} Y_{\ell m}(\theta,\phi) \right|^2 \qquad (3.5)$$

where $P(\theta,\phi)$ is the probability of detection for angles θ and ϕ and $a_{\ell m}$ are the population coefficients. These are determined by the spin and angular momentum statistics and the reaction mechanism. The summation over possible ℓ-values is limited by the constraint that

$$\underline{J} = \underline{J}_x + \underline{J}_b + \underline{\ell} \qquad (3.6)$$

where $\underline{J}_x$ and $\underline{J}_b$ are the intrinsic spins of the fragments x and b and $\underline{J}$ is the total spin of the ejectile. The assumption of isotropic decay is strictly true only for $\underline{J} = 0$. If $\underline{J} \neq 0$ there is a net alignment of the ejectiles which will affect the angular correlation. However, in the absence of any information on the ejectile alignment in the break-up reactions discussed here, it is of little value to treat the decay of non-zero spin states as being other than isotropic.

The coincidence detection system was designed to detect outgoing fragments from the break-up of PLF's with low relative energies.

Final state interactions have been assumed to be small, i.e. the momentum correlation between the outgoing fragments is unaffected. However, as has already been discussed in Section 3.2, this may not be true, particularly for direct break-up reactions. The effect of final state interactions would be to disturb or remove the momentum correlation of the outgoing fragments and therefore it is possible that these events would not be observed experimentally. The yield for the direct break-up of ^{7}Li should therefore be regarded as a lower limit.

In Tables 3.3-3.7 the differential cross sections for the various reaction mechanisms identified are preserved and compared with the observed inclusive yields of beam velocity d, t and α-particles at the grazing angle.

For the reactions $^{7}Li + ^{120}Sn$ and $^{7}Li + ^{208}Pb$ approximately 30-50% of the inclusive yield of d, t and α-particles is accounted for by the reaction mechanisms identified. The dominance of the inclusive α-particle yield can be seen to be a consequence of the cluster structure of ^{7}Li and the production of beam velocity α-particles in most of the reaction channels identified. The missing cross section can be attributed to projectile fragmentation. In this context projectile fragmentation refers to particle-particle correlations at large opening angles.

TABLE 3.3 Cross Section Balance for the Reaction 70 MeV $^{7}Li + {}^{12}C$ at $\theta_{lab.} = 10°$

Reaction	$d\sigma_d/d\Omega$[1] (mb/sr)	$d\sigma_t/d\Omega$[1] (mb/sr)	$d\sigma_\alpha/d\Omega$[1] (mb/sr)
$(^{7}Li, {}^{7}Li^{*}_{4.63})$	-	12 ± 2	12 ± 2
$(^{7}Li, {}^{6}Li^{*}_{2.18})$	48 ± 7	-	48 ± 7
$(^{7}Li, {}^{8}Be_{gs})$ $(^{7}Li, {}^{8}Be^{*}_{2.94})$	-	-	46 ± 7
Total	48 ± 7	12 ± 2	106 10
$(^{7}Li,X)$	100 ± 20	170 ± 25	460 ± 70

1) Quoted errors include estimates of statistical and systematic errors.

TABLE 3.4 Cross Section Balance for the Reaction 70 MeV $^{7}Li + ^{60}Ni$ at $\theta_{lab.} = 10°$

Reaction	$d\sigma_d/d\Omega$[1] (mb/sr)	$d\sigma_t/d\Omega$[1] (mb/sr)	$d\sigma_\alpha/d\Omega$[1] (mb/sr)
$(^{7}Li, ^{7}Li^{*}_{4.63})$	-	28 ± 5	28 ± 5
$(^{7}Li, ^{7}Li^{*})$	-	8 ± 1	8 ± 1
$(^{7}Li, ^{6}Li^{*}_{2.18})$	70 ± 10	-	70 ± 10
$(^{7}Li, ^{8}Be_{gs})$ $(^{7}Li, ^{8}Be^{*}_{2.94})$	-	-	30 ± 5
Total	70 ± 10	36 ± 5	140 ± 5
$(^{7}Li,X)$	170 ± 30	270 ± 40	890 ± 130

1) Quoted errors include estimates of statistical and systematic errors.

TABLE 3.5 Cross Section Balance for the Reaction 70 MeV $^{7}Li + {}^{96}Zr$ at $\theta_{lab.} = 15°$

Reaction	$d\sigma_d/d\Omega$[1] (mb/sr)	$d\sigma_t/d\Omega$[1] (mb/sr)	$d\sigma_\alpha/d\Omega$[1] (mb/sr)
$(^{7}Li, {}^{7}Li^{*}_{4.63})$	-	22 ± 3	22 ± 3
$(^{7}Li, {}^{7}Li^{*})$	-	4.4 ± 0.7	4.4 ± 0.7
$(^{7}Li, {}^{6}Li^{*}_{2.18})$	39 ± 6	-	39 ± 6
$(^{7}Li, {}^{8}Be_{gs})$	-	-	20 ± 4
$(^{7}Li, {}^{8}Be^{*}_{2.94})$			
Total	39 ± 6	26 ± 3	85 ± 8
$(^{7}Li, X)$	110 ± 20	190 ± 30	600 ± 90

1) Quoted errors include estimates of statistical and systematic errors.

TABLE 3.6: Cross Section Balance for the Reaction 70 MeV $^{7}Li + {}^{120}Sn$ at $\theta_{lab} = 17°$

Reaction	$d\sigma_d/d\Omega$[1] (mb/sr)	$d\sigma_t/d\Omega$[1] (mb/sr)	$d\sigma_\alpha/d\Omega$[1] (mb/sr)
$(^{7}Li, {}^{7}Li^{*}_{4.63})$	-	20 ± 3	20 ± 3
$(^{7}Li, {}^{7}Li^{*})$	-	7 ± 1	7 ± 1
$(^{7}Li, {}^{6}Li^{*}_{2.18})$	33 ± 5	-	33 ± 5
$(^{7}Li, {}^{8}Be_{gs})$	-	-	19 ± 1.4
$(^{7}Li, {}^{8}Be_{2.94})$			
$(^{7}Li, \alpha x n \gamma)$	-	25 ± 7	55 ± 16
$(^{7}Li, t x n \gamma)$	-	-	-
$(^{7}Li, d x n \gamma)$	7 ± 2	-	-
Total	40 ± 5	50 ± 10	150 ± 20
$^{7}Li,X$	90 ± 10	150 ± 20	510 ± 80

[1]Quoted errors include estimates of statistical and systematic errors.

TABLE 3.7: Cross Section Balance for the Reaction 70 MeV $^{7}Li + {}^{208}Pb$ at $\theta_{lab} = 32°$

Reaction	$d\sigma_d/d\Omega$[1] (mb/sr)	$d\sigma_t/d\Omega$[1] (mb/sr)	$d\sigma_\alpha/d\Omega$[1] (mb/sr)
$(^{7}Li, {}^{7}Li^{*}_{4.63})$	-	5.8 ± 0.9	5.8 ± 0.9
$(^{7}Li, {}^{7}Li^{*})$	-	0.9 ± 0.15	0.9 ± 0.15
$(^{7}Li, {}^{6}Li^{*}_{2.18})$	10 ± 15	-	10 ± 1.5
$(^{7}Li, {}^{8}Be_{gs})$ $(^{7}Li, {}^{8}Be_{2.94})$	-	-	5.4 ± 0.9
$(^{7}Li, \alpha x n \gamma)$	-	-	45 ± 15
$(^{7}Li, t x n \gamma)$	-	19 ± 5	-
$(^{7}Li, d x n \gamma)$	3.0 ± 0.9	-	-
Total	13 ± 2	25 ± 5	70 ± 15
$(^{7}Li, X)$	35 ± 5	50 ± 10	240 ± 40

1) Quoted errors include estimates of statistical and systematic errors.

CHAPTER 4

SUMMARY AND CONCLUSIONS

'I have seen the truth and it makes no sense'

G.K. Chesterton

The reaction mechanisms associated with the production of fast charged-particles in ^{7}Li induced reactions at 10 MeV/A have been investigated.

Inclusive measurements of beam velocity d, t, ^{3}He and α-particles were performed. These measurements demonstrated: (i) the reaction mechanisms involved were peripheral, (ii) that the reactions proceeded on a time-scale comparable to the transit time of the projectile, (iii) that the gross features of the reactions were related to the structure of the projectile and not the target and (iv) that the total angle integrated yields represented a significant fraction of the geometric cross section.

Kinematically complete measurements of particle-particle correlations were performed to study the sequential break-up of projectile-like fragments. An appropriate detection geometry permitted the unambiguous identification of both sequential and non-sequential reaction mechanisms. The sequential reaction mechanisms identified were

$$(^{7}Li,\ ^{7}Li^{*}_{4.63} \rightarrow \alpha + t), \qquad (^{7}Li,\ ^{6}Li^{*}_{2.18} \rightarrow \alpha + d),$$

$$(^{7}Li,\ ^{8}Be_{gs} \rightarrow \alpha + \alpha), \qquad (^{7}Li,\ ^{8}Be^{*}_{2.94} \rightarrow \alpha + \alpha).$$

In addition there was some evidence to suggest that the reaction $(^{7}Li,\ ^{5}Li_{gs} \rightarrow \alpha + p)$ occurs with appreciable yield but experimental

limitations make the identification of this reaction mechanism inconclusive. Further, the direct break-up reaction (^{7}Li, $^{7}Li^{*} \rightarrow \alpha + t$) was unambiguously identified for reactions on ^{60}Ni, ^{96}Zr, ^{120}Sn and ^{208}Pb. The peripheral localisation of these reaction mechanisms was demonstrated.

Particle-γ correlation measurements for the reactions $^{7}Li + ^{120}Sn$ and $^{7}Li + ^{208}Pb$ identified incomplete fusion reactions. The dominant reaction channels were (^{7}Li, $\alpha xn\gamma$) and (^{7}Li, $txn\gamma$). In-plane and out-of-plane measurements suggested spin alignment of the residual nucleus and capture of the participant fragment in the reaction plane.

Overall, it has been demonstrated that a variety of reaction mechanisms contribute to the large yield of fast (i.e. beam velocity) charged particles observed in ^{7}Li induced reactions. However, a large fraction of the total break-up yield remains unaccounted for. Possible reaction mechanisms are projectile fragmentation leading to particle-particle correlations with high relative momenta and multibody fragmentation reactions. The latter is less likely since previous studies with heavier projectiles (e.g. Bi 82, Wi 79c) indicate that multibody fragmentation is important beyond 15 MeV/A. Additional in-plane particle-particle correlations could therefore be expected to account for a large fraction (c. 50%) of the total break-up yield.

Further experimental studies of interest might involve the use of polarized $^{6,7}Li$ beams to elucidate semi-classical concepts of reaction mechanisms. A systematic survey of inclusive yields of charged particles from $^{6,7}Li$ induced reactions in the energy region 5 - 20 MeV/A would be of interest to examine the evolution of reaction mechanisms with bombarding energy.

Recently, particle-K x-ray correlation measurements (Si 85) have

been demonstrated to be a powerful tool in obtaining an overall picture of the reaction mechanisms involved in heavy-ion break-up.

Developments in silicon detector technology have resulted in large area 'strip' detectors which in principle possess a number of features useful in break-up studies: (i) arbitrarily good position resolution (to determine θ_{12} and therefore ε), (ii) small spatial separation ($\sim$ 100 μm) of individual detectors (to observe small values of ε), (iii) greater coincidence rates may be achieved. Maximal exploitation of these features requires the development of analogue/logic processing systems of reduced size, complexity and cost. Parallel developments will probably be required in data acquisition and analysis.

Continuing reaction studies with heavy-ions require sophisticated theoretical modelling to provide qualitative and quantitative analysis of data and a detailed microscopic description of the reaction processes. Two models appear appropriate in this context: post-form DWBA and CDCC type calculations. Post-form DWBA has enjoyed some success in describing light-ion break-up reactions. Recently, Shyam and Nagarajan (Sh 85) have re-formulated this model to include a local momentum approximation for finite-range effects and produce a tractable computational problem. CDCC calculations have been similarly successful in describing light-ion break-up. There are indications that application to heavy-ion induced sequential and non-sequential reaction mechanisms could be equally successful.

Much interesting physics may be investigated with break-up reactions. As a class of reaction mechanisms it is of interest if we only consider the large yields associated with break-up reactions. However further reasons for interest are: understanding the evolution

of a variety of reaction mechanisms with energy, the influence of break-up channels on other elastic or reaction channels and spectroscopic studies.

APPENDIX

Tabulation of Data

Inclusive Yields for the Reactions $^{12}C(^{7}Li,X)$ at E_{Lab} = 70 MeV

Lab. Angle (degrees)	$d\sigma_p/d\Omega$ (mb/sr)	$d\sigma_d/d\Omega$ (mb/sr)	$d\sigma_t/d\Omega$ (mb/sr)	$d\sigma_{^3He}/d\Omega$ (mb/sr)	$d\sigma_\alpha/d\Omega$ (mb/sr)
10.0	115 ± 2	101 ± 8	167 ± 4	13.5 ± 0.5	455 ± 9
18.0	93 ± 1	40 ± 2	56.9 ± 0.7	3.9 ± 0.1	152 ± 4
22.0	92 ± 8	26 ± 3	36 ± 4	2.5 ± 0.8	88 ± 5
26.0	76 ± 5	14 ± 2	21 ± 2	1.4 ± 0.4	49 ± 11
30.0	61 ± 3	9.4 ± 0.8	11.9 ± 0.8	0.7 ± 0.1	25 ± 4
35.0	45 ± 2	4.1 ± 0.5	6.8 ± 0.6	0.30± 0.06	10 ± 4

Inclusive Yields for the Reaction $^{60}Ni(^{7}Li,X)$ at E_{Lab} = 70 MeV

Lab. Angle (degrees)	$d\sigma_p/d\Omega$ (mb/sr)	$d\sigma_d/d\Omega$ (mb/sr)	$d\sigma_t/d\Omega$ (mb/sr)	$d\sigma_{^3He}/d\Omega$ (mb/sr)	$d\sigma_\alpha/d\Omega$ (mb/sr)
10.0	191 ± 3	172 ± 3	270 ± 3	17.8 ± 0.04	885 ± 9
14.0	160 ± 1	102.0 ± 0.7	147.0 ± 0.8	9.3 ± 0.2	444 ± 2
18.0	149 ± 1	74.1 ± 0.9	101 ± 1	6.3 ± 0.2	232 ± 2
21.0	139 ± 1	56.7 ± 0.7	65.3 ± 0.6	3.9 ± 0.1	138.0 ± 1.3
24.0	129.0 ± 0.7	39.9 ± 0.4	43.9 ± 0.4	2.29 ± 0.07	88.0 ± 0.9
27.0	121.0 ± 0.7	28.2 ± 0.3	31.0 ± 0.3	1.52 ± 0.06	52.0 ± 0.7
30.0	110.0 ± 0.7	19.0 ± 0.2	21.9 ± 0.3	1.01 ± 0.04	31.0 ± 0.6
33.0	99.4 ± 0.7	14.7 ± 0.2	15.7 ± 0.3	0.55 ± 0.03	15.9 ± 0.8

Inclusive Yields for the Reaction $^{96}Zr(^{7}Li,X)$ at E_{Lab} = 70 MeV

Lab. Angle (degrees)	$d\sigma_p/d\Omega$ (mb/sr)	$d\sigma_d/d\Omega$ (mb/sr)	$d\sigma_t/d\Omega$ (mb/sr)	$d\sigma_{^3He}/d\Omega$ (mb/sr)	$d\sigma_\alpha/d\Omega$ (mb/sr)
10.5	114 ± 25	150 ± 30	280 ± 40	23 ± 11	1020 ± 60
15.0	98 ± 7	107 ± 8	190 ± 10	11 ± 3	600 ± 20
20.0	76 ± 12	67 ± 11	122 ± 16	5 ± 3	264 ± 18
25.0	73 ± 6	50 ± 5	64 ± 5	2.2 ± 0.8	138 ± 7
30.0	58 ± 8	30 ± 5	41 ± 6	0.9 ± 0.8	62 ± 5

Inclusive Yields for the reaction $^{120}Sn(^{7}Li,X)$ at E_{Lab} = 70 MeV

Lab. Angle (degrees)	$d\sigma_p/d\Omega$ (mb/sr)	$d\sigma_d/d\Omega$ (mb/sr)	$d\sigma_t/d\Omega$ (mb/sr)	$d\sigma_{^3He}/d\Omega$ (mb/sr)	$d\sigma_\alpha/d\Omega$ (mb/sr)
11.5	81 ± 2	124 ± 3	242 ± 4	18.6 ± 0.7	786 ± 8
15.0	82 ± 1	109.0 ± 1.5	197 ± 2	10.7 ± 0.4	657 ± 5
17.0	71.4 ± 0.8	87 ± 1	152.0 ± 1.2	8.4 ± 0.3	508 ± 4
19.5	67.4 ± 0.9	76 ± 1	122.0 ± 1.3	5.4 ± 0.3	409 ± 5
22.0	62.8 ± 0.8	66.2 ± 0.8	94 ± 1	3.5 ± 0.3	320 ± 2
24.0	57.0 ± 0.7	53.5 ± 0.7	74.5 ± 0.9	2.73 ± 0.15	234 ± 2
27.5	52.8 ± 0.9	40.5 ± 0.8	56.7 ± 0.9	1.79 ± 0.16	152 ± 2
30.0	42.9 ± 0.4	29.4 ± 0.3	39.0 ± 0.4	1.03 ± 0.06	92.7 ± 0.7
35.0	39.8 ± 0.4	21.4 ± 0.3	25.1 ± 0.4	0.57 ± 0.06	49.0 ± 0.6
40.0	32.3 ± 0.4	14.8 ± 0.3	14.4 ± 0.3	0.27 ± 0.03	21.1 ± 0.5

Inclusive Yields for the Reaction $^{208}Pb(^{7}Li,X)$ at $E_{Lab.}$ = 70 MeV

Lab Angle (degrees)	$d\sigma_p/d\Omega$ (mb/sr)	$d\sigma_d/d\Omega$ (mb/sr)	$d\sigma_t/d\Omega$ (mb/sr)	$d\sigma_{^3He}/d\Omega$ (mb/sr)	$d\sigma_\alpha/d\Omega$ (mb/sr)
11.0	66 ± 9	96 ± 9	204 ± 15	9 ± 3	530 ± 20
13.0	55.5 ± 1.4	119 ± 2	212 ± 3	10.2 ± 0.8	533 ± 4
16.0	45.1 ± 0.5	109.0 ± 0.6	181 ± 1	-	492.0 ± 1.6
20.0	38.2 ± 0.7	80.9 ± 0.8	131.0 ± 1.20	7.1 ± 0.4	457 ± 2
27.0	26.7 ± 0.6	49.0 ± 0.8	69 ± 1	5.55 ± 0.16	339 ± 2
33.0	-	31.5 ± 0.8	50 ± 1	-	226 ± 2
36.0	13.3 ± 0.3	26.2 ± 0.3	36.5 ± 0.3	-	171.0 ± 0.7
40.0	14.3 ± 0.3	19.5 ± 0.4	29.7 ± 0.5	-	110.0 ± 0.9
47.0	5.7 ± 0.2	11.7 ± 0.3	15.0 ± 0.4	1.41 ± 0.16	42.1 ± 0.6

Sequential Break-Up $^{12}C(^{7}Li, {}^{7}Li^{*}_{4.63} \rightarrow \alpha + t)^{12}C_{gs}$ at E_{lab} = 70 MeV

Lab. Angle (degrees)	$d\sigma/d\Omega$[1] (mb/sr)
10.0	8.1 ± 0.6
15.0	2.6 ± 0.12
18.0	6.1 ± 0.3
22.0	1.1 ± 0.2
26.0	1.0 ± 0.14
30.0	0.8 ± 0.16
35.0	0.7 ± 0.1

Sequential Break-Up $^{12}C(^{7}Li, {}^{7}Li^{*}_{4.63} \rightarrow \alpha + t)^{12}C_{4.44}$ at E_{lab} = 70 MeV

Lab. Angle (degrees)	$d\sigma/d\Omega$[1] (mb.sr)
10.0	3.6 ± 0.5
15.0	1.55± 0.09
18.0	1.6 ± 0.16
22.0	1.9 ± 0.3
26.0	0.8 ± 0.13
30.0	0.6 ± 0.12
35.0	0.3 ± 0.1

1) Statistical errors only.

Sequential Break-Up $^{12}C(^{7}Li, {}^{6}Li^{*}_{2.18} \rightarrow \alpha + d)^{13}C$ at E_{lab} = 70 MeV[2].

Lab. Angle (degrees)	$d\sigma/d\Omega$[1] (mb/sr)
10.0	48.0 ± 1.1
15.0	28.6 ± 0.4
18.0	13.8 ± 0.2
22.0	8.6 ± 0.4
26.0	6.0 ± 0.2
30.0	3.5 ± 0.2
35.0	2.0 ± 0.14

Sequential Break-Up $^{12}C(^{7}Li, {}^{8}Be_{gs} \rightarrow \alpha + \alpha)^{11}B$
and $^{12}C(^{7}Li, {}^{8}Be^{*}_{2.94} \rightarrow \alpha + \alpha)^{11}B$ at E_{lab} = 70 MeV[2]

Lab. Angle (degrees)	$d\sigma/d\Omega$[1] (mb/sr)
10.0	23.0 ± 1.1
15.0	9.9 ± 0.2
18.0	4.2 ± 0.15
22.0	2.5 ± 0.2
26.0	1.00± 0.9
30.0	0.50± 0.07
35.0	0.19± 0.017

1) Statistical errors only.

2) Note that total differential cross sections are quoted.

Sequential Break-Up $^{60}Ni(^{7}Li, {}^{7}Li^{*}_{4.63} \rightarrow \alpha + t)^{60}Ni_{gs}$ at $E_{lab.}$ = 70 MeV.

Lab. Angle (degrees)	$d\sigma/d\Omega$[1] (mb/sr)
10.0	28.0 ± 1.5
14.0	13.3 ± 0.3
18.0	4.8 ± 0.2
21.0	2.6 ± 0.13
24.0	1.30 ± 0.07
27.0	0.49 ± 0.04
30.0	0.46 ± 0.04
33.0	0.07 ± 0.017

Direct Break-Up $^{60}Ni(^{7}Li, {}^{7}Li^{*} \rightarrow \alpha + t)^{60}Ni_{gs}$ at $E_{lab.}$ = 70 MeV.

Lab. Angle (degrees)	$d\sigma/d\Omega$[1] (mb/sr)
10.0	7.8 ± 0.4
14.0	2.55 ± 0.06
18.0	0.81 ± 0.05
21.0	0.46 ± 0.03
24.0	0.20 ± 0.016
27.0	0.064 ± 0.009
30.0	0.045 ± 0.008
33.0	0.017 ± 0.005

1) Statistical errors only.

Sequential Break-Up $^{60}Ni(^{7}Li, {}^{6}Li^{*}_{2.18} \rightarrow \alpha + d)\ ^{61}Ni$ at $E_{lab.}$ = 70 MeV[2]

Lab. Angle (degrees)	$d\sigma/d\Omega$[1] (mb/sr)
10.0	67 ± 1.4
14.0	30.5 ± 0.2
18.0	14.5 ± 0.2
21.0	8.4 ± 0.14
24.0	5.03 ± 0.09
27.0	2.95 ± 0.06
30.0	1.69 ± 0.05
33.0	1.35 ± 0.05

Sequential Break-Up $^{60}Ni(^{7}Li, {}^{8}Be_{gs} \rightarrow \alpha + \alpha)\ ^{59}Co$
and $^{60}Ni(^{7}Li, {}^{8}Be^{*}_{2.94} \rightarrow \alpha + \alpha)\ ^{59}Co$ at $E_{lab.}$ = 70 MeV[2]

Lab. Angle (degrees)	$d\sigma/d\Omega$[1] (mb/sr)
10.0	14.8 ± 0.5
14.0	7.8 ± 0.12
18.0	3.8 ± 0.12
21.0	2.14 ± 0.08
24.0	1.27 ± 0.04
27.0	0.75 ± 0.03
30.0	0.55 ± 0.02
33.0	0.32 ± 0.02

1) Statistical errors only.

2) Note that total differential cross sections are quoted.

Sequential Break-Up $^{96}Zr(^{7}Li, {}^{7}Li^{*}_{4.63} \rightarrow \alpha + t)^{96}Zr_{gs}$ at $E_{lab.}$ = 70 MeV

Lab. Angle (degrees)	$d\sigma/d\Omega$ [1] (mb/sr)
10.5	15.0 ± 0.7
15.0	22.3 ± 0.7
20.0	6.0 ± 0.3
25.0	1.9 ± 0.17
30.0	0.9 ± 0.3

Direct Break-Up $^{96}Zr(^{7}Li, {}^{7}Li^{*} \rightarrow \alpha + t)^{96}Zr_{gs}$ at $E_{lab.}$ = 70 MeV

Lab. Angle (degrees)	$d\sigma/d\Omega$ [1] (mb/sr)
10.5	13.7 ± 0.4
15.0	4.4 ± 0.2
20.0	0.76 ± 0.05
25.0	0.17 ± 0.03
30.0	0.05 ± 0.04

1) Statistical errors only.

Sequential Break-Up $^{96}Zr(^{7}Li, {}^{6}Li^{*}_{2.18} \rightarrow \alpha + d)^{97}Zr$ at $E_{lab.}$ = 70 MeV[2]

Lab. Angle (degrees)	$d\sigma/d\Omega$[1] (mb/sr)
10.5	42.2 ± 0.7
15.0	38.9 ± 0.7
20.0	12.6 ± 0.2
25.0	6.2 ± 0.2

Sequential Break-Up $^{96}Zr(^{7}Li, {}^{8}Be_{gs} \rightarrow \alpha + \alpha)^{95}Y$
and $^{96}Zr(^{7}Li, {}^{8}Be^{*}_{2.94} \rightarrow \alpha + \alpha)^{95}Y$ at $E_{lab.}$ = 70 MeV[2]

Lab. Angle (degrees)	$d\sigma/d\Omega$[1] (mb/sr)
10.5	13.1 ± 0.4
15.0	10.1 ± 0.3
20.0	2.71± 0.09
25.0	1.20± 0.09

1) Statistical errors only.

2) Note that total differential cross sections are quoted.

Sequential Break-Up $^{120}Sn(^{7}Li, {}^{7}Li^{*}_{4.63} \rightarrow \alpha + t)^{120}Sn_{gs}$ at $E_{lab.}$ = 70 MeV

Lab. Angle (degrees)	$d\sigma/d\Omega$[1] (mb/sr)
11.5	9.5 ± 0.8
15.0	21.8 ± 0.6
17.0	20.0 ± 0.4
19.5	17.3 ± 0.5
22.0	12.0 ± 0.3
24.0	8.0 ± 0.3
27.5	4.2 ± 0.2
30.0	1.64± 0.08
35.0	0.60± 0.05
40.0	0.15± 0.03

Direct Break-Up $^{120}Sn(^{7}Li, {}^{7}Li^{*} \rightarrow \alpha + t)^{120}Sn_{gs}$ at $E_{lab.}$ = 70 MeV

Lab. Angle (degrees)	$d\sigma/d\Omega$[1] (mb/sr)
11.5	20.2 ± 0.8
15.0	12.9 ± 0.3
17.0	7.2 ± 0.16
19.5	4.2 ± 0.14
22.0	2.22 ± 0.09
24.0	1.10 ± 0.06
27.5	0.67 ± 0.06
30.0	0.31 ± 0.02
35.0	0.10 ± 0.014
40.0	0.026± 0.007

1) Statistical errors only

Sequential Break-Up $^{120}Sn(^{7}Li, {}^{6}Li^{*}_{2.18} \rightarrow \alpha + d)^{121}Sn$ at $E_{lab.}$ = 70 MeV[2]

Lab. Angle (degrees)	$d\sigma/d\Omega$[1] (mb/sr)
11.5	34.9 ± 1.1
15.0	36.5 ± 0.5
17.0	33.2 ± 0.3
19.5	26.4 ± 0.3
22.0	18.6 ± 0.2
24.0	13.1 ± 0.2
27.5	7.6 ± 0.2
30.0	4.10 ± 0.07
35.0	2.00 ± 0.05
40.0	0.80 ± 0.04

Sequential Break-Up $^{120}Sn(^{7}Li, {}^{8}Be_{gs} \rightarrow \alpha + \alpha)^{119}In$

and $^{120}Sn(^{7}Li, {}^{8}Be^{*}_{2.94} \rightarrow \alpha + \alpha)^{119}In$ at $E_{lab.}$ = 70 MeV[2]

Lab. Angle (Degrees)	$d\sigma/d\Omega$[1] (mb/sr)
11.5	10.3 ± 0.5
15.0	11.3 ± 0.3
17.0	9.3 ± 0.2
19.5	7.1 ± 0.2
22.0	4.9 ± 0.17
24.0	3.0 ± 0.12
27.5	1.8 ± 0.13
30.0	0.90 ± 0.04
35.0	0.32 ± 0.02
40.0	0.16 ± 0.02

1) Statistical errors only.

2) Note that total differential cross sections are quoted.

Sequential Break-Up $^{208}Pb(^{7}Li, {}^{7}Li^{*}_{4.63} \rightarrow \alpha + t)^{208}Pb_{gs}$ at $E_{lab.}$ = 70 MeV

Lab. Angle (degrees)	$d\sigma/d\Omega$ [1] (mb/sr)
11.0	4.5 ± 0.7
18.0	2.5 ± 0.3
23.0	2.7 ± 0.6
28.0	6.8 ± 0.9
32.0	5.8 ± 0.3
36.0	3.2 ± 0.4

Direct Break-Up $^{208}Pb(^{7}Li, {}^{7}Li^{*} \rightarrow \alpha + t)^{208}Pb_{gs}$ at $E_{lab.}$ = 70 MeV

Lab. Angle (Degrees)	$d\sigma/d\Omega$ [1] (mb/sr)
11.0	15.2 ± 0.6
18.0	1.8 ± 0.1
23.0	2.9 ± 0.3
28.0	1.8 ± 0.2
32.0	0.92 ± 0.07
36.0	0.47 ± 0.08

1) Statistical errors only.

Sequential Break-Up $^{208}Pb(^{7}Li, {}^{6}Li^{*}_{2.18} \rightarrow \alpha + d)^{209}Pb$ at $E_{lab.} = 70$ MeV[2]

Lab. Angle (Degrees)	$d\sigma/d\Omega$[1] (mb/sr)
11.0	25.5 ± 0.8
18.0	4.1 ± 0.2
23.0	11.7 ± 0.7
28.0	12.2 ± 0.6
32.0	9.7 ± 0.2
36.0	5.7 ± 0.3

Sequential Break-Up $^{208}Pb(^{7}Li, {}^{8}Be_{gs} \rightarrow \alpha + \alpha)^{207}Tl$

and $^{208}Pb(^{7}Li, {}^{8}Be^{*}_{2.94} \rightarrow \alpha + \alpha)^{207}Tl$ at $E_{lab.} = 70$ MeV[2]

Lab. Angle (Degrees)	$d\sigma/d\Omega$[1] (mb/sr)
11.0	8.2 ± 0.5
18.0	2.2 ± 0.1
23.0	5.6 ± 0.5
28.0	4.1 ± 0.4
32.0	2.7 ± 0.13
36.0	1.7 ± 0.17

1) Statistical errors only.

2) Note that total differential cross sections are quoted.

Incomplete Fusion Yields[1,2] for the Reaction $^{7}Li + ^{120}Sn$ at $E_{lab} = 70$ MeV

Lab. Angle (Degrees)	(^{7}Li, t2nγ) dσ /dΩ (mb /sr)	(^{7}Li, t3nγ) dσ /dΩ (mb /sr)	(^{7}Li, t4nγ) dσ /dΩ (mb /sr)	(^{7}Li, d4nγ) dσ /dΩ (mb /sr)
13	10 ± 1 (24 ± 1.4)	12.0 ± 0.6 (30 ± 1)	5.0 ± 0.4 (7.2 ± 0.5)	6.8 ± 0.6 (12.1 ± 0.8)
20	9 ± 1 (17 ± 12)	10.4 ± 0.6 (26 ± 1)	6.1 ± 0.5 (12.9 ± 0.8)	6.7 ± 0.5 (15.2 ± 0.7)
33	< 1 (-)	1.7 ± 0.2 (3.0± 0.3)	< 1 (-)	< 1 (-)
40	< 1 (-)	< 2 (-)	0.7 ± 0.2 (-)	< 1 (-)

1) Statistical errors only.

2) In-plane data is presented. Out-of-plane data are in brackets.

Incomplete Fusion Yields[1,2] for the Reaction $^{7}Li + {}^{120}Sn$ at E_{lab} = 70 MeV

Lab. Angle (degrees)	$(^{7}Li, \alpha 2n\gamma)$ $d\sigma/d\Omega$ (mb/sr)	$(^{7}Li, \alpha 3n\gamma)$ $d\sigma/d\Omega$ (mb/sr)	$(^{7}Li, \alpha 4n\gamma)$ $d\sigma/d\Omega$ (mb / sr)
13	15 ± 1.6 (21 ± 2)	31 ± 1.6 (50 ± 2)	12.0 ± 1.6 (26 ± 2)
20	14 ± 1.6 (23 ± 2)	28 ± 1.5 (58 ± 2)	12 ± 1.5 (26 ± 2)
33	< 4 (–)	3.5 ± 0.6 (-)	3 (–)
40	1.2 ± 0.5 (–)	1.9 ± 0.6 (3.5 ± 0.7)	1.4 ± 0.4 (< 2)

1) Statistical errors only

2) In-plane data is presented. Out-of-plane data are in brackets.

Incomplete Fusion Yields[1,2] for the Reaction $^{7}Li + ^{208}Pb$ at E_{lab} = 70 MeV

Lab. Angle (degrees)	(^{7}Li, $\alpha 2n\gamma$) $d\sigma/d\Omega$ (mb/sr)	(^{7}Li, $\alpha 3n\gamma$) $d\sigma/d\Omega$ (mb/sr)	(^{7}Li, $\alpha 4n\gamma$) $d\sigma/d\Omega$ (mb/sr)
13	19 ± 3 (33 ± 4)	36 ± 3 (73 ± 4)	16 ± 1 (24 ± 1.7)
20	26 ± 2 (51 ± 3)	44 ± 5 (79 ± 5)	19 ± 2 (28 ± 2)
27	9 ± 1.2 (15 ± 1.6)	32 ± 3 (59 ± 4.)	12 ± 3 (16 ± 3)
33	6 ± 1.7 (10 ± 2)	25 ± 2 (37 ± 3)	13 ± 1.2 (13 ± 1.2)
40	3.3 ± 0.5 (6.1 ± 0.7)	12 ± 1.4 (22 ± 1.7)	9 ± 2 (10 ± 2)
47	2.2 ± 0.7 (3.5 ± 0.2)	9 ± 1.7 (13 ± 2)	5 ± 1.5 (6 ± 2)

1) Statistical errors only.

2) In-plane data is presented. Out-of-plane data are in brackets.

Incomplete Fusion Yields[1,2] for the Reaction $^{7}Li + {}^{208}Pb$ at E_{lab} = 70 MeV

Lab Angle (Degrees)	(^{7}Li, t3nγ) dσ/dΩ (mb/sr)	(^{7}Li, t4nγ) dσ/dΩ (mb/sr)	(^{7}Li, d4nγ) dσ/dΩ (mb/sr)
13	17 ± 3 (30 ± 4)	32 ± 5 (45± 6)	11 ± 2 (16 ± 3)
20	14 ± 2 (21 ± 2)	18 ± 2 (31± 3)	9 ± 1.6 (18.2 ± 2)
27	7 ± 1 (11 ± 1.3)	10 ± 1.3 (17± 1.7)	4.5 ± 0.8 (7 ± 1)
33	5 ± 1.5 (11 ± 2)	10 ± 3 (24± 4)	3 ± 1 (6 ± 3)
40	4.3 ± 0.8 (6 ± 1)	5 ± 1 (9± 1.3)	< 2 (-)
47	2.2 ± 0.6 (3.4 ± 0.7)	3.5 ± 0.13 (7 0.7)	< 2 (-)

1) Statistical errors only.

2) In-plane data is presented. Out-of-plane data are in brackets.

REFERENCES

Aa82 E.H.L. Aarts, R.A.R.L. Malfliet, S.Y. van der Werf and R.J. de Meijer, Nucl. Phys. A380 (1982) 465.

Aa85 E.H.L. Aarts, R.A.R.L. Malfliet, R.J. de Meijer, S.Y. van der Werf, G. Baur, R. Shyam, F. Rösel and D. Trautmann, Nucl. Phys. A439 (1985) 45.

Aj84 F. Ajzenberg-Selove, Nucl. Phys. A413 (1984) 1.

Al56 K. Alder, A. Bohr, T. Huus, B. Mottelson and A. Winther, Rev. Mod. Phys. 28 (1956) 432.

Am79a H. Amakawa, S. Yamaji, A. Mori and K. Yazaki, Phys. Lett. 82B (1979) 13.

Am79b H. Amakawa and K. Yazaki, Phys. Lett. 87B (1979) 159.

Am81 H. Amakawa, A. Mori, H. Nishioka, K. Yazaki and S. Yamaji, Phys. Rev. C23 (1981) 583.

Am82 H. Amakawa and T. Tamura, Phys. Rev. C26 (1982) 904.

Am83 H. Amakawa and N. Austern, Aust. J. Phys. 36 (1983) 633.

Au79 R.L. Auble, Nuclear Data Sheets 26 (1979) 385.

Ba76 G. Baur and D. Trautmann, Phys. Rep. 25C (1976) 293.

Ba79 G. Baur, M. Pauli, F. Rösel and D. Trautmann, Nucl. Phys. A315 (1979) 241.

Ba80a B.B. Back, K.L. Wolf, A.C. Mignerey, C.K. Gelbke, T.C. Awes, H. Brewer, V.E. Viola Jr. and P.Dyer, Phys. Rev. C22 (1980) 1927.

Ba80b G. Baur, R. Shyam, F. Rösel, and D. Trautmann, Phys. Rev. C21 (1980) 2668.

Ba83 G. Baur, R. Shyam, F. Rösel and D. Trautmann, Phys. Rev. C28 (1983) 946.

Ba84 G. Baur, F. Rösel, D. Trautmann and R. Shyam, Phys. Rep. 111C (1984) 333 and G.S.I. preprint GSI-83-32.

Be72 F.E. Bertrand, Nuclear Data Sheets B7 (1972) 419.

Be78 I. Bergstrom, J. Blomqvist, C.J. Herrlander, J. Hattula, O. Knuuttila, E. Luikkonen and V. Rahkonen, Z. Phys. A287 (1978) 219.

REFERENCES (Contd.)

Bh78 R.K. Bhowmik, E.C. Pollacco, N.E. Sanderson, J.B.A. England and G.C. Morrison, Phys. Lett. 80B (1978) 41.

Bh79 R.K. Bhowmik, E.C. Pollacco, N.E. Sanderson, J.B.A. England and G.C. Morrison, Phys. Reve. Lett. 43 (1979) 619.

Bh81 R.K. Bhowmik, E.C. Pollacco, N.E. Sanderson, J.B.A. England and C.G. Morrison, Nucl. Phys. A363 (1981) 516 and Daresbury Laboratory preprint DL/NUC/P123E.

Bh82 R.K. Bhowmik, J. van Driel, R.H. Siemssen, G.J. Balster, P.B. Goldhoorn, S. Gonggrijp, Y. Iwasaki, R.V.F. Janssens, H. Sakai, K. Siwek-Wilczyński, W.A. Sterrenburg and J. Wilczyński, Nucl. Phys. A390 (1982) 117.

Bi79 R. Billerey, C. Cerutti, A. Chevalier, N. Chevalier, B. Cheynis and A. Demeyer, Z. Phys. A292 (1979) 293.

Bi80a A.N. Bice, Ph.D. Thesis, University of California, 1980 (unpublished).

Bi80b M. Bini, C.K. Gelbke, D.K. Scott, T.J.M. Symons, P. Doll, D.L. Hendrie, J.L. Laville, J. Mahoney, M.C. Mermaz, C. Olmer, K. van Bibber and H.H. Wieman, Phys. Rev. C22 (1980) 1945.

Bi81 A.N. Bice, A.C. Shotter, D.P. Stahel, and J. Cerny, Phys. Lett. 101B (1981) 27.

Bi82 A.N. Bice, A.C. Shotter and J. Cerny, Nucl. Phys. A390 (1982) 161 and LBL preprint LBL-14100.

Br61 H.C. Britt and A.R. Quinton, Phys. Rev. 124 (1961) 877.

Bu76 M. Buernard, C.K. Gelbke, B.G. Harvey, D.L. Hendrie, J. Mahoney, A. Menchala-Rocha, C. Olmer and D.K. Scott, Phys. Rev. Lett. 37 (1976) 1191.

Bu78 A. Budzanowski, G. Baur, C. Alderliesten, J. Bojowald, C. Mayer-Böricke, W. Oelert, P. Turek, F. Rösel and D. Trautmann, Phys. Rev. Lett. 41 (1978) 635.

Bu79 A. Budzanowski, G. Baur, R. Shyam, J. Bojowald, W. Oelert, G. Riepe, M. Rogge, P. Turek, F. Rösel and D. Trautmann, Z. Phys. A293 (1979) 293.

REFERENCES (Contd.)

Ca78 C.M. Castenada, H.A. Smith Jr., P.P. Singh, J. Jastrzebski, H. Karwowski and A.K. Gaigalas, Phys. Lett. 77B (1978) 371.

Ca80 C.M. Castenada, H.A. Smith Jr., P.P. Singh and H. Karwowski, Phys. Rev. C21 (1980) 179.

Ch82 P. Chowdbury, W.F. Piel Jr., and D.B. Fossan, Phys. Rev. C25 (1982) 813.

Da83a E. Dafni, M.H. Rafailovich, T. Marshall, G. Shatz and G.D. Sprouse, Nucl. Phys. A394 (1983) 245.

Da83b Program written by T. Davinson.

Do75 D.J. Donahue, O. Häusser, R.L. Hershberger, R. Lutter and F. Reiss, Phys. Rev. C12 (1975) 1547.

Dr80 J. van Driel, Ph.D. Thesis, University of Groningen, 1980 (unpublished).

Dr81 J. van Driel, S. Gonggrijp, R.V.F. Janssens, R.H. Siemssen, K. Siwek-Wilczyńska and J. Wilczyński, Phys. Lett. 98B (1981) 351.

Dr82 O. Dragoun, V. Brabec, A. Mastalka, A. Kovalík, M. Rysavý, M. Ya. Kuznetsova and Yu. V. Norseev, Nucl. Phys. A391 (1982) 29.

Eg81 Ch. Egelhaaf, G. Bohlen, H. Fuchs, A. Gamp, H. Homeyer and H. Kluge, Phys. Rev. Lett. 46 (1981) 318.

Fe73 H. Feshbach and K. Huang, Phys. Lett. 47B (1973) 300.

Fr83 W.A. Friedman, Phys. Rev. C27 (1983) 569.

Fu82 H. Fuchs, NIM 200 (1982) 361.

Fu83 T. Fukuda, M. Ishihara, M. Tanaka, H. Ogata, I. Miura, M. Inoue, T. Shimoda, K. Katori and S. Nakayama, Phys. Rev. C27 (1983) 2029.

REFERENCES(Contd.)

Ge77a C.K. Gelbke, D.K. Scott, M. Bini, D.L. Hendrie, J.L. Laville, J. Mahoney, M.C. Mermaz and C. Olmer, Phys. Lett. 70B (1977) 415.

Ge77b C.K. Gelbke, M. Bini, C. Olmer, D.L. Hendrie, J.L. Laville, J. Mahoney, M.C. Mermaz, D.K. Scott and H.H. Wieman, Phys. Lett. 71B (1977) 83.

Ge78a C.K. Gelbke, C. Olmer, M. Buenard, D.L. Hendrie, J. Mahoney, M.C. Mermaz and D.K. Scott, Phys. Rep. 42C (1978) 311.

Ge78b H. Gemmeke, B. Deluigi, L. Lassen and D. Scholz, Z. Phys. A286 (1978) 73.

Ge79 K.A. Geoffrey, D.G. Sarantites, M.L. Halbert, D.C. Hensley, R.A. Dayras and J.H. Barker, Phys. Rev. Lett. 43 (1979) 1303.

Ge80 H. Gemmeke, B. Deluigi, D. Scholz and L. Lassen, Phys. Lett. 96B (1980) 47.

Go64 F.S. Goulding, D.A. Landis, J. Cerny and R.H. Pehl, NIM 31 (1964) 1.

Go74 A.S. Goldhaber, Phys. Lett. 53B (1974) 306.

Go84 P.B. Goldhoorn, G.J. Balster, H.J. Koeslag, R.J. de Meijer, R.H. Siemssen, Z. Sujkowski and H.W. Wilschut, Phys. Lett. 142 (1984) 14.

Gr75 D.E. Greiner, P.J. Lindstrom, H.H. Heckman, B. Cook and F.S. Beiser, Phys. Rev. Lett. 35 (1975) 152.

Ha72 O. Häusser, F.C. Khanna and D. Ward Nucl. Phys. A194 (1972) 113.

Ha77 J.W. Harris, T.M. Cormier, D.F. Geesaman, L.L. Lee Jr., R.L. McGrath and J.P. Wurm, Phys. Rev. Lett. 38 (1977) 1460.

Ha79 U. Hagemann, H.J. Keller, Ch. Protochristow and F. Stary, Nucl. Phys. A329 (1979) 157.

Ha81 B. Harmatz, Nuclear Data Sheets 34 (1981) 735.

He47 A.C. Helmholz, E.M. McMillan, and D.C. Sewell, Phys. Rev. 72 (1947) 1003.

REFERENCES (Contd.)

Ho77 H. Ro, R. Albrecht, W. Dünnweber, G. Graw, S.G. Steadman, J.P. Wurm, D. Disdier, V. Rauch and F. Scheibling, Z. Phys. A283 (1977) 235.

Ho79 H.R. Hooper, P.W. Green, H.E. Siefken, G.C. Neilson, W.J. McDonald, D.M. Sheppard and W.K. Dawson, Phys. Rev. C20 (1979) 2041.

Ho80 H. Ho, P. Gonthier, M.N. Namboodiri, J.B. Natowitz, L. Adler, S. Simon, K. Hagel, R. Terry and A. Khodai, Phys. Lett. 96B (1980) 51.

Ho81 H. Ho and P. Gonthier, NIM 190 (1981) 75.

Hu78 J. Hüfner, C. Sander and G. Wolschin, Phys. Lett. 73B (1978) 289.

In77 T. Inamura, M. Ishihara, T. Fukuda, T. Shimoda and H. Hiruta, Phys. Lett. 68B (1977) 51.

Ja70 D.F. Jackson, Nuclear Reactions (Methuen, London, 1970).

Ja76 R. Jahn, D.P. Stahel, G.J. Wozniak, J. Cerny and H.P. Morsch, Phys. Lett. 65B (1976) 33.

Jo70 R.C. Johnson and P.J.R. Soper, Phys. Rev. C1 (1970) 976.

Ka79 R. Kamermans, H.P. Morsch, R.J. de Meijer and J. van Driel, Nucl. Phys. A314 (1979) 37.

Ka84 K. Katori, private communication.

Ka85 M. Kamimura, M. Yahiro, Y. Iseri, M. Nakano and Y. Sakuragi, Invited paper, 4th Int. Conf. on Clustering Aspects of Nuclear Structure and Nuclear Reactions (Reidel, 1985).

REFERENCES (Contd.)

Kl81 J. Kleinfeller, J. Bisplinghoff, J. Ernst, T. Mayer-Kuckuk, G. Baur, B. Hoffman, R. Shyam, F. Rösel and D. Trautmann, Nucl. Phys. A370 (1981) 205 and Daresbury Laboratory preprint DL/NUC/P135T.

Ko76 D.C. Kocher, Nuclear Data Sheets 17 (1976) 39.

Ko82 D. Kohmoto, M. Isihara, H. Kamitsubo, T. Nomura, Y. Gono, H. Utsunomiya, T. Sugitate and K. Ieki, Phys. Lett. 114B (1982) 107.

Lo78 T. Lönnroth and B. Fant, Physica Scripta 18 (1978) 172.

Lo79 T. Lönnroth, J. Blomqvist, I. Bergström and B. Fant, Physica Scripta 19 (1979) 233.

Lu85 W. Lücking, R. Schreck, K. Keller, L. Lassen, A. Nagel and H.G. Emmeke, Z. Phys. A320 (1985) 585.

Ma77 M.J. Martin, Nuclear Data Sheets 22 (1977) 545.

Ma78 N. Matsuoka, A. Shimizu, K. Hosono, T. Saito, M. Kondo, H. Sakaguchi, Y. Toba, A. Goto, F. Ohtani and N. Nakanishi, Nucl. Phys. A311 (1978) 173.

Ma80 N. Matsuoka, A. Shimizu, K. Hosono, T. Saito, M. Kondo, H. Sakaguchi, Y. Toba, A. Goto, F. Ohtani and N. Nakanishi, Nucl. Phys. A337 (1980) 269.

Ma82 N. Matsuoka, K. Hatanaka, T. Saito, T. Itahashi, K. Hosono, A. Shimizu, M. Kondo, F. Ohtani and O. Cynshi, Nucl. Phys. A391 (1982) 357.

Ma83 K.H. Maier, T. Nail, R.K. Sheline, W. Stöffl, J.A. Becker, J.B. Carlson, R.G. Lanier, L.G. Mann, G.L. Struble, J.A. Cizewski and B.H. Erkkila, Phys. Rev. C27 (1983) 1431.

Mc60 J.A. McIntyre, T.L. Watts and F.C. Jobes, Phys. Rev. 119 (1960) 1331.

Mc80 K. McVoy and M.C. Nemes, Z. Phys. A295 (1980) 177.

REFERENCES (Contd.)

Mo84 T. Motabayashi, H. Ejiri, T. Shibata, K. Okado, M. Sasao, K. Maeda, H. Suzuki, A. Shimizu and H. Sakai, Nucl. Phys. A413 (1984) 290.

Na82 M.A. Nagarajan, I.J. Thompson and R.C. Johnson, Nucl. Phys. A385 (1982) 525 and Daresbury Laboratory preprint DL/NUC/P151T.

Ne80 B. Neumann, H. Rebel, J. Buschmann and H.J. Gils, H. Klewe-Nebenius and S. Zagromski, Z. Phys. A296 (1980) 113.

Ne82 B. Neumann, H. Rebel, H.J. Gils, R. Planeta, J. Buschmann, H. Klewe-Nebenius, S. Zagromski, R. Shyam and H. Machner, Nucl. Phys. A382 (1982) 296 and Daresbury Laboratory Preprint DL/NUC/P148T.

Oh65 G.G. Ohlson, NIM 37 (1965) 240.

Op35a J.R. Oppenheimer, Phys. Rev. 47 (1935) 845.

Op35b J.R. Oppenheimer and M. Phillips, Phys. Rev. 48 (1935) 500.

Pa78 J. Pampus, J. Bisplinghof, J. Ernst, T. Mayer-Kuckuk, R. Ramarao, G. Baur, F. Rösel and D. Trautmann, Nucl. Phys. A311 (1978) 141.

Pa84a D.J. Parker, J. Asher, T.W. Conlon and I. Naqib, Phys. Rev. C (1984) and A.E.R.E. preprint AERE-R-11217.

Pa84b D.J. Parker, Ph.D. Thesis, University of Oxford, 1984, (AERE-R-11464).

Pr73 D. Proetel, F. Reiss, E. Grosse, R. Ley, M.R. Maier and P. von Brentano, Phys. Rev. C7 (1973) 2137.

Ra80 W.D.M. Rae, R.G. Stokstad, B.G. Harvey, A. Dacal, R. Legrain, J. Mahoney, M.J. Murphy and T.J.M. Symons, Phys. Rev. Lett. 45 (1980) 884.

REFERENCES (Contd.)

Ra81 W.D.M. Rae, J. Cole, A. Dacal, R. Legrain, B.G. Harvey, J. Mahoney, M.J. Murphy, R.G. Stokstad and I. Tserruya, Phys. Lett. 105B (1981) 417.

Ra84a W.D.M. Rae and R.K. Bhowmik, Nucl. Phys. A420 (1984) 320.

Ra84b Program written by Dr. V. Rapp.

Ra85a W.D.M. Rae, Invited Paper, 4th Int. Conf. on Clustering Aspects of Nuclear Structure and Nuclear Reactions (Reidel, 1985).

Ra85b V. Rapp, private communication.

Ru82 J.J. van Ruyven, W.H.A. Hesselink, J. Akkermans, P. van Nes and H. Verheul, Nucl. Phys. A380 (1982) 125.

Sa83a Y. Sakuragi, M. Yahiro and M. Kamimura, Prog. Theor. Phys. 70 (1983) 1047.

Sa83b M. Sasagase, M. Sato, S. Hanashima, K. Furuno, Y. Nagashima, Y. Tagishi, S.M. Lee and T. Mikumo, Phys. Rev. C27 (1983) 2630.

Sc77 D. Scholz, H. Gemmeke, L. Lassen, R. Ost and K. Bethge, Nucl. Phys. A288 (1977) 351.

Se47 R. Serber, Phys. Rev. 72 (1947) 1008.

Sh79a R.E. Shroy, A.K. Gaiglas, G. Schatz and D.B. Fossan, Phys. Rev. C19 (1979) 1324.

Sh79b R. Shyam, G. Baur, F. Rösel and D. Trautmann, Phys. Rev. C19 (1979) 1246.

Sh80 R. Shyam, G. Baur, F. Rösel and D. Trautmann, Phys. Rev. C22 (1980) 1401.

Sh81 A.C. Shotter, A.N. Bice, J.M. Wouters, W.D. Rae and J. Cerny, Phys. Rev. Lett. 46 (1981) 12.

Sh83 R. Shyam, G. Baur, A. Budzanowski, J. Bojowald, H. Dabrowski, G. Mayer-Böricke, W. Oelert, G. Riepe, M. Rogge, P. Turek, F. Rösel and D. Trautmann, Phys. Rev. C27 (1983) 2393.

Sh84a A.C. Shotter, V. Rapp, T. Davinson, D. Branford, N.E. Sanderson and M.A. Nagarajan, Phys. Rev. Lett. 53 (1984) 1539.

Sh84b R. Shyam, G. Baur, F. Rösel and D. Trautmann, Phys. Rev. C30 (1984) 1109.

REFERENCES (contd.)

Sh85 R. Shyam and M.A. Nagarajan, Annals of Physics 163 (1985) 265.

Si62 T. Sikkeland, E.L. Haines and V.E. Viola, Phys. Rev. 125 (1962) 1350.

Si85 R.H. Siemssen, G.J. Balster, H.W. Wilschut, P.D. Bond, P.C.N. Crouzen, P.B. Goldhoorn, HAN Shukui and Z. Sujkowski, Phys. Lett. 161B (1985) 261.

St79 D.P. Stahel, Ph.D. Thesis, University of California, 1979 (LBL 9706)

Su85 M. Sugawara, Y. Gono, Y. Ishikawa, M. Fukuda and I. Fujiwara, Nucl. Phys. A443 (1985) 461.

Ta79 T. Tamura, Z. Matumoto, A. Hashizume, Y. Tendow, K. Miyano, J. Ohya, K. Kitao and M. Kanbe, Nuclear Data Sheets 26 (1979) 385.

Ta81a S.L. Tabor, L.C. Dennis and K. Abdo, Phys. Rev. C24 (1981) 2552.

Ta81b E. Takada, T. Shimoda, N. Takahashi, T. Yamaya, K. Nagatani, T. Udagawa and T. Tamura, Phys. Rev. C23 (1981) 772.

Th81 I.J. Thompson and M.A. Nagarajan, Phys. Lett. 106B (1981) 163 and Daresbury Laboratory preprint DL/NUC/P136T.

Th83 I.J. Thompson and M.A. Nagarajan, Phys. Lett. 123B (1983) 379.

Ud80 T. Udagawa and T. Tamura, Phys. Rev. Lett. 45 (1980) 1311.

Ud81 T. Udagawa and T. Tamura, Phys. Rev. C24 (1981) 1348.

Ut83 H. Utsunomiya, S. Kubono, M.H. Tanaka, M. Sugitani, K. Morita, T. Nomura and Y. Hamajima, Phys. Rev. C28 (1983) 1975.

Ut84 H. Utsunomiya, Phys. Rev. C30 (1984) 1748.

REFERENCES (Contd.)

Va83 S. Vajda, W.F. Piel Jr., M.A. Quader, W.A. Watson III, F.C. Yang and D.B. Fossan, Phys. Rev. C27 (1983) 2995.

Vi78 Y.P. Viyogi, T.J.M. Symons, P. Doll, D.E. Greiner, H.H. Heckman, D.L. Hendrie, P.J. Lindstrom, J. Mahoney, D.K. Scott, K. van Bibber, G.D. Westfall, H. Wieman, H.J. Crawford, C. McParland and C.K. Gelbke, Phys. Rev. Lett. 42 (1979) 33.

Wi73 J. Wilczyński, Nucl. Phys. A216 (1973) 386.

Wi79a K. Siwek-Wilczyńska, E.H. du Marchie van Voorthuysen, J. van Popta, R.H. Siemssen and J. Wilczyński, Phys. Rev. Lett. 42 (1979) 1599.

Wi79b K. Siwek-Wilczyńska, E.H. du Marchie van Voorthuysen, J. van Popta, R.H. Siemssen and J. Wilczyński, Nucl. Phys. A330 (1979) 150.

Wi79c J. Wilczyński, R. Kamermans, J. van Popta, R.H. Siemssen, K. Siwek-Wilczyńska and S.Y. van der Werf, Phys. Lett. 88B (1979) 65.

Wi80 J. Wilczyński, K. Siwek-Wilczyńska, J. van Driel, S. Gonggrijp, D.C.J.M. Hageman, R.V.F. Janssens, J. Kukasiak and R.H. Siemssen, Phys. Rev. Lett. 45 (1980) 606.

Wi83 H.W. Wilschut, R.K. Bhowmik, P.B. Goldhoorn, J.F.W. Jansen, R.H. Siemssen, K. Siwek-Wilczńska, Z. Sujkowski and J. Wilczyński, Phys. Rev. 123B (1983) 173.

Wu78 J.R. Wu, C.C. Chang and H.D. Holmgren, Phys. Rev. Lett. 40 (1978) 1013.

Ya79 H. Yamada, D.R. Zolnowski, S.E. Cala, A.C. Kahler, J. Pierce and T.T. Sugihara, Phys. Rev. Lett. 43 (1979) 605.

Ya82 M. Yahiro, M. Nakano, Y. Iseri and M. Kamimura, Prog. Theor. Phys. 67 (1982) 1467.

Ya84 M. Yahiro, Y. Iseri, M. Kamimura and M. Nakano, Phys. Lett. 141B (1984) 19.

REFERENCES (Contd.)

Yo80 G.R. Young, R.L. Ferguson, A. Gavron, D.C. Hensley, F.E. Obenshain, F. Plasil, A.H. Snell, M.P. Webb, C.F. Maguire and G.A. Petitt, Phys. Rev. Lett. 45 (1980) 1389.

Zo78 D.R. Zolnowski, H. Yamada, S.E. Cala, A.C. Kahler and T.T. Sugihara, Phys. Rev. Lett. 41 (1978) 92.